The Effect of Surface Processing Methods on the Laser Induced Damage Threshold of Fused Silica

by

Weiran Duan

A thesis submitted in partial fulfilment for the requirements for the degree of PhD at the University of Central Lancashire

October 2014

To my family

Declaration

I declare that while registered as a candidate for the research degree, I have not been a registered candidate or enrolled student for another award of the University or other academic or professional institution. I declare that no material contained in the thesis has been used in any other submission for an academic award and is solely my own work.

Weiran Duan

Abstract

High peak power laser systems, such as National Ignition Facility (NIF), Laser Mega Joule (LMJ), and High Power laser Energy Research facility (HiPER), include a large amount of optics. Fused silica glass is one of the most common optical materials which is used in these high peak power laser systems owing to its excellent optical properties, especially for the 355nm ultraviolet laser. However, it is generally found that fused silica optics damage under irradiation with a high peak power laser beam, and the laser induced damage (LID) becomes the limit to increasing the laser power. Theoretically, the laser induced damage threshold (LIDT) of fused silica substrates is high, while it drops significantly due to the poor surface quality created in the manufacturing process.

This project aims to find a series of fused silica optical surface processing techniques which are able to improve the surface quality and increase its LIDT when irradiated using high peak power lasers. This work consists of the following contents：

1. According to the mechanisms of LID, the effects of surface structural defects and contaminants on the LID are analysed and some simulation work is done.
2. By means of the Magnetorheological Finishing (MRF) method, surface structural defects, i.e. surface and sub-surface damage, are removed because the MRF method is a non-fracture polishing process.
3. Parameter optimisation in the MRF process is done by the Taguchi designing method. This optimisation mainly focuses on the surface roughness because it is also another factor that limits the LIDT.
4. Two post polishing treatments, Ion Beam Etching (IBE) and a HF-based etching process (buffered oxide etch (BOE)), are used in this work to remove contaminants left by the former polishing steps (conventional polishing and MRF

processes).

5. A series of LIDT tests are done to verify the validity of the above work. Results show that the MRF process, BOE etching and IBE treatment are all useful in improving the LIDT of fused silica optics.

The main contribution to knowledge of this work is that this work provides a series of processing techniques to increase the LIDT of fused silica optics. These techniques involve the MRF procedure, IBE method and BOE etching in sequence after the conventional grinding and lapping processes. These processing techniques are validated by several groups of LIDT tests.

Table of Contents

List of Tables

List of Figures

Nomenclature

AMP – Advanced Mitigation Process

ANOVA – Analysis of Variation

BOE –Buffered Oxide Etch

CCD – Charge-coupled Device

CCOS – Computer Controlled Optical Surfacing

CI – Carbonyl Iron

CMP – Chemical Mechanical Polishing

CNC – Computerised Numerical Control

CW – Continuous Wave

DKDP –Deuterated potassium dihydrogen phosphate (KD_2PO_4)

D-T – Deuterium-Tritium

EEM – Elastic Emission Machining

EEO – Electrical Energy per Order

FEA – Finite Element Analysis

FDTD –Finite Difference Time Domain

FJP – Fluid Jet Polishing

FOA – Final Optics Assembly

HF –Hydrofluoric

HiPER–High Power laser Energy Research facility

IBE – Ion Beam Etching

ICF – Inertial Confinement Fusion

KDP –Potassium dihydrogen phosphate (KH_2PO_4)

LB – Lower is Better

LID – Laser Induced Damage

LIDT – Laser Induced Damage Threshold

LIEF – Light Intensity Enhancement Factor

LIL – Ligne d'integration laser

LLNL – Lawrence Livermore National Laboratory

LMJ– Laser Mega Joule

MR –Magnetorheological

MRF –Magnetorheological Finishing

MRR – Material Removal Rate

NIF –National Ignition Facility

NUDT – National University of Defense Technology

PMC – Perfect Magnetic Conductor

PRF – Pulse-Repetition-Frequency

PSD – Power Spectral Density

RMS – Root Mean Square

SEM – Scanning Electron Microscopy

SIMS – Secondary Ion Mass Spectroscopy

SSD –Sub-surface damage

SWLI – Scanning White Light Interferometer

TE – Transverse Electric

UNHT – Ultra Nanoindentation Tester

UV – Ultraviolet

YAG – Yttrium aluminium garnet

List of Symbols

a, length of indentation mark

B, temporal shape of laser beam

C, heat capacity of component material

c, length of median crack

D, diffusivity of component

d_c, mean diameter of polishing particles

d_{crit}, critical indentation depth

E, electric field

E_0, electric field in the uniform dielectric bulk

E_{inc}, incident electric field

E_{th}, damage threshold electric field

E_w, Youngs modulus

E_x, electric field in x-direction

E_y, electric field in y-direction

E_z, electric field in z-direction

$\boldsymbol{e_s}$, wave propagation direction

F_z, buoyant force

F_N, normal force imposed on abrasive particle

F_P, the normal load on abrasive particle imposed from soft polishing film

F_S, tangential shear force imposed on abrasive particle

f_l, fraction of abrasive particles between the polishing pad and work-piece surface involved in polishing

g, acceleration due to gravity

H_w, hardness

H_x, magnetic field in x-direction

H_y, magnetic field in y-direction

H_z, magnetic field in z-direction

K_{IC}, fracture toughness

κ, thermal conductivity of component

L_{LB}, loss function for objective of the LB

M, ferric induction of magnetic fluid

N, the number of measurements in a trial, used in Taguchi method

N_L, the number of loaded abrasive particles between the polishing pad and work-piece surface

N_T, the number of total abrasive particles between the polishing pad and work-piece surface

n, refractive index

n_c, the number density of the nuclei

n_{wheel} is wheel rotating speed

n_λ, refractive index on light wavelength λ

P, peak load on the Vickers indenter in the fracture toughness test

P_T, total load applied on the polishing pad

p, normal load per polishing particle

p_c, initiation load for median crack

p_{crit}, critical normal load

p_l, initiation load for lateral crack

R, surface reflectivity

R_{wheel}, the radius of polishing wheel

r_a, mean radius of the abrasive particle

r_p, radius of indentation area on MR fluid polishing tool

r_w, radius of indentation area on work-piece

S, critical damaging stress of component

S/N_{ratio}, S/N ratio

T, temperature of component

T_m, melting temperature optical material

V, volume of abrasive particle

$wt\%$, weight concentration

x_1, the diameter of an abrasive particle for the interaction between MR fluid polishing tool and abrasive particle

x_2, he diameter of an abrasive particle for the interaction between abrasive particle and work-piece surface

y_i, the ith measured value in a run, used in Taguchi method

α, a nondimensional proportionality coefficient, around $(1.0\sim1.6)\times10^4$

δ, an empirical constant used in the fracture toughness test, taken to be 0.16

δ_p, depth for an abrasive particle penetrating into MR fluid polishing tool

δ_w, depth for an abrasive particle penetrating into work-piece

ε, permittivity for the isotropic media

ε_0, dielectric permittivity, equals to $8.85\times10^{-12}\mathrm{F/m}$

λ, wavelength, 355 nm used in this thesis

μ, permeability for the isotropic media

μ_0, magnetic permeability, equals to $4\pi\times10^{-7}\mathrm{H/m}$

ρ_a, mass density of abrasive particle

ρ_f, mass density of MR fluid

σ, root mean square (RMS) roughness of optical surface

τ, the nuclear fusion reaction time

ω, basic frequency of Nd:YAG laser, its correlative wavelength is 1.06 μm

Acknowledgements

My graduate career has been a long journey. Although at times it was very difficult, I have learned from my experiences and they have been very rewarding. The experience will benefit me in the rest of my life. There have been a great number of people that have touched my life and to them I extend my deepest appreciation.

First of all, I would like to thank my PhD Director of Studies, Prof. Ian Sherrington. Prof. Sherrington has a lot of experience to supervise a research student. I am truly fortunate to have had an opportunity to learn from him. He also spent a lot of time on my thesis and I really appreciate for his help.

I also would like to thank my supervisor, Prof. Xiongwei Liu. He introduced me to University of Central Lancashire and gave me this opportunity to study in this university. He helped me a lot in terms of both studying and living in the UK. When I came to the UK the very first time, he gave me a very warmly welcome and accommodation. He also spent much time on my project and I am thankful for his help.

Dr. Nathalie Revenier is another supervisor of mine. She is helpful for my PhD study. She seems knows everything about engineering and never minds helping me when I had problems. Moreover, she is a very nice lady even though sometimes I could not understand her accent very well.

I also would like to thank Prof. Yifan Dai, who works in National University of Defense Technology (NUDT), Changsha, China. I first started working with Prof. Dai as an undergraduate and his love of research inspired me to continue on with graduate school. In my final year in China, he gave me a lot of support and provided the experimental facilities I used in China. He has a lot of knowledge about optical fabrication, and I am luckily to have had the opportunity to learn from him.

I was very fortunate to have the opportunity to conduct my research in school of Computing, Engineering, and Physical Science and receive funding both from the Chinese Scholarship Council and University of Central Lancashire.

I also want thank Dr. Sha Ma, Dr. Xiao Xiao Cai, Dr. Ruitao Peng, Dr. Xinzi Tang, Dr Hongzhi Chen, Dr. Yingzhu Li, Dr. Yifan Xu, Dr, Xiaoyin Guan, Dr. Gan Lu, Han Cao, Hong Gao, Jiakang Chang, and Qian Hong, Guangyao Zhang. They are my best friends in the University of Central Lancashire. I also want thank Zhicheng Liu, Zhangqing Liu, who were my ex-housemates in the UK. I wish everyone a good future life.

I also want thank my international friends, Dr. Kaushik Nag, Dr. Sarma Volety and his wife Anjani Volety, and Dr. David George and his wife Sue George. They helped me a lot to learn the UK culture and improve my English skill. I hope I can continue our friendship for many years.

I also would like to thank all staffs in the Precision Engineering Laboratory in NUDT, especially Dr. Feng Shi, my colleague Yong Shu, and technicians who conducted some experiments for me. I also would like to give special thanks to my classmates Dr. Ci Song, Dr. Lingyan Ding and Yong Liu. They worked with me for many years and gave me a lot support when I was in China. I also would like to thank the staff of Tongji University and Central South University who helped me to finish my tests.

I also want to thank Prof. Guoxi Li and Dr. Peidong Han. Prof. Guoxi Li was an academic visitor in 2011 and gave me some help both for my research and life. Dr. Peidong Han studied in the UK in 2009 – 2012 and also gave me a lot of support.

My whole family is just absolutely fantastic. No matter what, they are always there for me, and I am just truly supported. I especially want to thank my parents. Throughout my entire life I have always been given love and encouragement.

CHAPTER 1

INTRODUCTION

1.1 High peak power laser systems

1.1.1 Demand of high peak power laser systems

We have two methods, nuclear fission and nuclear fusion, to get the huge amount of nuclear energy from high-powered atomic bonds. Nuclear fission is the process during which large atoms split into smaller ones. Nuclear fusion, on the contrary, is the process that two or more lighter atoms are combined and form a larger one [1].

Currently the nuclear fission-type reactor has been developed greatly and is well used for energy systems in countries such as France and Japan. However, the high-level of radioactive wastes, which are created during the fission reaction, are extremely hazardous to human health and the environment. Nuclear power plant accidents, such as the Chernobyl disaster (Pripyat, Ukraine, 1986) and Fukushima Daiichi nuclear disaster (Okuma, Japan, 2011), had a catastrophic outcome.

Nuclear fusion technologies usually occur at such high temperature that atoms are able to be ionised as electrons of the atoms are stripped off by the heat. Therefore atoms in fusion processes are described as ‘nuclei’ instead of ‘atoms’. Nuclear fusion processes have some advantages which has made fusion become a hot research topic over the world. These advantages are as follows:

1. In a nuclear fusion process, the best fuel from an energy perspective is a one to one mix of deuterium (D) and tritium (T). Both D and T are heavy isotopes of

hydrogen which have rich stores in the oceans.

2. The energy released by a nuclear fusion process is 3~4 times higher than that released by nuclear fission process.

3. Nuclear fusion is an environment friendly method as few radioactive wastes are generated by nuclear fusion process.

4. Nuclear fusion requires a high density and high temperature environment to work. It means that fusion the process will stop automatically if the reaction goes out of control.

To keep a fusion reactor running, the energy released in the fusion process should be greater than the energy needed for feeding the fusion auxiliary devices. In other words, for running self-sustained, a net energy gain should be nonnegative. Lawson [2] in 1957 gave the so-called Lawson criterion for D-T fusion reaction:

$$n_c \tau \geq 3.9 \times 10^{14} \left(\mathrm{s} \cdot \mathrm{cm}^{-3} \right) \tag{1.1}$$

where n_c is the number density of the nuclei (cm^{-3}), and τ is the nuclear fusion reaction time (s). The Lawson criterion provides two ways to meet the nuclear fusion ignition condition: a) increasing the number density of nuclei; and b) increasing the fusion reaction time. Moreover, fusion reactions also require a minimum fuel temperature of 100 million K [3].

There are two major branches of fusion energy research over the world to achieve controlling nuclear fusion reaction. One is inertial confinement fusion (ICF) and the other is magnetic confinement fusion. ICF is to compress and heat the fuel target which is typically a pellet generally contains a mixture of D-T fuel [4]. The aim of ICF is to provide the fusion condition that is known as 'ignition'. Generally ICF devices deliver high energy beams of laser light to the outer layer of target pellet to compress and

heat the fuel in a short time. The heated outer layer of the fuel pellet explodes and produces a reaction force against the remainder of the fuel. This reaction force pushes the fuel inward and compresses the fuel target. Figure 1.1 demonstrates the schematic picture of the ICF stages, where the blue, orange, and purple arrows are respectively the laser radiation, blow off, and thermal energy transported inwardly. The four stages shown in Figure 1.1 are:

1. Laser beams irradiate the target surface and heat it rapidly to form a plasma envelope;
2. The hot surface fuels explode and blow off, which induces compression of the fuels;
3. The fuel core is compressed to high density and ignites at temperature of 10^8 K;
4. Thermal nuclear burns rapidly and generates many times energy greater than input energy.

To achieve a high enough power laser beam to reach the 'ignition' condition in the ICF device, the laser beam is required to compress extremely in terms of time and space. Therefore high peak power laser systems, which are under development at different stages over the world, are used in ICF devices to achieve the requirement of the 'ignition' condition.

1.1.2 Examples of high peak power laser systems

1. National Ignition Facility (NIF) [5-10]

The NIF, the world's most energetic laser system, started its construction in 1997 at University of California Lawrence Livermore National Laboratory (LLNL) in the USA and successfully completed its first experiment in 2009. The NIF consists of 192 laser beams

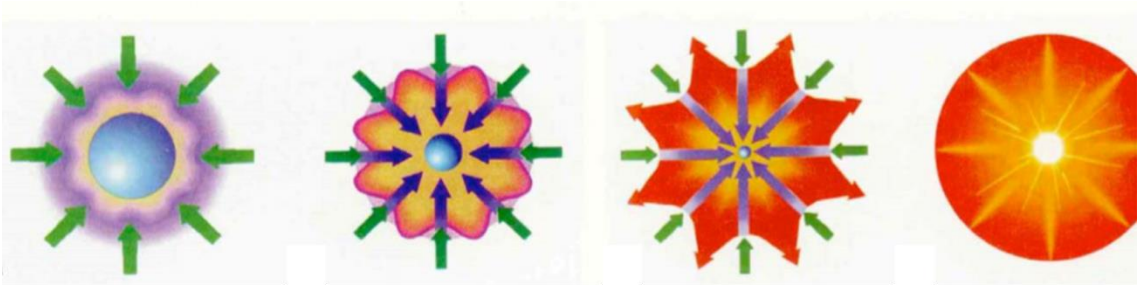

Figure 1.1 Schematic picture of ICF stages using laser [11]

which are able to focus up to 1.8 megajoules (MJ) of energy and 500 terawatts (TW) of power on the fuel target. The huge energy is greater than the essential energy to make the target fuel compress to reach the 'ignition' condition. The NIF is about 150m in length, 90m in width, and seven storeys tall. Figure 1.2 shows an engineering rendering of the NIF. Upper left are the two laser bays and lower right is the switch yard (in red). The spherical fuel target chamber (in silver) is in the centre of lower right where the 192 laser beamlines converge. Figure 1.3 is schematic of one of 192 laser beamlines in the NIF.

The NIF includes 7360 metre-scale (around 0.5m to 1m) aperture optics which make the NIF not only the largest laser but also the largest optical system in the world. These large numbers of optics contain 6 main types of functional optics which can achieve the requirement of the laser systems for ICF. Table 1.1 summaries the type, number and key materials of large aperture optics used in the NIF. This large amount of high quality optics often requires the manufacturing rate to be very high, in the case of the NIF system, over 100 precision optics per month [6].

Table 1.1 Summary of large aperture optics used in the NIF [8]

Optic	**Number required**	**Key material(s)**
Amplifier slabs	3072	Phosphate glass
Mirrors and polarisers	1600	HfO_2/SiO_2 coating on BK-7
Windows and lenses	1728	SiO_2
Crystals	576	DKDP and KDP
Gratings	192	SiO_2
Debris shields	192	SiO_2
	Total:7360	

Figure 1.2 An engineering rendering of the NIF [9]

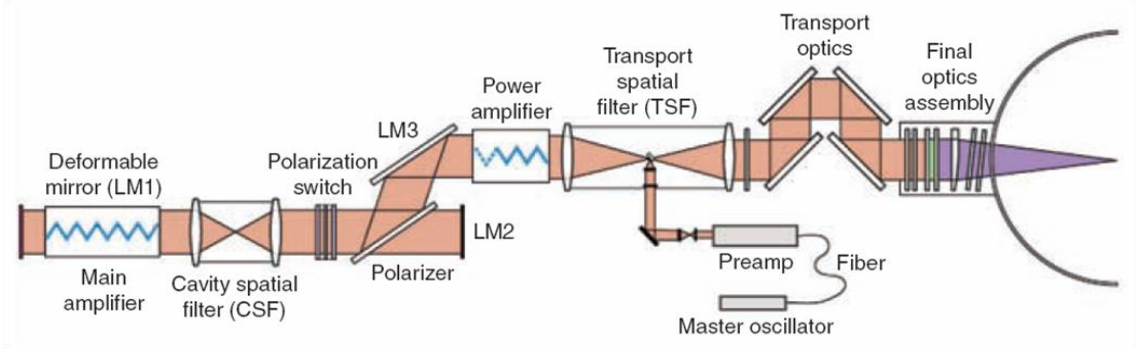

Figure 1.3 Schematic of one of 192 NIF beamlines [9]

The NIF that consists of such plenty optics is a very complex laser system. In the NIF the fundamental laser frequency is infrared light (frequency at 1ω and wavelength at 1.06 μm). But it will be tripled to its third harmonic ultraviolet 3ω (355 nm) in the final optics assembly (FOA) to solve the failure which used to happen in Shiva laser system [9]. The light is converted by a nonlinear crystal frequency converter (comprised of KDP and DKDP). The converted laser light then enters the wedged focus lens to refract any unconverted light (at 1ω and 2ω) away from the target. In FOA, the debris shields, which are made of relatively low-cost fused silica glass, are used to block the target debris and protect the more expensive optics in the FOA. Another optical component in the FOA is the diffraction grating which is used to diffract a small amount of the beam energy to the diagnostic package. The schematic layout of one FOA in the NIF is demonstrated in Figure 1.4.

2. Laser Megajoule (LMJ) [12-15]

LMJ is the French project which started in 2003 after the Ligne d'integration laser (LIL, LMJ prototype) was commissioned in 2002. It consists of up to 240 laser beamlines and is planned to output a 1.8 MJ and 550TW ultraviolet laser beam (wavelength at 355nm). The LMJ facility covers a total area of more than 40,000 m^2 (300m in length and 150m in width) and around 35m in height. Figure 1.5 shows a rendering view of the LMJ facility, where a target chamber is located in the centre.

The target chamber is comprised of an aluminium sphere which is 10m in diameter and with 260 holes. The 240 laser beams are grouped into 8 groups of 30 clusters. Then each laser beam is passed through glass amplifiers and optical frequency multipliers to get high energy and triple the light frequency into the ultraviolet. Mirrors are also used in the LMJ system to optimise the beam lights and arrange them to impinge the target which is filled with D-T fuel from all sides. The target chamber is shown in Figure 1.6.

The first experiment of LMJ facility will be carried out at the end of 2014.

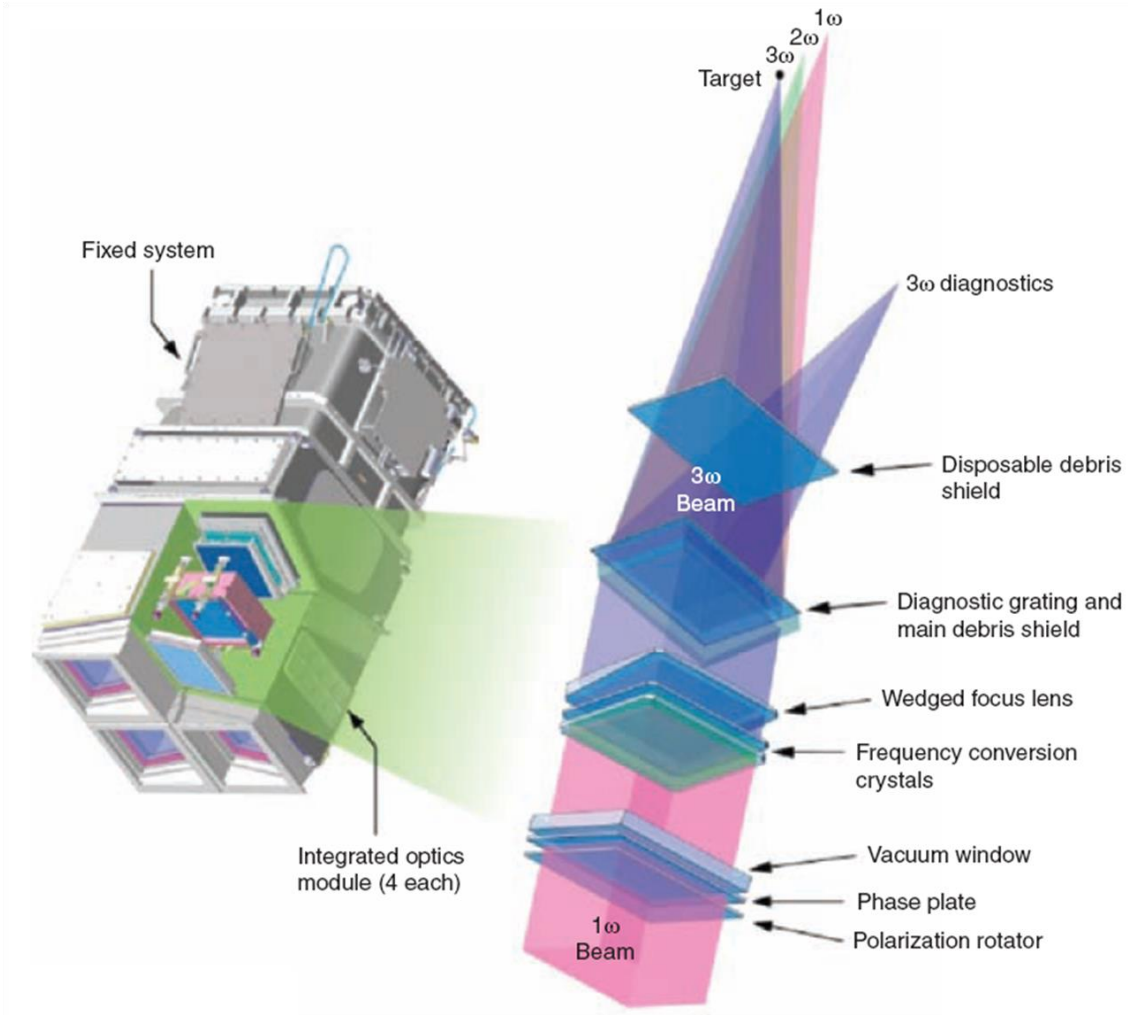

Figure 1.4 Schematic layout of one final optics assembly in the NIF [9]

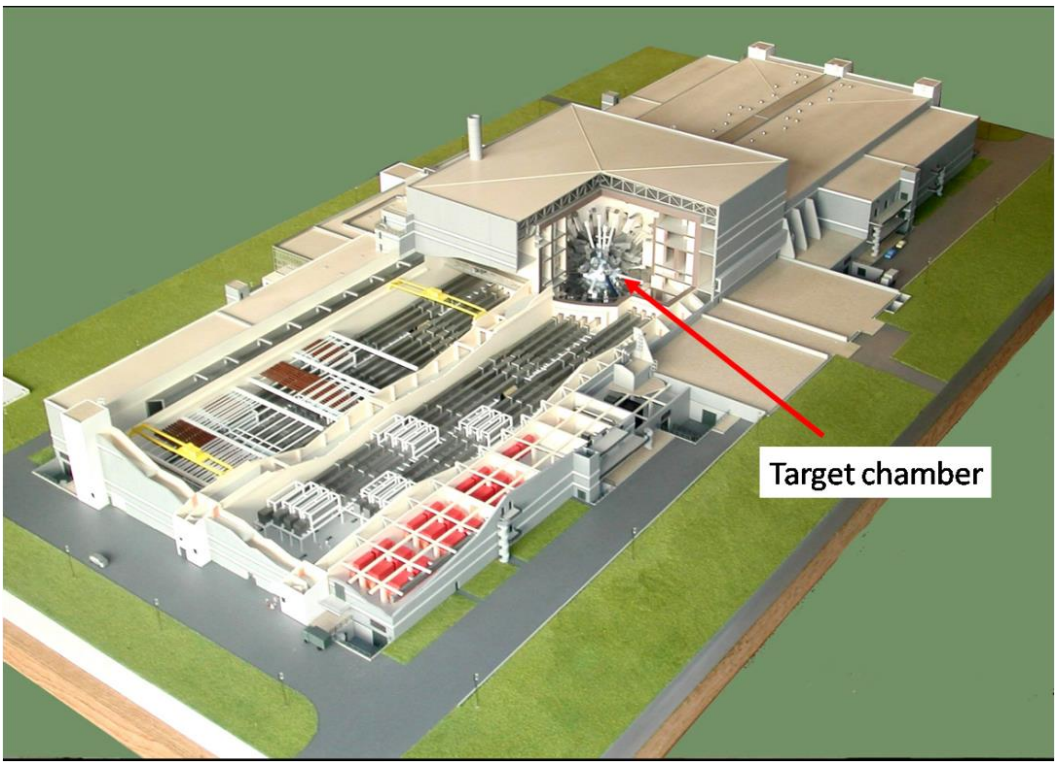

Figure 1.5 Rendering view of the LMJ facility [14]

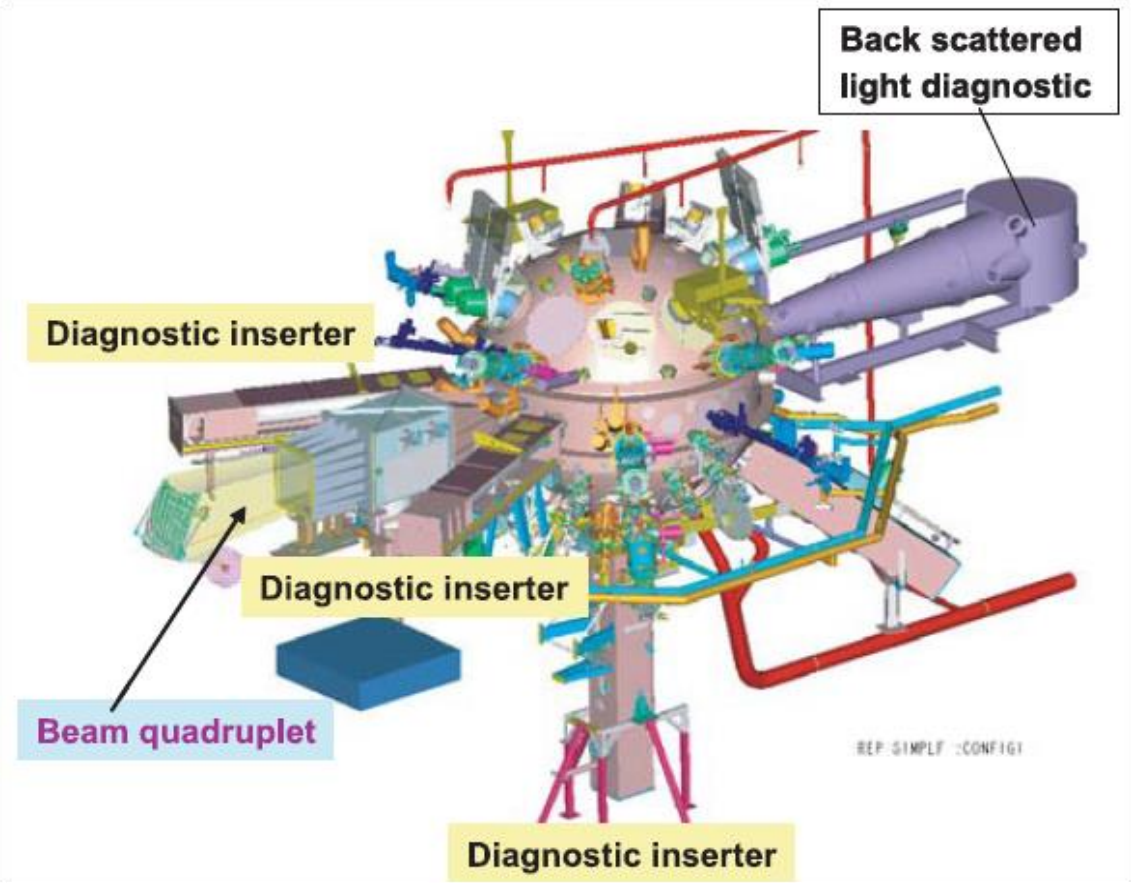

Figure 1.6 CAD view of the target chamber of LMJ system

3. High Power laser Energy Research facility (HiPER)

HiPER is a proposed experimental ICF device which is driven by lasers and is still at the design stage for possible building in the Europe Union. Figure 1.7 is a schematic of the planned HiPER facility [16]. HiPER is the first plan which is designed for using the 'fast ignition' approach to generate nuclear fusion. This nuclear fusion generated by 'fast ignition' technology produces power outputs of about the same magnitude as conventional designs, but uses a much smaller laser system. Therefore, HiPER will get much higher 'fusion gain' than typical devices such as NIF, and reduce the construction costs by about 10 times [17].

HiPER is planning to use a few petawatts (PW) of power – more than 10 000 times the entire capacity of the UK National Grid – in less than a picosecond (ps) to ignite the fuel. HiPER may need a series of laser beams to work coherently. The aperture of the optical lens is about $25m^2$, which is also a big challenge [18]. Figure 1.8 is a sketch map of a laser bay in the HiPER project. Four PW-level laser beams at 3ω (355nm in wavelength) plus one PW-level laser beam at 1ω will be combined and delivered to the target bay for 'fast ignition'.

1.2 Technical justification of the work

Fused silica glass (SiO_2) is one of the most common optical materials which is used in these high peak power laser systems owing to its near perfect optical properties, such as excellent transmission characteristics, especially for the 3ω (355nm) ultraviolet lasers [8]. However, it is generally found that fused silica optics are damaged under the irradiation of high peak power laser beams, and this Laser Induced Damage (LID) could be bulk annealing, surface melting, material softening and bending, cracking, pitting, bulk melting, vaporization and violent shattering and therefore is a non-reversible change in the optical material [19]. LID is usually created when the laser fluence is

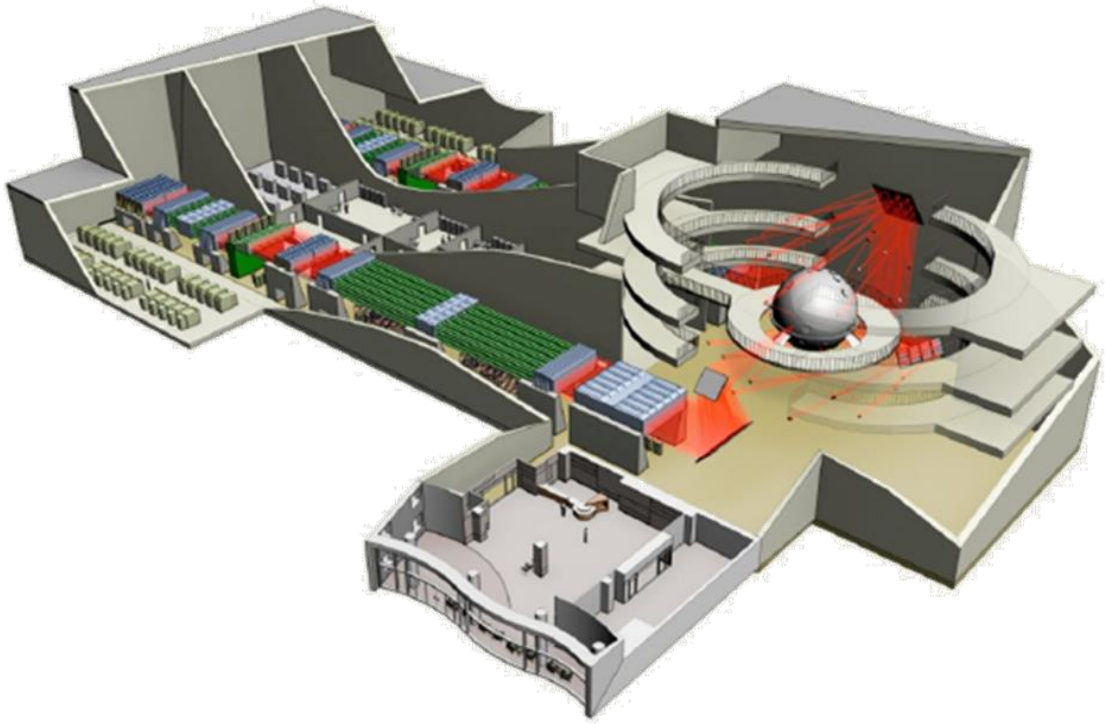

Figure 1.7 HiPER facility (in planning) [16]

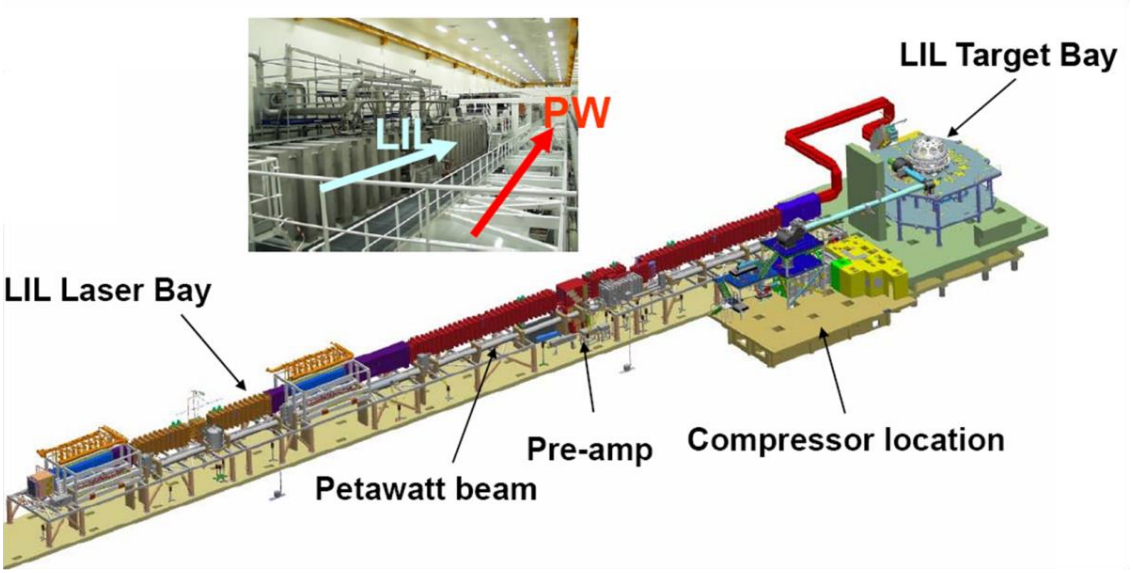

Figure 1.8 High energy beam in the HiPER project [18]

higher than its damage threshold, so it becomes the limit in the laser power that can be transmitted.

Obscuration loss and near-field intensity modulation generated due to LID on the optical surface largely determines the lifetime of fused silica optical components [20]. In relation to the cost, the complete laser system is required to tolerate the high laser power. A reduced laser power handling capability results in an increase number of laser beamlines or enlarging the aperture size of optics, and leads to a dramatic increase in manufacturing cost. Therefore, increasing the Laser Induced Damage Threshold (LIDT) will enhance the performance of high peak power laser systems and effectively reduce the manufacturing cost [21].

Theoretically, the LIDT of fused silica substrates is high (can reach to 100 J/cm^2) [22], but it drops significantly due to poor surface quality created in the manufacturing processes. However, it is possible to increase the LIDT and enhance the laser resistance of fused silica optics. Taking the NIF as an example, in 1997, under irradiation of 8 J/cm^2 at 3ω (355 nm) laser fluence, the number of laser-initiated damage sites on half-metre fused silica optics was about 10^4 per optic. This was poor in relation to the demand (no damage under irradiation of 8 J/cm^2 at 3ω laser fluence) of the NIF. However, after 10-15 years' work by the researchers, the number of damage sites reduced to <5 per optic (2009) under the same laser irradiation [23]. The development of the NIF is shown in Figure 1.9.

Even though researchers at the NIF have been investigating the laser damage for many years and made great progress, it is still not easy to understand how to get a higher LIDT for fused silica optics because of the unclear initiation mechanism of LID in fused silica. Therefore, it is appropriate to research method for improving the LIDT of fused silica surfaces.

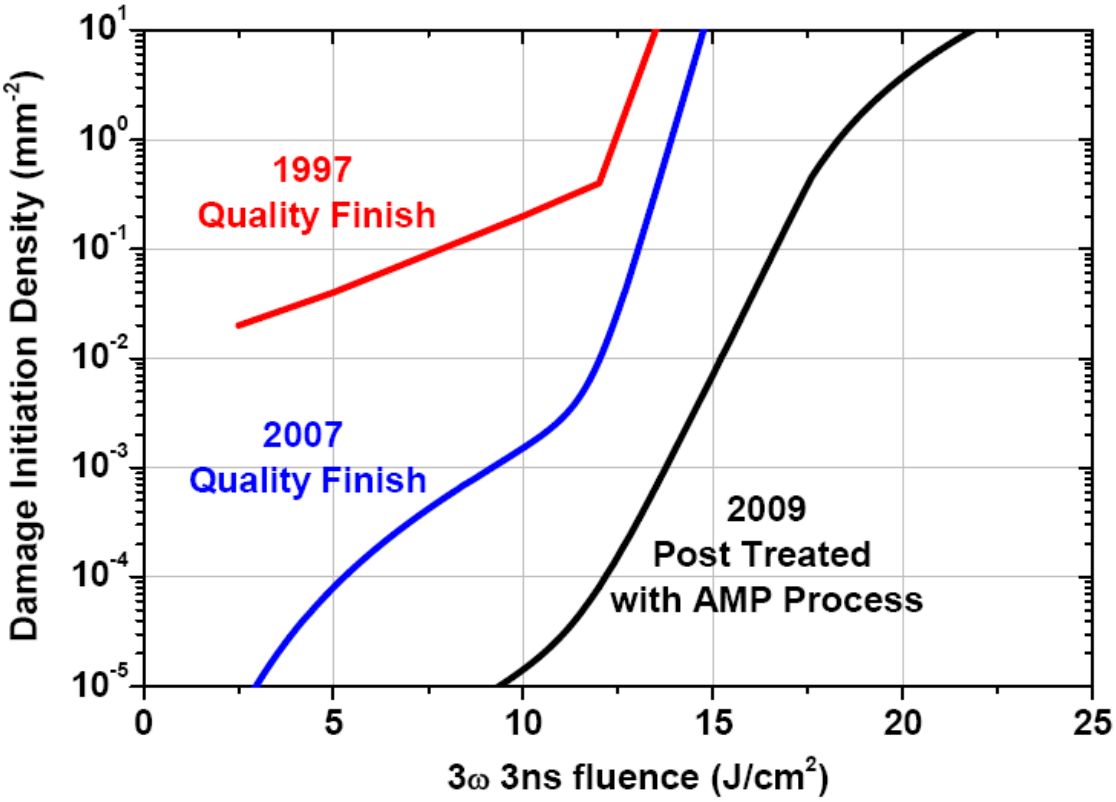

Figure 1.9 Damage initiate density at fused silica surfaces after various manufacturing processes under the irradiation of laser influence (3ω, 3ns) [23]. Before 2007, they mainly focused on fabrication improvement for the fused silica surface; while they introduced the Advanced Mitigation Process (AMP), which is a post polishing treatment method using ultrasonic/megasonic agitation during HF-based etching and rinsing, and got much better result in 2009.

1.3 Aim and objectives of the project

As the LID of fused silica optics is an important factor which limits the performance of high peak power laser systems, it is very urgent to explore new finishing techniques because desired properties not yet reached.

The aim of this work is to find a series of fused silica optical surface processing techniques which are able to improve the surface quality and increase its LIDT under the irradiation of high peak power laser.

To achieve this aim, main objectives of this work are as follows:

- To investigate the effects of surface damage and impurities on inducing damage of fused silica optics under the irradiation by high peak power lasers.
- To analyse the effect of using magnetorheological finishing (MRF) for removing surface damage on fused silica optics.
- To optimise polishing parameters in the MRF process to reduce the roughness of fused silica optical surfaces.
- To remove contaminants from fused silica surfaces after polishing processes by means of post polishing treatments.
- To report a set of surface processing techniques which improve LIDT of fused silica.

1.4 Collaborations

The works in this thesis were conducted by UCLan and many other collaborators. The information of these collaborations is shown in Table 1.2. The nanoindentation test and contaminant test were operated by the technicians of Central South University and SAE Magnetics (HK) Ltd., respectively. The LIDT test was conducted by the author and staff

Table 1.2 Collaboration of this thesis

Collaborator	Location	Equipment	Work	Operator
NUDT	Changsha, China	Lapping machine	Surface polishing	Weiran Duan
NUDT	Changsha, China	MRF machine	Surface polishing	Weiran Duan
NUDT	Changsha, China	Zygo NewView 700s	Surface roughness measurement	Weiran Duan
NUDT	Changsha, China	KEYENCE Digital Microscope VHX-600E	Surface observation	Weiran Duan
NUDT	Changsha, China	Ultrasonic cleaner	After polishing treatment	Weiran Duan
NUDT	Changsha, China	KDIBF 700-5V	After polishing treatment	Weiran Duan
NUDT	Changsha, China	CILAS particle size analyzer 1090	Particle size measurement	Weiran Duan
Central South University	Changsha, China	CSM Ultra Nanoindentation Tester	Nanoindentation test	Technician
Tongji University	Shanghai, China	LIDT test system	LIDT test	Technician & Weiran Duan
SAE Magnetics (HK) Ltd.	Dongguan, China	Model 2100 Trift II TOF-SIMS	Contaminants test	Technician

of Tongji University. The rest of the experimental work were done by the author in National University of Defense Technology (NUDT).

1.5 Overview of the thesis

The thesis is divided into eight chapters.

Chapter 2 is a literature survey. This chapter introduces optical properties of fused silica. Then some details about laser induced damage (LID) are reviewed. Optical surface polishing methods and post polishing treatments are also introduced. At last laser induced damage threshold (LIDT) evaluation methods are presented.

Chapter 3 mainly focuses on facilities and metrology methods. It introduces three surface processing facilities which are used in this work. These facilities include an MRF machine, a conventional lapping machine, and an ion beam etching (IBE) machine. This chapter also presents several measurement instruments which are used for quantifying the surface quality and the mechanical properties of fused silica substrate.

Mechanisms of the LID are discussed in Chapter 4. Mechanisms for surface and sub-surface damage are investigated. Then light intensity enhancement by the surface and sub-surface defects is discussed by theoretical calculations and simulations which utilise the finite difference time domain (FDTD) method. Finally thermal stress distributions are discussed through application of finite element analysis (FEA) simulations.

Chapter 5 analyses the non-fracture polishing mechanisms of the magnetorheological finishing (MRF) method. Then some experiments are outlined in which it is found that the MRF method is able to create high quality optical surfaces without obvious surface and sub-surface structural defects.

Chapter 6 mainly focuses on the role of surface roughness on LIDT, and outlines an

investigation of polishing parameters in the MRF process, optimised by the Taguchi method.

In Chapter 7, two post polishing treatments, a hydrofluoric acid (HF)-based etching method and Ion Beam Etching (IBE), are used to reduce the surface contaminants. Surface contaminants distributions in various surfaces are also tested in this chapter.

Chapter 8 describes LIDT test experiments to investigate the effectiveness of the aforementioned surface processing methods for improving the LIDT of fused silica optics.

Chapter 9 summaries this work and draws a conclusion of the thesis and suggestions for future work are also given in this chapter.

References

1. Brink, D.M., F. Bassani, G.L. Liedl and P. Wyder, "Nuclear Fission and Fusion", in *Encyclopedia of Condensed Matter Physics*. 2005, Elsevier: Oxford. pp. 113-114.

2. Lawson, J.D. "Some criteria for a power producing thermonuclear reactor". in *Proceedings of the Physical Society*. 1957. **B 70**: pp. 6-10

3. Lindl, J.D., R.L. McCrory and E.M. Campbell, "Progress toward ignition and burn propagation in inertial confinement fusion", *Physics Today*, , September 1992, p.32

4. Moses, E.I., "Advances in inertial confinement fusion at the National Ignition Facility (NIF)". *Fusion Engineering and Design*, 2010. **85**(7-9): pp. 983.

5. Moses, E. "Livermore Lab's giant laser system will bring star power to Earth". [Online]; Available from: Https://e-reports-ext.llnl.gov/pdf/391112.pdf.

6. Stolz, C.J. "The National Ignition Facility: The world's largest optical system". in *Proc. of SPIE*. 2007. **6834**: pp. 683402-1 -- 683402-9

7. Wootton, A. "The National Facility Physics and Diagnostics". [Online]; Available from: Https://e-reports-ext.llnl.gov/pdf/236219.pdf.

8. Campbell, J.H., R.A. Hawley-Fedder, C.J. Stolz, J.A. Menapace, M.R. Borden, P.K. Whitman, J. Yu, M. Runkel, M.O. Riley, M.D. Feit and R.P. Hackel. "NIF optical materials and fabrication technologies: An overview". in *Proceeding of SPIE*. 2004. Bellingham, WA. **5341**: pp. 84-101

9. Sacks, R.A. and C.A. Haynam, "The National Iginition Facility Laser ", in *High-Power Laser Handbook*. 2011. pp. 357-410.

10. Lowdermilk, W.H. "Status of the National Ignition Facility Project". in *Proceeding of SPIE*. 1997. **3047**: pp. 16-37

11. Cohen, D., J. MacFarlane, D. Haynes, P. Jaanimagi and N. Landen. "Inertial Confinement Fusion:Experiments & Modeling". [Online]; Available from: http://astro.swarthmore.edu/~cohen/omega/presentation-sep00.pdf.

12. Arnoul, J.P., F. Signol and J. Nicoloso. "The Laser Megajoule Facility:Control System Status Report". in *Proceedings of ICALEPCS2011*. October 2001. Grenoble, France. pp. 600-602

13. Besnard, D., "The megajoule laser program - ignition at hand"*. The European Physical Journal D*, 2007. **44**: pp. 207.

14. Perez, S. "Laser Megajoule Facility (L.M.J.)". [Online]; Available from: https://www.tango-controls.org/Events/meetings/May-2010/LMJ-TangoMeeting_2010.pdf.

15. Andre, M.L. "Status of the LMJ Project". in *Proceeding of SPIE*. 1997. **3047**: pp. 38-42

16. "Laser fusion shifts into HiPER drive", *Fusion challenges and solutions*, December, 2009, Bristol: IOP Publishing Ltd., p.7

17. Dunne, M. "Hiper: A laser fusion facility for Europe". [Online]; Available from: http://fsc.lle.rochester.edu/pub/workshops/FIW06/Dunne_FI06.pdf.

18. "HiPER: Laser Fusion Energy". [Online]; Available from: Http://workspace.imperial.ac.uk/plasmaphysics/public/CIFS/final%20talks/Dunne.pdf.

19. Wood, R.M., "Laser-Induced Damage of Optical Materials". 1 ed. Series in

Optics and Optoelectronics, ed. R.G.W. Brown and E.R. Pike. 2003, Bristol: Institute of Physics Publishing.

20. Wong, J., J.L. Ferriera, E.F. Lindsey, D.L. Haupt, I.D. Hutcheon and J.H. kinney, "Morphology and microstructure in fused silica induced by high fluence ultraviolet 3w (355nm) laser pulses". *Journal of Non-crystalline Solids*, 2006. **352**: pp. 255.

21. Li, C.H., "Mechanism Study on High Power UV Laser-Induced Damage in Fused Silica Optics" [PhD Thesis]. Beijing, China: University of Science and Technology Beijing; 2011.

22. Suratwala, T., P. Miller, J. Bude, W. Steele and N. Shen, "HF-Based Etching Processes for Improving Laser Damage Resistance of Fused Silica Optical Surface". *Journal of American Ceramic Society*, 2011. **94**(2): pp. 416-428.

23. Suratwala, T.I. "Optical Fabrication and Post Processing Techniques for Improving Laser Damage Resistance of Fused Silica Optics". in *International Optical Design Conference and Optical Fabrication and Testing*. 2010. Jackson Hole, Wyoming: Optical Society of America. pp. OWA1

CHAPTER 2

LITERATURE REVIEW

2.1 Optical properties of fused silica

Fused silica, as a type of optical material, has very good optical properties. It therefore plays a very significant role on the high power laser systems.

2.1.1 Transmission

The transmission characteristic of an optical material is its most important factor. Fused silica is an optical material that has excellent transmission characteristics, which are expected to meet the requirements for high power laser systems. Fused silica can transmit not only visible light, but also infrared and ultraviolet light. The spectral ranges of two forms of fused silica materials (10mm in thickness, from Heraeus, Germany) are shown in Figure 2.1 [1]. The results show that fused silica transmits very well (>90%) at 355 nm wavelength.

2.1.2 Refractive index

The refractive index for fused silica is another important property, especially when considering the light intensity in the optical substrate under the laser radiation. For optical materials, the refractive index varies with the wavelength of incident light. Researchers [2-5] did a lot of research on the refractive index (n_λ) of fused silica, of which the form is unclear, on various wavelengths of incident light; and Malitson gave an experimental Sellmeier equation [3]:

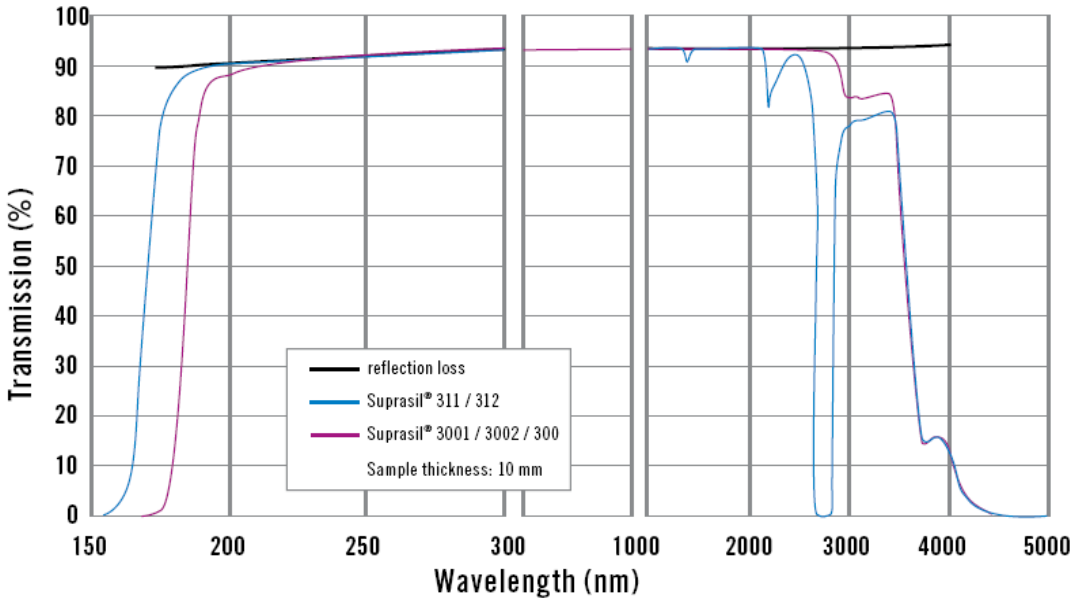

Figure 2.1 Typical transmission of various forms of fused silica manufactured by Heraeus [1]

$$n_\lambda^2 = 1 + \frac{0.6961663\lambda^2}{\lambda^2 - (0.0684043)^2} + \frac{0.4079426\lambda^2}{\lambda^2 - (0.1162414)^2} + \frac{0.8974794\lambda^2}{\lambda^2 - (9.896161)^2} \quad (2.1)$$

where λ is the wavelength in micrometres. Tan [2] proved that Equation (2.1) is valid up to 6.7μm. According to the Equation (2.1) Figure 2.2 is obtained. Figure 2.2 demonstrates that the calculated refractive index for fused silica at 355nm UV light is 1.48, though it could vary among the specify samples.

2.2 Laser induced damage (LID) of bulk fused silica

Fused silica (SiO_2) optics are widely used in the NIF device due to their excellent transparency and uniformity in the ultraviolet (UV) region. However, the lifetime of the optics is a major limit for their performance in high peak power laser systems[6, 7]. The lifetime of fused silica optics in a high peak power laser system is largely determined by obscuration loss which results from LID on optical surfaces [8-10].

2.2.1 Definition of LID of fused silica

When fused silica is irradiated by a high peak power laser beam, the laser interaction can cause permanent changes in the material. These changes are called LID. Salleo [11] gave a precise definition of LID: the LID is laser induced changes which may compromise its functionality. Salleo also defined functional damage as any change in the material which makes its designed function fail in some tolerance limits.

For the SiO_2 optics used for the ICF system, the criterion for functional damage is the total obscuration area on the optic because the obscuration could reduce energy from the laser beam which is to ignite the fuel target. Therefore, in the rest of this thesis, the LID of SiO_2 optics will be defined as any detectable morphological change in the material. The detection method could be visual inspection or light microscopy.

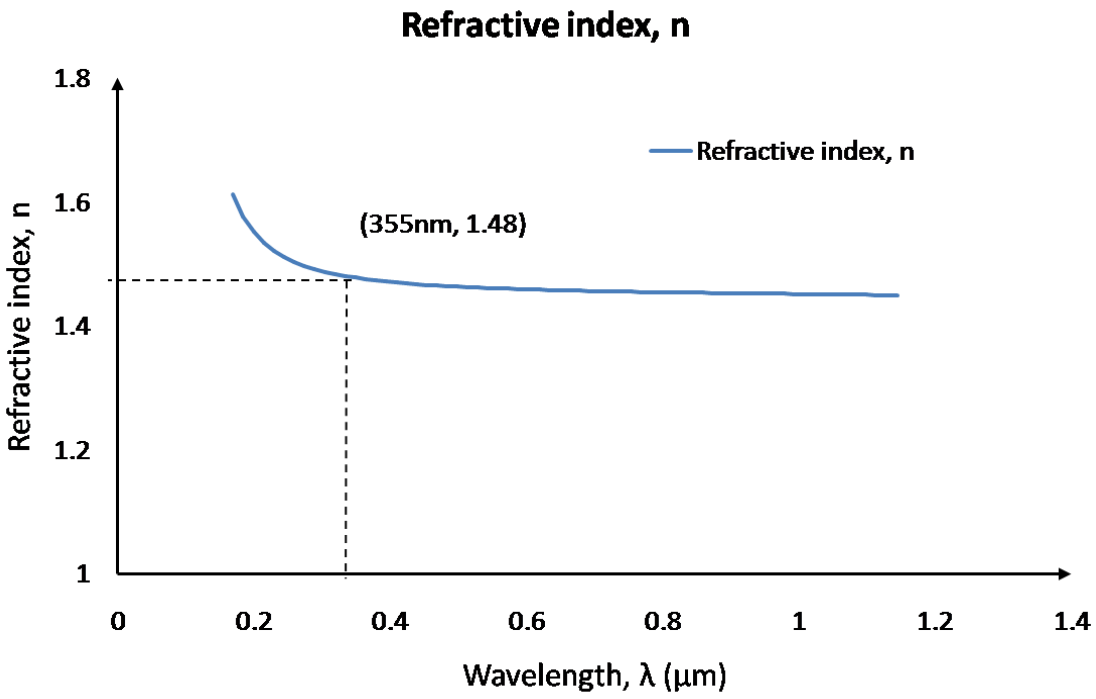

Figure 2.2 Refractive index for fused silica as a function of wavelength plotted from Equation (2.1).

2.2.2 Initiations of LID of fused silica

Unlike Potassium dihydrogen phosphate (KH_2PO_4, KDP) and Deuterated potassium dihydrogen phosphate (KD_2PO_4, DKDP), of which bulk damage usually happens, surface damage is generated on the optical surface [11-13]. Generally researchers believe that surface scratches, sub-surface damage, and impurities embedded into the surface layer, are the initiation sites of LID on fused silica surfaces [14, 15].

For the mechanisms of the LID, many researchers have done a lot of research. According to a series of simulations, Feit, et al. [16] indicated that high temperatures can be reached by heating up even small absorbers (contaminant particles) by UV laser irradiation in the NIF range, and the following thermal stress and possible thermal explosion could lead to high pressure and surface damage.

Based on Papernove's research [17],Liu, et al. [18]investigated the time-resolved dynamics of 355nm UV LID at the entrance and exit surfaces of fused silica optics by means of shadowgraph techniques. The results illustrated that damage mechanisms at entrance and exit surfaces are different. Laser-plasma interactions at the entrance surface during the laser pulse cause large absorption and reflection in the air (shown in Figure 2.3a). This plasma shielding limits the laser energy deposition at the entrance surface, while no plasma shielding occurs at the exit surface because energy is mostly retained in material (shown in Figure 2.3b). Therefore more damages occur at the exit surface than the entrance surface. Figure 2.4 confirms the mechanisms mentioned above.

Salleo, et al. [15] investigated the LID of fused silica optics at 355 nm UV laser irradiation at different surface scratches, which were generated by a diamond tip. Laser induced damage threshold (LIDT) of the unscratched surface was 15 J/cm^2 at 3 ns laser irradiation. Thin scratches on entrance surface (less than 10 μm) did not initiate

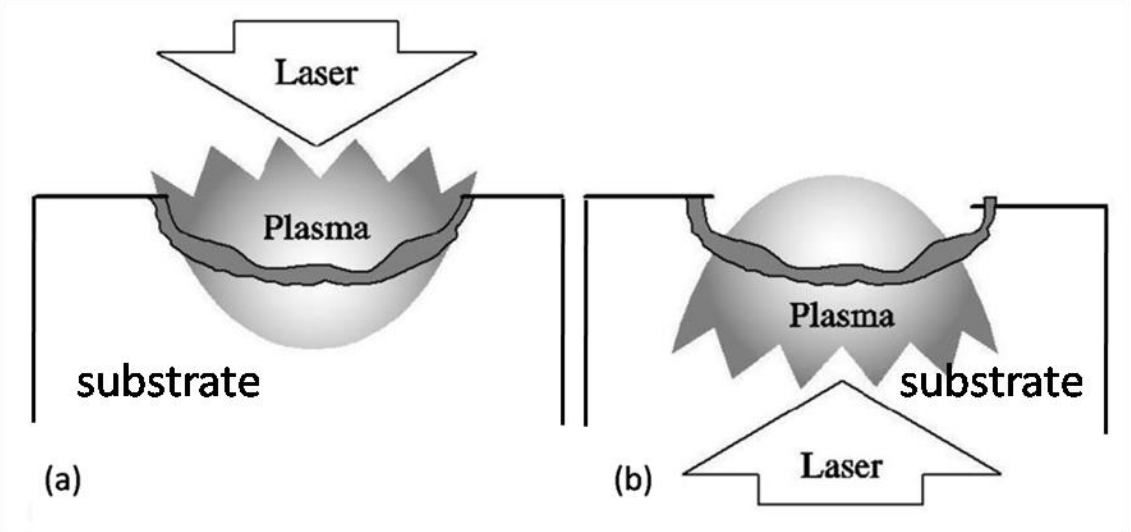

Figure 2.3 Schematic of the laser-plasma interaction at (a) entrance and (b) exit surfaces of optical material during laser irradiation [17]

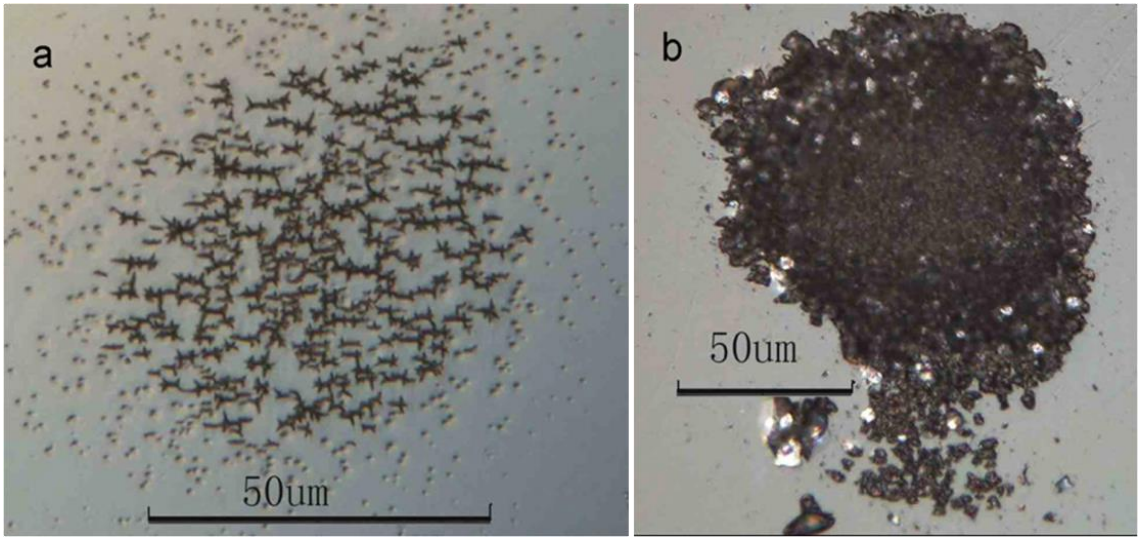

Figure 2.4 LID of fused silica optics at (a) entrance surface and (b) exit surface under single shot of 355 nm laser fluence 15J/cm^2[18]

damage below 15 J/cm^2. Salleo also found that plastic scratches (shown in Figure 2.5a) did not initiate damage at the entrance surface while a brittle scratch (wider than 10 µm, shown in Figure 2.5b) initiated damage on the entrance surface at 12 J/cm^2.However, at the exit surface, 7 µm wide scratches could initiate damage and lowered the LIDT to 8 J/cm^2 and scratches wider than 20 µm caused the LIDT to drop to 5 J/cm^2.

2.2.3 Morphology of LID of fused silica

Because of the enhanced scattering and/or absorption and macroscopic change of material integrity, the presence of LID in the optical materials causes loss of transmission of laser light. These areas of obscuration of the LID site on fused silica optical surfaces largely determine the lifetime of optical components.

Considering the morphology of LID, two key aspects of LID usually can be discussed: damage initiation by a single laser pulse and damage growth under the irradiation of subsequent laser pulses. Demos, et al. [10, 19] reported a damage growth process on a NIF-sized fused silica optic at 355 nm, 3ns laser irradiation (around 5 J/cm^2), as shown in Figure 2.6. A small surface damage site (Figure 2.6a) initiated by a surface imperfection grew in size after subsequent exposure up to 38 laser pulses (Figure 2.6b).

Wong, et al. [20] also showed a series of optical micrographs of damage sites at the exit surface of fused silica optics as a function of number of laser pulses (shown in Figure 2.7). Each damage site was irradiated with a 355 nm laser beam at 35 J/cm^2, and the pulse length is 7.5 ns and repetition rate is 10 Hz. Figure 2.7a is for a super polish surface and Figure 2.7b is for a regular polish surface. From the picture it can be seen that damage sites also grow in size with increasing number of laser pulses. We can also see that a super polished surface has smaller damage size than that of a regular polished surface.

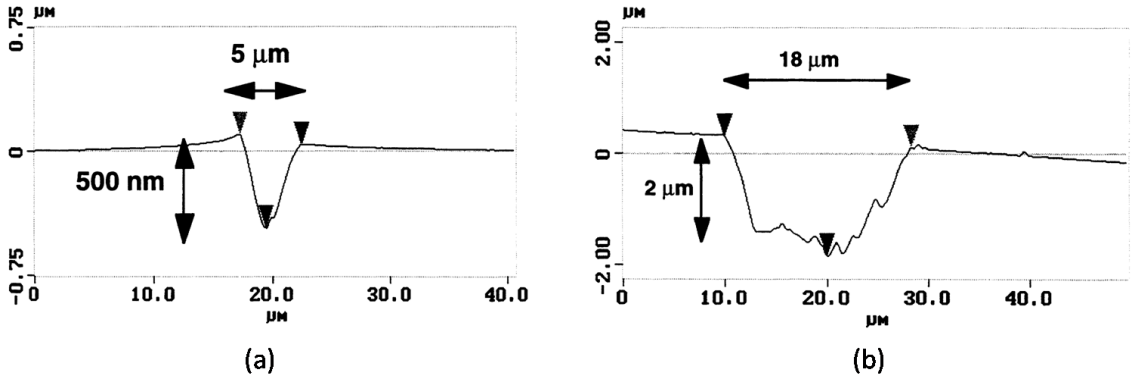

Figure 2.5 Line scan of (a) plastic scratch and (b) brittle scratch in fused silica after Salleo [15]

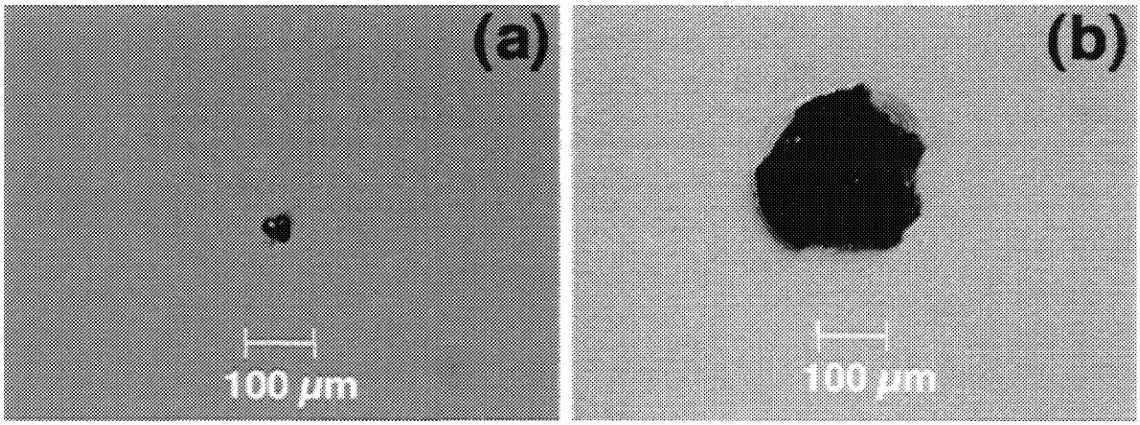

Figure 2.6 Same damage site on NIF-size fused silica component after (a) one laser pulse and (b) 38 laser pulses [10]

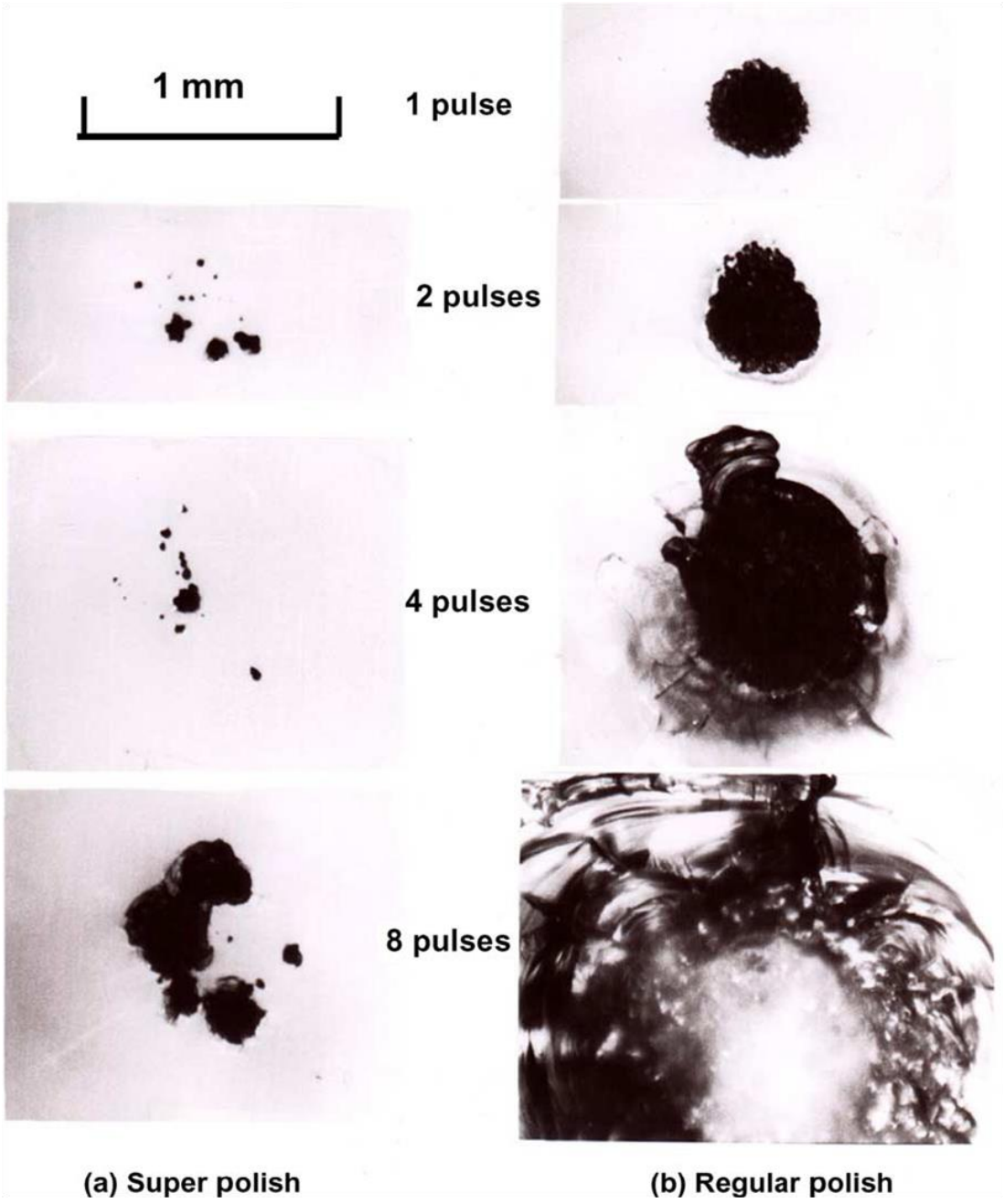

Figure 2.7 Damage sites on fused silica surfaces (exit) as a function of number of 3ω laser pulses after Wong [20]

The influence of laser irradiation also affects the size of LID on fused silica surfaces. Figure 2.8 shows how the size and overall morphology of LID varies with laser fluence at location [20]. The laser here was 355 nm, 7.5 ns, and with the same repetition rate as before. From Figure 2.8 it can be seen that the size of LID reduces with the decreasing of laser fluence.

2.3 Mechanisms of laser induced damage

The origin of laser induced damage (LID) in an optical component is a complex process and depends both on laser beam parameters and on the optical components performance. For the same bulk material, laser beams with different parameters (wavelength, shape and size of beam cross-section, irradiating pulse duration, and polarisation) could lead to different damage, while the same laser beam irradiating different bulk materials could also induce different damage. Even the same laser beam irradiating components of the same bulk material, LIDs are also observed differently due to different machining processes. What's more, same laser beam irradiating the same optical components could also induce different damage due to any other incidental defects or impurities. Therefore the generation of LID in optical components is a complex process with high uncertainty.

In order to improve the LIDT of fused silica optics, it is important to investigate the mechanisms for the generation of LID, though it is a complex process. Some fundamental mechanisms which give rise to LID are still commonly accepted by researchers. There are two main categories: thermal mechanisms and electronic mechanisms[11, 21-24].

2.3.1 Thermal LID mechanisms

Thermal process is one of the principles which cause LID in the optical components. An excess of thermal energy, in many practical cases, may give rise to LID by leading to a

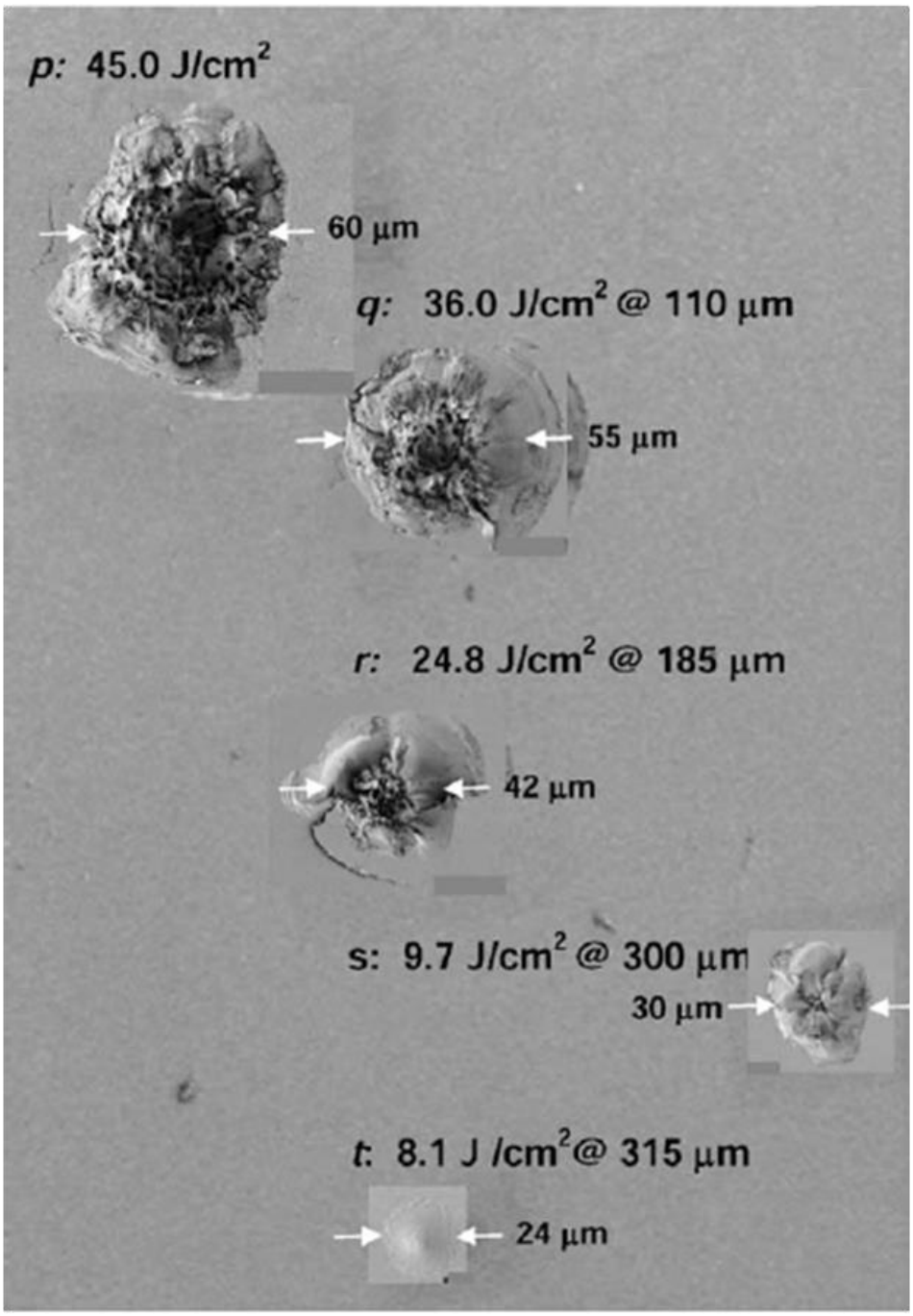

Figure 2.8 Size of LID in fused silica as a function of laser fluence for 355 nm irradiation at 10 Hz with a pulse duration of 7.5 ns [20]

catastrophic failure by overheating or mechanical disruption. The thermal energy arises from absorption of the laser radiation in the material. When an optical component is irradiated by a laser beam, some of the laser energy is absorbed causing heating of the sample. The thermal interaction generally depends on the mechanical, optical, and thermal properties of the component irradiated, on the laser properties, and on the ambient conditions.

Suppose the component occupying half space ($x \geq 0$), no temperature rise occurs at $x \gg 0$. For one-dimension condition, the incident laser is in the normal direction from space ($x \leq 0$) to component surface and with uniform intensity I_0. When the incident irradiation is a surface laser source, and the laser beam has temporal shape $B(t)$, then the risen temperature field in the component is given by [24],

$$\Delta T(x,t) = \frac{\sqrt{D}(1-R)I_0}{\kappa\sqrt{\pi}} \int_0^t \frac{B(t-t_1)\exp(-x^2/4Dt_1)}{\sqrt{t_1}} dt_1 \qquad (2.2)$$

where D is the thermal diffusivity, R is surface reflectivity, and κ is thermal conductivity.

Figure 2.9(a)-(e) shows, according to the Equation (2.2), schematic figures of variation of temperature (in the same depth x) obtained by the irradiation of some typical laser beams with same peak values (I) and different temporal shapes and/or frequencies, i.e. short pulse (Figure 2.9(a)), long pulse (Figure 2.9(b)), low pulse-repetition-frequency (PRF) pulse (Figure 2.9(c)), high PRF pulse (Figure 2.9(d)), and continuous wave (CW) beam (Figure 2.9(e)).

Figure 2.9 shows that the absorption of energy results in a rise in temperature. The temperature rise could lead to thermal expansion, strain, and even LID such as cracking, melting, and catastrophic shattering. Figure 2.9 also displays that variations of laser beams could induce variations of thermal interactions. Several LIDT test

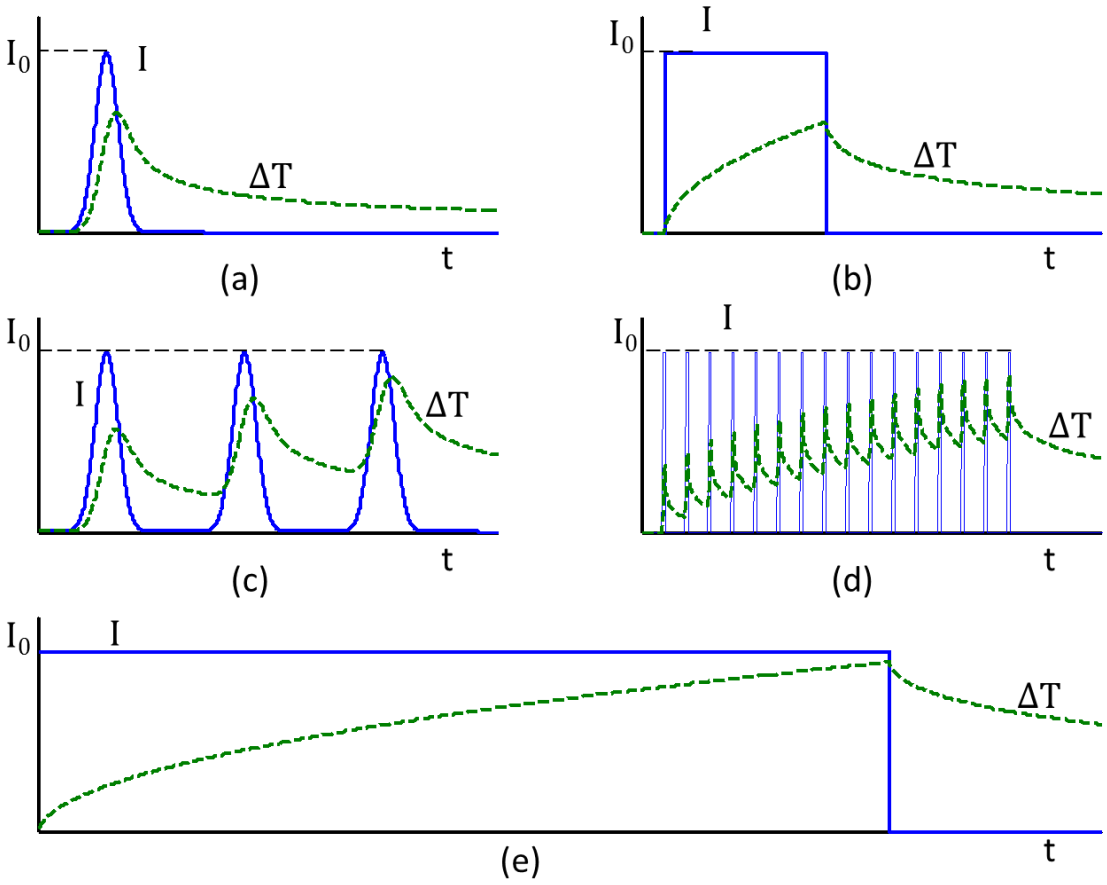

(a) Short pulse, (b) Long pulse, (c) Low PRF pulse, (d) High PRF pulse, (e) CW beam

Figure 2.9 Risen temperature (ΔT) and laser beam intensity (I) versus time (t).

methods (see section 2.7) are established in terms of different laser-component interactions.

Generally, the optical components are made of transparent materials which are usually transmitting media in the laser system. Therefore, laser radiation absorption is in a cylinder passing through the optics on the axis of the incident laser beam (shown in Figure 2.10), and causes a temperature rise at the centre of this laser cylinder and heating-induced radial strain between the centre of this laser irradiated cylinder and the edge of the optics. Similarly, the temperature rise and heating-induced mechanical strain also depend on the material properties, component size, and laser beam details (intensity, pulse duration, frequency, etc.).

In the thermal processes, LID could occur in two main forms: melting and catastrophic cracking. If the temperature in the centre of the laser heated cylinder reaches the melting point of the irradiated optical material, T_m, or if heating-induced stress in the laser cylinder reaches the critical damaging stress (generally tensile stress), S, LID will occur [22]. Therefore two damage thresholds, E_{D_m} and E_{D_c}, are defined for the melting condition and the cracking condition, respectively.

Combining the damage thresholds E_{D_m} and E_{D_c}, the theoretical damage threshold due to thermal processes is when the absorbed thermal energy reaches the minimum of melting point and cracking point, i.e.

$$E_D = \min\{E_{D\_m}, E_{D\_c}\} \tag{2.3}$$

Equation (2.3) means that thermal damage threshold is E_{D_m} if the material melts before it cracks, and vice versa.

Wood [22] indicated that smaller absorption coefficient, volume expansion coefficient, and greater heat capacity, melting temperature and damaging stress of optical

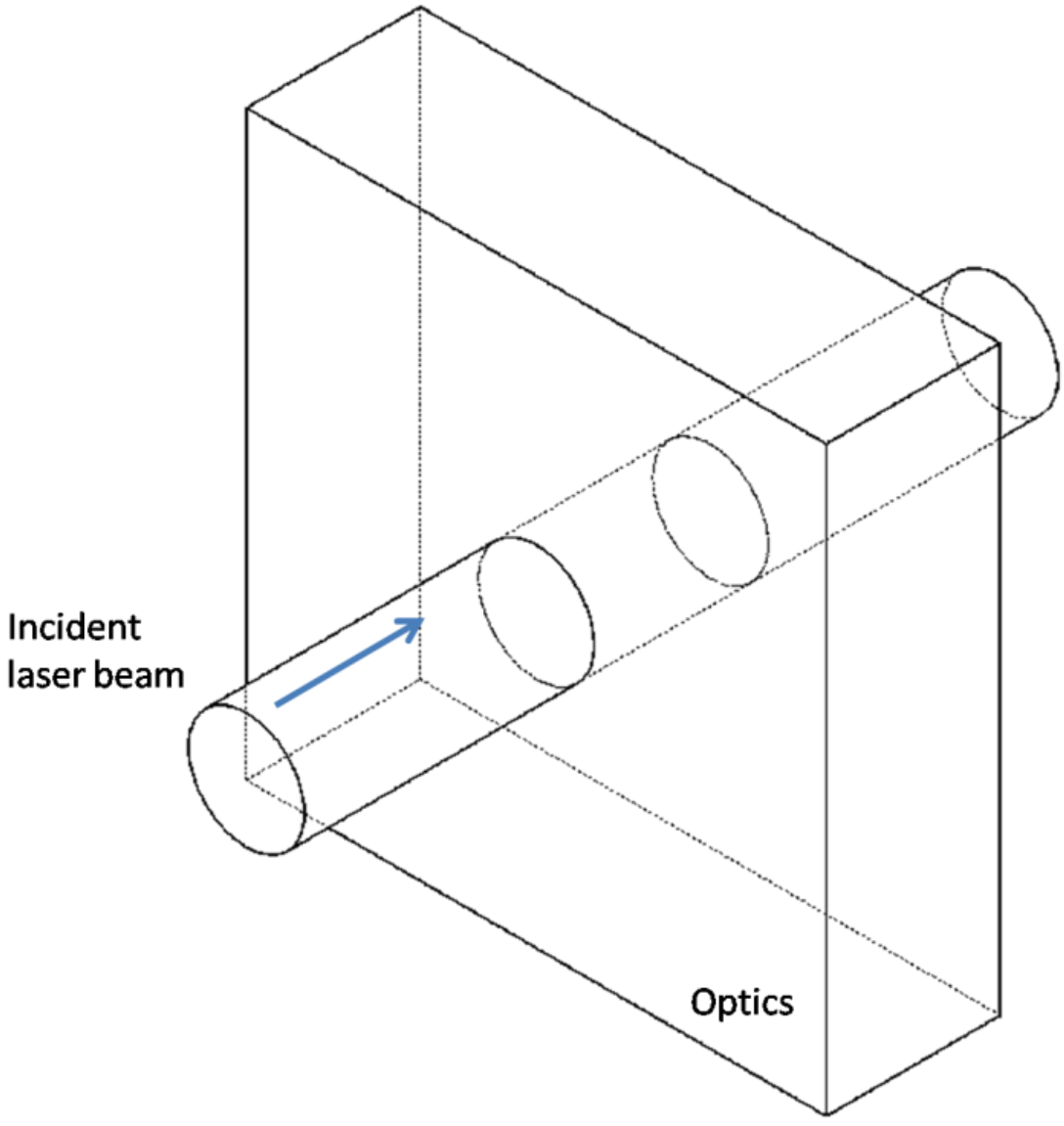

Figure 2.10 Transmitting optical component irradiated by a laser beam, after Wood [22]

material, lead to higher damage threshold. Therefore, damage due to thermal processes generally occurs in the cases of long pulse ($> 10^{-13}$ s), high PRF pulse, and CW laser beams.

2.3.2 Electric LID mechanisms

The second class LID mechanisms are the electric processes. When the electromagnetic field density is high enough to cause dielectric breakdown of optical material, LID occurs. There are two mechanisms due to the electric processes, i.e. electron avalanche breakdown, and multiphoton ionisation. Both the two mechanisms can describe the cause correctly, but in general their results are the same.

1. Electron avalanche breakdown

When the optical component material is in the presence of an electromagnetic field, energy is transferred from the electromagnetic field to the material by means of exciting its electrons from the valence band to the conduction band [11]. An electron in the presence of an electric field, E, gains energy due to the electro-photon collisions. The electron energy, ε, follows the equation that [22],

$$\left.\frac{d\varepsilon}{dt}\right|_{\varepsilon} = \frac{e^2\tau_k E^2}{m(1+\omega^2\tau_k^2)} \tag{2.4}$$

Where e is the charge of an electron, ω is the frequency of the electric field, m is the number of laser pulses, τ_k is the electron relaxation frequency.

When the electron obtains enough energy it can excite and ionise another valence electron via collision. In other words, energy is transferred from one excited electron to another and two excited electrons exist. Repetition of this multiplication process increases the number of free electrons rapidly until avalanche breakdown occurs. Then plasma which absorbs laser light strongly is generated locally.

Wood [22] also indicated that the shorter pulse lengths induce greater energy absorption by electron. Therefore the electron avalanche ionisation generally occurs when laser pulse lengths are short enough (between 10^{-8} s and 10^{-11} s) and when the avalanche threshold is below the thermal threshold.

2. Multiphoton absorption

The multiphoton absorption mechanism is similar to the electron avalanche breakdown mechanism. In terms of both mechanisms, LID occurs because the number of free electrons increases dramatically. The electron can absorb the large energy of the photon in the case where an electron interacts with both a phonon and a photon, and the large wavevector of the phonon allows wavevectors to be conserved. So the starting electrons are excited by multiphoton absorption or tunnel emission.

Multiphoton absorption occurs for sub-picosecond or femtosecond laser pulse lengths [11, 22]. In this case, while multiphoton absorption is allowed by the ultra-high intensity of ultra-short laser pulses ($< 10^{-13}$ s). Therefore the valence electrons obtain energy by multiphoton absorption and hence the number of free electron increases.

2.4 Machining techniques for the production of optics for a laser system

During the manufacturing processes, such as grinding and polishing, of high quality fused silica optical surfaces, surface imperfections and contaminants are inevitably left. It is believed that the morphology of LID on fused silica surfaces could vary with choice of polishing method. This can be proved by Figure 2.7. Therefore the manufacturing methods of optical surfaces do make sense in the research on LID of fused silica optics.

To prepare fused silica optics from blank materials, the common processes include rough grinding, fine grinding, rough polishing and final polishing. Hence this section

will review some ultra-precision polishing techniques. Ultra-precision polishing techniques have developed rapidly over recent years and a lot of deterministic optical polishing methods have been established. These methods include abrasive jet polishing [25, 26], ion beam-based finishing, lapping [27], elastic emission machining (EEM) [28, 29], and magnetorheological finishing (MRF).

2.4.1 Abrasive jet polishing

To meet the challenge to shape and finish optical surfaces with steep and concave sections in brittle materials such as glass, Fahnle and Brug developed Fluid Jet Polishing (FJP) using the idea that a stream of prepared fluid is ejected at a high speed and guided by a nozzle onto the optical surface under pressure [30]. Usually in the FJP process, abrasive fluid is composed of water and a polishing compound such as Cerium Oxide (CeO_2). Therefore the FJP method is called water jet polishing sometimes. Figure 2.11 shows a schematic diagram of FJP, of which the T, G, P and N are fluid container, work-piece, pump and nozzle respectively.

Horiuchia, et al. [31] developed a method of ultraprecision abrasion machining named “Nano-abrasion machining”, which is similar to FJP and uses machining liquid composed of pure water and small amount of abrasive grits. In this nano-abrasion machine, because the collision energy is low and the collision angle is shallow, the removal rate may decrease to a few nanometres per minute and machined surface roughness may reach a few nanometres even for brittle materials such as glass, diamond and ceramics.

Normally, a typical abrasive jet disperses at a very short distance from the nozzle. Therefore it is a challenge in conventional abrasive jet polishing to ensure that material removal is deterministic and stable. To avoid the disadvantages of instability, Tricard, et al. [25] developed a method of jet stabilization, named magnetorheolgical (MR) jet

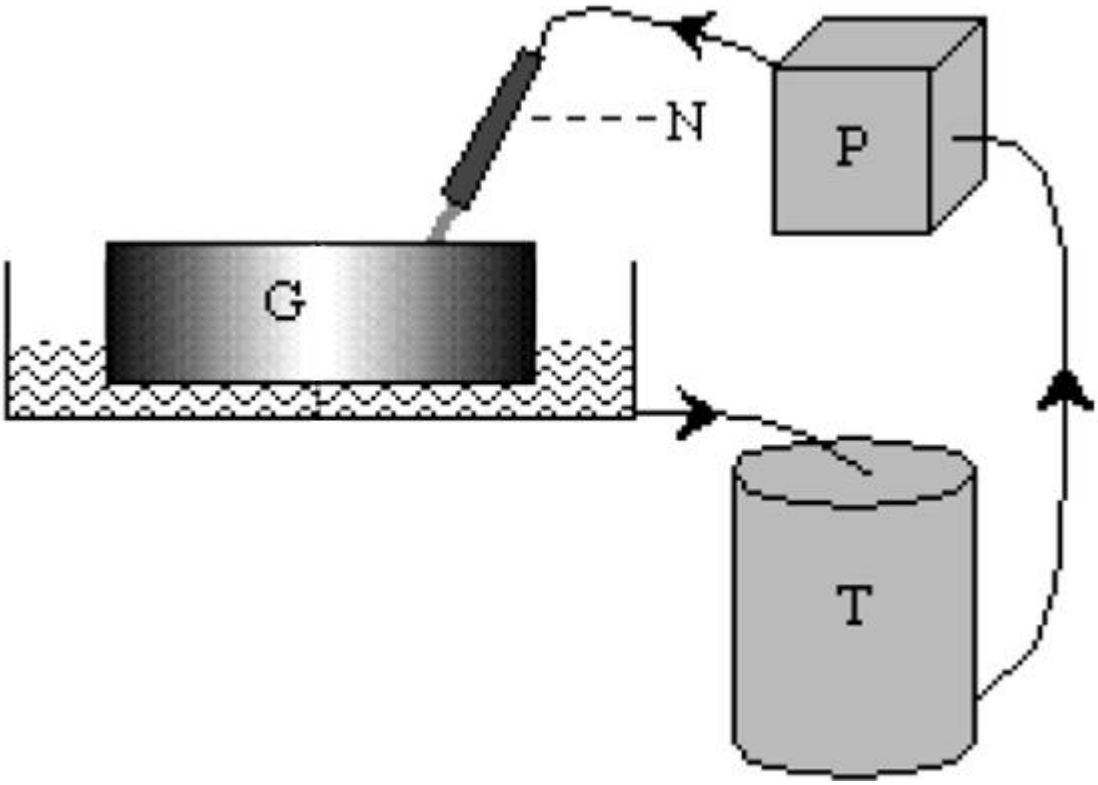

Figure 2.11 Schematic diagram of Fluid Jet Polishing [31]

finishing. In MR jet finishing, the abrasive fluid is not a typical abrasive fluid. An MR fluid consists of water, carbonyl iron particles and abrasives. The jet of magnetorheological (MR) fluid can be concentrated and forms a stable and slender jet because it is magnetised in a magnetic field when it is ejected out of the nozzle. This stable jet may keep its structure when travelling a long distance (200 nozzle diameters, i.e. 0.4 metre for 2 mm nozzle diameter) [25]. Therefore, MR jet polishing is a very good method for machining steep concave surfaces and cavities stably.

2.4.2 Ion beam-based finishing

Ion beam-based finishing, also called 'Ion Beam Etching (IBE)','Ion Beam Figuring (IBF)', 'ion beam polishing', or 'ion beam sputtering', is a form of highly deterministic polishing method which has been developed rapidly in some companies and research institutions, such as the Eastman Kodak Company [32], Cannon, Nikon [33], and Centre Spatial de Liege (CSL). Ion beam-based finishing technologies are developed for correcting and figuring of high precision and large scale optical components [34].

Unlike other polishing methods, ion beam-based finishing is a non-contact technique that avoids problems such as edge effect, tool wear, and force loading of the work-piece. In an ion beam-based finishing process, material is removed from the optical surface via a sputtering phenomenon. A typical sputtering event is a knocking out phenomenon which usually begins with energetic ion particles bombarding surface atoms or molecules. It is based on an ion beam etching system and utilises a beam of noble ions, such as argon (Ar), krypton (Kr), and xenon (Xe) ions, which is generated and accelerated in a discharge chamber, to remove material from the surface selectively [35].

Figure 2.12 shows the mechanism of the ion beam-based finishing process. Ions with high energy hit the surface of the work-piece, of which some atoms get enough energy

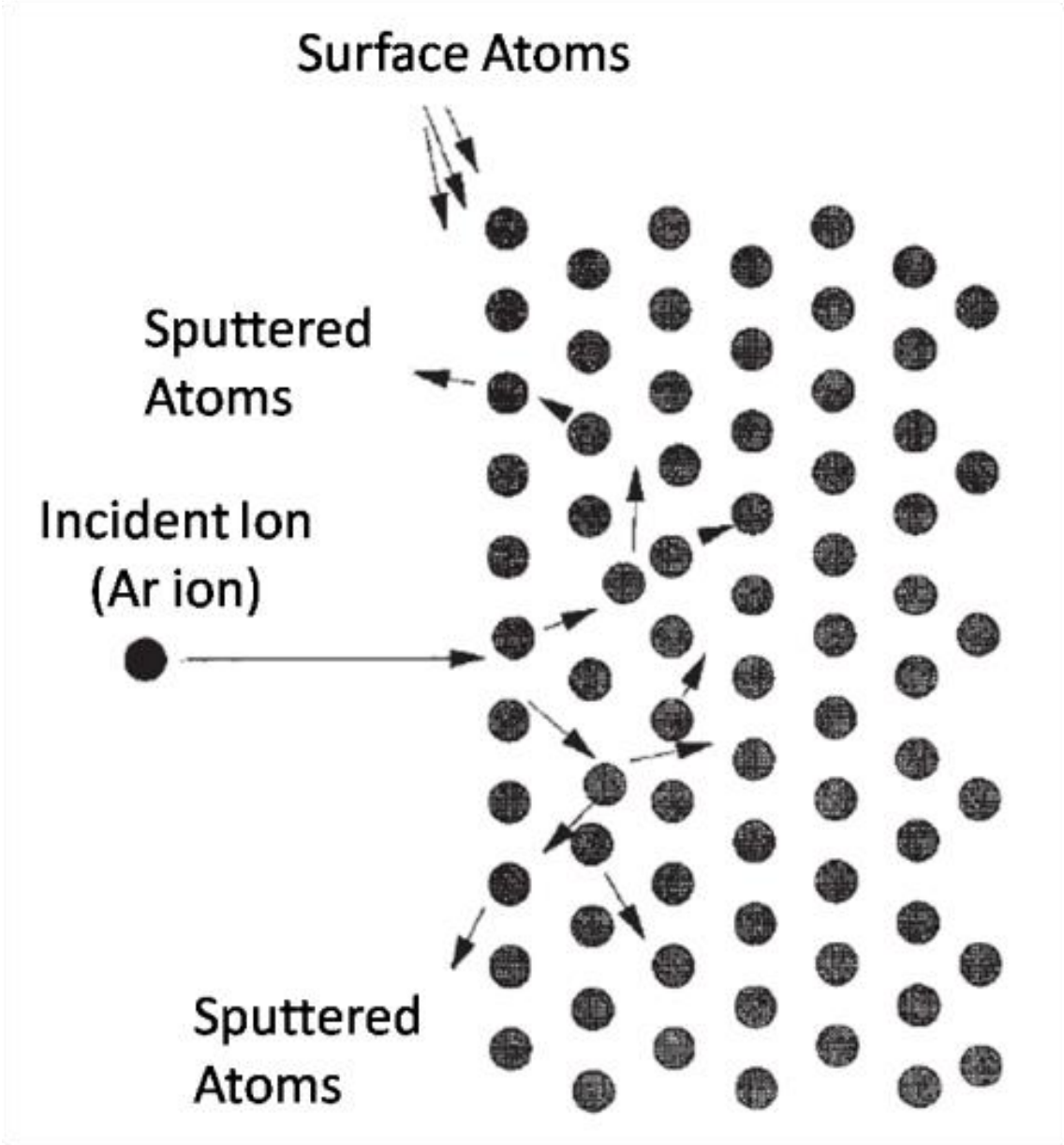

Figure 2.12 Mechanism of the ion beam-based finishing process[36]. Some surface or near-surface atoms, namely sputtered atoms, obtain enough energy from incident (Ar) ions and move away from substrate surface.

from the ions and move away from work-piece. The surface or near-surface atoms of the substrate material, of which if some atoms obtain enough energy from ions and move away from substrate surface, they are named sputtered atoms. Sputtered atoms occur when the actual energy transferred exceeds the usual binding energy of 5-10 eV [37].

2.4.3 Lapping/Chemical Mechanical Polishing (CMP)

Lapping may be one of the oldest manufacturing processes for optical components. A uniform load is applied to the polishing pad which usually is made of pitch or polyurethane which are much softer than the abrasives and work-piece surface [38, 39]. Lapping utilises abrasive slurry which is sandwiched between a lapping pad and the surface of the work-piece. Abrasives are fixed on a lapping pad and motion between the work-piece surface and the lapping pad provides the polishing process. Usually the abrasive slurry is an aqueous suspension of colloidal abrasive particles with specific chemical properties depending on the needs. Consequently, lapping is also known as chemical mechanical polishing (CMP). The schematic setup of the lapping process is illustrated in Figure 2.13.

In a traditional lapping processes, expert opticians perform most of work manually with a precisely shaped rigid lap [38]. However, because of well-developed computing technology, aspherical optical surfaces can also be manufactured by computer controlled polishing with sub-aperture pads. Figure 2.14 (a) and (b) present a photograph and motion schematic view of a computer controlled lapping tool.

2.4.4 Elastic Emission Machining (EEM)

Elastic emission machining (EEM), was developed by Y. Mori, K. Yamauchi and K. Endo [28, 29]. It is an ultraprecision machining method that utilizes the chemical reaction

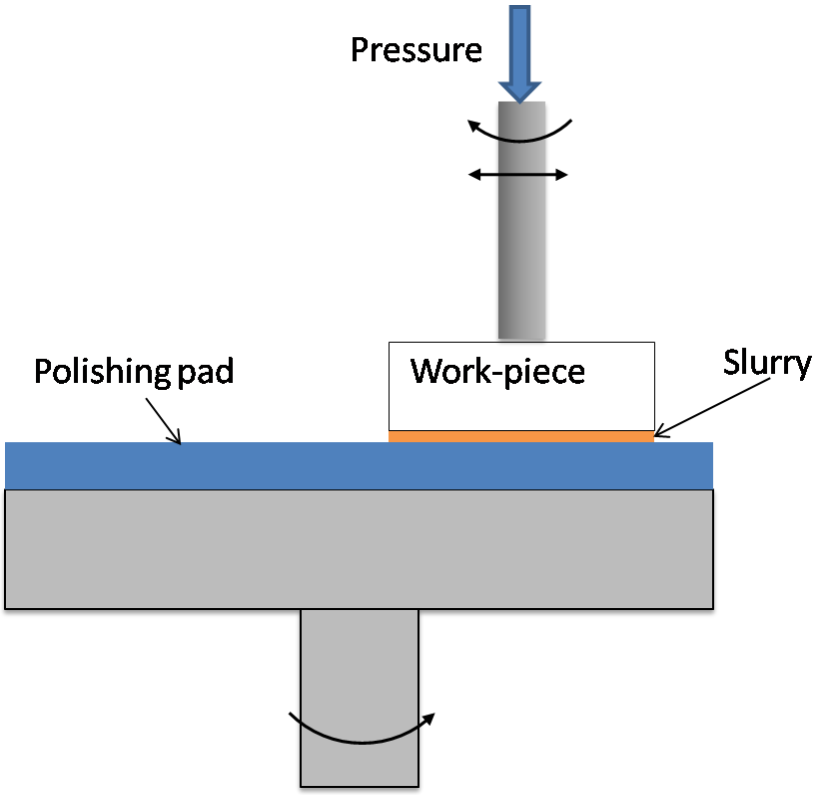

Figure 2.13 Schematic diagram of a lapping process, after [38]

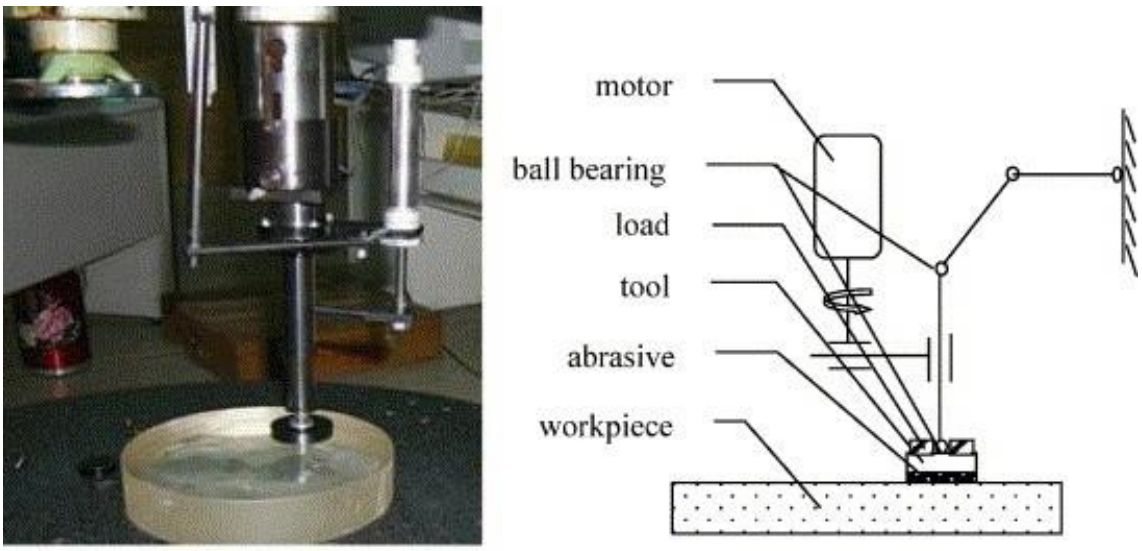

(a) Motion pictorial view (b) The tool planar motion model

Figure 2.14 Computer controlled polishing with a lapping pad [40]

between two solid surfaces as the machining principle.

In the EEM process, two solid materials touch each other and make chemical bonds at their interface; one of the solids may bring away the atoms of the other solid surface when they are separated. Thus, this process is a chemical reaction between reactive solid surfaces and the material removal occurs at the atomic level. The removal mechanism of EEM is shown in Figure 2.15.

2.4.5 Magnetorheological Finishing (MRF)

1. Introduction of MRF process

The Magnetorheological Finishing (MRF) process is a deterministic optical polishing method first developed by a team of scientists lead by William Kordonski at the Luikov Institute of Heat and Mass Transfer in Minsk, Belarus in 1988. Kordonski and his team developed the use of magnetically sensitive – or magnetorheological (MR) – fluid to polish optics. Then Kordonski collaborated with the Center for Optics Manufacturing (COM) at the University of Rochester, New York, and came to Rochester to work with Jacobs and Golini to perfect MRF and develop a stable finishing process[41]. The team spent several years studying and refining MRF which in 1996 became the foundation of a new-start up company, QED Technologies, which is the most famous research institute to focus on MRF and on the leading edge of optics manufacturing technology [42].

Besides QED Technology, many other researchers, such as Schinhaerl et al. [43] in Germany, Seok et al. [44]in Republic of Korea, and Cheng et al. [45]in China, are studying the MRF technology or some relevant technology, for example magnetorhelogical abrasive flow finishing (MRAFF) and magnetic abrasive finishing (MAF) which was developed by Jha and Jain [46, 47] in the Indian Institute Technology Kanpur, India. After a decade of research and development, MRF has

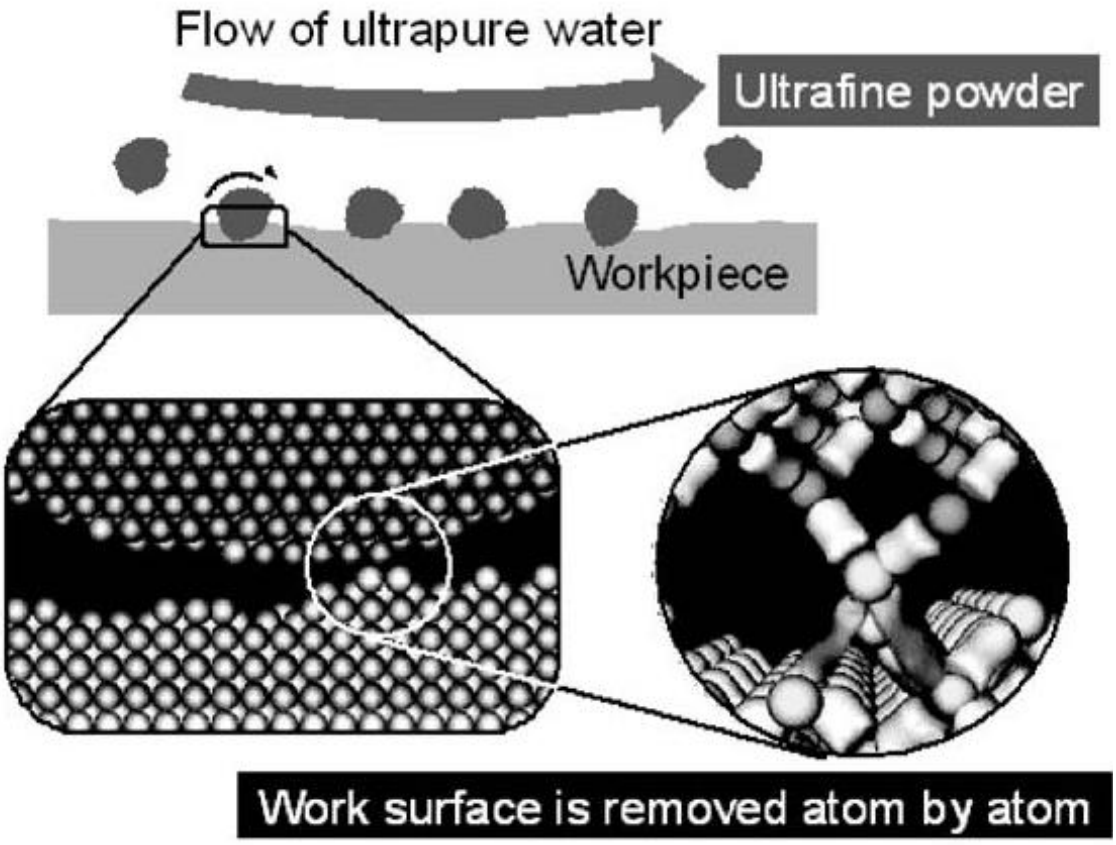

Figure 2.15 Removal mechanism of elastic emission machining [29]

become an accepted technology and is used by optics manufacturers around the globe. Peng [48], from National University of Defense Technology (NUDT), China, has also studied the MRF processes for years.

The key element of magnetorheological finishing (MRF) is a magnetorheological (MR) fluid, which is a slurry consisting of magnetic particles (typically carbonyl iron (CI) particles), nonmagnetic abrasive particles (e.g. CeO_2, Al_2O_3, and nanodiamonds), stabilizing agents, and an aqueous carrier medium such as deionised (DI) water or a nonaqueous liquid. The MR fluid has very low viscosity when in the absence of a magnetic field, but viscosity increases immediately in a magnetic field and acts as a polishing tool.

A schematic diagram of the MRF processes is shown in Figure 2.16. The MR fluid acts as a Newtonian fluid when it is delivered by a pump to a rotating wheel rim via a nozzle. The fluid is pulled against the wheel rim because of the magnetic field which is generated by an electromagnet mounted below the wheel surface. On the wheel surface, the fluid simultaneously stiffens and thus becomes a Bingham fluid (a kind of non-Newtonian fluid that behaves like rigid solids if the applied stress is below a certain threshold and as viscous fluids if the stress exceeds that threshold) which acts as a polishing tool. A suction inlet draws the fluid off the wheel where the Bingham fluid becomes a Newtonian fluid again. It is transported back to the conditioner by a second pump. The conditioner and the circulation guarantee that the fluid on the wheel, and thus the polishing tool, has continuously stable conditions.

Figure 2.17 illustrates the contact zone with an applied magnetic field. MR fluid, which is delivered by the pump into the magnetic field, acts as a stiff and viscous ribbon attaching to the rim of the wheel and is dragged by the rotating polishing wheel into polishing zone. Significant forces are generated by the interaction between the work-piece surface, the wheel and ribbon when the ribbon is compressed. In the

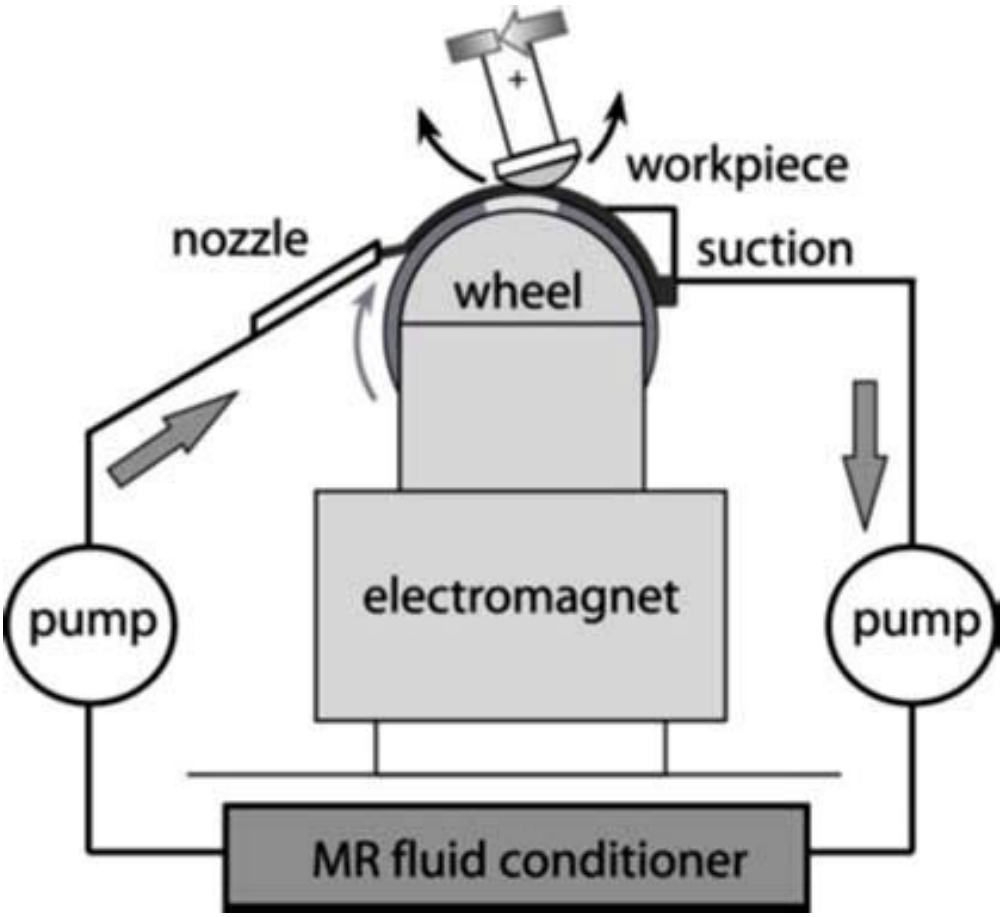

Figure 2.16 Schematic diagram of MRF process[49]

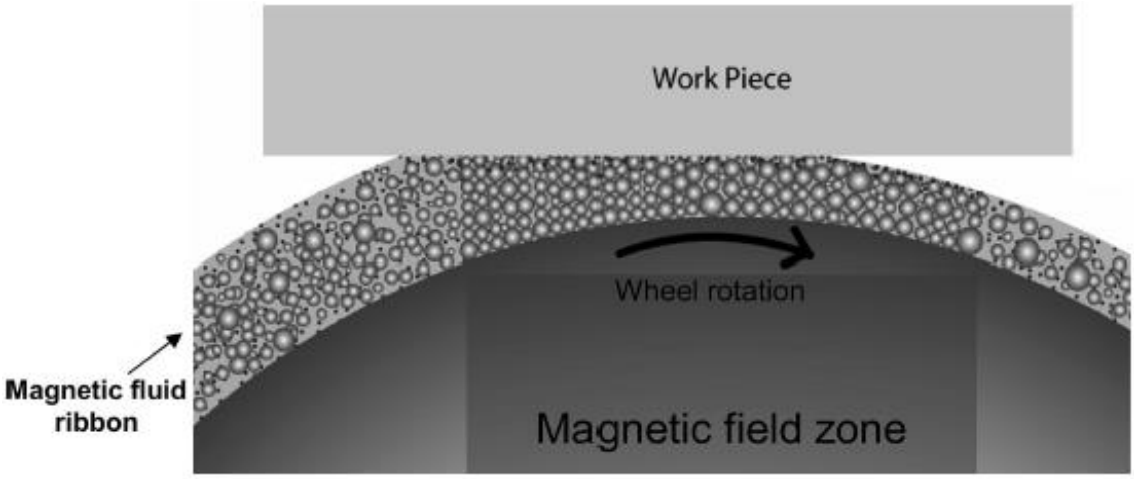

Figure 2.17 Schematic diagram of the MRF contact zone [50]

ribbon, CI particles are dragged towards the wheel by the magnetic field, which gives a magnetic buoyancy force to the nonmagnetic abrasive particles. This buoyancy force moves nonmagnetic abrasive particles towards to the surface of ribbon where it is in contact with the work-piece surface. This is the basic process in MRF.

Due to the stability of the MR fluid and magnetic field of the electromagnet, the material removal rate (MRR) in the MRF processes is stable. In addition, the material can be removed locally because the contact area between the MRF ribbon and the work-piece surface is small. The stable and local material removal allows MRF to be used as a deterministic polishing method in the manufacture of large and complex optics with a computer control.

A function that describes MRF material removal includes information about the material removal characteristic of the MRF ribbon. This information contains the geometric size and the distribution of material removal of MRF ribbon. Here, we usually describe an MRF removal function with an MRF spot, which is created by compressing the MRF ribbon into the work-piece surface for a setting time. Figure 2.18 shows an image of an MRF spot acquired by interferometer. The spot is with a D-shape, and a “tail” is towed in the flow’s reverse direction. Figure 2.19 shows a photo of a typical MRF spot.

As the polishing ribbon in the MRF processes is relatively softer than a conventional polishing tool (e.g. pitch and polyurethane), the MRF processes achieves micron-scale and nano-scale material removals and machines high quality surfaces.

2. MRF Development in NUDT

(a) Magnetic field in the MRF processes

As we know that the MR fluid behaves differently in a magnetic field which is generated by a magnet set into the polishing wheel. Generally, an electromagnet is

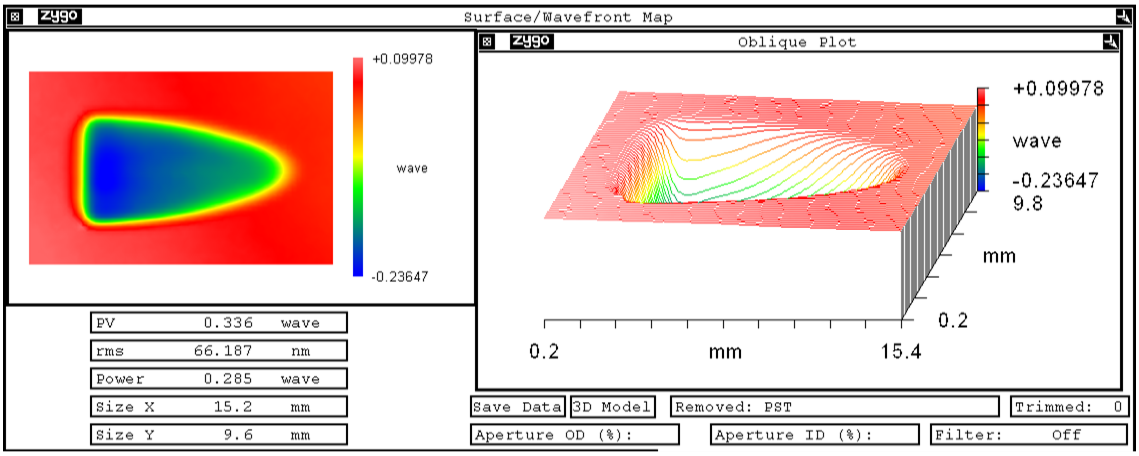

Figure 2.18 Image of an MRF spot acquired by interferometer, in which the peak-valley depth of the spot is 0.336 wave (here, a wave equals to 620 nm which is the wavelength of red light).

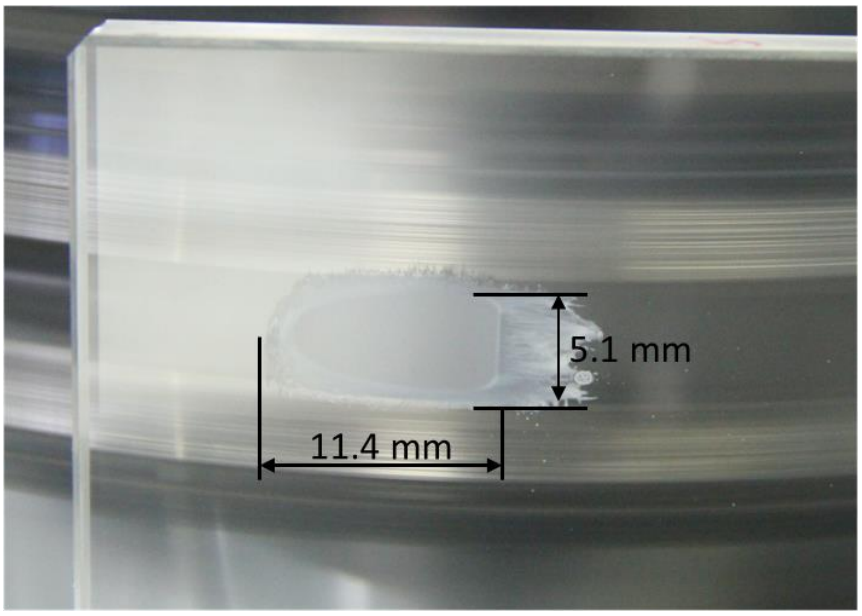

Figure 2.19 Photo of a typical MRF spot applied in an external magnetic field.

used for easy control. Figure 2.20 is a sketch of an electromagnet used in the National University of Defense Technology (NUDT, China), where the established Cartesian coordinate for the magnetic field is also shown [48]. This MRF machine is able to polish large optics up to 1 m scale.

Peng [48] and Hu [51] gave the method to calculate the magnetic field strength in the MRF process area according to Maxwell's equations and the shape of the electromagnet. In their research, the z component of the magnetic field strength was ignored as the assumption that the polishing area in the MRF processes is small enough to neglect edge effects of the electromagnet in the z direction (shown in Figure 2.20). With Peng's electromagnetic parameters, the magnetic field strength on the polishing area was calculated and shown in Figure 2.21.

In addition to the magnetic field, Peng also studied the force acting on CI particles in the magnetic field. Figure 2.22a and Figure 2.22b illustrated the force distributions in x and y component (at y=6mm) respectively. The F_x performance reveals that the CI particles is drawn to the centre; the F_y indicates that the MR fluid would congregate on the polishing wheel (at $x = 0$) and form a single stable polishing ribbon.

As magnetic CI particles can be magnetised by an external magnetic field, a phenomenon, namely the magnetorheological effect, exists. The magnetorheological effect is displayed in the Figure 2.23. Normally, magnetic CI particles and nonmagnetic abrasive particles are distributed evenly in the MR fluid (Figure 2.23a). However, as shown in Figure 2.23b, when the MR fluid is in presence of an external magnetic field, the magnetic CI particles are magnetised and form magnetic dipoles and consequently realign as chains due to the interaction of the magnetic dipoles. The direction of CI particles' chain-structure is along the external magnetic field flux line. Figure 2.24 is a photograph of magnetic chain.

The y-component magnetic force acting on CI particles (Figure 2.22b) illustrates that CI

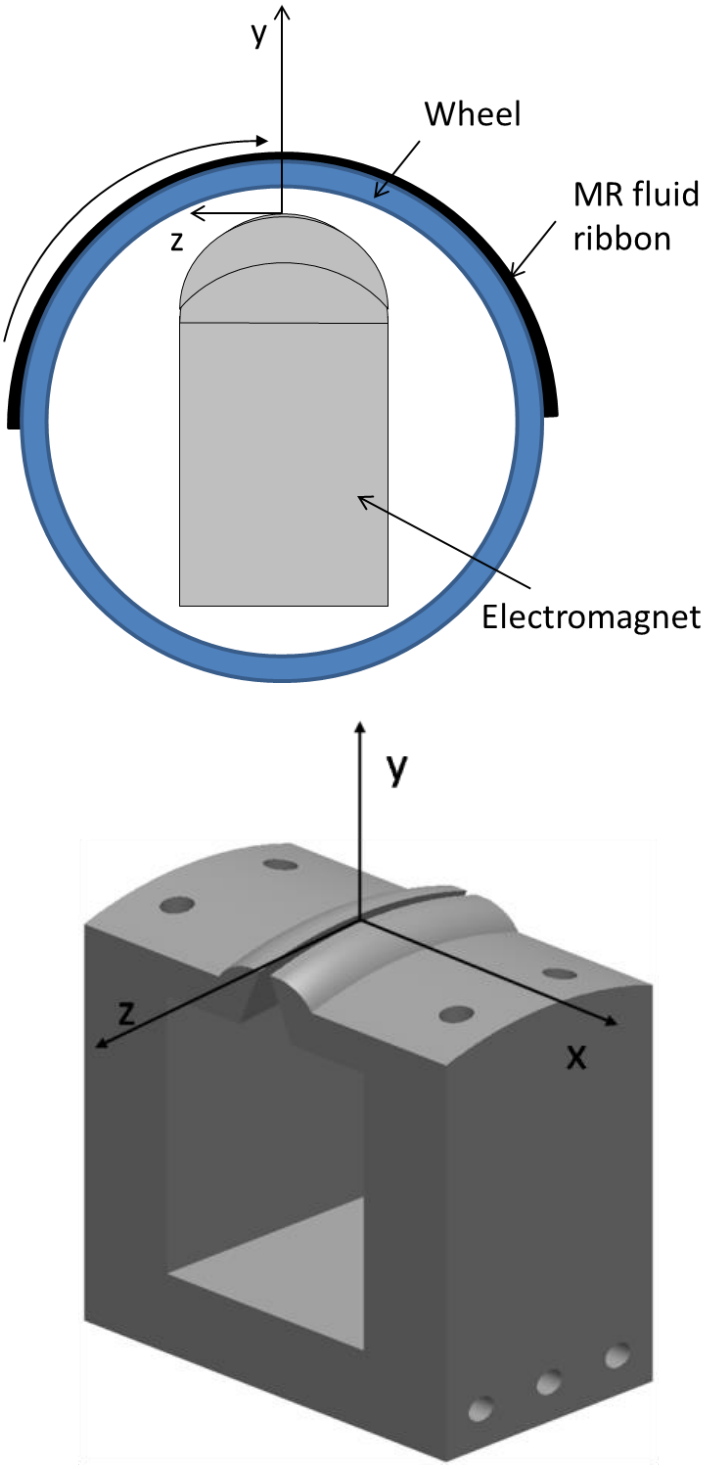

Figure 2.20 Schematic diagram of an electromagnet setting into polishing wheel, after Peng [48]

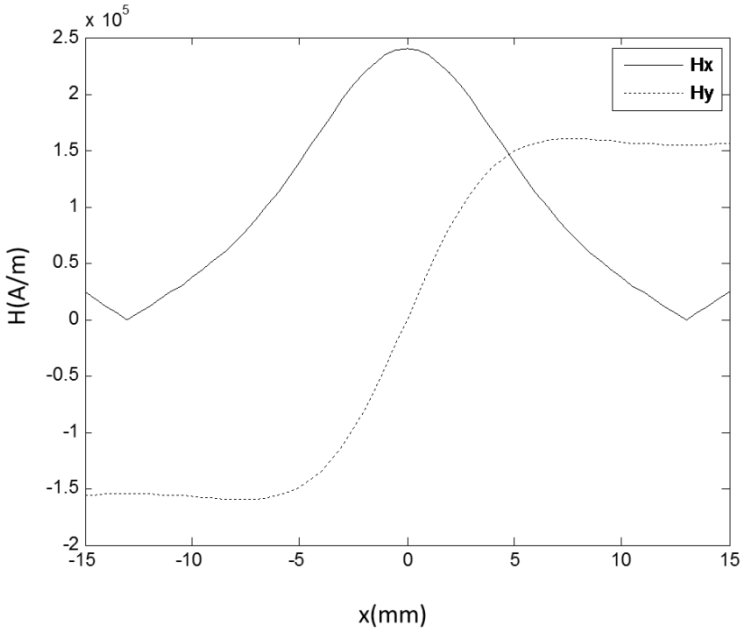

Figure 2.21 The calculated magnetic field strength on the surface of polishing wheel [48, 51]

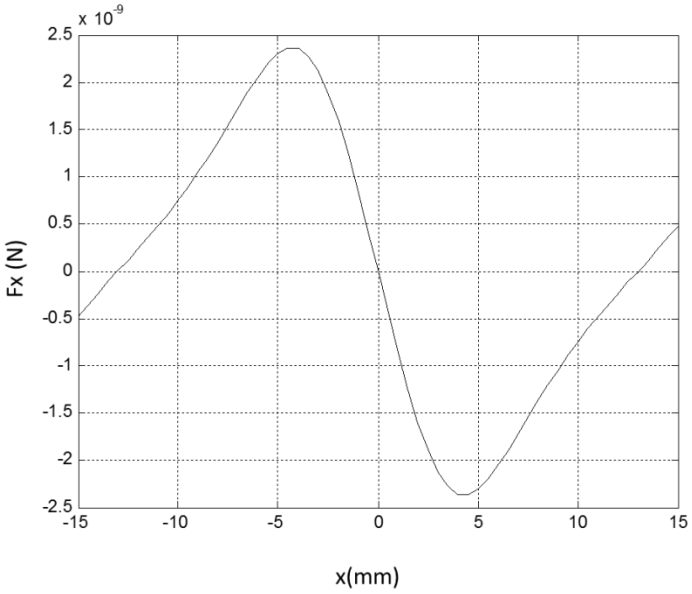

(a) Force in the x-component

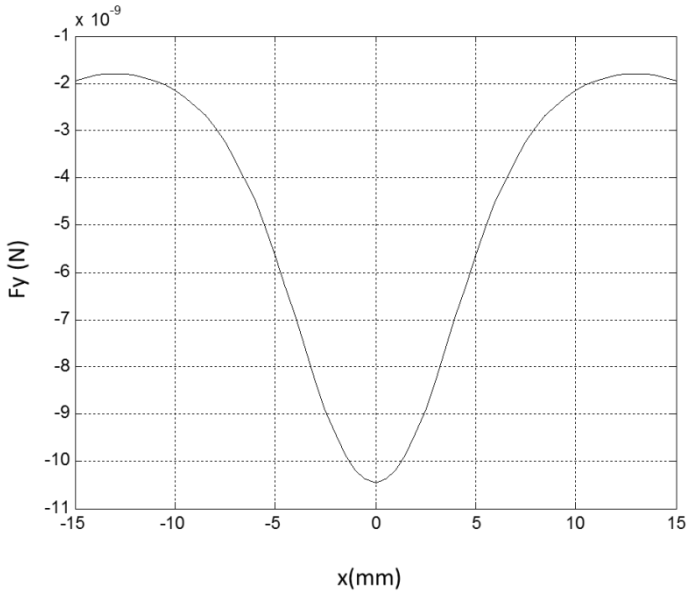

(b) Force in the y-component

Figure 2.22 Calculated force acting on CI particles (at y=6mm) [48, 51]. The negative force means the force is in inverse direction of the Cartesian coordinate positive direction.

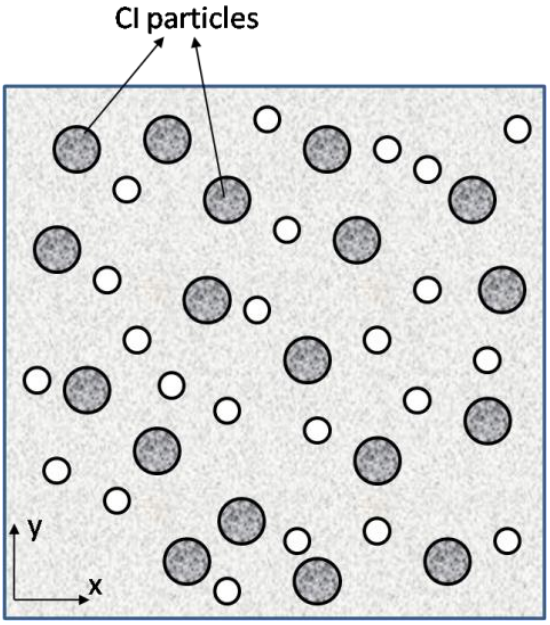

(a) MR fluid in nonmagnetic field

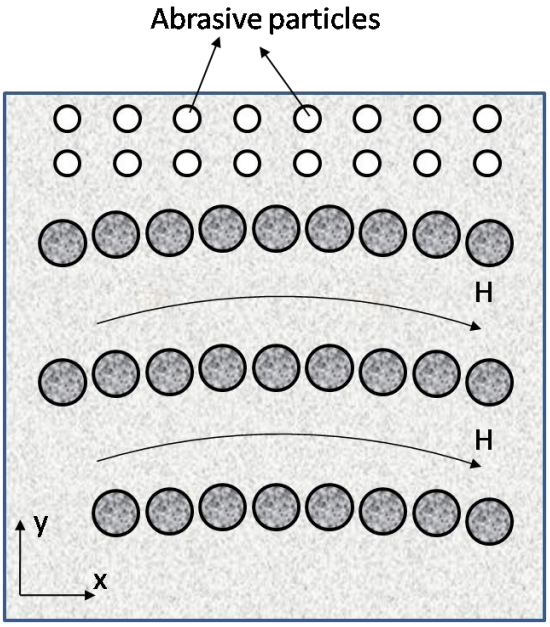

(b) MR fluid in magnetic field H.

Figure 2.23 Schematic diagram of the magnetorheological effect, after Peng [48]

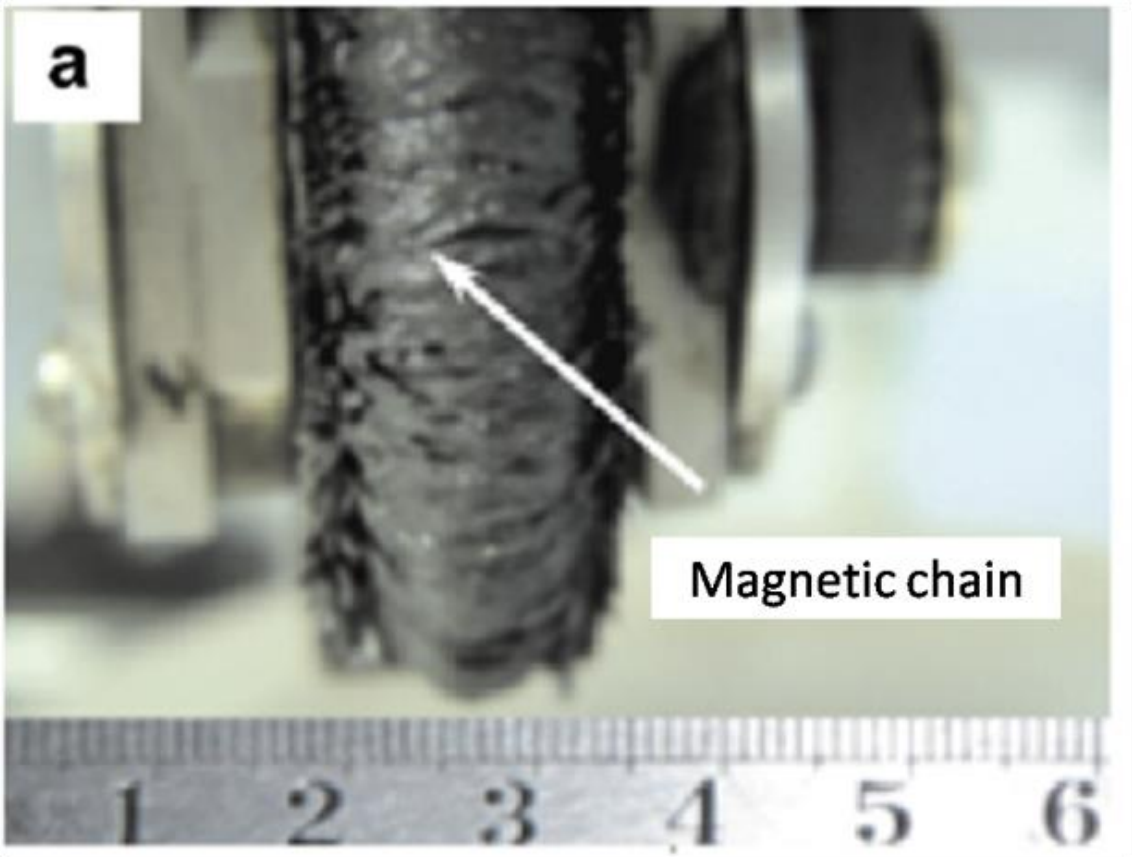

Figure 2.24 Photograph of magnetic chain taken by Cheng [52]

particles in the magnetic field are drawn towards the polishing wheel rather than the outside of the MR fluid ribbon (i.e. the direction of the work-piece). This case causes nonmagnetic abrasive particles to be displaced to the work-piece surface. The phenomenon illustrates that CI particles are drawn to the wheel and act as a “polishing pad” with abrasive particles floating to the top of this “polishing pad”.

In the presence of magnetic field, due to chain-structure formed, the MR fluid stiffens. Therefore the MR fluid behaves differently in magnetic field from which is in nonmagnetic field. In the MRF processes, hydrodynamic behaviour of MR fluid which acts as a polishing tool should be studied to get more details of this “polishing tool”.

(b) Hydrodynamic behaviour of MR fluid

The MRF machine shown in Figure 2.20 is a structure in which the work-piece is above the polishing wheel. However, the polishing wheel could be upside-down and then the work-piece is under the wheel in the MRF machine that is utilised for polishing very large and/or heavy work-pieces which are fixed on the machine’s workbench more easily than above the wheel.

Figure 2.25 illustrates a sketch of the MR fluid contacting work-piece zone for an upside-down wheel, and Figure 2.26 is the established Cartesian coordinate for the MR fluid in the gap between wheel rim and work-piece surface[53]. Here, the invisible electromagnet (Figure 2.20) is set in the wheel.

As the MR fluid behaves as a Bingham fluid in the presence of magnetic field rather than Newtonian fluid, Shi [53] used modified Reynolds Equations to calculate the normal pressure and shear stress distribution of the MRF spot (shown in Figure 2.27). The maximum normal pressure and shear stress of the MRF spot shown in Figure 2.27 were 159.8 KPa and 58.5 KPa, respectively. The stress distribution is useful for understanding the material removal in MRF process.

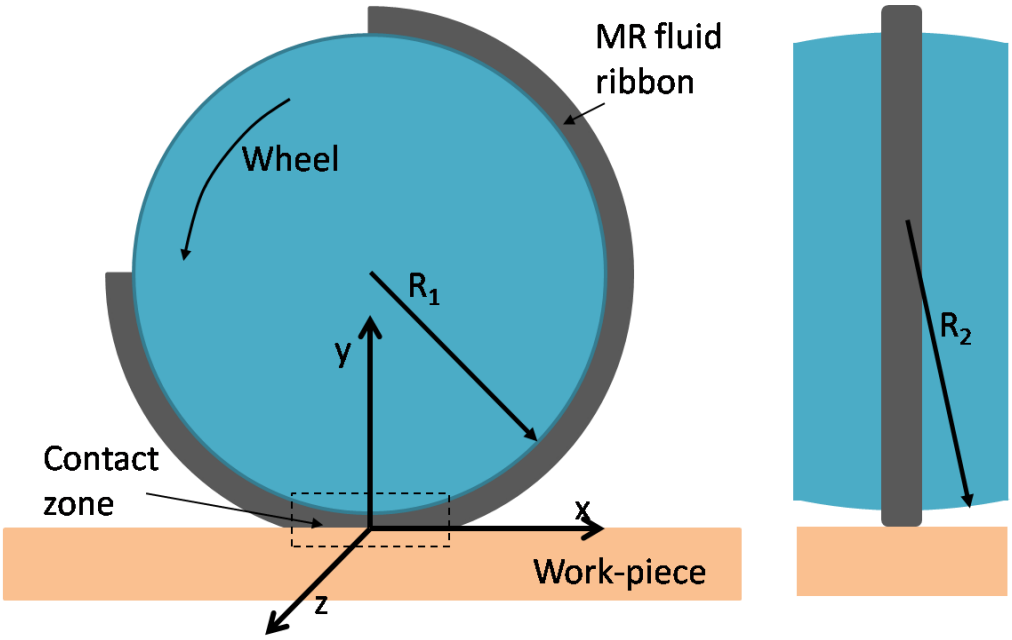

Figure 2.25 MR fluid contact zone for a upside-down wheel, after Shi [53]

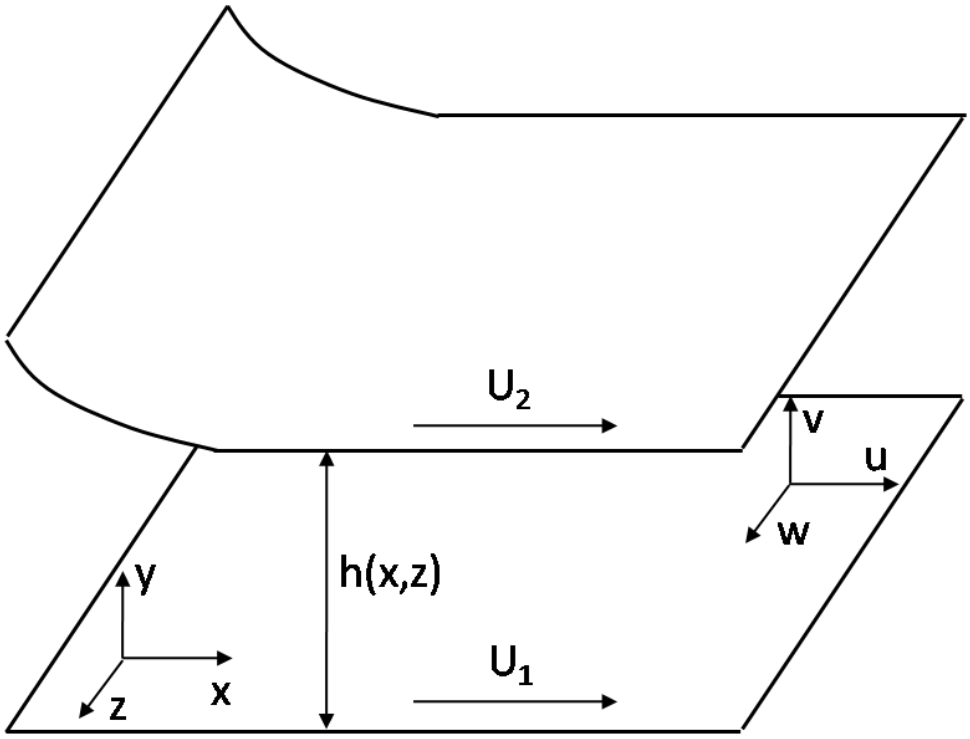

Figure 2.26 Cartesian coordinate of contact zone[53]

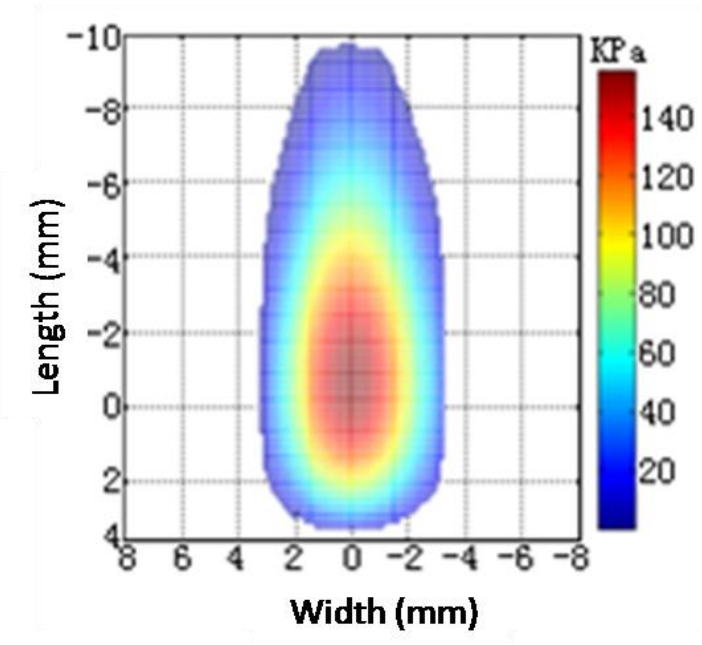

(a) Normal pressure

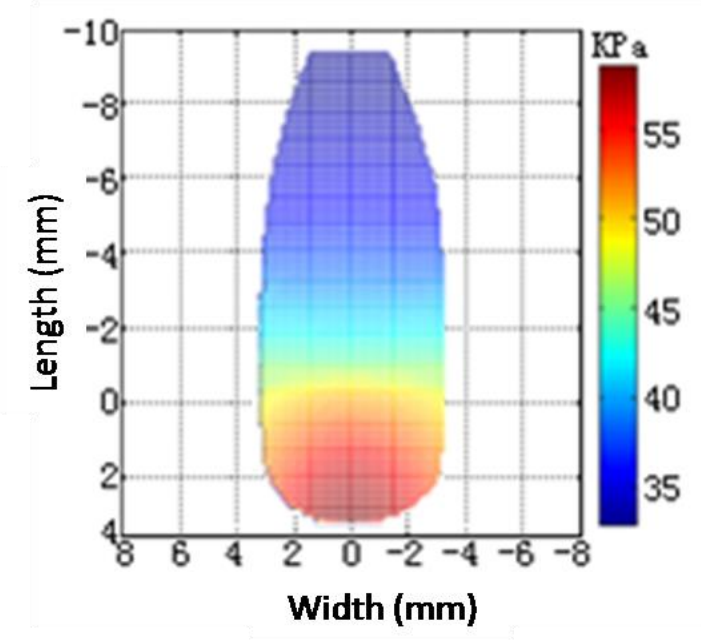

(b) Shear stress

Figure 2.27 Calculated normal pressure and shear stress of the polishing spot [53]

2.4.6 Comparison of machining techniques

The advantages and disadvantages of the aforementioned polishing processes are listed in Table 2.1. Table 2.1 indicates that the MRF process has high and stable material removal rate, and the polished surface has fine surface roughness, low surface/sub-surface damage. Moreover, the MRF process does not require strictly fine environment. Therefore, the MRF process is a good choice for polishing the fused silica optical surfaces.

Table 2.1 Comparison of polishing methods

Polishing method	Abrasive jet polishing	IBE	Lapping/CMP	EEM	MRF
MRR	Low	Medium	High	Very low	High
MRR stability	Medium	High	Low	High	High
Surface roughness	Medium	Medium	Low	Very low	Low
Surface/sub-surface damage	Depends on prior process	Depends on prior process	Low	Depends on prior process	Very low
Environment requirement	Low	High	Medium	High	Low
Cost	Low	High	Low	High	Medium

2.5 Post polishing treatments

Post polishing treatments are used to improve the LIDT after polishing processes. Three post polishing treatments will be introduced in this chapter.

2.5.1 HF-based etching process

HF-based etching technology is one of the most conventional post polishing treatments for improving the quality and increasing the LIDT of a fused silica optical surface. This method has the advantages of:

- Removing all the pre-existing absorbing precursors (i.e. fracture surface damage, impurities in the redeposition layer), which are the potential initiation sites of laser induced damage.
- Isotropically and globally treating the fused silica optics simultaneously.
- Blunting surface cracks and scratches to increase the mechanical strength and make them less likely to lead to laser induced damage, and ultimately increasing the LIDT of fused silica optics.

Therefore the HF-based etching method is widely used in the post polishing treatment in optics manufacturing.

1. Mechanisms of HF-based etching process

During the HF-based etching process, polished fused silica optics are submerged in different HF-based etchants (HF acid or NH_4F:HF at various ratios and concentrations) under certain etching conditions surface layers of the optics are removed by dissolution of fused silica [54-57].

The overall reaction of HF-based etching technology is described by the following processes [55, 58, 59]

$$SiO_{2\,(solid)} + 6HF_{(aq)} \rightarrow SiF_{6\ (aq)}^{2-} + 2H_2O_{(aq)} + 2H^{+}_{(aq)} \qquad (2.5)$$

In this process, only SiO_2 is solid phase while all of the reaction products (including

SiF_6^{2-}) are of aqueous phase. Therefore the aqueous reaction product SiF_6^{2-} anion dissolves into the etching solution and leaves the substrates of fused silica optics clean.

The reaction (2.5) involves a number of steps and intermediate products. For instance, for the HF in aqueous solution, an equilibrium exists between H^+ ion, F^- anion, and the undissociated HF:

$$HF \rightarrow F^- + H^+ \tag{2.6}$$

The fluoride anion (F^-) and undissociated acid react to generate the bifluoride anion (HF_2^-), and the reaction can be summarised as

$$HF + F^- \rightarrow HF_2^- \tag{2.7}$$

The product HF_2^- is believed to be the first species to react with the SiO_2. Therefore, the set of etchant, NH_4F:HF at various ratios and concentrations, is commonly referred to as solutions of buffered oxide etch (BOE) and generally used in the etching processes. In BOE, NH_4F can provide plentiful F^- anions because it dissociates completely. These F^- anions are free to join with HF and form HF_2^- anions, and the H^+ ions which are provided by HF via reaction (2.6) have catalytic effect for the etching processes [59, 60].

In the HF-based etching processes, the concentration of HF in the etchant solution plays an important role on the dissolution rate of SiO_2. Figure 2.28 illustrates the activation energy of the dissolution reaction of SiO_2 as a function of HF content in HF etchant and BOE etchant. The results show that the activation energy for the dissolution of SiO_2 depends on the HF content in the HF etchant. The activation energy goes up significantly with increasing the HF content when it is at low concentration, while it drops down after the concentration is higher than 5 wt%. However, for the BOE etchant, the activation energy is higher than that of HF etchant for the HF

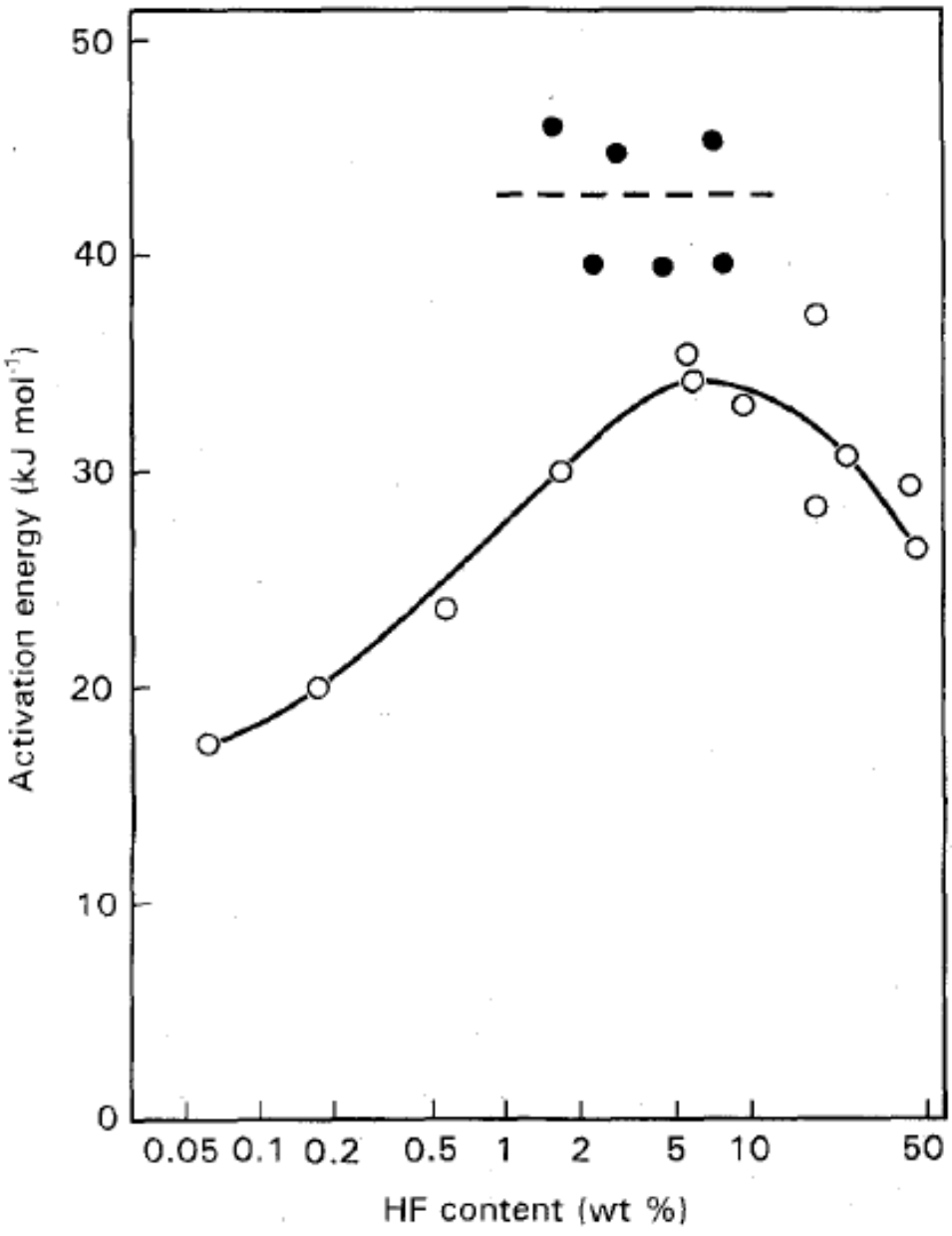

Figure 2.28 Activation energy of the dissolution reaction of SiO_2 as a function of the HF content in HF etchant (○) and BOE etchant (●) [59]. Here, the activation energy of BOE etchant is more stable than that of HF etchant

concentration below 50 wt% and is more stable in the etching processes. Therefore, in comparison with HF etchant, the BOE etchant is a better solution for SiO_2 in the HF-based etching processes.

2. Precipitates in HF-based etching processes

Although SiO_2 can dissolve in the HF-based etching processes, the aqueous reaction product SiF_6^{2-} just has limited solubility in the etching solution because it is easy to form some precipitates due to the reaction that [55]

$$SiF_{6\ (aq)}^{2-} + \frac{2}{N} M^{N+}{}_{(aq)} \rightarrow (M)_{2/N} SiF_{6\ (solid)} \tag{2.8}$$

Where M is cation and N is the charge quantity of the cation.

Therefore in the solution of BOE, the ammonium cation (NH_4^+) will form a hexafluorosilicate precipitate, $(NH_4)_2SiF_6$, by the reaction that

$$SiF_{6\ (aq)}^{2-} + 2NH_{4(aq)}^{+} \rightarrow (NH_4)_2 SiF_{6\ (solid)} \tag{2.9}$$

Apart from the NH_4^+ cation, other metallic cations, such as Al^{3+}, Na^+, etc, can also generate hexafluorosilicate precipitates via reaction (2.8) with the SiF_6^{2-} ions. Figure 2.29 shows the solubility of HF_2^- and SiF_6^{2-} in solution with various common cations. From Figure 2.29 it can be seen that common cations, especially K^+ and Na^+ form hexafluorosilicate salts that have much lower solubility than NH_4^+. Therefore it is necessary to minimise these impurities during the whole etching processes.

3. Cleaning in the HF-based etching processes

As it is easy to generate hexafluorosilicate precipitates in the HF-based etching processes due to the reaction described in (2.8), the ultrasonic cleaning technique is usually introduced in the HF-based etching processes to remove the formed

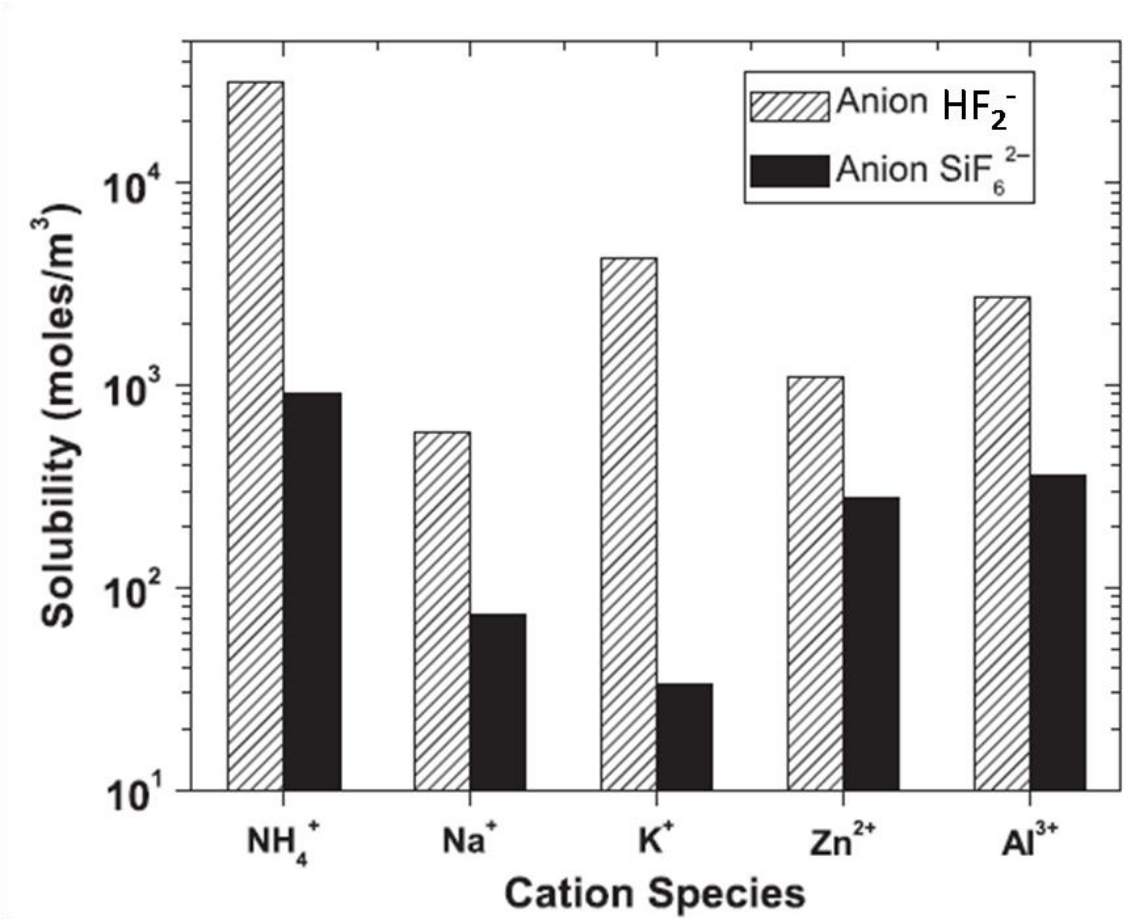

Figure 2.29 Solubility of HF_2^- and SiF_6^{2-} in solution with various cations [55]

precipitates [55, 61].

It has been investigated theoretically that various ultrasonic frequencies in the cleaning processes have different cleaning effects [55]. Figure 2.30 represents the simulation result that SiF_6^{2-} concentration at crack centre varies for different rinse times and various ultrasonic frequencies. The results illustrate that higher frequency leads to faster mass transport of SiF_6^{2-} reaction precipitates. Hence, in the etching processes, a higher frequency should be introduced to clean the reaction hexafluorosilicate precipitates.

2.5.2 Ion beam etching (IBE) process

Ion beam etching (IBE) technology, also called 'Ion beam sputter etching', which is the same process as mentioned in Section 2.3.2, is well established for removing material from high performance optical surfaces. The IBE process has been developed for correcting and figuring optical components, cleaning surfaces, micromachining, depth profiling, and other applications which need careful microscopic erosion of a surface [34, 36].

Besides the HF-based etching method, IBE technology is another effective post polishing treatment to remove the Beilby layer (redeposition layer) embedded impurities for fused silica optics. The IBE method has the following advantages:

1. IBE is a non-contact method to remove material from the optical surface, hence there is not mechanical damage in the IBE cleaning process and no edge effect exists when IBE is utilised for figuring the optical surface.

2. No polishing slurry is involved.

However, there are also some disadvantages for the IBE treatment:

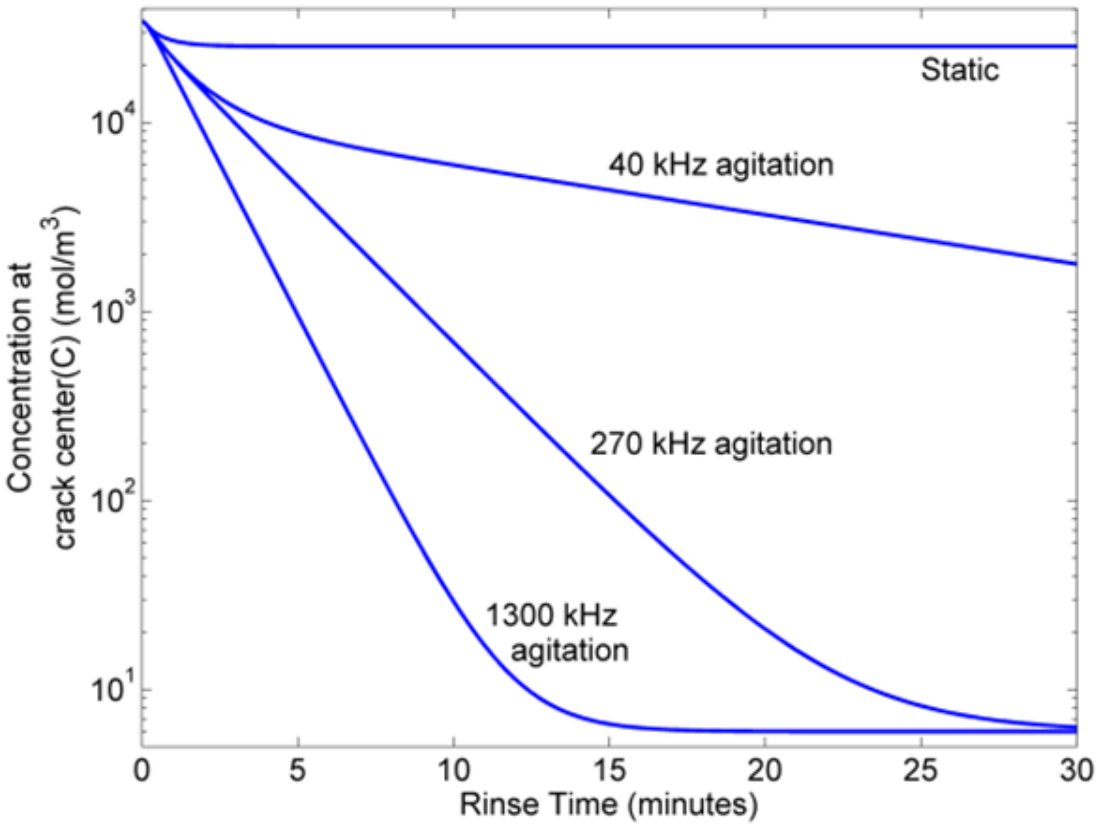

Figure 2.30 SiF_6^{2-} concentration at crack centre as a function of rinse time at various frequency ultrasonic cleaning processes[55]

1. Low efficiency. The peak material removal rate for an IBE process is just several tens of nanometres per minute which is a very low rate to process a large fused silica optical surface.
2. IBE is only suitable for materials with low coefficients of thermal expansion because it generates heat during the IBE process. However, this disadvantage can be neglected due to the low thermal expansion coefficient ($5.5 \times 10^{-7}/℃$) of fused silica.
3. High cost. The IBE system includes an ion source and vacuum chamber which are complex and expensive.

2.5.3 CO_2 laser mitigation technique

The CO_2 laser irradiation technique is a method to mitigate the LID of fused silica optical surfaces. Bass, et al. [62] used CO_2 10.6 μm laser in a CW (continuous wave) mode which heated the area to be mitigated to high temperature resulting in thermo-capillary flow. This mitigation process is shown in Figure 2.31. After irradiation by a CW CO_2 laser, the surface damage is completely annealed. A raised rim (bright circle ring shown in Figure 2.31) around the mitigation pit is generated by thermo-capillary flow under large temperature gradient. The rim refracts laser light toward to the centre and generates a downstream intensification, on-axis hot-spot that could damage other optical surfaces. Then the on-axis hot-spot is broken-up by dimpling the raised rim and therefore its intensity is reduced. However the dimpling of rim will generate a lot of re-deposit around the mitigation pit. The re-deposit could cause subsequent laser damage, so is re-melted at temperature below the evaporation temperature. At last, it must be annealed by another larger laser spot to remove the high residual stresses which is resulting from the rapid cooling process.

The technique aforementioned is sensitive to the position of the focusing lens and power of the CO_2 laser, especially in the re-melting step where excessive melting recreates high intense hot-spot while insufficient re-melting does not remove the

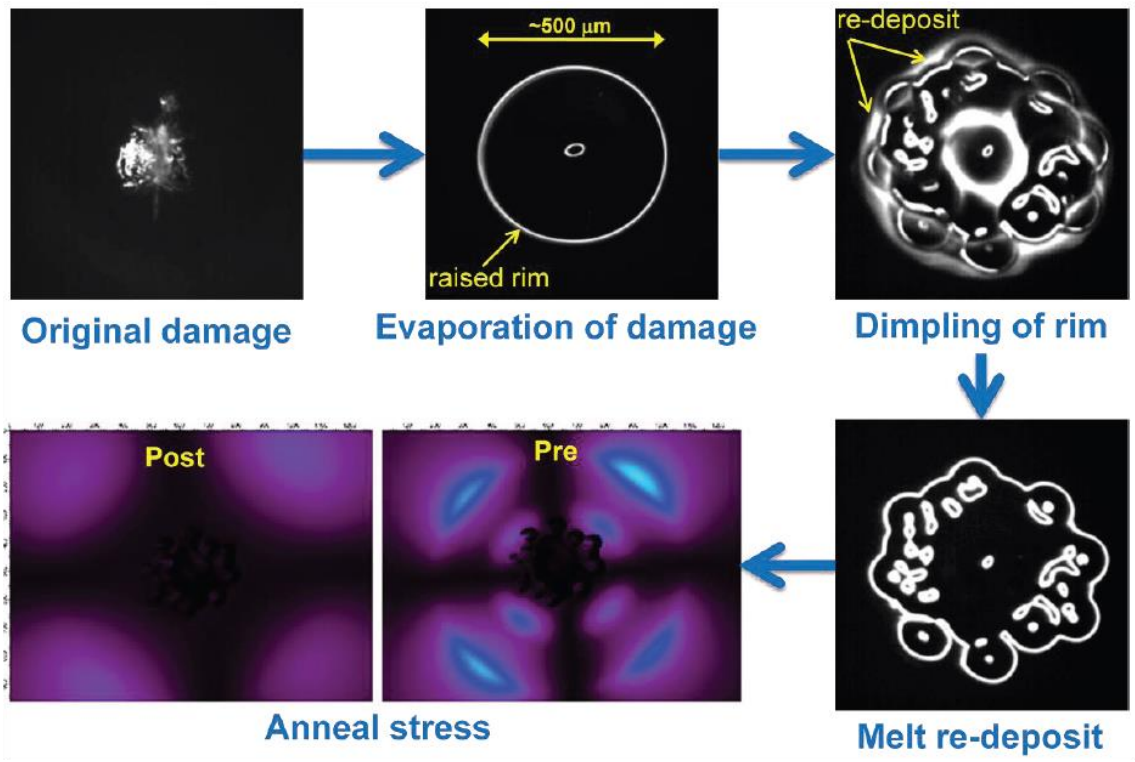

Figure 2.31 Process of CO_2 laser mitigation [63]

re-deposit enough and increase the LIDT enough.

Because of the disadvantage of the aforementioned work, Bass, et al. [63] introduced a new mitigation technique based on heating using the CO_2 10.6 μm laser. One critical difference from previous work is that the laser is operated in a pulsed mode rather than CW mode used in previous work. The pulsed mode limits the thermo-capillary flow to the area of the focused spot size and also allows cooling between pulses. Hence the raised-rim is limited to a small area and downstream intensification is reduced to an acceptable level. High evaporation temperature can be reached in the pulsed modeand ejects material away from optical surface at high speed and leaves negligible amount of re-deposit. Therefore the pulsed mode CO_2 laser mitigation technique is more advanced than the CW mode one.

2.5.4 Comparison of post polishing processes

Summary of the three aforementioned post polishing treatments is listed in Table 2.2.

Table 2.2 Comparison of post polishing treatments

Post polishing treatments	**Principle**	**Cost**
HF-based etching	Contaminants removal	Low
IBE	Contaminants removal	High
CO_2 laser mitigation	Mitigation	High

HF-based etching and IBE processes are used to remove surface contaminants while the CO_2 laser mitigation technique is used to mitigate and repair fused silica optics. In this thesis, due to the limit of experimental facility, only the first two techniques were

used.

2.6 Surface roughness influence on LIDT

2.6.1 Surface topography

For a fused silica optical component, if it is assumed that the bulk material is perfect (i.e. the material is homogenous and without strain and defects), then the optical performance of such a 'perfect' component would then depend mainly upon the total topographic information.

The total topography of a given optical surface consists of form specification and texture information. Generally texture information could be classified to waviness, roughness, and imperfections. The total topography of an optical surface is shown in Figure 2.32. Apart from the surface imperfections, which will be discussed in Chapter 4, the total surface topography could be defined in terms of its spatial frequency. Form specification is a low spatial frequency feature, while waviness and roughness are medium and high spatial frequency features, respectively. Figure 2.33 shows a surface figure obtained by a laser interferometer and its low, medium and high spatial frequency features.

In high-energy optical applications such as the NIF device, for an optical surface with diameter 400mm, surface topography is defined as four separate bands (shown in Table 1) according to its spatial frequency [13]. The surface topography in band 1 (i.e. spatial scale length is greater than 33mm) is defined as RMS Gradient; those in band 2 and band 3 are Waveness-1 (PSD-1) and Waveness-2 (PSD-2), respectively; and roughness is defined as surface texture in band 4, i.e. spatial scale length less than 0.12 mm.

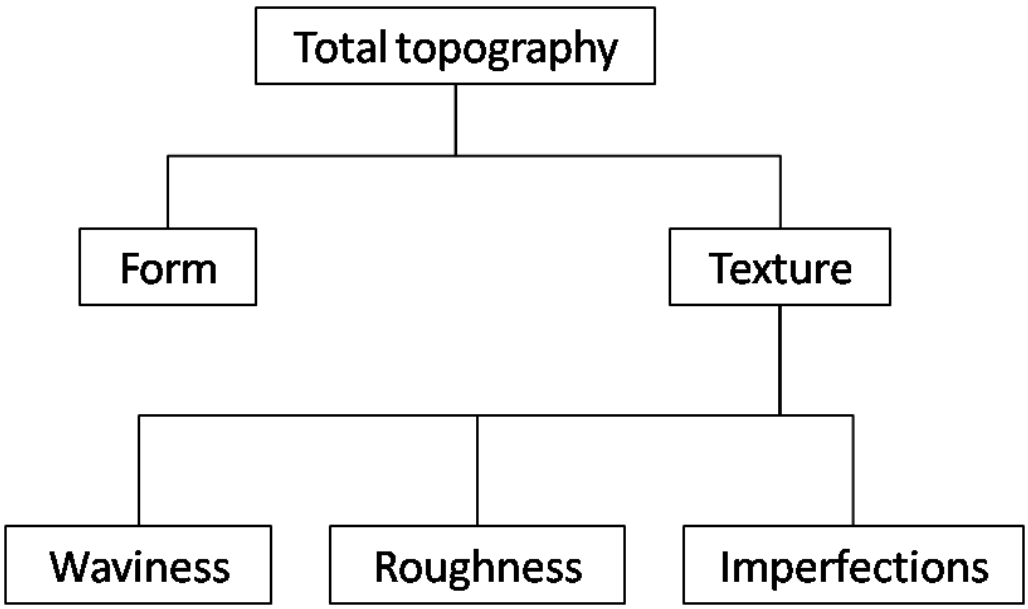

Figure 2.32 Topographic information of optical surface[22]

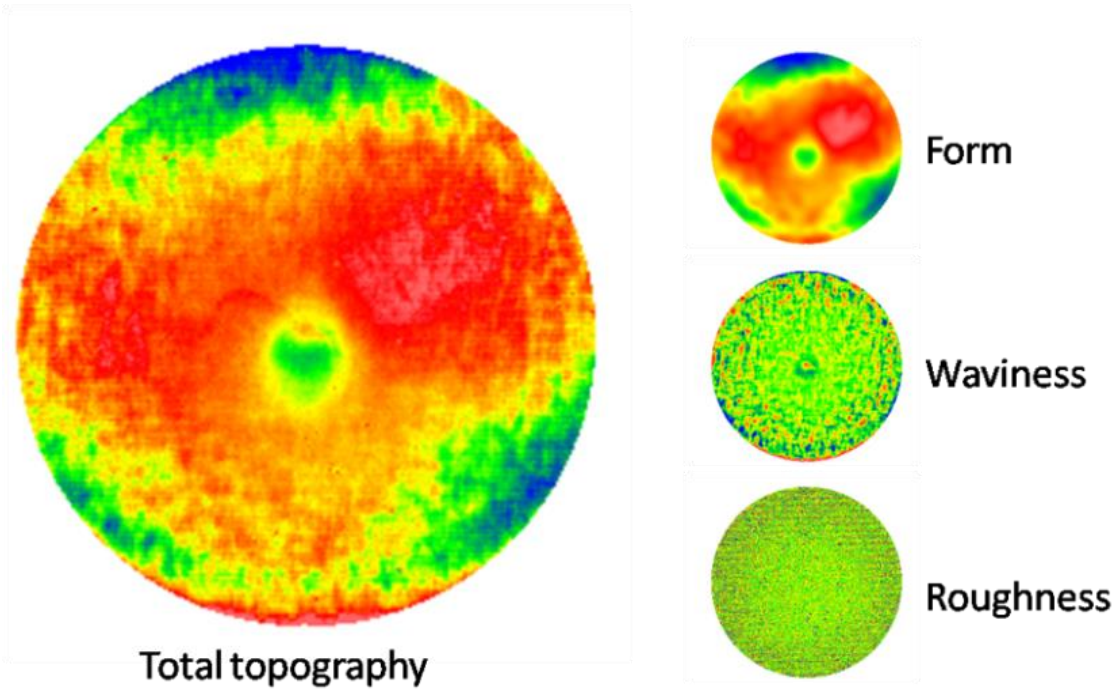

Figure 2.33 Surface topography captured by interferometer

Table 2.3 Bands of surface spatial frequencies defined by NIF[13]

	Band 1	Band 2	Band 3	Band 4
Spatial scale length [mm]	400 to 33	33 to 2.5	2.5 to 0.12	0.12 to 0.01
Spatial frequency [mm^{-1}]	0.0025 to 0.03	0.03 to 0.4	0.4 to 8.3	8.3 to 100
Designation	RMS Gradient	Waveness-1 or PSD-1	Waveness-2 or PSD-2	Roughness

Figure 2.35 shows the power spectral density (PSD) versus various spatial frequency of surface topography, and provides a limit-line which gives the maximum value for surface topography at every specific spatial frequency.

In practice, the specific spatial frequency for each definition of surface topography varies with the optical surface size, in other words, the spatial frequency regions for form, waviness and roughness are not constant. However, to simplify the issue, in this thesis, the roughness was measured by a scanning white light interferometer (SWLI) of Zygo NewView 700s with 10x optical lens. The sample distance is 1.46535μm, and the scanning area is 937.82×703.37 μm^2.

2.6.2 Effect of surface roughness on LIDT

Wood [22]indicates that the LIDT for the same optical materials when normalised to the same incident laser beam vary mainly due to the different surface finish processes. Bloembergen [64] provided a 10 nm limit, which could be width or depths, and supposed that surface defects less than this limit would play unimportant role on the LIDT in view of electric field. However, experimental observations show that an optical surface with higher surface roughness will normally have a lower LIDT. Researchers'

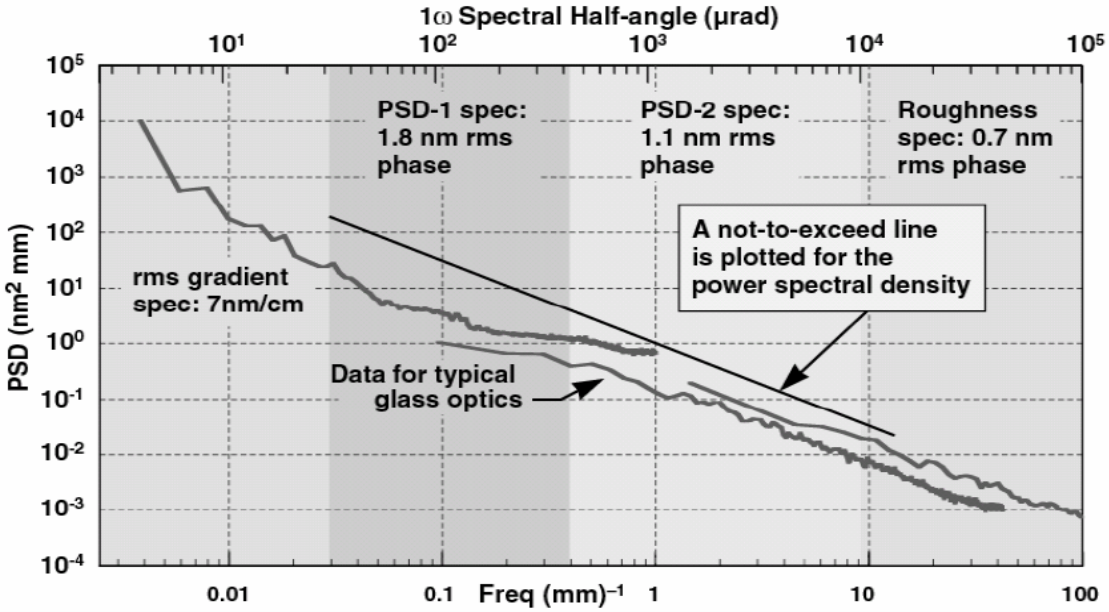

Figure 2.35 The wavefront quality of the NIF optics is specified across four contiguous spatial frequency regions from 0.0025 mm^{-1}to100 mm^{-1} [13].

work [65-67] have also suggested that surface roughness play an important role on the laser induced damage threshold of optical surfaces. The LIDT of optical surfaces related to the surface roughness is given by an empirical relation that[65]

$$E_{th}\sigma^{m} = \text{Constant} \tag{2.10}$$

where E_{th} is the corresponding electric field of damage threshold, the σ is the root mean square (RMS) roughness of optical surface, the exponent m and constant C are various for different surface treatments and surface materials. Equation (2.10) provides a dependence of breakdown electric field on surface roughness for given conditions (same optical material and same finishing processes). There is not yet a well-determined explanation for the relation between E_{th} and surface roughness and the particular values of exponent m and constant C, however several considerations have already been issued as follows [65]

1. The power absorbed by rough surface is proportional to σ^2. Therefore the laser beam power density at threshold should be proportional to σ^{-2}.

2. It is assumed that the total exposed surface area of an optical surface irradiated by the laser beam is strongly and directly related to its LIDT. For a given irradiation area, a rougher surface is generally believed to have a larger exposed surface area which could contain surface imperfections such as micro fractures and trapped contaminants. Surface imperfections are likely to initiate surface damage (discussed in Chapter 4), so a rougher surface would have lower LIDT.

House II et al. [65, 66] gave a general exponent value, $m = 0.5$, for the fused silica surface finished by lapping. However, it is still unclear for surfaces machined by different methods.

2.7 LIDT evaluation methods

LIDT measurement is a statistical process in nature. This parameter is used to evaluate the performance of processing the optical surface under the irradiation of high peak laser.

Figure 2.36 indicates a basic approach to laser damage testing. A well-characterised stable laser beam, generated by the laser system, is adjusted to the desired energy or power with a group of attenuating filters. A focussing system in the test system is used to create the destructive energy density or power density. The laser beam then is delivered through the focussing system to the specimen that is located at or near the focus of the focussing system. Generally the LIDT varies with the different sizes of irradiation laser beam.

In a testing process, the specimen is installed in the specimen platform which is able to set different test sites and adjust the incidence angle. A beam diagnostic device is equipped at a proper position with a calibrated detector to measure the laser energy or power delivered to the specimen. Damage is detected by an on-line damage detector.

Several test methods are generally used to evaluate the LIDT by experiments. Three common test methods, i.e. 1-on-1, S-on-1, and R-on-1, are introduced in this work.

2.7.1 1-on-1 test

1-on-1 test is a single-shot damage testing method [68]. In a 1-on-1 test, no matter whether laser induced damage occurs or not, each test site on the specimen surface is irradiated by a laser beam for only one shot.

A typical 1-on-1 test is conducted according to the following steps:

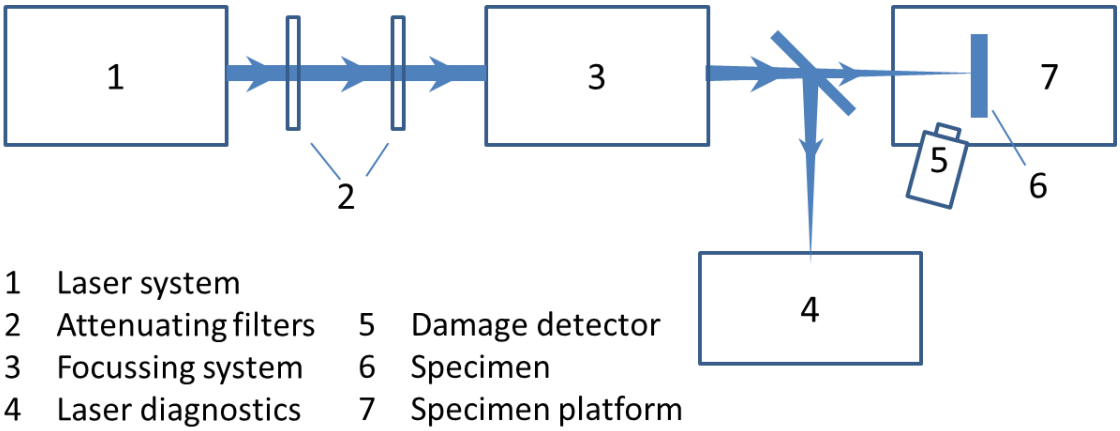

Figure 2.36 Basic approach to laser damage testing

a) Laser beam, with a given irradiating level, irradiates the specimen at a setting test site once. An irradiating level for a laser beam means the laser beam is at a specific energy-density or power-density. Record the result whether damage occurs or not.

b) Repeat step a, with the same irradiating level, at a number of non-overlapping test sites (10 sites at least) in regard to the laser beam.

c) Calculate the damage probability, i.e. the fraction of sites which are damaged, DP, at the fixed irradiating level for step a-b using the following equation.

$$\mathrm{DP} = \frac{\text{Number of damage sites}}{\text{Number of total test sites}} \times 100\% \tag{2.11}$$

d) Repeat steps a-c at different laser beam irradiating levels until the range of irradiating levels employed is sufficiently wide to include the points of no damage, as well as points where all sites are damaged.

The LIDT in 1-on-1 tests is obtained by the damage-probability method. The damage probability data are then plotted versus the corresponding irradiating level. An example is shown in Figure 2.37. The LIDT of the specimen is named zero-probability damage fluence. In other words, the LIDT value is the irradiating level at which the probability of specimen damage occurs is zero (i.e. where the horizontal-axis intercept value).

2.7.2 S-on-1 test

S-on-1 test is a repetitive testing method [69]. As a repetitive testing method, irradiation in the S-on-1 test may deteriorate or improve the optical surface's performance compared with those in the measurement for single-shot. During a laser beam irradiating process, reversible and irreversible mechanisms can occur. The

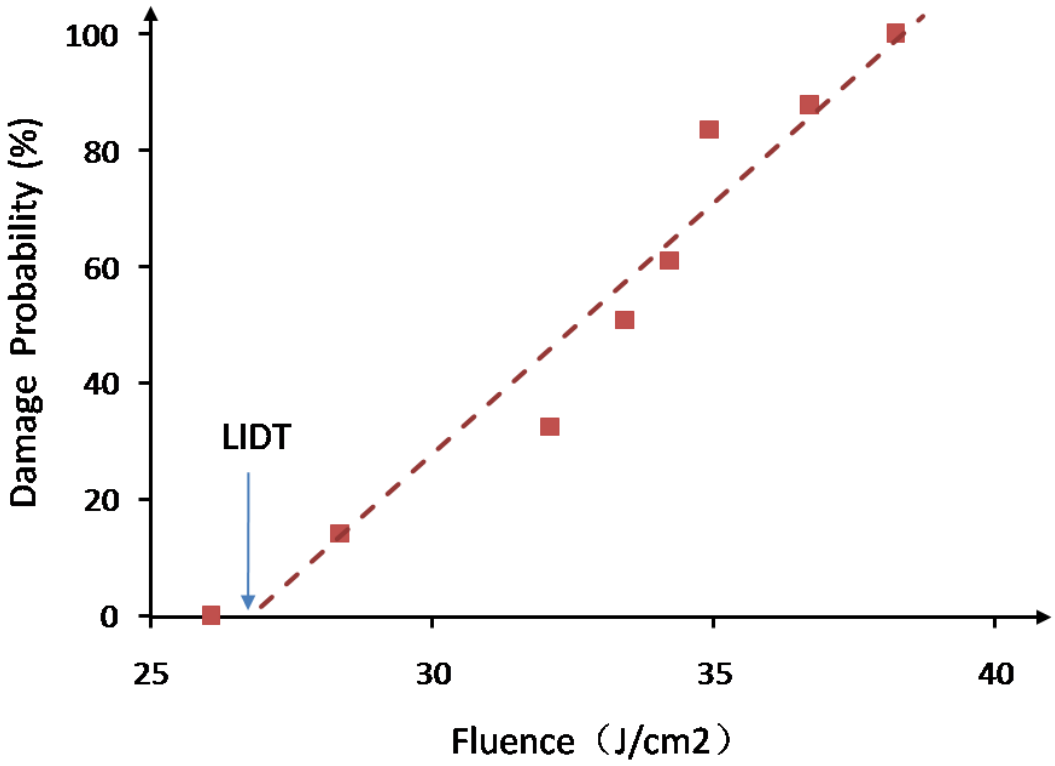

Figure 2.37　Example of damage probability plot to determine LIDT

reversible mechanisms, including distortion and thermal heating, normally have no influence on the damage under repetitively pulsed laser beam irradiation; while the irreversible mechanisms, such as micro-damage, ageing, the generation or migration defects, impurities redistribution, and surface annealing, are able to degrade or upgrade the LIDT under the influence of repetitively pulsed laser beams [22].

Nearly the same as it is carried out the single-shot testing method (1-on-1 test), the measurement procedure of the S-on-1 test has only one different aspect that each test site is irradiated repetitively several times. To be detailed, the only difference between an S-on-1 test and a 1-on-1 test is the first step aforementioned in 1-on-1 test method. In an S-on-1 test procedure, the first step should be that

a) Laser beam, with a given irradiating level, irradiates the specimen at a same setting test site at some agreed laser beam repetitive irradiating frequency, or until laser induced damage occurs.

The evaluation of LIDT in S-on-1 test is same as that in 1-on-1 test.

2.7.3 R-on-1 test

R-on-1 test is also a repetitive testing method. In this measurement procedure usually it starts at a very low laser fluence and then increases constantly step by step until the surface damage is observed [70].

For the R-on-1 test facility reported by NIF [71, 72], a laser pulse train with a ramping fluence irradiates each site with a specific pulse repetition frequency (PRF).The ramping fluence is defined by a starting fluence and the increment fluence step. During this ramping train, a scatter diagnostic device is utilised to detect the bulk or surface condition of the optical material whether it is damaged or not in the test process.

The R-on-1 test is useful to roughly estimate the LIDT of optics, especially when the

surface is too limited to do an S-on-1 or 1-on-1 test. However, it is not accurate to evaluate the LIDT in comparison with the S-on-1 and 1-on-1 test methods because it is very depended on the irradiation conditions such as irradiation site, starting fluence, increment fluence step, and so on. What's more, the R-on-1 is not a standard LIDT test method because it does not have an ISO standard.

Figure 2.38(a) to Figure 2.38(c) illustrate the three types of laser irradiation methods on a single position at the optical surface.

2.8 Summary

This chapter reviews some background knowledge which is involved in this research.

First of all, the optical properties of fused silica, such as transmission and refractive index, were introduced in this chapter. The good transmission for fused silica makes it be a well-used material in the UV laser system. The refractive index ($n_\lambda = 1.48$) of fused silica at 355nm UV light was also given.

Mechanisms of laser induced damage were reviewed. It is believed that thermal process and electric process are the main reason causing LID of optical components.

The definition of LID of fused silica optics in the high peak power laser system, especially in the ICF system, was given. LID of fused silica optics is defined as any detectable morphological change in the material. The detection method could be visual inspection or light microscopy. LID usually occurs on the optical surface and reduces the lifetime of the optics. Therefore some details such as initiations and morphology of LID were introduced in this chapter.

Manufacturing processes of optical surfaces are believed to be able to change the LID condition. Hence several optical surface polishing methods were presented

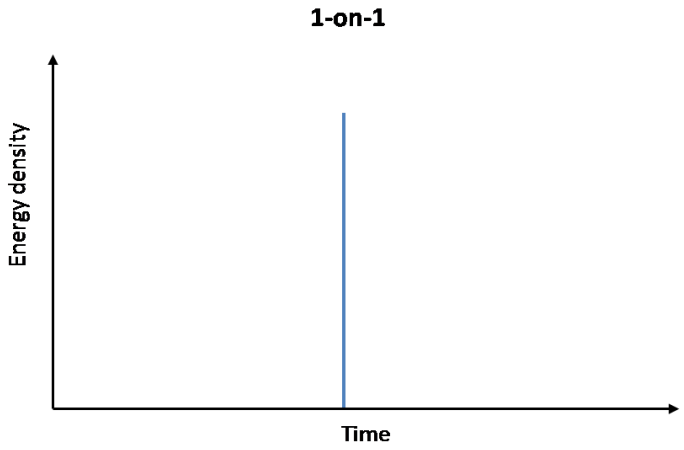

(a)

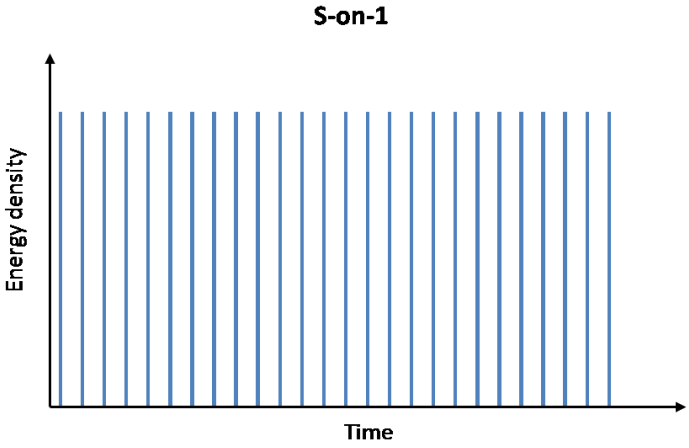

(b)

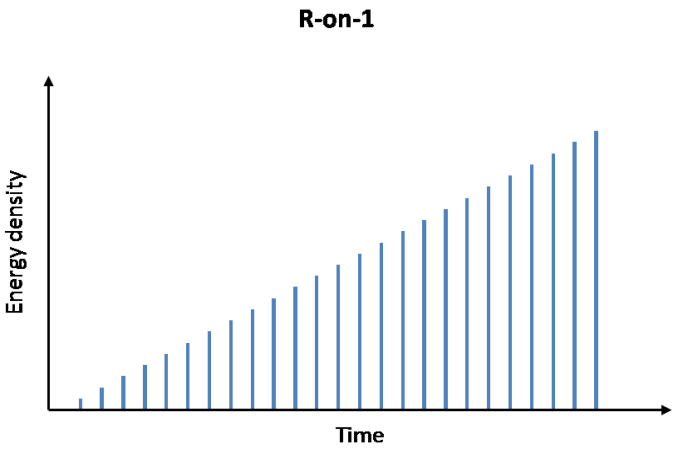

(c)

Figure 2.38 Laser irradiation methods of (a) 1-on-1 test, (b)S-on-1, and (c) R-on-1

subsequently. The MRF process, which is an advanced polishing method, was detailed.

Three post polishing treatments which are used to improve the LIDT of fused silica optics were listed. Due to the conditions of our laboratory, only HF-based etching process and IBE process will be used in the following work of this thesis.

Surface topography includes form, waviness and roughness according to the spatial frequency. The influence of surface roughness on LIDT was also reviewed.

At last, three LIDT evaluation methods (i.e. 1-on-1, S-on-1, and R-on-1) were introduced in this chapter. 1-on-1 method will be used in this thesis.

References

1. "Quartz Glass for Optics Data and Properties". [Online]; Available from: http://optics.heraeus-quarzglas.com/media/webmedia_local/downloads/FusedsilicaandQuartzGlassforOpticsDataandProperties.pdf.

2. Tan, C., "Determination of refractive index of silica glass for infrared wavelengths by IR spectroscopy". *Journal of Non-crystalline Solids*, 1998. **223**: pp. 158-163.

3. Malitson, I., "Interspecimen comparison of the refractive index of fused silica". *Journal of Optical Society of America*, 1965. **55**: pp. 1205-1209.

4. Rodney, W. and R. Spindler, "Index of refraction of fused quartz for ultraviolet, visible, and infrared wavelengths". *Journal of Optical Society of America*, 1954. **44**: pp. 677-679.

5. Kitamura, R., L. Pilon and M. Jonasz, "Optical constants of silica glass from extreme ultraviolet to far infrared at near room temperature". *Appl. Opt.*, 2007. **46**(33): pp. 8118-8133.

6. Lowdermilk, W.H. "Status of the National Ignition Facility Project". in *Proceeding of SPIE*. 1997. **3047**: pp. 16-37

7. Andre, M.L. "Status of the LMJ Project". in *Proceeding of SPIE*. 1997. **3047**: pp. 38-42

8. Stevens-Kalceff, M.A., A. Stesmans and J. Wong, "Defects induced in fused silica by high fluence ultraviolet laser pulses at 355 nm". *Applied Physics Letters*, 2002. **80**(5): pp. 758-760.

9. Wong, J., J.L. Ferriera, E.F. Lindsey, D.L. Haupt, I.D. Hutcheon and J.H. Kinney,

"Morphology and microstructure in fused silica induced by high fluence ultraviolet 3w (355nm) laser pulses". *Journal of Non-crystalline Solids*, 2006. **352**(3): pp. 255-272.

10. Demos, S.G., M.R. Kozlowski, M.C. Staggs, L.L. Chase, A.K. Burnham and H.B. Radousky. "Mechanisms to explain damage growth in optical materials". in *Proceeding of SPIE*. 2001. **4347**: pp. 277-284

11. Salleo, A., "High-Power Laser Damage in Fused Silica" [PhD Thesis]: University of California, Berkeley; 2001.

12. Burnham, A., R.P. Hackel, P. Wegner, T. Parham, L.W. Hrubesh, B. Penetrante, P. Whitman, S.G. Demos, J. Menapace, M. Runkel, M. Fluss, M.D. Feit, M. Key and T. Biesiada. "Improving 351-nm damage performance of large-aperture fused silica and DKDP optics". in *Proceeding of SPIE*. 2002. **4679**: pp. 173-185

13. Campbell, J.H., R.A. Hawley-Fedder, C.J. Stolz, J.A. Menapace, M.R. Borden, P.K. Whitman, J. Yu, M. Runkel, M.O. Riley, M.D. Feit and R.P. Hackel. "NIF optical materials and fabrication technologies: An overview". in *Proceeding of SPIE*. 2004. Bellingham, WA. **5341**: pp. 84-101

14. Miller, P.E., T.I. Suratwala, J.D. Bude, T.A. Laurence, N. Shen, W.A. Steele, M.D. Feit, J.A. Menapace and L.L. Wong. "Laser damage precursors in fused silica". in *Proceeding of SPIE*. 2009. **7504**: pp. 75040X-75040X-14

15. Salleo, A., F.Y. Genin, J.M. Yoshiyama, C.J. Stolz and M.R. Kozlowski. "Laser-induced damage of fused silica at 355nm initiated at scratches". in *Proceeding of SPIE*. 1998. **3244**: pp. 341-347

16. Feit, M.D., J.H. Campbell, D. Faux, F.Y. Genin, M.R. Kozlowski, A.M. Rubenchik, R. Riddle, A. Salleo and J. Yoshiyama. "Modeling of laser-induced surface cracks in

silica at 355 nm". in *Proceeding of SPIE*. 1998. **3244**: pp. 350-355

17. Papernov, S. and A.W. Schmid. "Laser-induced surface damage of optical materials: Absorption sources, initiation, growth, and mitigation". in *Proceeding of SPIE*. 2008. **7132**: pp. 71321J-1 - 71321J-27

18. Liu, H., X. Zhou, J. Huang, Z. Zheng, F. Wang, X. Jiang, W. Wu and W. Zheng, "The damage mechanism of fused silica surface induced by 355 nm nanosecond laser". *Optik - International Journal for Light and Electron Optics*, 2011. **122**: pp. 1663-1665.

19. Demos, S.G., L.M. Sheehan and M.R. Kozlowski. "Spectroscopic Investigation of SiO_2 Surfaces of Optical Materials for High Power Lasers". in *Proceeding of SPIE*. 2000. **3933**: pp. 316-320

20. Wong, J., J.L. Ferriera, E.F. Lindsey, D.L. Haupt, I.D. Hutcheon and J.H. kinney, "Morphology and microstructure in fused silica induced by high fluence ultraviolet 3w (355nm) laser pulses". *Journal of Non-crystalline Solids*, 2006. **352**: pp. 255-272.

21. Ristau, D., M. Jupe and K. Starke, "Laser damage thresholds of optical coatings". *Thin Solid Films*, 2009. **518**: pp. 1607-1613.

22. Wood, R.M., "Laser-Induced Damage of Optical Materials". 1 ed. Series in Optics and Optoelectronics, ed. R.G.W. Brown and E.R. Pike. 2003, Bristol: Institute of Physics Publishing.

23. Li, C.H., "Mechanism Study on High Power UV Laser-Induced Damage in Fused Silica Optics" [PhD Thesis]. Beijing, China: University of Science and Technology Beijing; 2011.

24. Sun, C.W., "Effects of laser irradiation". 2002, Beijing, China: National Defence

Industry Press.

25. Tricard, M., W.I. Kordonski, A.B. Shorey and C. Evans, "Magnetorheological Jet Finishing of Conformal, Freeform and Steep Concave Optics". *CIRP Annals - Manufacturing Technology*, 2006. **55**(1): pp. 309-312.

26. Hashish, M., "A Model for Abrasive-Waterjet (Awj) Machining". *Journal of Engineering Materials and Technology-Transactions of the Asme*, 1989. **111**(2): pp. 154-162.

27. Tam, H.Y., H.B. Cheng and Y.W. Wang, "Removal rate and surface roughness in the lapping and polishing of RB-SiC optical components". *Journal of Materials Processing Technology*, 2007. **192-193**: pp. 276-280.

28. Mori, Y., K. Yamauchi and K. Endo, "Elastic emission machining". *Precision Engineering*, 1987. **9**(3): pp. 123-128.

29. Mori, Y., K. Yamamura, K. Endo, K. Yamauchi, K. Yasutake, H. Goto, H. Kakiuchi, Y. Sano and H. Mimura, "Creation of perfect surfaces". *Journal of Crystal Growth*, 2005. **275**(1-2): pp. 39-50.

30. Fahnle, O.W.H.v.B., "Finishing of optical materials using fluid jet polishing". *14th ASPE Annual Meeting*, 1999: pp. 509-512.

31. Horiuchi, O., J. Ikeno, H. Shibutani, H. Suzuki and Y. Mizukami, "Nano-abrasion machining of brittle materials and its application to corrective figuring". *Precision Engineering*, 2007. **31**(1): pp. 47-54.

32. Allen L N, K.R.E. "An ion figuring system for large optic fabrication". in *Proceeding of SPIE*. 1989. **1168**: pp. 33-50

33. Takaharu, M., M. Katsuhiko, S. Kazuaki, K. Yoshiaki, O. Yukiharu and A. Takeshi.

"Nikon EUVL development progress summary". in *Proceeding of SPIE*. 2006. **6151**: pp. 615105-01 - 615105-10

34. Frost, F., R. Fechner, B. Ziberi, D. Flamm and A. Schindler, "Large area smoothing of optical surfaces by low-energy ion beams". *Thin Solid Films*, 2004. **459**(1-2): pp. 100-105.

35. Drueding, T.W., T.G. Bifano and S.C. Fawcett, "Contouring algorithm for ion figuring". *Precision Engineering*, 1995. **17**(1): pp. 10-21.

36. Seshan, K., "Handbook of Thin-Film Deposition Processes and Techniques". 2 ed. 2002, New York: Noyes Publications/ William Andrew Publishing.

37. Spencer, E.G. and P.H. Schmidt, "Ion beam techniques for device fabrication". *The Journal of Vacuum science and technology*, 1972. **13**(5): pp. S52-S70.

38. Paula, G., "Automating lens manufacturing". *Mechanical Engineering*, 1997. **119**(3): pp. 88-91.

39. Luo, J. and D. Dornfeld. "Material removal mechanism in chemical mechanical polishing: theory and modeling". in *IEEE transactions on semiconductor manufacturing*. 2001. **14**: pp. 112-133

40. Cheng, H.-B., Z.-J. Feng, K. Cheng and Y.-W. Wang, "Design of a six-axis high precision machine tool and its application in machining aspherical optical mirrors". *International Journal of Machine Tools and Manufacture*, 2005. **45**(9): pp. 1085-1094.

41. Jacobs, S.D., D. Golini, Y. Hsu, B.E. Puchebner, D. Strafford, I.V. Prokhorov, E.M. Fess, D. Pietrowski and W.I. Kordonski, "Magnetorheological finishing: a deterministic process for optics manufacturing". *Optical Fabrication and Testing*, 1995: pp. 372-382.

42. Golini, D., S.D. Jacobs, W.I. Kordonski and P. Dumas, "Precision Optics Fabrication Using Magnetorheological FInishing". *Advanced Materials for Optics and Precision Structures*, 1997: pp. 251-274.

43. Schinhaerl, M., G. Smith, R. Stamp, R. Rascher, L. Smith, E. Pitschke, P. Sperber and A. Geiss, "Mathematical modelling of influence functions in computer-controlled polishing: Part I". *Applied Mathematical Modelling*, 2008. **32**(12): pp. 2888-2906.

44. Seok, J., Y.-J. Kim, K.-I. Jang, B.-K. Min and S.J. Lee, "A study on the fabrication of curved surfaces using magnetorheological fluid finishing". *International Journal of Machine Tools and Manufacture*, 2007. **47**(14): pp. 2077-2090.

45. Cheng, H.B., Y.P. Feng, L.Q. Ren, S. To and Y.T. Wang, "Material removal and micro-roughness in fluid-assisted smoothing of reaction-bonded silicon carbide surfaces". *Journal of Materials Processing Technology*, 2009. **209**(9): pp. 4563-4567.

46. Jha, S. and V.K. Jain, "Design and development of the magnetorheological abrasive flow finishing (MRAFF) process". *International Journal of Machine Tools and Manufacture*, 2004. **44**(10): pp. 1019-1029.

47. Jain, V.K., S.C. Jayswal and P.M. Dixit, "Modeling and simulation of surface roughness in magnetic abrasive finishing using non-uniform surface profiles". *Materials and Manufacturing Processes*, 2007. **22**: pp. 256-270.

48. Peng, X., "Study on the Key Techniques of Deterministic Magnetorheological Finishing" [PhD Thesis]. Changsha: National Universtiy of Defense Technology; 2004.

49. COM. "Magnetorheological". [Online]; Available from:

http://www.opticsexcellence.org/SJ_TeamSite/RS_mrf.html.

50. DeGroote, J.E., A.E. Marino, J.P. Wilson, A.L. Bishop and S.D. Jacobs. "The role of nanodiamonds in the polishing zone during magnetorheological finishing (MRF)". in *Proceeding of SPIE*. 2007. **6671**: pp. 66710Z-1 - 66710Z-15

51. Hu, H., "Study on the Key Technology of Magnetorheoligcal Finishing for Large Optical Surface" [MSc Dissertation]. Changsha, China: National University of Defense Technology; 2006.

52. Cheng, H., Y. Yeung and H. Tong, "Viscosity behavior of magnetic suspensions in fluid-assisted finishing". *Progress in Natural Science*, 2008. **18**(1): pp. 91-96.

53. Shi, F., "Study on the Key Techniques of Magnetorheological Finishing for High-precision Optical Surfaces" [PhD Thesis]: National University of Defense Technology; 2009.

54. Feit, M.D., T. Suratwala, L. Wong, W. Steele and J. Bude. "Modeling Wet Chemical Etching of Surface Flaws on Fused Silica". in *Proceeding of SPIE*. 2009. **7051**: pp. 70540L-70540L-13

55. Suratwala, T., P. Miller, J. Bude, W. Steele and N. Shen, "HF-Based Etching Processes for Improving Laser Damage Resistance of Fused Silica Optical Surface". *Journal of American Ceramic Society*, 2011. **94**(2): pp. 416-428.

56. Battersby, C.L., L.M. Sheehan and M.R. Kozlowski. "Effects of wet etch processing on laser-induced damage of fused silica surfaces". in *SPIE of Part of the symposium on laser-induced damage in optical materials*. 1998. Boulder, Colorado. **3578**: pp. 446-455

57. Hrubesh, L.W., M.A. Norton, W.A. Molander, P.J. Wegner, M.C. Staggs, S.G. Demos, J.A. Britten, L.J. Summers, E.F. Lindsey and M.R. Kozlowski. "Chemical

etch effects on laser-induced surface damage growth in fused silica". in *Proceeding of SPIE*. 2001. **4347**: pp. 553-559

58. Zheng, Z., X. Zu and X. Jiang, "Effect of HF etching on the surface quality and laser-induced damage of fused silica". *Optics and Laser Technology*, 2012. **44**: pp. 1039-1042.

59. Spierings, G., "Wet chemical etching of silicate glasses in hydrofluoric acid based solutions". *JOURNAL OF MATERIALS SCIENCE*, 1993. **28**: pp. 6261-6273.

60. Wong, L., T. Suratwala, M.D. Feit, P. Miller and R. Steele, "The Effect of HF/NH4F Etching on the Morphology of Surface Fractures on Fused Silica". 2008, Lawrence Livermore National Laboratory. p. 1-53.

61. House II, R.A., J.R. Bettis and A.H. Guenther, "Ultrasonic cleaning and laser surface damage threshold". *Applied Optics*, 1977. **16**: pp. 1130-1131.

62. Bass, I.L., G.M. Guss and R.P. Hackel. "Mitigation of laser damage growth in fused silica with a galvanometer scanned CO2 laser". in *Proceeding of SPIE*. 2005. **5991**: pp. 59910C-59910C-9

63. Bass, I.L., G.M. Guss, M.J. Nostrand and P.J. Wegner. "An improved method of mitigating laser-induced surface damage growth in fused silica using a rastered pulsed CO2 laser". in *Proceeding of SPIE*. 2010. **7842**: pp. 784220-784220-12

64. Bloembergen, N., "Role of cracks, pores, and absorbing inclusions on laser induced damage threshold at surfaces of transparent dielectrics". *Applied Optics*, 1973. **12**(4): pp. 661-664.

65. House II, R.A., J.R. Bettis and A.H. Guenther, "Surface roughness and laser induced damage threshold". *IEEE Journal of Quantum Electronics*, 1977. **QE-13**: pp. 361-363.

66. House II, R.A., J.R. Bettis and A.H. Guenther, "Efficacy of ion polishing optical surfaces". *Applide Optics*, 1977. **16**: pp. 1486-1488.

67. Milam, D., W.L. Smith, M.J. Weber, A.H. Guenther, R.A. House and J.R. Bettis. "The effects of surface roughness on 1064-nm, 150-ps Laser damage". in *9th Annual Symposium on Optical Materials for High Power Lasers*. 1977. Colorado. **509**: pp. 166-173

68. "Lasers and laser-related equipment- Determination of laser-induced damage threshold of optical surfaces- Part 1: 1-on-1 test". 2000, ISO 11254-1.

69. "Lasers and laser-related equipment- Determination of laser-induced damage threshold of optical surfaces- Part 2: S-on-1 Test". 2001, ISO 11254-2.

70. Hue, J., P. Garrec, J. Dijon and P. Lyan. "R-on-1 automatic mapping : a new tool for laser damage testing". in *Process of SPIE*. 1996. **2714**: pp. 90-101

71. Sheehan, L.M., S. Schwartz, C.L. Battersby, R.K. Dickson, R.T. Jennings, J.F. Kimmons, M.R. Kozlowski, S.M. Maricle, R.P. Mouser, M.J. Runkel and C.L. Weinzapfel. "Automated damage test facilities for materials development and production optic quality assurance at Lawrence Livermore National Laboratory". in *Proceeding of SPIE*. 1999. **3578**: pp. 302-313

72. Sheehan, L.M. "NIF Small Optics Laser Damage Test Specifications". [Online]; Available from: https://e-reports-ext.llnl.gov/pdf/235905.pdf.

CHAPTER 3

EXPERIMENTAL APPROACHES AND METROLOGY

3.1 Surface processing facilities

In this project, three processing methods, which are the MRF process, conventional polishing process and post polishing treatments, are used to manufacture fused silica optical surfaces. The facilities involved in these processes will be introduced in this chapter.

3.1.1 Abrasive lapping machine

Abrasive lapping is the most popular conventional polishing method. It utilises abrasive slurry which is sandwiched between a lapping pad and the surface of the fused silica optic. Abrasives are fixed on a lapping pad and motion between work-piece surface and the lapping pad provides the polishing process. Usually the lapping pad is made of pitch or polyurethane because they have lower hardness and Young's modulus[1, 2]. Low hardness and Young's modulus of lapping pad can make the pad deform and self-fit the shape of the work-piece. The abrasive slurry is generally an aqueous suspension of colloidal abrasive particles (CeO_2 for fused silica glass in this project) with specific chemical properties depending on the needs. Consequently, lapping is also known as chemical mechanical polishing (CMP).

In this project, an abrasive lapping machine with two laps was used to pre-prepare the optical surfaces. A polyurethane pad was used for rough polishing the fused silica surfaces, and a pitch pad was used for fine polishing because it is softer than

polyurethane. Figure 3.1 shows the lapping machine used in this project. This machine is only able to polish plane surfaces. To polish spherical or aspheric surfaces, a computer controlled optical surfacing (CCOS) machine is needed. However, in this project only surface quality was focused on, so only this machine was used. The load pressure can be adjusted by the control buttons on the panel. A temperature and humidity metre is used to monitor the working conditions. Rotation speed and swing speed can also be adjusted by control buttons and be monitored by corresponding metres.

3.1.2 MRF machine

MRF is the main polishing process in this project. An MRF machine, KDUPF 700-7, which was developed by National University of Defence Technology (NUDT), was used in this thesis. The machine is composed of three main parts: multi-axis motion system, computerised numerical control (CNC) system, and MR fluid circulatory system. The schematic structure of this multi-axis motion system is shown in Figure 3.2. It consists of five motion axes, which include two rotational axes (axis-A and axis-B) and three translational axes (axis-X, axis-Y and axis-Z). Moreover, for the MRF process, a rotational polishing wheel is essential. The five-axis motion system can make the polishing wheel follow complex paths by the control of CNC system which ensures the MRF machine to have the ability to polish complex surfaces. The MR fluid circulatory system provides the stable MR fluid in the polishing process.

Key parameters used in the MRF machine are wheel rotation speed, MR fluid flow rate, current through the electromagnet, depth of work-piece penetrated in MR fluid ribbon, and viscosity of MR fluid. Besides these, details of abrasive particles and work-piece are also important.

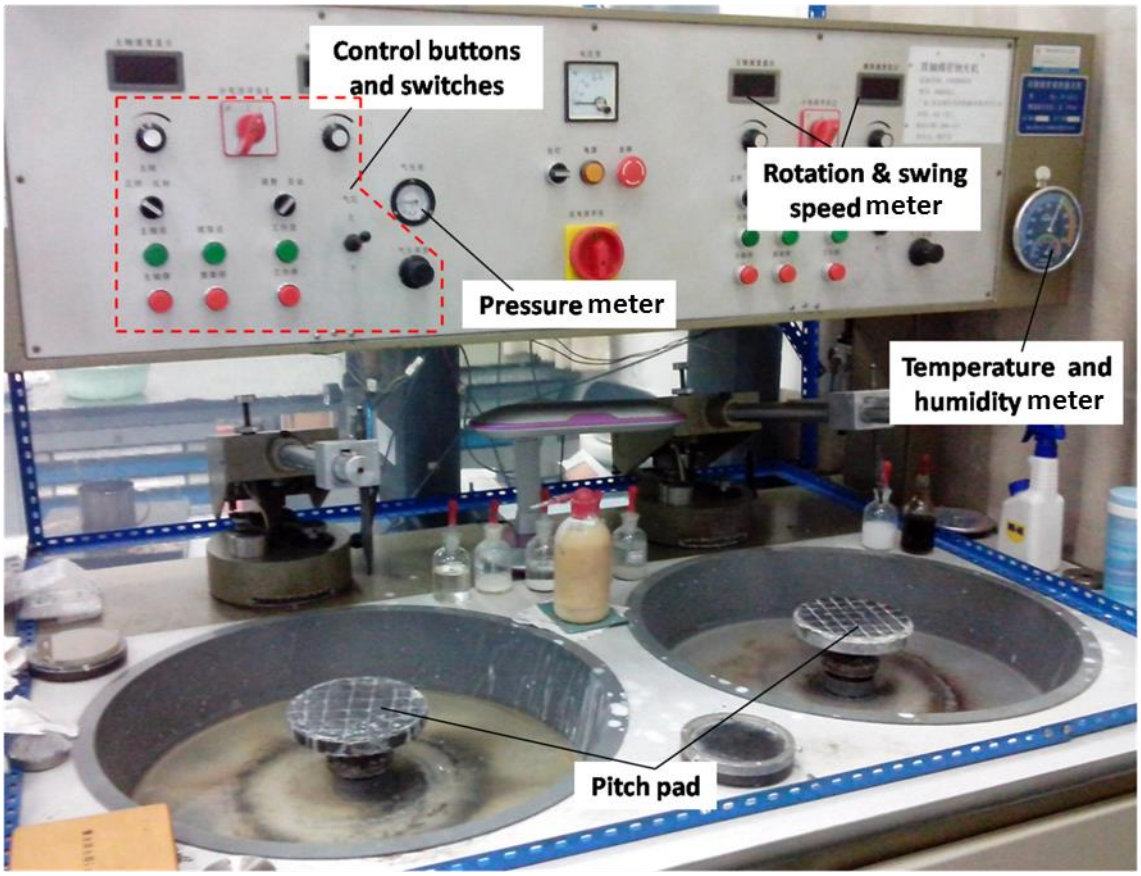

Figure 3.1 Lapping machine used in this project

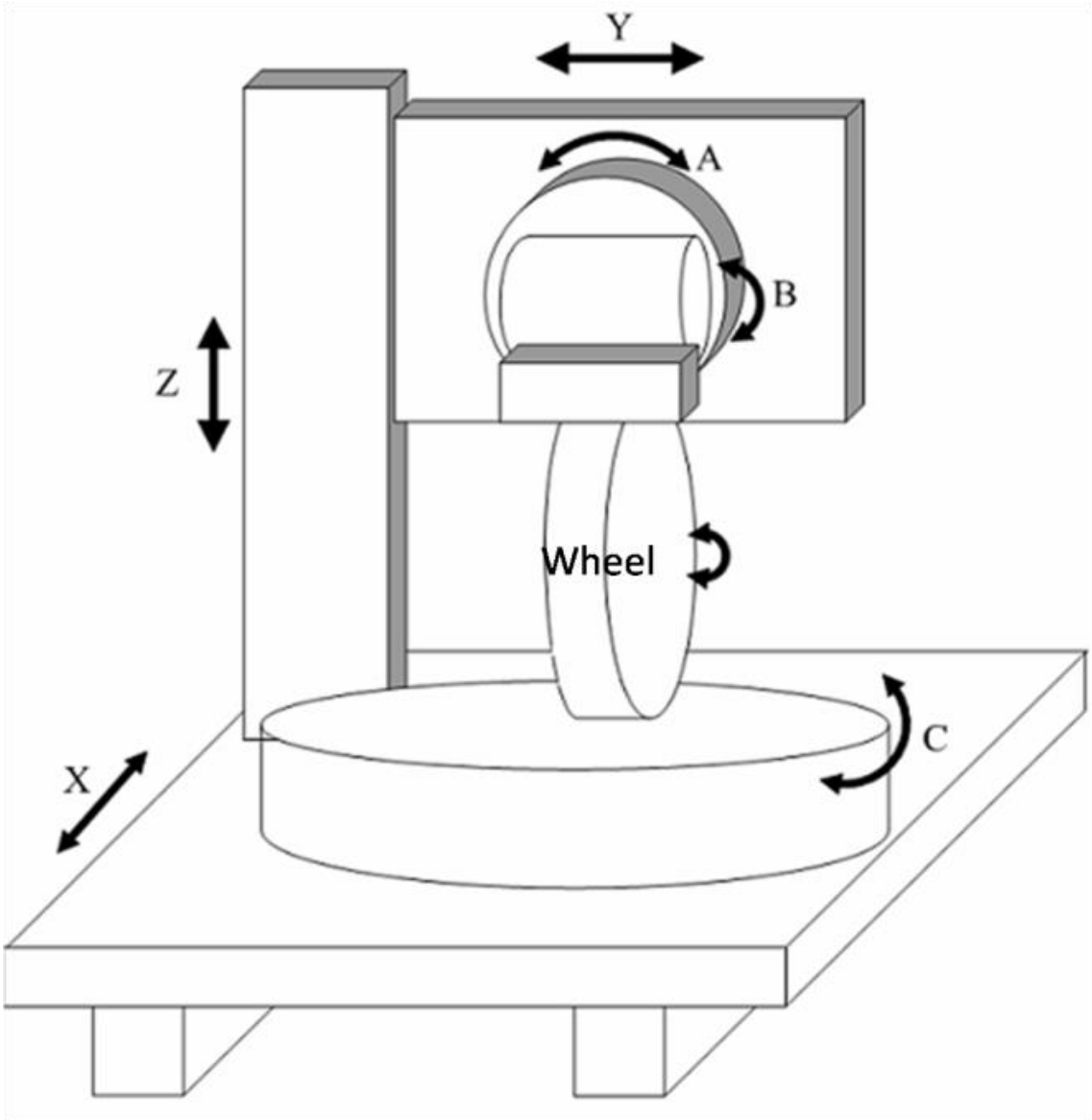

Figure 3.2 Schematic structure of the MRF machine

3.1.3 Ion Beam Etching (IBE) facility

IBE processing is one of the post polishing treatments involved in this project. The IBE facility in this thesis is KDIBF 700-5V, which was developed by NUDT. As shown in Figure 3.3, this IBE facility is apparently composed of three parts: Vacuum chamber, Ion source controlling system, and CNC system. An ion source as well as a multi-axis motion system is equipped in the vacuum chamber because the ion source needs to work without oxygen. The ion source generates the ion beam and the multi-axis motion system ensures the optical component receives a proper path. The ion source controlling system controls the energy or power of the generated ion beam, and the CNC system makes the motion system run as programmed. The incident angle is another factor that greatly affects the surface roughness and material removal rate. The multi-axis motion system is able to set the incident angle.

3.2 Metrology

3.2.1 Surface quality measurements

In this project, the quality of optical surfaces is one of the main issues being focused upon. In this project, the surface properties measured include, surface roughness, surface texture, and surface contaminants.

1. Surface roughness measurement

In this project surface roughness was measured by a scanning white light interferometer (SWLI), Zygo NewView 700s (Zygo Corporation, USA). It is a non-contact and three-dimensional scanning facility to get the profile data from the optical surface. The specification of this SWLI is shown in Table 3.1. Figure 3.4 shows the photo of this SWLI.

Figure 3.3 Photo of KDIBF 700-5V

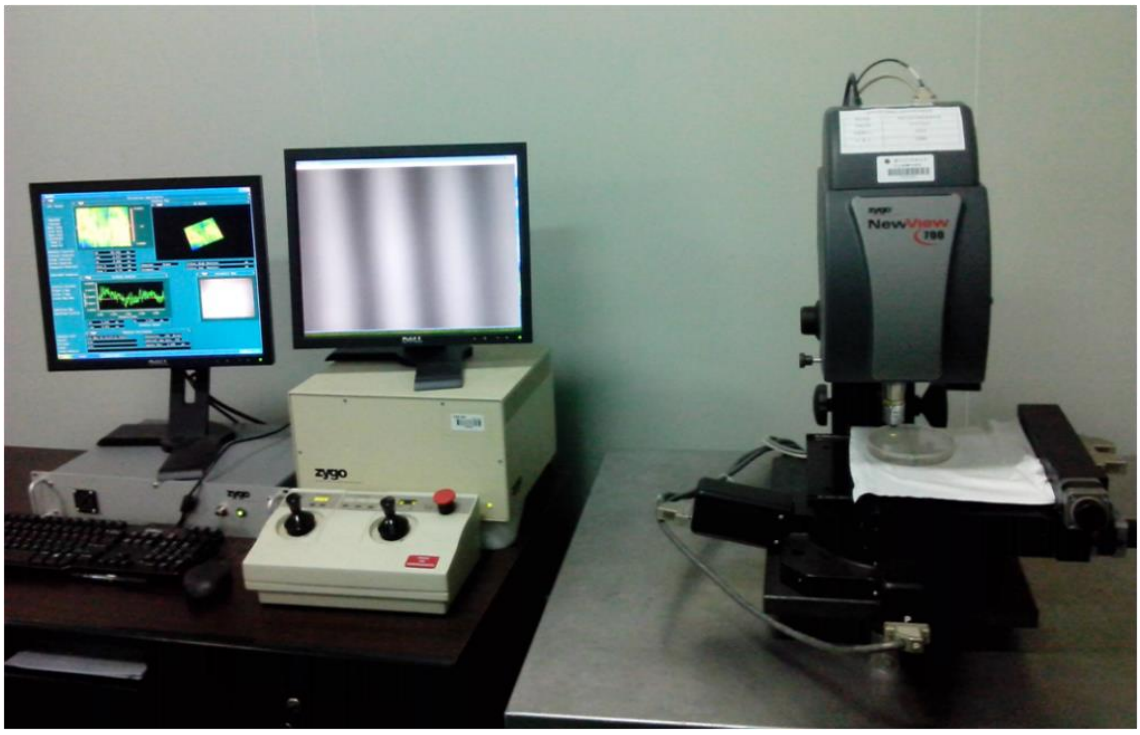

Figure 3.4 Photo of ZygoNewView 700s

Table 3.1 Parameters of ZygoNewView 700s [3]

Item	**Value**
Vertical Scan Range	< 150 μm
Vertical Resolution	< 0.1 nm
Optical Resolution	0.36 to 9.50 μm, objective dependent
Data Scan Rate	≤15 μm/sec
Maximum Data Points	307200 (640 x 480)
RMS Repeatability	< 0.01 nm
Step Height	Accuracy ≤ 0.75%; Repeatability ≤ 0.1% @1σ
Field of View	0.07 to 9.3 mm with standard camera, objective dependent
Measurement Array	640 x 480 standard
Objectives	1x, 2x, 2.5x, 5x, 10x, 20x, 50x, 100x

2. Surface texture observation

It is very usual that defects, such as scratches and pits, exist on the optical surface no matter before or after polishing processes. These defects are probably the reason that reduces the laser induced damage threshold of the optical component. Therefore it is very important to observe the optical surface texture, and a digital microscope is well used to get pictures of the optical surface.

In this thesis, a digital microscope VHX-600E (KEYENCE Corporation, Japan) is used to observe the optical surface. For this facility, the lens power is from 5x to 5000x, and 3D picture can also be acquired via the vertical scanning motion. Hence it is very convenient to get clear picture of the observed surface. This microscope is shown in Figure 3.5.

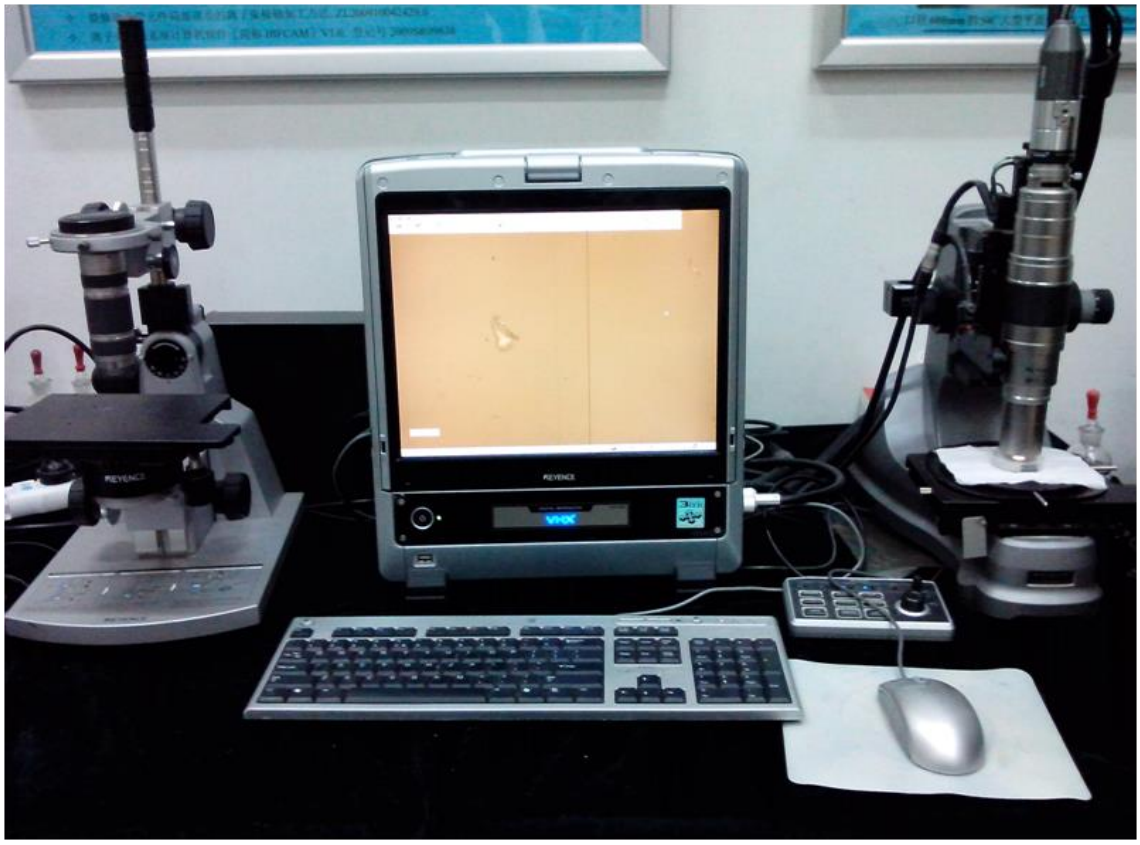

Figure 3.5 KEYENCE Digital Microscope VHX-600E

3. Surface contaminants metrology

It is common that polishing particles or other contaminants are left on the surface layer of the optical surface after polishing processes, and these contaminants could probably initiate the LID. Therefore, it is important to detect these contaminants on the surface layer in this research.

A secondary ion mass spectroscopy (SIMS), Trift II TOF-SIMS(Physical Electronics, USA), was used in this project to measure the distribution of different chemical species as a function of depth from the surface. The picture of this SIMS is shown in Figure 3.6.

3.2.2 LIDT test system

The LIDT test work in this thesis was completed in Tongji University (Shanghai, China). A schematic diagram of test system used in this work is shown in Figure 3.7. A 3ω (355 nm in wavelength) Nd-YAG laser (Quanta-Ray Pro-350, Spectra-Physics, USA) was used in these tests. An energy meter was used to measure the laser energy. Both the temporal and spatial distributions (shown in Figure 3.8) of the laser beam were of Gaussian shape. The laser beam pulse duration was 8.2 ns (FWHM), and the diameter was 689 μm (width at the energy down to $1/e^2$). A CCD camera was used to take pictures of each test site. The CCD was focusing on, or near, the back surface of the fused silica specimen because most damage was on or near the back surface. Self-developed software was used to detect whether damage occurred in a laser beam shot by the pictures taken by the CCD, automatically. A picture of damage sites and non-damage sites taken by the CCD is shown in Figure 3.9. A PC was used in this system to control and monitor the test process.

In the laser damage test system, the laser beam size (689 μm in this work) was far smaller than the characteristic sizes of the components in use (these diameters were of from several centimetres up to one metre) [4]. This allowed the number of test sites

Figure 3.6 Photo of Trift II TOF-SIMS

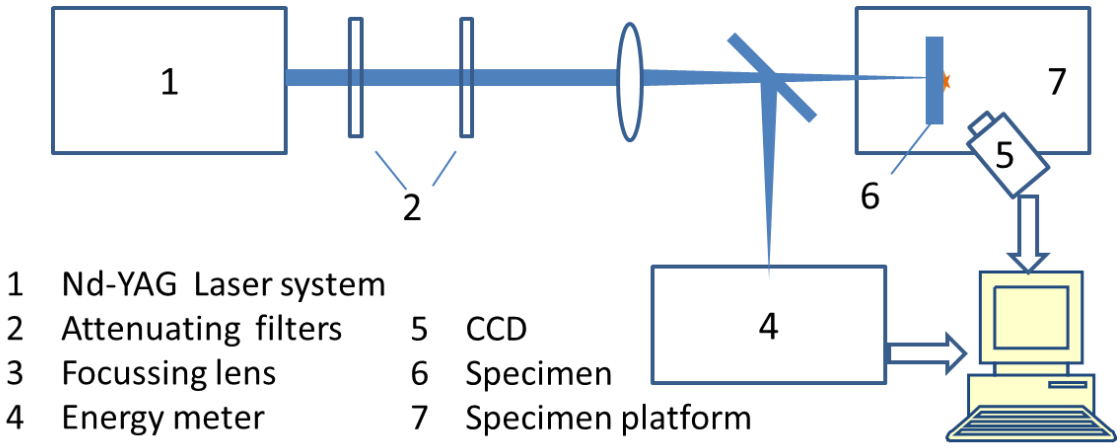

Figure 3.7 Schematic diagram of testing system in tests for rear surface

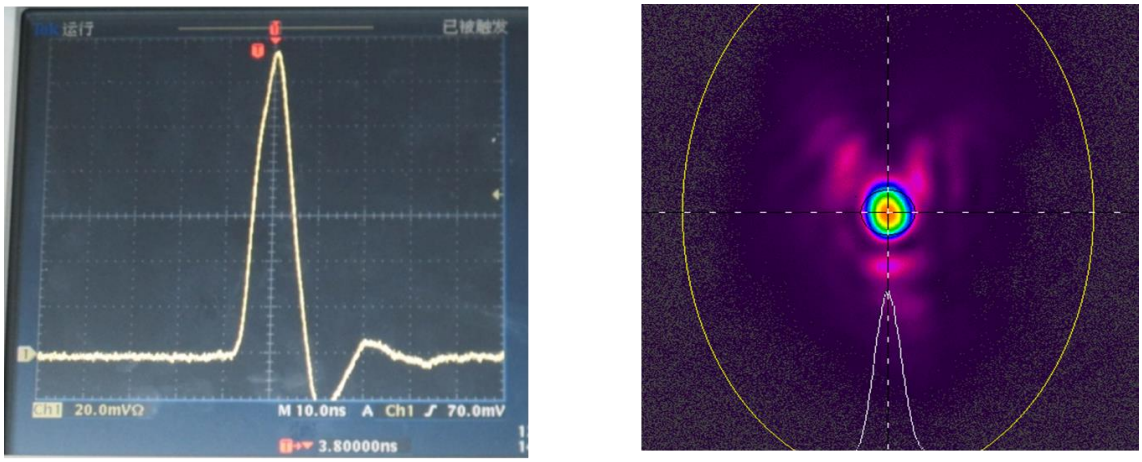

(a) Laser beam pulse time FWHM= 8.2ns

(b) Gaussian distribution, diameter= 689μm

Figure 3.8 Information of laser beam used in tests

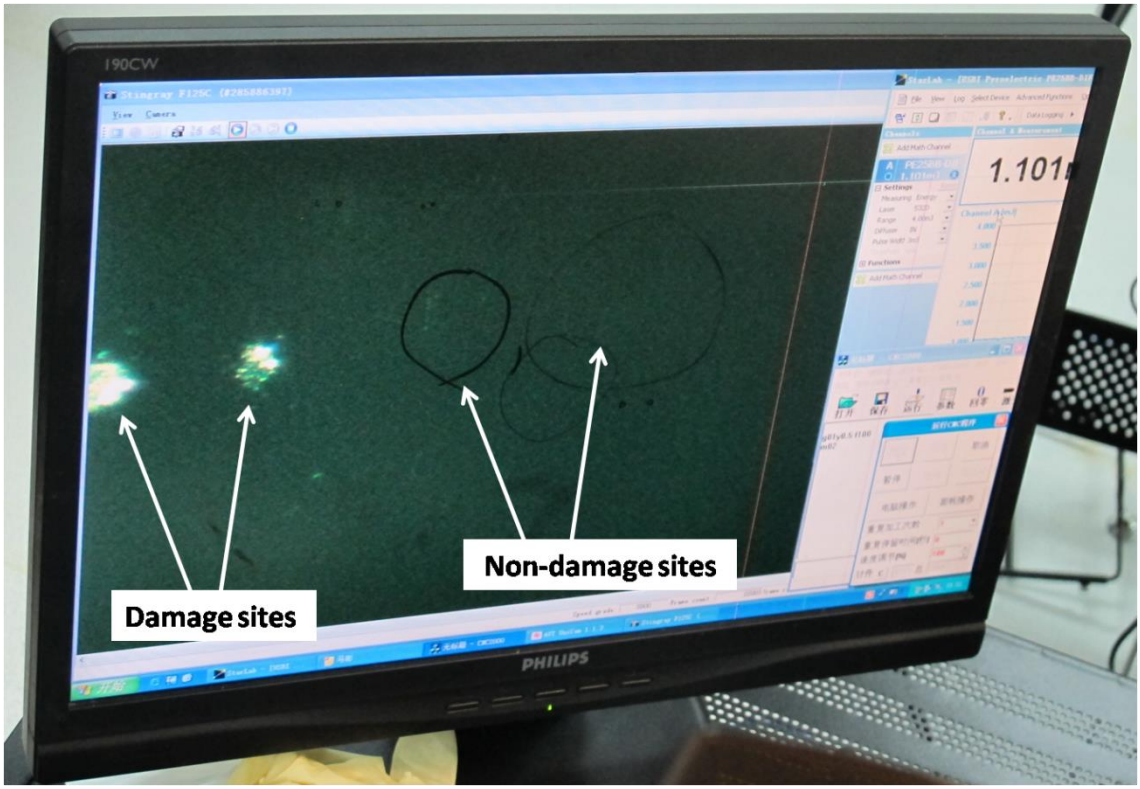

Figure 3.9 Damage sites and non-damage sites taken by CCD

and their distribution to be even and sufficient. Therefore a 1-on-1 testing method, rather than repetitive testing methods, was adopted in this work due to the large cost and low efficiency of the latter.

In this thesis, the test sites at each irradiating level were distributed as a 7x7 square (shown in Figure 3.10). In order to avoid any interaction due to overlap between two adjacent test sites, the sites interval was set to 1 mm. When testing at another irradiating level, the new test areas were positioned to be non-overlapping (5 mm away) with the previous test area.

3.2.3 Particle size analysis

In the optical surface polishing processes, the size of polishing particles is one of key factors to control the quality of a polished surface. Generally smaller particles are able to generate finer surfaces but with lower efficiency, while larger particles have greater material removal rate but create worse surface quality.

In this project, a CILAS particle size analyzer 1090, which is from CILAS, France, is used to measure the sizes of polishing particles and carbonyl iron particles. The particle size analyser is based on a laser diffraction technique and can measure the particle size (0.04μm~500μm) with high repeatability (< 1%) and accuracy (< 3%) in the wet mode[5]. Figure 3.11 is the photo of CILAS particle size analyzer 1090.

3.2.4 Measurement of mechanical properties for fused silica

Mechanical properties of fused silica can be obtained from a lot of references. However in order to get the accurate properties of the samples which are used in this project, especially the mechanical properties which are critical for the machining performance, indentation testing is a good method.

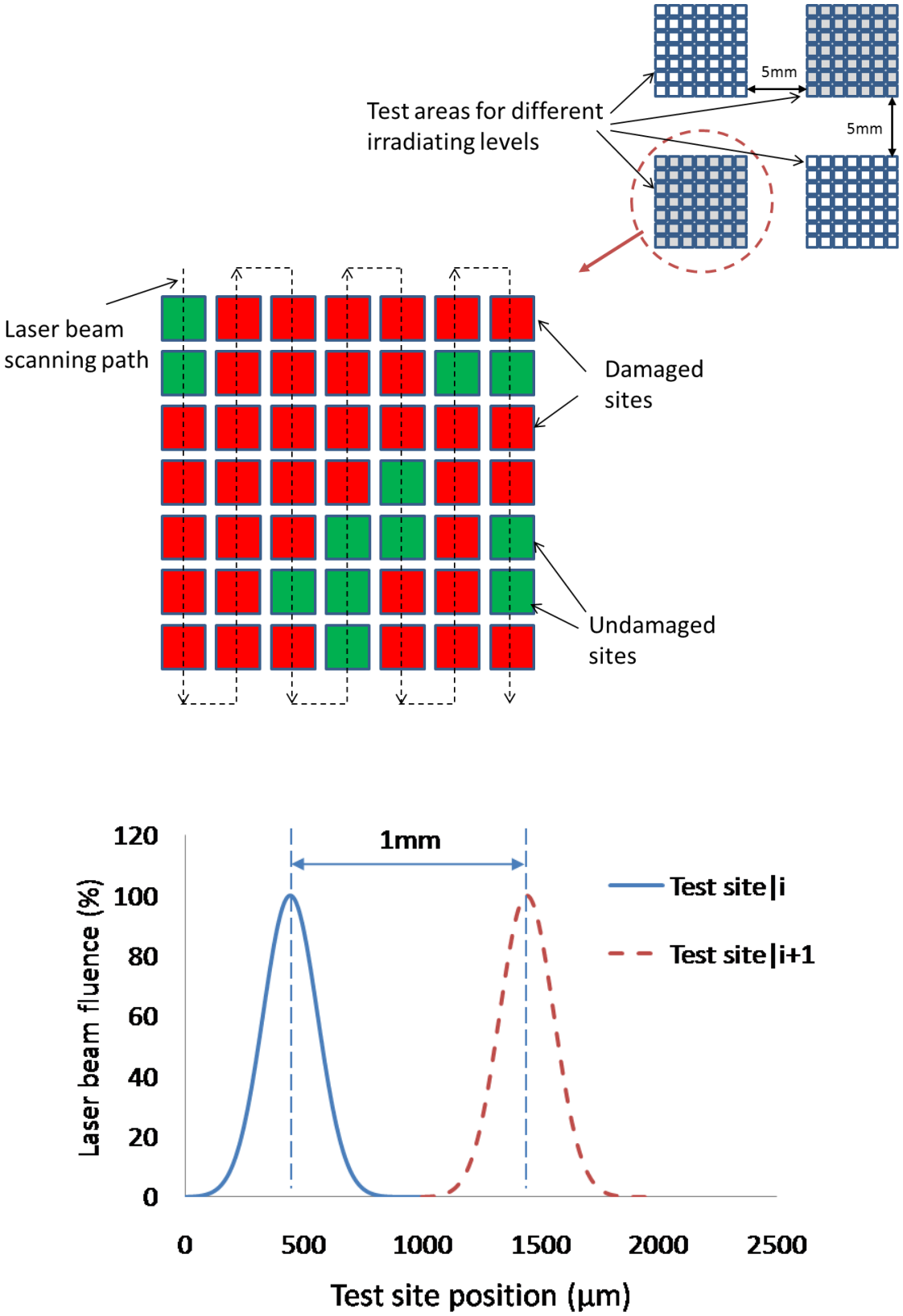

Figure 3.10 A 1-on-1 test area at a irradiating level includes 7x7 test sites

Figure 3.11 CILAS particle size analyzer 1090

An indentation facility, CSM Ultra Nanoindentation Tester (UNHT, from CSM Instruments, Switzerland), was used in this project to get the mechanical properties of the fused silica material. The UNHT is based on marble platform and with high resolution capacitive sensors for depth detection and load control. The force resolution and its noise floor of this tester are 0.01μN and around 0.5 μN, respectively; and depth resolution and its noise floor is 0.001 nm and around 0.1 nm [6]. This tester is equipped with a series of indenters, such as Berkovich indenter (used for nanoindentation) and Vickers indenter (used for micro-indentation). Figure 3.12 is the photo of this indentation tester.

Typical mechanical properties, such as hardness, Young's modulus, and fracture toughness, play significant roles in the optical material's manufacturing processes. Normally it is more difficult to machine a harder material. In this thesis mechanical properties of fused silica glass were tested via the CSM nanoindentation instrument.

A typical loading and unloading curves in these tests are illustrated in Figure 3.13. Then, according to these curves, the hardness and Young's modulus can be obtained.

Fracture toughness (K_{IC}) is another important property for a brittle glass such as fused silica. It is a property that describes the ability of a material with a crack to resist fracture. The assessment of fracture toughness for brittle materials commonly utilises experimental indentation methods such as Vickers and Berkovich indentation because it is a simple technique and specimen preparation [7-11].

In this thesis, Vickers micro-indentation, rather than Berkovich, was used because it is easier to get cracks on the fused silica surface owing to the performance of the CSM instrument. The Vickers indentation method is derived from the common hardness test procedure and is relative to the crack lengths after the indentation test. The schematic picture of fracture mark produced by Vickers indentation is shown in Figure 3.14. In Figure 3.14, P is the peak load on the Vickers indenter, and a and c are the length

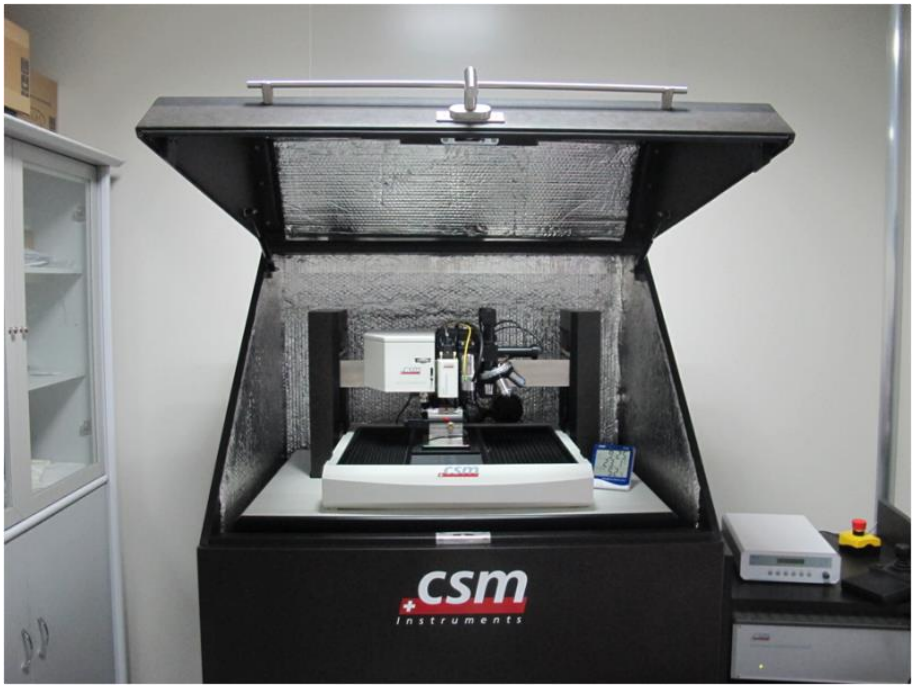

Figure 3.12 Photo of CSM UNHT

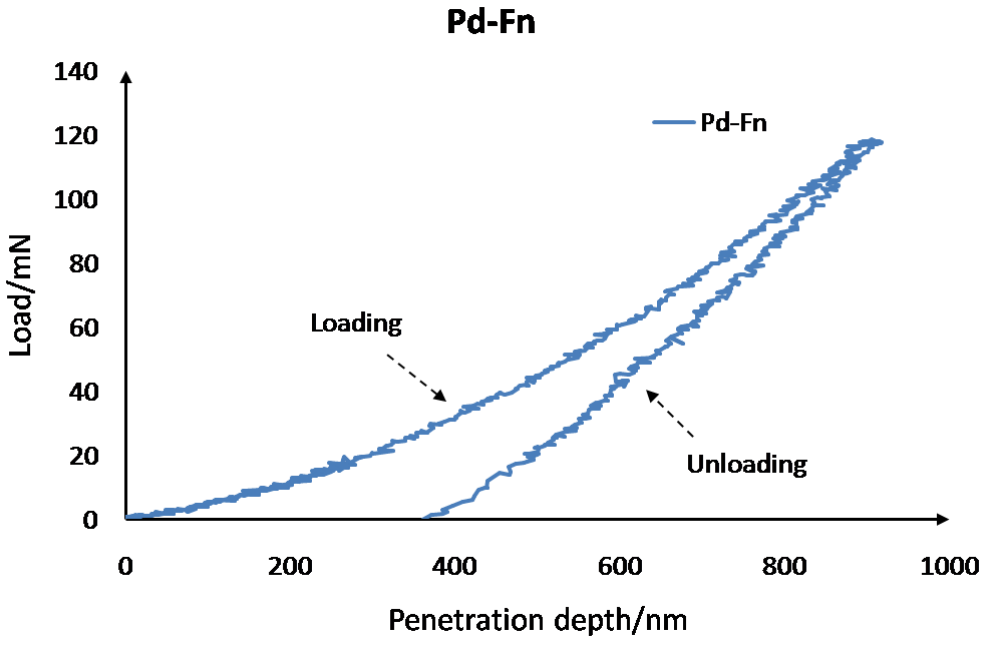

Figure 3.13 Typical loading and unloading curve for a nanoindentation test on fused silica with Berkovich intender

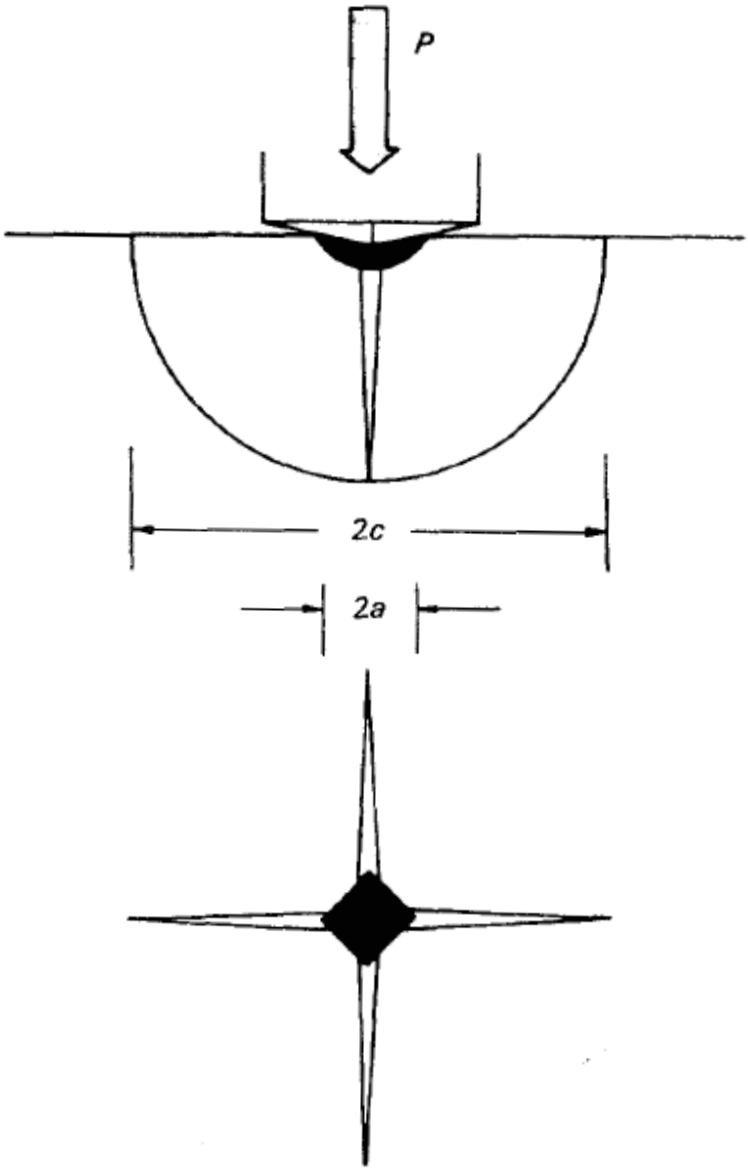

Figure 3.14 Schematic picture of Vickers indentation fracture mark (after [11])

of the indentation mark and median crack, respectively. Then the fracture toughness can be calculated by the following equation [11]:

$$K_{IC} = \delta\left(\frac{E_w}{H_w}\right)^{1/2}\frac{P}{c^{3/2}} \tag{3.1}$$

where δ is an empirical constant and taken to be 0.16; H_w and E_w are hardness and Young's modulus, respectively.

3.3 Summary

This chapter introduced the experimental approaches and metrology used in this thesis.

First of all, some surface processing facilities, which are used to polish the fused silica optical surface, were introduced. These facilities, including a lapping machine, an MRF machine and an IBE facility, are set in NUDT, China.

Then some measurements were listed in this chapter. Surface roughness and contaminants could be acquired by the surface quality measurements. An LIDT test system which is located in the Tongji University, China, was also detailed. At last, particle size analyzer and nanoindentation facilities, both of which would be used in Chapter 5, were introduced.

References

1. Xie, Y. and B. Bhushan, "Effect of particle size, polishing pad and contact pressure in free abrasive polishing". *Wear*, 1996. **200**: pp. 281-295.

2. Luo, J. and D. Dornfeld. "Material removal mechanism in chemical mechanical polishing: theory and modeling". in *IEEE transactions on semiconductor manufacturing*. 2001. **14**: pp. 112-133

3. "NewView^{TM} 700s Specifications". [Online]; Available from: Http://www.zygo.com/met/profilers/newview700s/newview700sspec.pdf.

4. Hue, J., P. Garrec, J. Dijon and P. Lyan. "R-on-1 automatic mapping : a new tool for laser damage testing". in *Process of SPIE*. 1996. **2714**: pp. 90-101

5. "CILAS 1090 particle size analyzer". [Online]; Available from: http://www.cilas.com/particle-size-distribution.htm.

6. "Ultra Nanoindentation Tester (UNHT)". [Online]; Available from: Http://www.csm-instruments.com/en/Ultra-Nanoindentation.

7. Lawn, B.R., A.G. Evans and D.B. Marshall, "Elastic/Plastic Indentation Damage in Ceramics: The Median/Radical Crack System". *Journal of American Ceramic Society*, 1980. **63**(9-10): pp. 574-581.

8. Mullins, L.P., M.S. Bruzzi and P.E. McHugh, "Measurement of the microstructural fracture toughness of cortical bone using indentation fracture". *Journal of Biomechnics*, 2007. **40**: pp. 3285-3288.

9. Kruzic, J.J., D.K. Kim, K.J. Koester and R.O. Rechie, "Indentation techniques for evaluating the fracture toughness of biomaterials and hard tissues". *Journal of the Mechanical Behavior of Biomedical Materials*, 2009. **2**: pp. 384-395.

10. Zhang, J. and J. Lewandowski, "Interfacial fracture toughness measurement using indentation". *Journal of Material Science*, 1994. **29**: pp. 4022-4026.

11. Anstis, G.R., P. Chantikul, B.R. Lawn and D.B. Marshall, "A critical evaluation of indentation techniques for measuring fracture toughness. I. Direct crack measurements". *Journal of American Ceramic Society*, 1981. **69**: pp. 533-538.

12. "Quartz Glass for Optics Data and Properties". [Online]; Available from: http://optics.heraeus-quarzglas.com/media/webmedia_local/downloads/FusedsilicaandQuartzGlassforOpticsDataandProperties.pdf.

CHAPTER 4

INITIATIONS OF LASER INDUCED DAMAGE

Optical components generally have lower LIDT than intrinsic materials in the influence of high-energy laser radiation [1]. In this chapter, the relationship between LID and several typical defects, which are generated on the components surface or/and sub-surface by CMP processes, are analysed via simulations.

4.1 Defects on surface/sub-surface

4.1.1 Factors lowering LIDT of fused silica

Laser induced damage (LID) may occur in the bulk of the optical component, at the faces of optical components, or at the interfaces between optical components (especially if they are in contact). For a single optical component, experimental observations [2] illustrate that LID occurs normally first at or near the exit surface (material-air interface, relative to the direction of laser beam) of a fused silica optical component. Experiments [2] also indicate that the LIDT of fused silica optical components are lower than the theoretical LIDT of bulk material.

Figure 4.1 shows the factors which possibly lower the LIDT of fused silica optical components. In this chapter, conventional polishing induced factors, such as surface or sub-surface damage, surface roughness, and polishing induced impurities, which are possibly the initiators of LID, are investigated utilising theoretical and/or experimental methods.

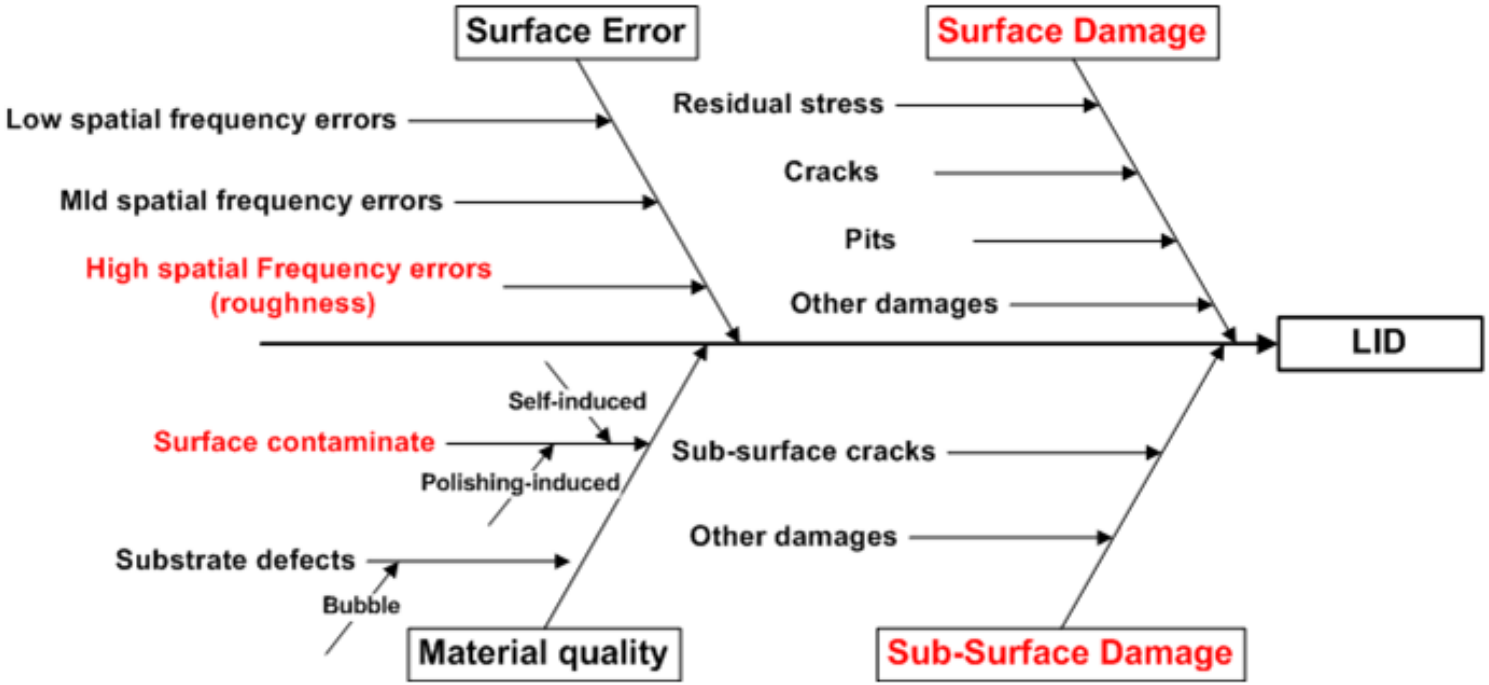

Figure 4.1 Possible factors that lower the LIDT of fused silica optics

The conventional preparation of optical surface comprises of three steps (shown in Figure 4.2): rough grinding, fine grinding or pre-polishing, and polishing. The rough grinding focuses on shaping and removing the bulk materials from the blank rapidly; fine grinding, or namely pre-polishing, is using to prepare the surface for subsequent polishing; and during polishing, surfaces with optical quality can be finely machined.

4.1.2 Surface and sub-surface damage

Generally surface or sub-surface damage (SSD) of fused silica optics are created during grinding and/or polishing processes. Many researchers indicated that a Beilby layer, also referred to as the redeposition layer, commonly covers the polished optical surface [3-6]. Beneath the Beilby layer, a defect layer consisting of micro cracks is usually found. The defect layer is also known as the SSD layer and not detectable by visual methods. Above the defect-free bulk, a deformed layer, which contains compressive stresses or tensile stresses, is found below the defect layer. Figure 4.3 shows the surface and sub-surface morphology of polished fused silica.

In order to reduce the depth of the defect layer, a common method is used that the subsequent process removes the overall amount of SSD generated by the preceding process. This method is illustrated in Figure 4.4. However, surface and sub-surface damage are still found usually even after fine polishing.

The creation of SSD is commonly believed as a moving indentation process. In other words, when the mechanically loaded hard indenters (abrasives) are sliding on the optical surface during manufacturing processes, SSD occurs. Figure 4.5 shows the sequence of a static indentation process with the increasing indention load on a sharp indenter. Plastic deformation, median crack, and lateral crack are generated with the increasing load (though lateral crack occurs during unloading) in the static indentation process. For a blunt indenter, the situation is a little different in that the Hertzian cone

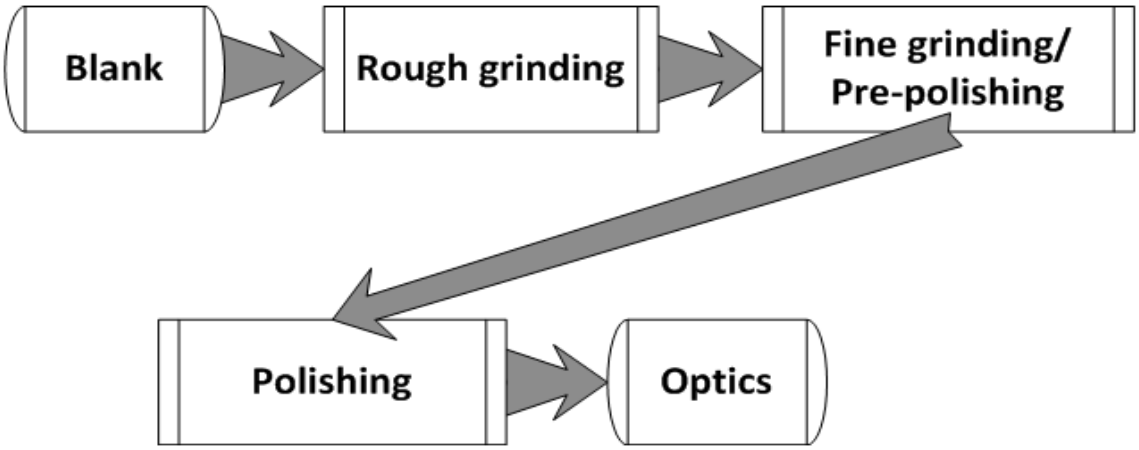

Figure 4.2 The steps of the conventional optics production process

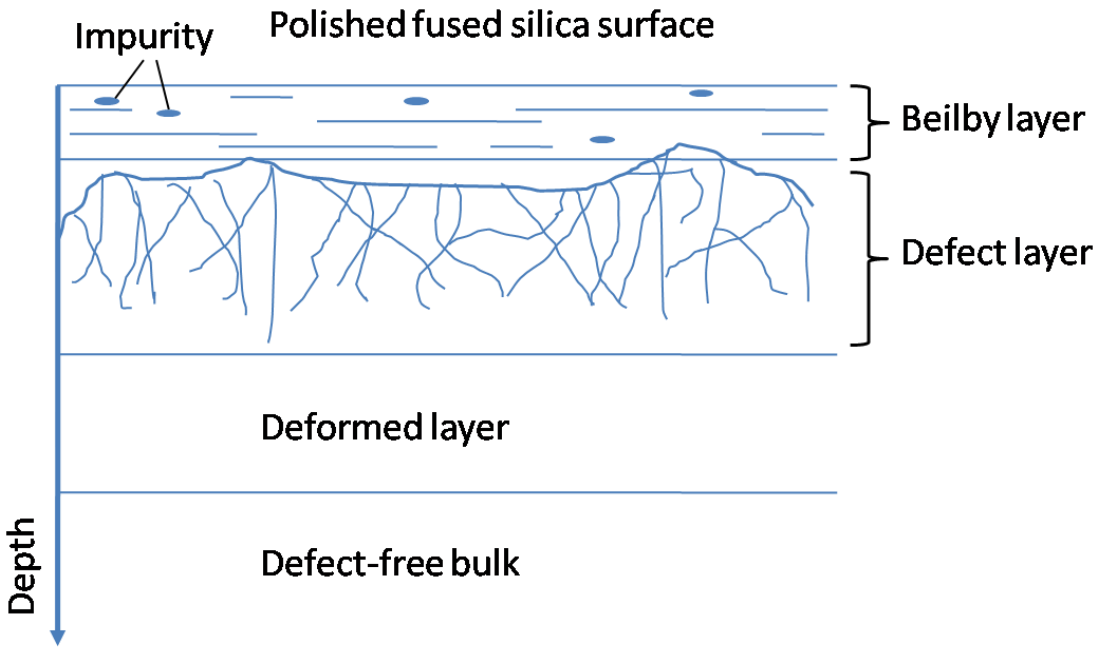

Figure 4.3 Schematic of surface/sub-surface morphology of polished fused silica[6]

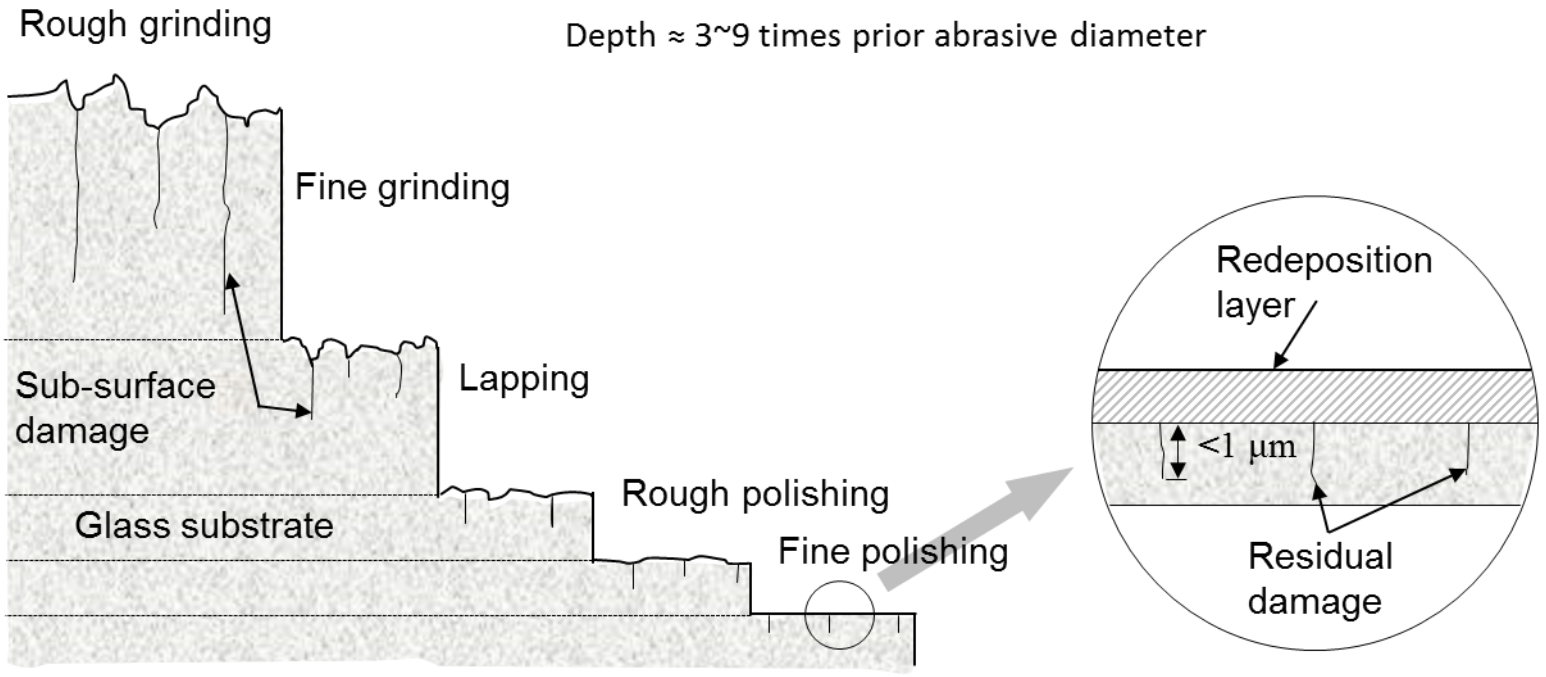

Figure 4.4 The depth evolutions of SSD from grinding to polishing processes, after [7]

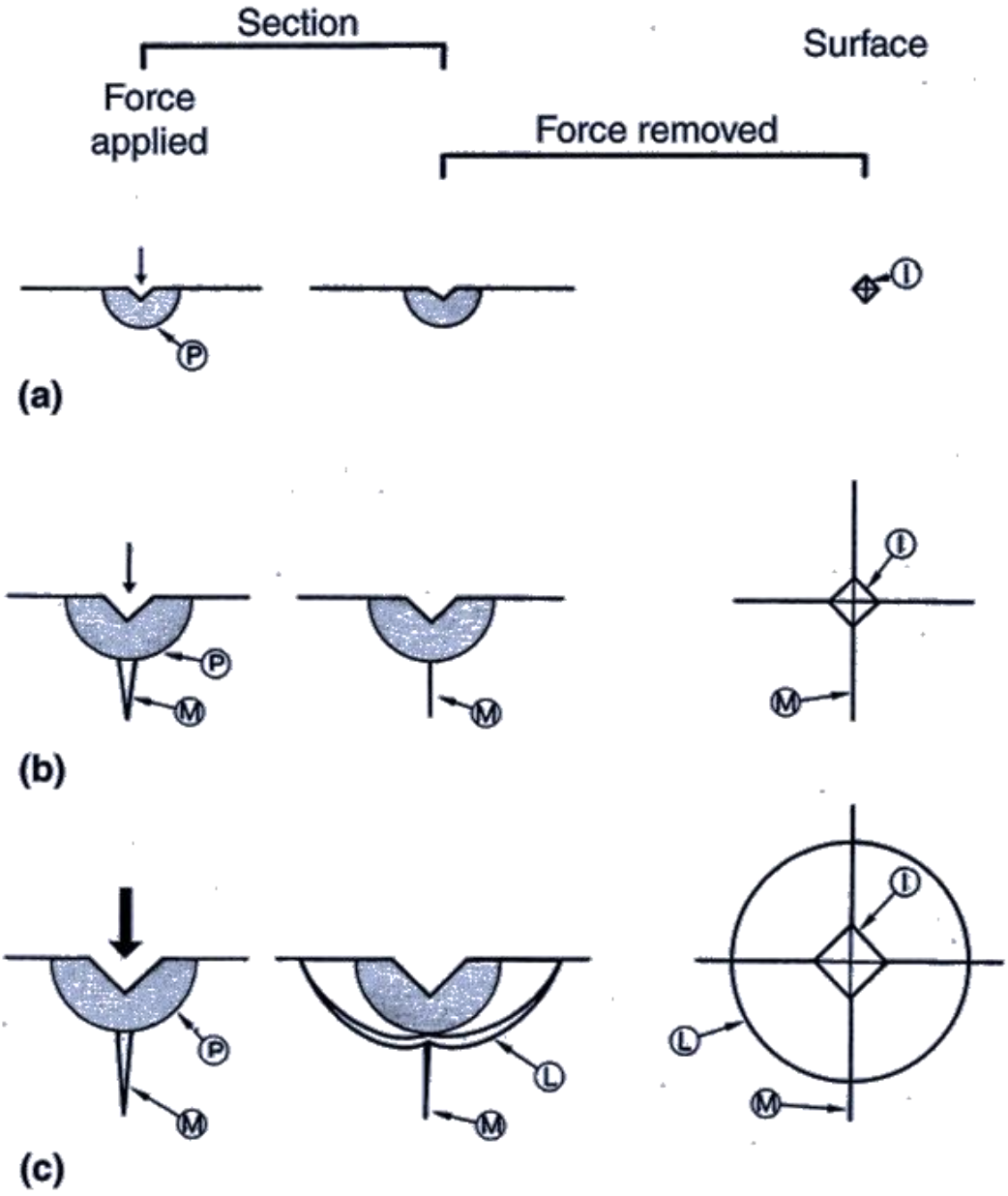

Figure 4.5 Sharp indenter impact into surface of brittle glass under increasing force (top to bottom), and the corresponding unloading events. P, plastic deformation; I, indentation mark; M, median crack; L, lateral crack [8, 9]

crack rather than lateral crack initiates and propagates in isotropic materials (such as fused silica) beyond the load under which only plastic deformation occurs. The Hertzian cone crack is shown in Figure 4.6.

Figure 4.5 and Figure 4.6 are the situations for static indentations, i.e. non-moving indenters penetrate into a frictionless interface. When considering polishing processes, sliding/rolling and frictions between abrasive particles and work-piece surface become important and must be taken into account. For a sliding abrasive particle, the movement results in a change in the stress distribution that the peak stress is at the tailing edge of the particle. Therefore fracture occurs as an arc-shape rather than trailing ring-shape which is observed in frictionless Hertzian cone contact [10, 11]. The trailing crack on fused silica surface is shown in Figure 4.7.

It is believed that a critical load, p_c, which is the initiation load for fracture (i.e., scratch and sub-surface crack), does exist. The critical load varies with the local shape of polishing particle and mechanical properties of both work-piece and particles[11, 12]. If the normal load acting on a polishing particle, p, is greater than the critical load (p_{crit}), fracture occurs. The fracture initiation condition is written as

$$p \geq p_{\mathrm{crit}} \tag{4.1}$$

During an ideal polishing process, the normal load acting on each polishing particle is quite low (10^{-9}-10^{-6}N), which is well below the critical fracture initiation load that is on the order of 0.001N for plastic and 0.1 N for brittle fracture[11, 13, 14].

Assume (1) only a very small fraction (less than 0.5), f_l,of abrasive particles that loaded between the polishing pad and work-piece surface are actually involved in polishing [15]; and (2)abrasive particles between polishing pad and work-piece surface are mechanically loaded evenly. Therefore normal load per polishing particle can be calculated by

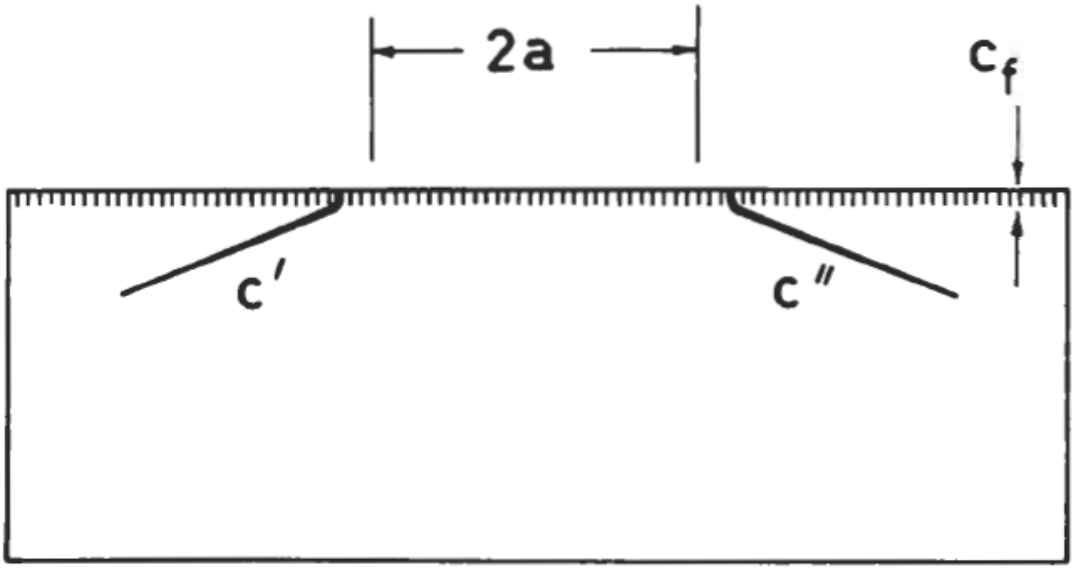

Figure 4.6 Section view of Hertzian cone crack [16]

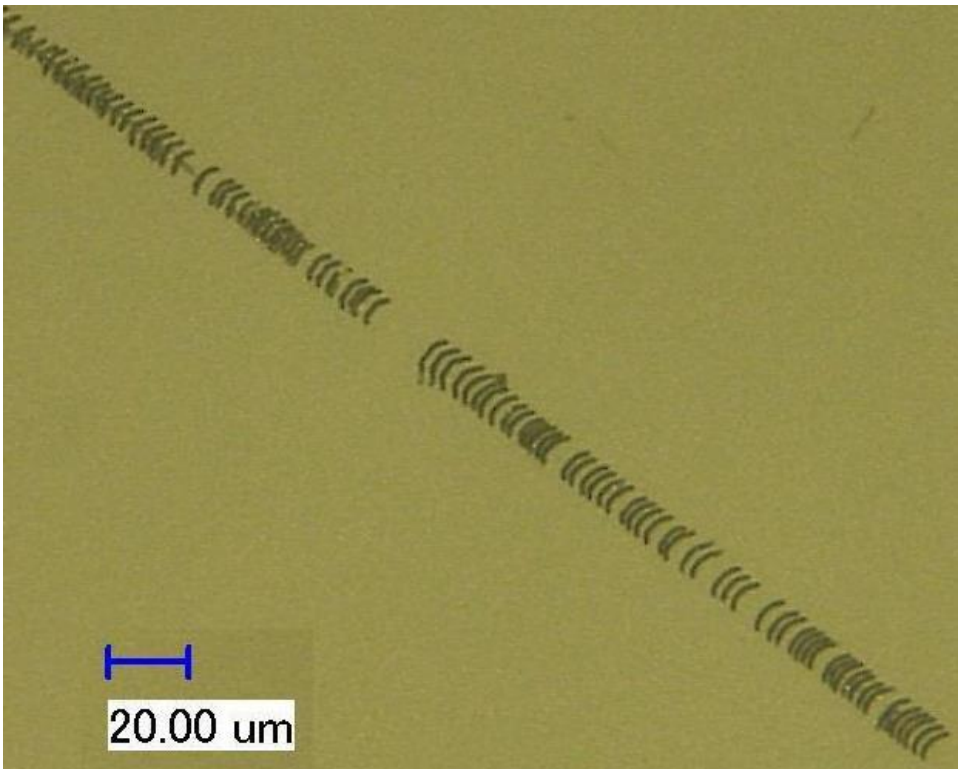

Figure 4.7 A crack on fused silica surface produced by a sliding ceria particle

$$p = \frac{P_T}{N_L} = \frac{P_T}{f_l N_T} \tag{4.2}$$

where P_T is the total load applied on the polishing pad,N_L is the number of loaded abrasive particles between the polishing pad and work-piece surface, and N_T is the total number of abrasive particles between the polishing pad and work-piece surface.

It is commonly assumed that the polishing pad is a purely elastic material, and therefore according to elastic contacting theory, the load applied on each particle is proportional to the depth of penetration for a fixed gap which is the mean particle size in the vertical direction. In other words, loads on particles actually vary with the size of particles, i.e. greater load is applied on larger particle. Therefore Equation (4.2) is true only if the polishing particles between the polishing pad and work-piece surface have the same sizes.

Figure 4.8 shows the tested (by Cilas Particle Size Analyzer) size distribution of the ceria particles, which we used in the experiments, with nominal diameter of 2.5 μm. In other words, the sizes of particle involved in polishing process are various. So the modified load on a polishing particle with diameter of, d, is given by

$$p(d) = \frac{P_T}{N_L}\left(\frac{d}{d_c}\right) = \frac{P_T}{f_l N_T}\left(\frac{d}{d_c}\right) \tag{4.3}$$

here, assume the polishing particles are sphere in shape, d_c is mean diameter of polishing particles. According to the Equation (4.3), as shown in Figure 4.9, $\mathrm{d_3} > \mathrm{d_1} > \mathrm{d_2}$, leads to $\mathrm{p_3} > \mathrm{p_1} > \mathrm{p_2}$.

The variation of load on particle could possibly induce fracture on the work-piece surface if loads on some bigger particles are greater than the critical fracture initiation load. Especially when some rogue particles (such as dust or glass debris which are much bigger than the polishing particles) are involved in the polishing process due to

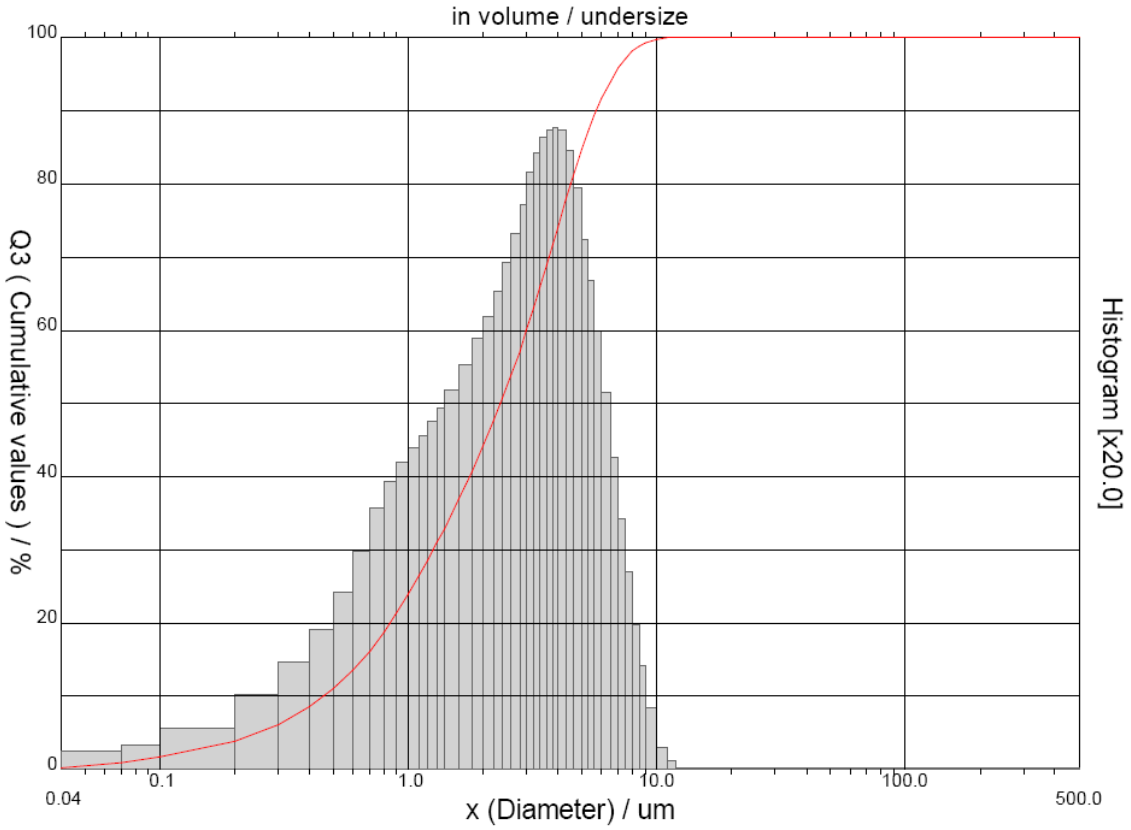

Figure 4.8 Size distribution of ceria particles with nominal diameter of 2.5 µm measured using Cilas Particle Size Analyzer. The histogram stands for the numerical ratio of abrasive versus sizes; and the red line stand for the cumulative percentage of abrasive versus sizes.

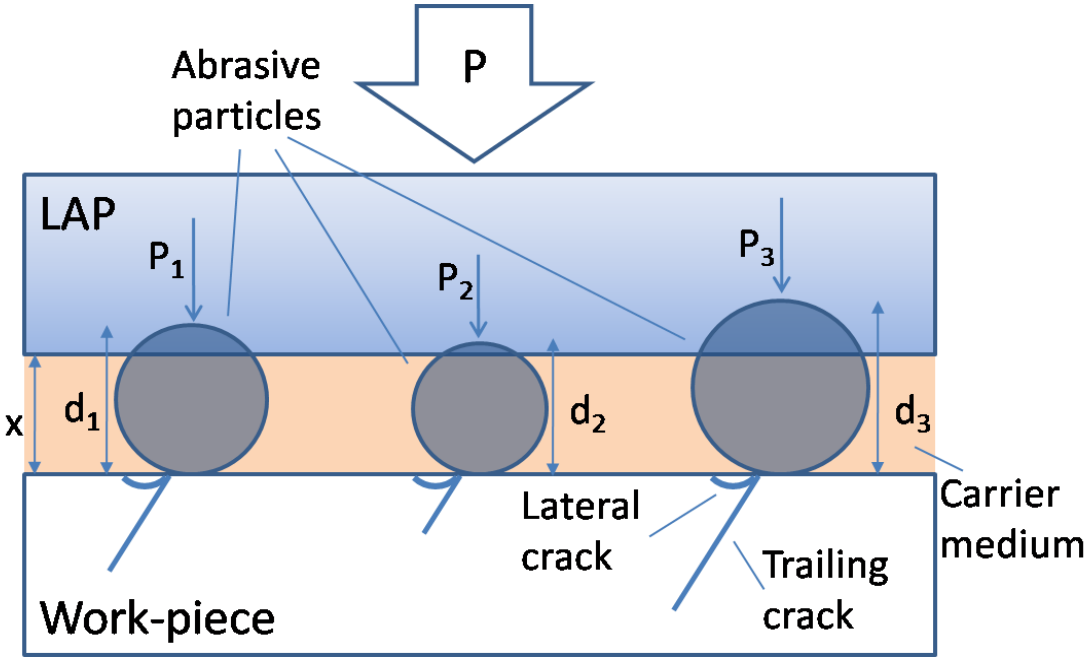

Figure 4.9 Mechanisms of damage generation in polishing process (after [12])

poorly maintained polishing conditions and environment. Therefore, surface scratches and sub-surface damage are generated in the polishing processes. Figure 4.7 is a typical scratch created in the polishing process.

4.1.3 Impurities at the surface/sub-surface

Figure 4.3 shows the surface and sub-surface morphology of polished fused silica. In Figure 4.3 are deposition layer (or named Beilby layer), which is usually created during the polishing process, exists on the polished surface of optical component. The depth of redeposition layer is in the range of approximately 10-100 nm[17].

According to the widely accepted chemo-mechanical description of conventional polishing process, the redeposition layer is usually softer than the bulk material. Therefore during the polishing processes, the sample surface could be contaminated by polishing particles, debris from polishing pad (e.g. pitch) and any other impurities.

The redeposition layer contamination can be measured by means of secondary ion mass spectroscopy (SIMS). Figure 4.10 is the detected Ce element (coming from ceria, polishing particles) as a function of depth beneath the surface polished by the conventional method. It is found in Figure 4.10 that the Ce contamination induced by the conventional polishing process is as deep as 99.28 nm.

4.2 Light intensity enhancement

In order to investigate the relationship between LIDT and the damage at the surface or/and sub-surface, the incident laser beam intensity near damage should be discussed in advance. According to the electromagnetic field theory, light intensity is proportional to the square of the electric field[18, 19]. Therefore, in this chapter only electric field is introduced to analyse the enhancement of light intensity.

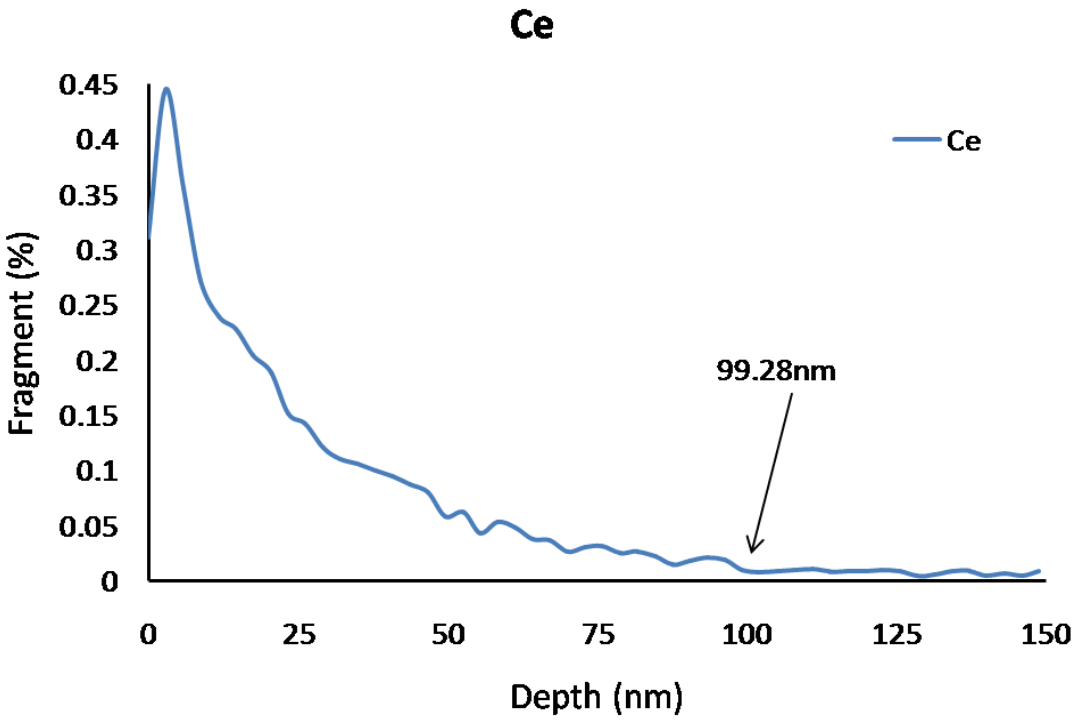

Figure 4.10 Ce distribution versus depth of surface layer after conventional polishing process measured using SIMS. An area of $10\ \mathrm{mm} \times 10\ \mathrm{mm}$ fused silica sample was prepared via conventional polishing for this result. Result shows that Ce distribution goes down with the decreasing depth until it becomes stable at the depth of 99.28 nm.

4.2.1 Theoretical solutions

Bloembergen proposed that the enhancement of electric field in the neighbourhood of damage could lower the LIDT of optical components[1]. Figure 4.11 shows a linearly polarised laser beam incident on a transparent optical component with refractive index, n. The incident electric field strength is E_{inc}, and it generally reduces to E_0 in the uniform dielectric bulk due to refraction and can be higher locally.

If the wavelength of incident laser beam is longer than the dimensions of all damage characteristics (i.e. crack, cylindrical groove, and spherical pore, shown in Figure 4.11), then the electric fields near these characteristics are given by

$$E_A = n^2 E_0$$

$$E_B = \frac{2n^2}{n^2+1} E_0 \qquad (4.4)$$

$$E_C = \frac{3n^2}{2n^2+1} E_0$$

According to Equation (4.4), the light intensity enhancement factors (LIEF) for crack, groove, and pore, are given by

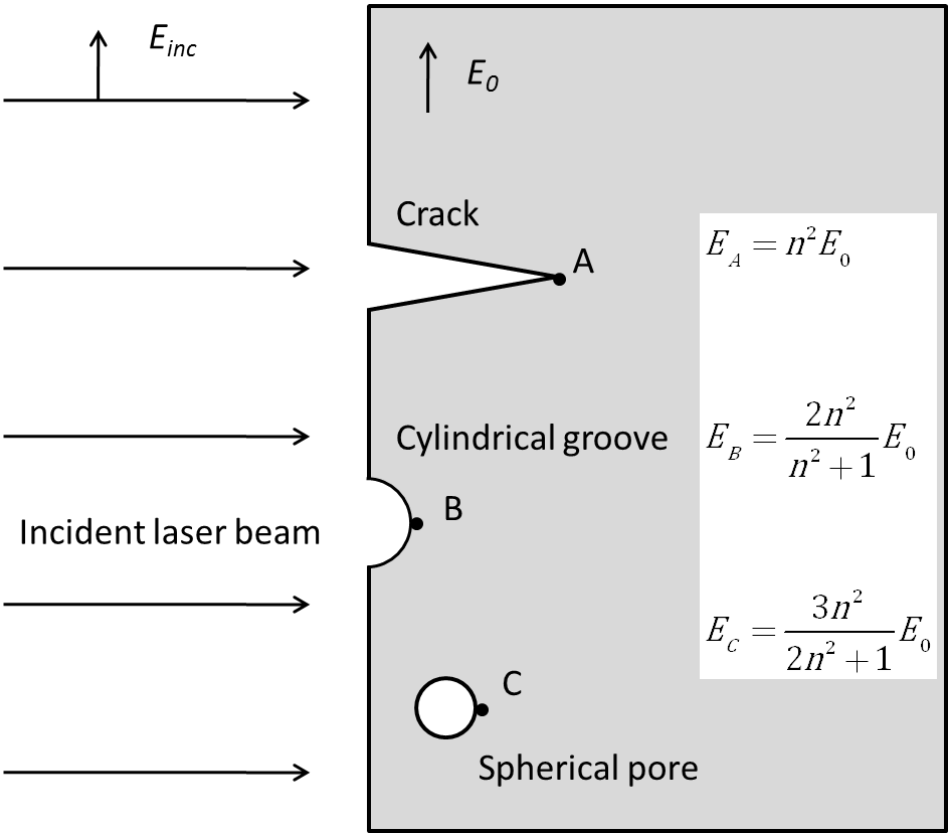

Figure 4.11 Local enhancement of electric field after Bloembergen's theory [1]

$$LIEF_A = \left(\frac{E_A}{E_0}\right)^2 = n^4$$

$$LIEF_B = \left(\frac{E_B}{E_0}\right)^2 = \frac{4n^4}{n^2+1^{\,2}} = \frac{4}{\left(1+\frac{1}{n^2}\right)^2} \tag{4.5}$$

$$LIEF_C = \left(\frac{E_C}{E_0}\right)^2 = \frac{9n^4}{2n^2+1^{\,2}} = \frac{2.25}{\left(1+\frac{1}{2n^2}\right)^2}$$

Figure 4.12 shows the increase of LIEF against the refractive index of bulk material, and indicates that LIEF of crack increases rapidly with the refractive index, while that of groove and pore increase slowly. Equation (4.5) indicates that LIEF of groove and pore have limit values of 4 and 2.25, respectively. For fused silica (n=1.48 at a wavelength of 355 nm, see Chapter 2), the LIEF for crack, groove and pore are around 4.42, 1.84, and 1.47, respectively.

Bleombergen's theory illustrates some useful assumption such as (1) damage enhances the laser intensity compared to bulk; (2) a sharp crack has much bigger LIEF. However, it suffers many shortcomings. Many damage created by manufacturing processes are dimensionally greater than the laser beam wavelength, especially for UV applications. And the theory does not include the case of LIEF due to multiple damage sites in close proximity. As a result, a numerical simulation method is introduced in this chapter.

4.2.2 Numerical simulations

A laser beam, well known as a kind of electromagnetic wave, satisfies Maxwell's equations. Therefore solving the Maxwell's equations should be a way to calculate the LIEF for incident laser beams.

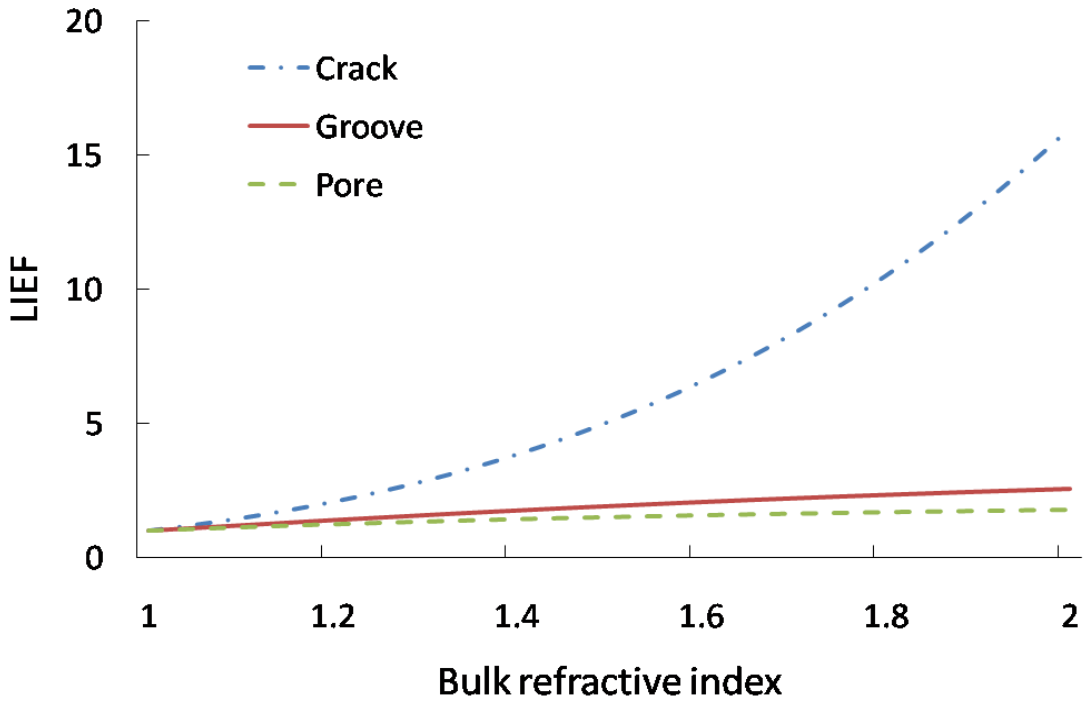

Figure 4.12 LIEF of crack, groove and pore in optics

In many cases, a 2-dimensional wave is useful to simplify the problem. A kinds of 2-D wave, TE wave (shown in Figure 4.13), is used in this chapter. For TE wave (shown in Figure 4.13a), only the electric field, $\boldsymbol{E}$, is perpendicular to the propagation direction $\boldsymbol{e_s}$ [18].

To solve the Maxwell's equations, finite difference time domain (FDTD) method is used. The FDTD method utilises Yee unit cell [20] and discretises the simulation domain spatially and temporally. The details of FDTD method is introduced in Appendix A.

In this chapter, an FDTD software, OptiFDTD (version 8.0.0.428, Optiwave Systems Inc, Canada), was used to calculate the LIEF of various surface damage sites. In all simulations, the incident laser beam was a CW TE wave with $\lambda = 355\ \mathrm{nm}$ wavelength. The electric field of incident laser beam was set as 1. The dielectric materials were air and fused silica. The fused silica used in the simulations is sandwiched between two air layers (shown in Figure 4.14). The fused silica layer was 8 μm in thickness and both air layers were 1 μm in thickness; and for the width, both were set as 10 μm. All the simulations were using 2-dimentional FDTD method. To save the simulation time, each simulation was lasted for 1.60 ps which were 8 times of the duration that the laser beam passed through the dielectric field. All the following simulations used Perfect Magnetic Conductor (PMC) boundary condition for the boundaries because it is a symmetric wall and can absorb the laser wave perfectly which made the laser beam reflection not occur in boundaries. Therefore the PMC boundary condition has perfect performances for simulation of plane wave, such as TE wave input.

1. Effect of damage location

Figure 4.15 shows the distributions of electric field intensity in fused silica samples which have the same V-shape crack on its surface. It must be noticed that the entrance and exit surfaces of fused silica were the boundaries of fused silica layer and air layers

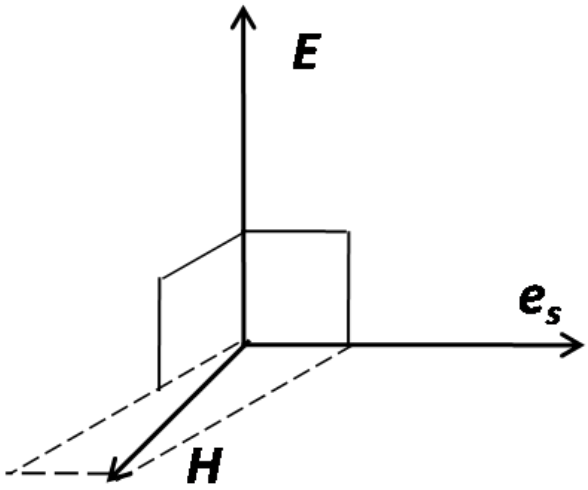

Figure 4.13 TE wave [18]

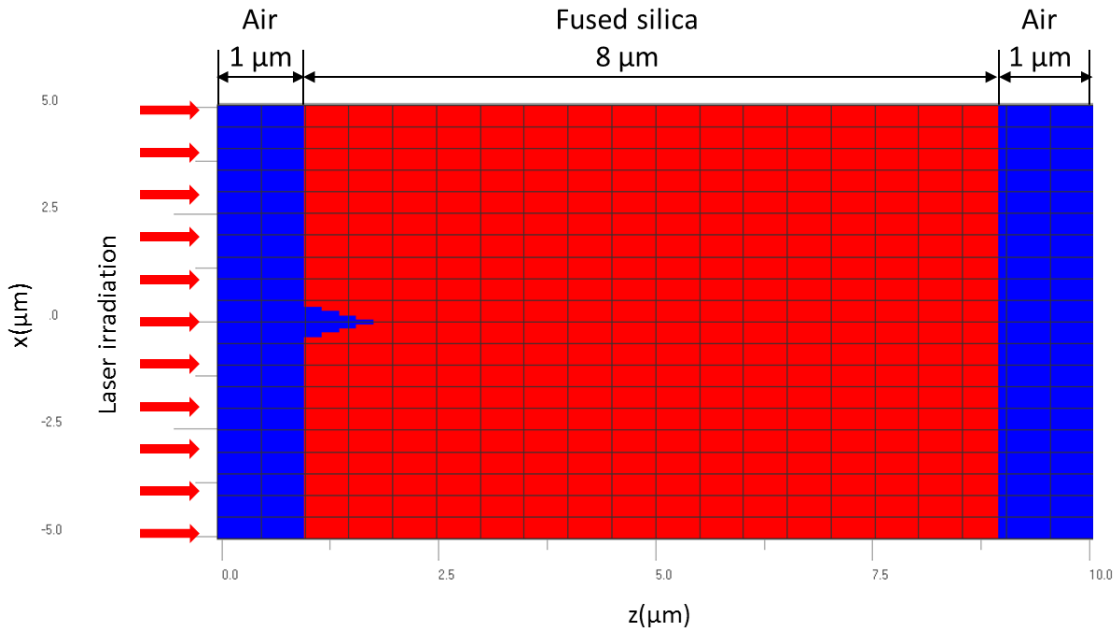

Figure 4.14 Schematic of dielectric materials used in simulations. A fused silica layer (8 µm in thickness) with defect is sandwiched between two air layers (1 µm in thickness for each)

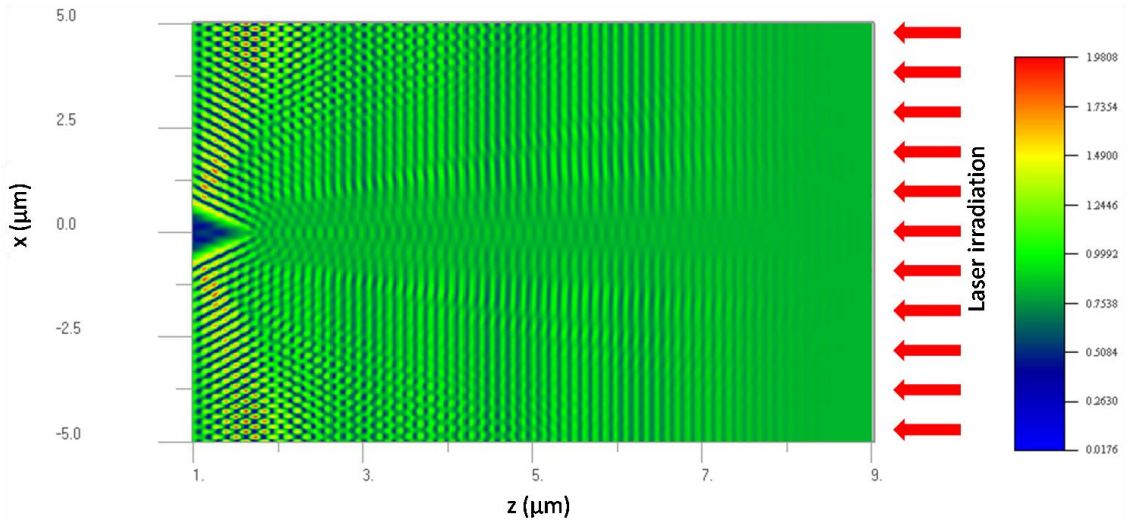

(a) Crack is on output surface

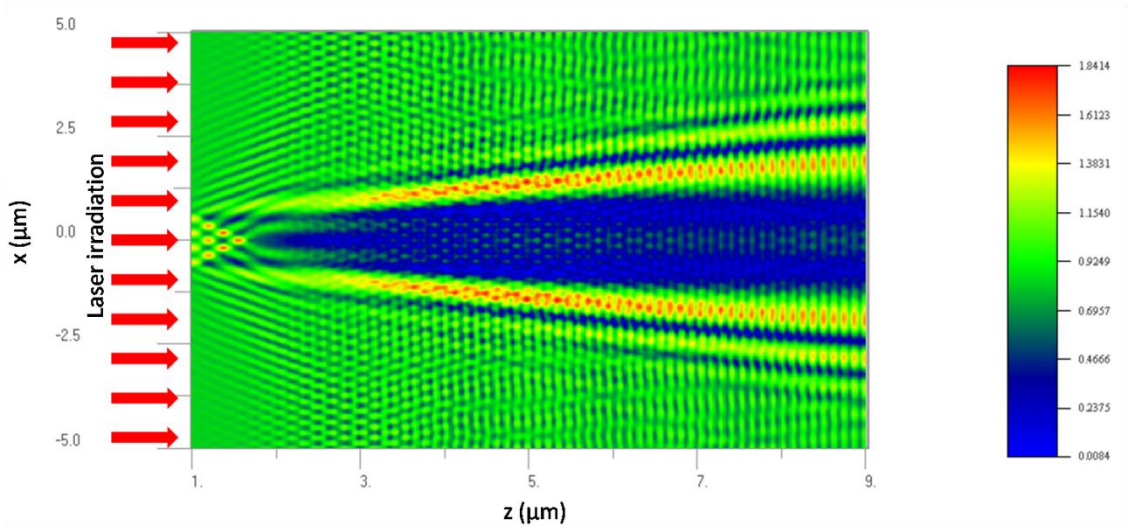

(b) Crack is on input surface

Figure 4.15 Electric field intensity distributions in fused silica samples with a V-shape crack.

rather than the simulation boundaries, so laser beam reflection could occur. The rest figures of simulation results are same setting as Figure 4.15.

The width and depth of the V-shape cracks on both samples are, 4λ and 2λ, respectively. For the crack on the exit surface (Figure 4.15 a), the peak electric field intensity is near the crack and inside the fused silica sample. And the peak electric field intensity is 1.98, which means the peak electric field increase 1.98 times. Therefore the peak LIEF is 3.92 because it is direct proportion with the square of electric field.

While for the same crack on the entrance surface (Figure 4.15 b), the peak electric field intensity is 1.84 and peak LIEF is 3.39, which are smaller than that of the exit crack. Moreover, the peak LIEF is located inside the sample but not near the crack. Even some strong point of electric field intensity is near the entrance crack (Figure 4.15 b), but they occur at in the clearance of crack where is in the air not fused silica.

As it gets higher peak LIEF for crack at exit surface than entrance surface, the simulations in the rest of the chapter are calculating cracks at the exit surfaces.

2. Effect of crack geometry

Figure 4.12 compares the theoretical LIEF of V-shape and cylindrical grooves. Therefore a predicted result is that the smoother crack has lower LIEF than that of sharper crack. Here, after a series of simulations of a laser beam radiating on the sample with cracks on the exit surface, the simulated peak LIEF of the V-shape and cylindrical cracks are demonstrated in Figure 4.16. In these simulations, in order to get the closest incident conditions with the cylindrical geometry, the widths of V-shape cracks are 2 times of the corresponding depths. Figure 4.16 indicates that (1) both LIEF of V-shape and cylindrical grooves increase with the increase of crack depth; (2) when the crack is shallow enough (less than about 2.5λ), the LIEF of V-shape and cylindrical grooves

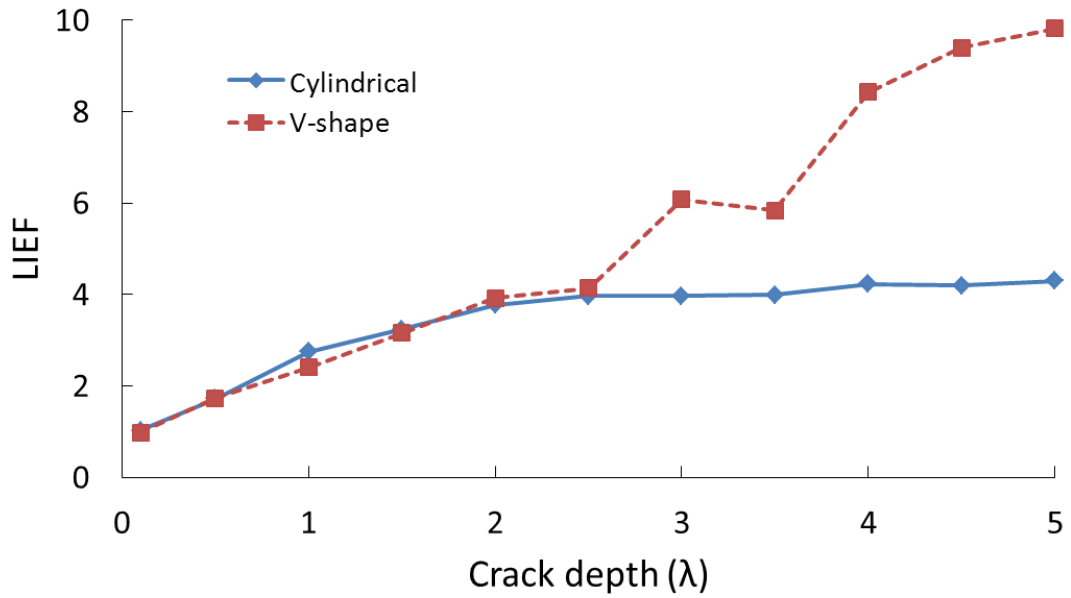

Figure 4.16 Peak LIEF, of V-shape and cylindrical grooves, versus crack depth at the exit surfaces. The width of each crack is 2 times of the corresponding depths.

increase slowly to 4 and both lines are nearly same; (3) when the depth of crack is greater than 2.5λ, the LIEF of cylindrical levels off to 4 while that of V-shape crack increases dramatically. Compared with Figure 4.12, Figure 4.16 got the similar results.

In order to extend it to cracks with any width and depth, a cosine groove was introduced to imitate the groove pattern. Figure 4.17 shows the peak LIEF of V-shape and cosine grooves of which the ratio between width and depth is 1.6. For both types of cracks, the peak LIEF rises with the increase of crack depth. Similar with the cylindrical grooves, the peak LIEF of cosine cracks increase slowly while that of V-shape cracks go up sharply after the crack depth is greater than 3λ.

3. Effect of the crack depth and width

Figure 4.16 and Figure 4.17 illustrate that the peak LIEF of samples go up with the rise of crack depth. Moreover, comparing the peak LIEF of a V-shape crack with depth of 5λ in Figure 4.16 and Figure 4.17, it is found that it reaches to 14.17 and 9.82, respectively. In other words, for V-shape cracks of 5λ, the peak LIEF is 14.17 for width of 8λ (ratio between width and depth is 1.6), while that for width of 10λ (ratio between width and depth is 2) is 9.82.

Figure 4.18 is a plot of peak LIEF as a function of ratio between V-shape crack width and depth. Both lines indicate that the peak LIEF increases with the increase of ratio of width/depth when width/depth is less than around 1.6; while they go down with the increase of width/depth when it is greater than 1.6, until becoming stable to about 1.5 when width/depth is greater than 6. This illustrates that the peak LIEF is sensitive to the ratio between width and depth when it is small.

4. Effect of interactions between multi-cracks

Figure 4.19 compares the distributions of electric field intensity in fused silica samples which has two consecutive cosine cracks which width/depth is 2 (width=2λ, depth=λ)

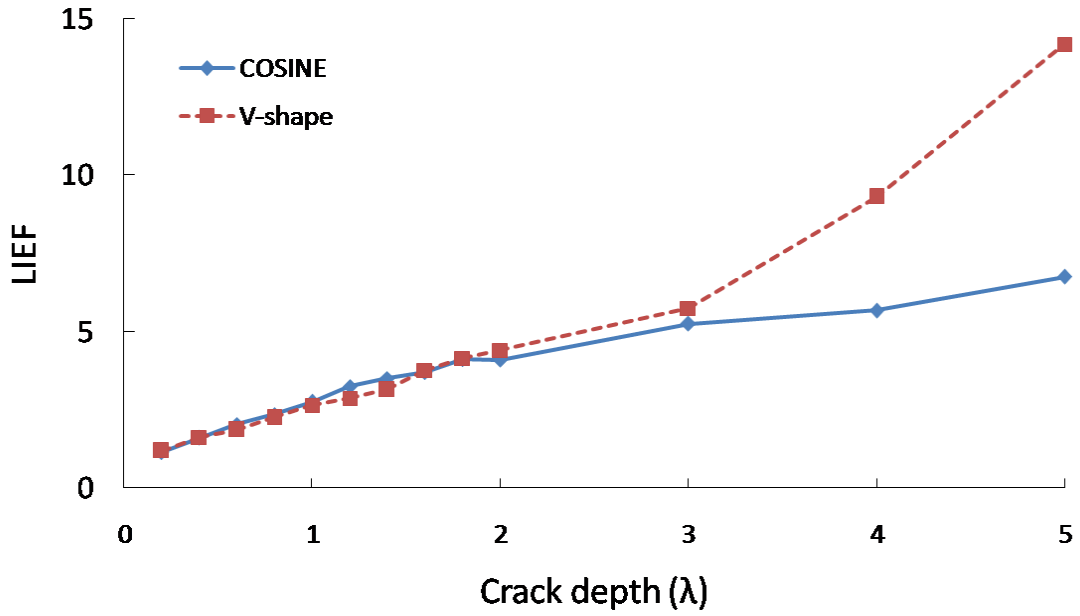

Figure 4.17 Peak LIEF, of V-shape and cosine grooves, versus crack depth. The ratio between width and depth is 1.6 for every crack.

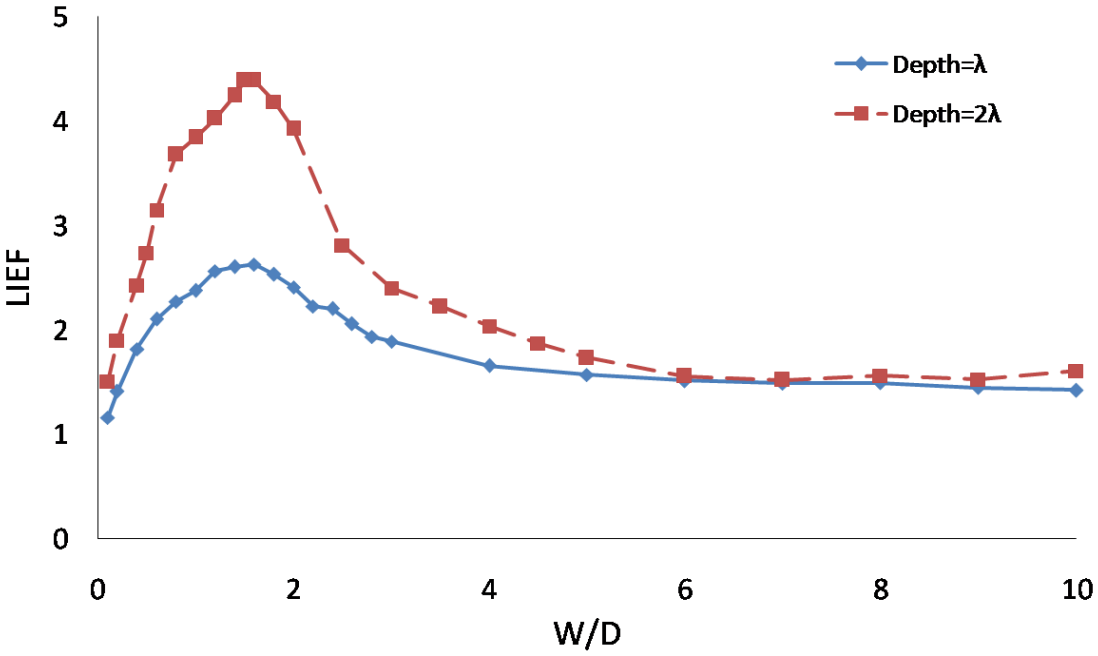

Figure 4.18 Peak LIEF versus crack width/depth

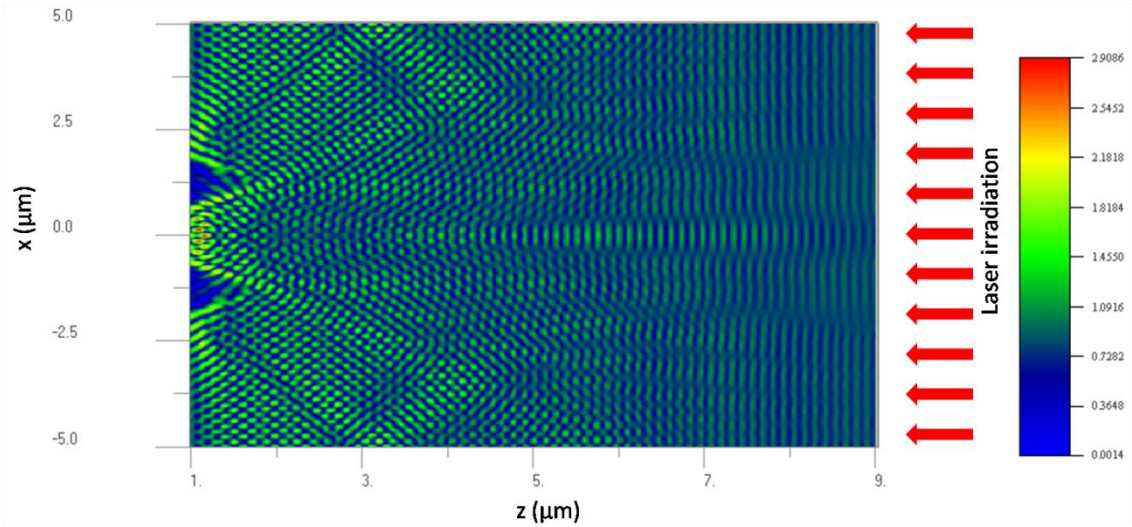

(a) Double-crack at exit surface

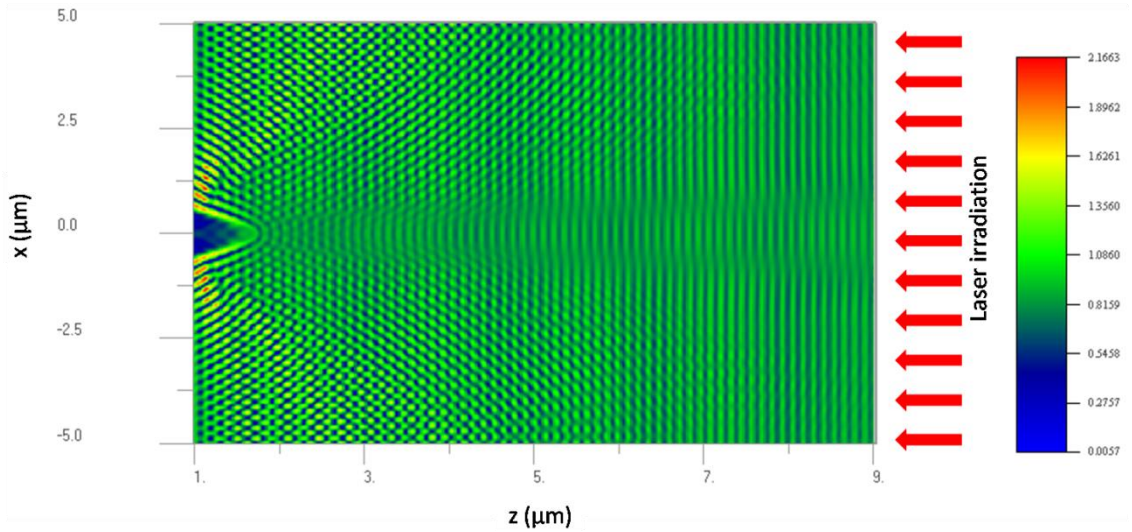

(b) Single-crack at exit surface

Figure 4.19 Electric field intensity distributions of surface with double- and single-crack

and single crack with same geometry. For the double-crack surface, the peak LIEF is 8.45 and located inside of the sample between the two cracks; while for the single-crack surface, it is 4.69 and located at the outside of the crack inside of sample.

Moreover, the distance between two cracks is crucial. As shown in Figure 4.20, the peak LIEF increases with the crack distance until reaching its maximum value when the crack distance is around $1.2W$ (W stands for the width of a single cosine crack), then it goes down to the stable value that is for the single crack after crack distance is around $3W$.

5. Effect of pore

Figure 4.21 shows the peak LIEF of small spherical pores at depth λ and 0.5λ beneath the surface. Both lines indicate that the peak LIEF goes up slowly with the increase of pore size. Moreover, Figure 4.21 also illustrates that the peak LIEF of the same pore at depth λ and 0.5λ beneath the surface are very close.

In order to investigate the correlation between peak LIEF and location beneath the surface, simulations were performed. Figure 4.22 demonstrates the peak LIEF as a function of distance from the sample surface. It shows that the peak LIEF rises to 2.39 until the pore is located at depth of one λ under the surface and then goes down slowly to around 2; nevertheless it is not a big change.

6. Effect of impurity

Suppose spherical metallic impurity particle, of which both the diameter and depth are λ and reflective index is $n = 5$ (because the reflective index for a metallic impurity is high), embedded below the surface, the electric field intensity distribution is shown in Figure 4.23. The peak electric field is located on the particle and peak LIEF is 5.11, which is larger than 2.39 which is peak LIEF of a pore with same size at the same location.

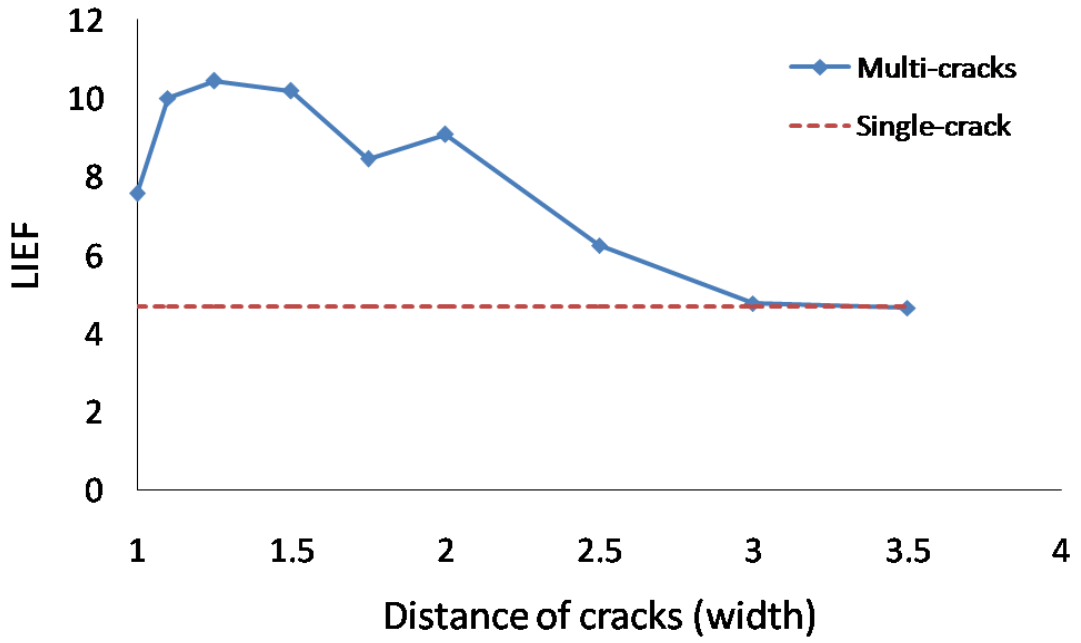

Figure 4.20 Peak LIEF versus crack distance in multiplies of λ

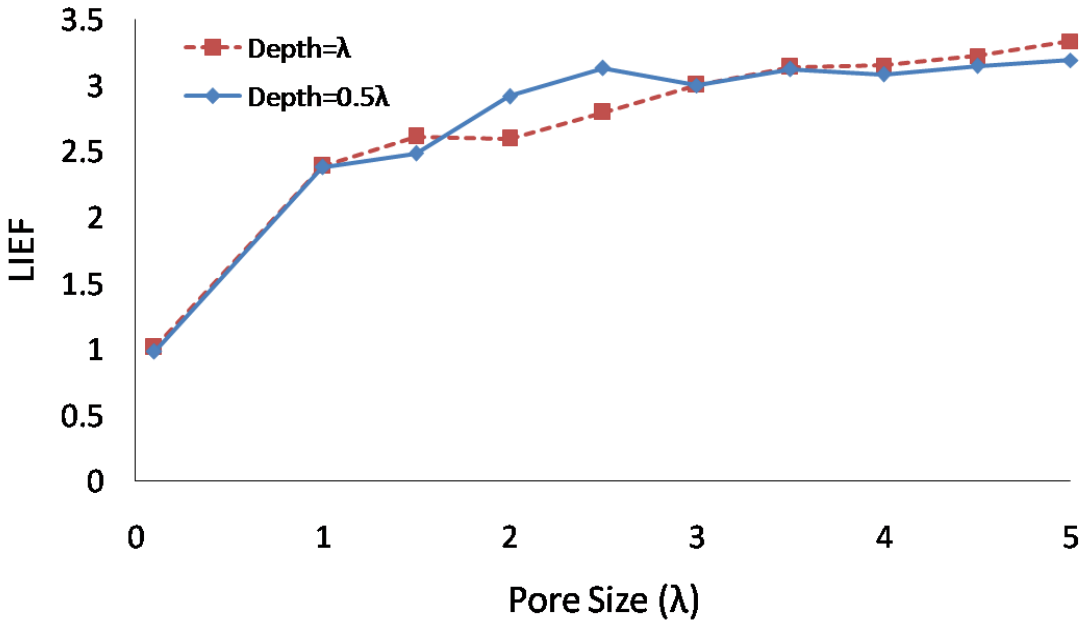

Figure 4.21 Peak LIEF versus pore size

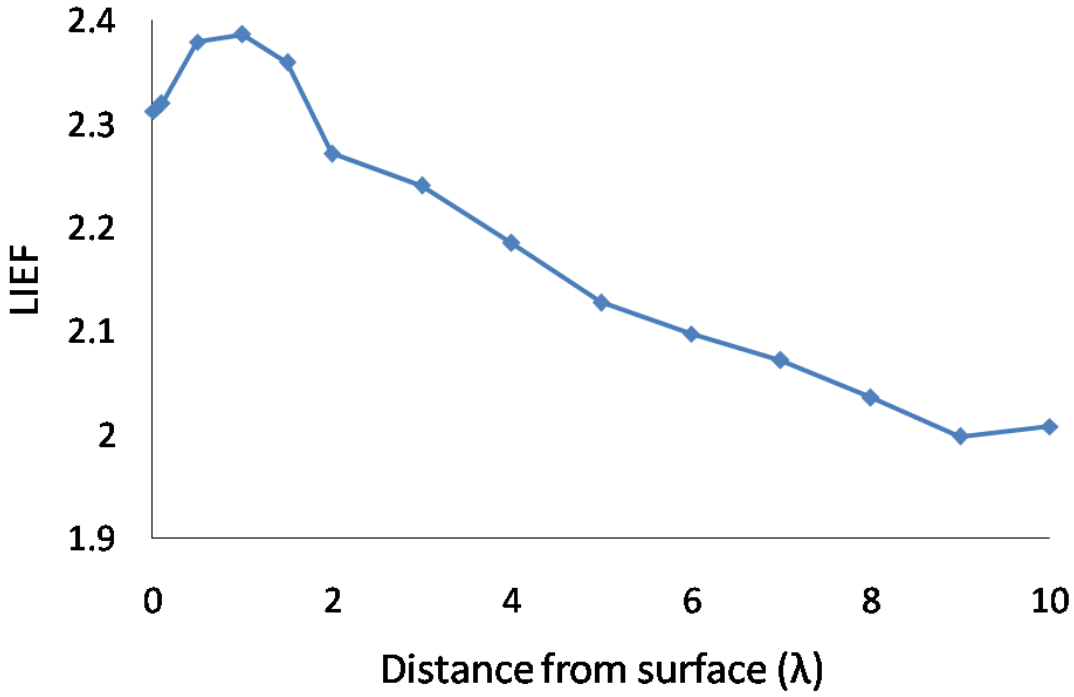

Figure 4.22 Pore peak LIEF versus distance from surface

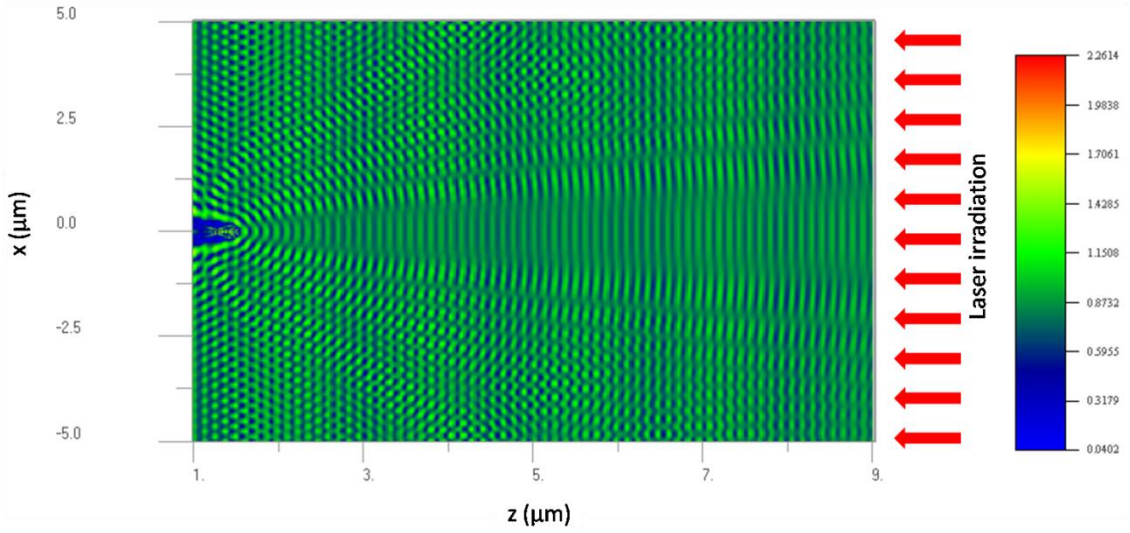

Figure 4.23 Electric field intensity distributions of surface with spherical impurity

4.2.3 Conclusions

The purpose of the numerical simulations is not to get the peak LIEF of surfaces with cracks quantitatively but to understand that the cracks can lower the LIDT of a surface significantly because higher LIEF could induce lower the LIDT. Several conclusions can be drawn from the simulations,

1. Crack at exit the surface (relative the incident laser beam) causes higher LIEF than that at the entrance surface. This is proved by laser radiation experiments that LID generally occurs at the exit surface of fused silica samples [2].

2. Peak LIEF of a smoother groove is lower than that of the sharper crack when the conditions of width and depth are the same. This means smoothing the sharp groove could increase the LIDT of surface. The crack- smoothing method will be discussed in chapter 5.

3. The deeper the crack in the surface, the higher the peak LIEF of the sample, especially for the shaper cracks. Therefore, reducing the crack depth could improve the LIDT of surface.

4. The ratio between crack width and depth is crucial and that the peak LIEF reaches to highest value when the width/depth is around 1.6. This provides a solution, increasing the width of surface cracks to much wider than $1.6D$ (D stands for depth), to lower the LIDT of surface.

5. Multi-crack at surface cause higher LIEF than single-crack, however when the distance between two cracks is longer than 3 times of crack width the LIEF value reduces to that of single crack. Therefore reducing the number of cracks, i.e. decreasing the density of cracks, could lower the LIDT of surface.

6. Pore beneath the surface also induces LIEF and bigger pore could cause higher LIEF

of sample. Hence to avoid generating pores in the manufacturing processes is also a way to increase the LIDT of surface.

7. Impurity with larger reflective index would generate larger peak LIEF and that is located on the impurity.

4.3 Thermal stress distribution of specimen

4.3.1 Simulation design

As the thermal stress is a mechanism that causes LID in optical components, to analyse the thermal stress of the optical component is a way to investigate and to analyse the correlation between LID and surface/sub-surface defects.

Section 4.3 illustrates that the light enhancement introduced by defects of surface/sub-surface does occur in the optical component, therefore with taking account of the geometry of damage, a series of simulations are conducted to numerical calculate the thermal stress distribution for a surface with various defects. The transient thermal stress calculation is made on the basis of the finite element analysis (FEA) method. The FEA software ANSYS (vision 8.1, Ansys Inc., USA) is used in this chapter.

In the simulations, the thermal fluxes applied on the components are obtained by the light intensity simulation in Section 4.3 by means of FDTD method. Therefore, combining the light intensity simulations in Section 4.3, the simulation processes are shown in Figure 4.24. In Figure 4.24, the laser beam is that used in the FDTD simulation;the properties of fused silica are shown in Table 4.1.

The element type used in the FEA simulations is Solid70; simulation setting time is 300 nanoseconds; the original temperature is 20℃. For the simulation for an impurity embedded in the optical component, the impurity material is a ceria particle.

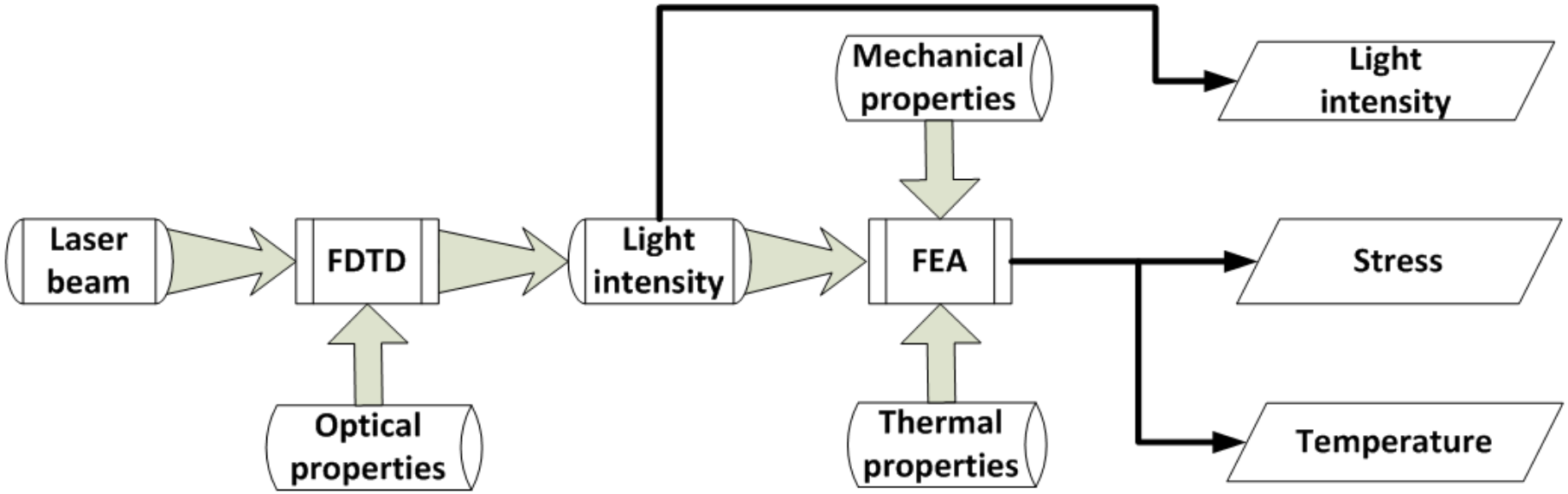

Figure 4.24 Flow chart of simulation processes

Table 4.1 Properties of fused silica [21]

Item	Value
Refractive index	1.48
Heat capacity ($\mathrm{J/kg \cdot K}$)	740
Thermal conductivity ($\mathrm{W/m \cdot K}$)	1.38
Coefficient of thermal expansion ($10^{-7}/\mathrm{K}$)	5.5
Young's Modulus (GPa)	73
Density ($\mathrm{kg/m^3}$)	2200

4.3.2 Simulation results

1. Surface with V-shape crack

For a surface with a V-shape crack, of which both the width and depth are 2λ ($\lambda = 355nm$) in the irradiation of a laser beam ($\lambda = 355nm$), the thermal stress concentration does occur and the peak thermal stress is located at the valley point of the groove. Figure 4.25 shows the simulation results. The peak thermal stress is 60 KPa in this simulation.

2. Surface with cylindrical groove

For the simulation for a cylindrical groove on a surface, similar results are gained. Figure 4.26 and Figure 4.27 illustrate the simulation results for cylindrical groove with diameter of 4λ and 2λ, respectively. Results indicate that thermal stress concentrations also occur at the valley of the grooves and the peak thermal stresses (54 KPa and 48 KPa) for cylindrical grooves are less than that of V-shape crack (60 KPa). Moreover, wider groove generates larger peak thermal stress.

(a)

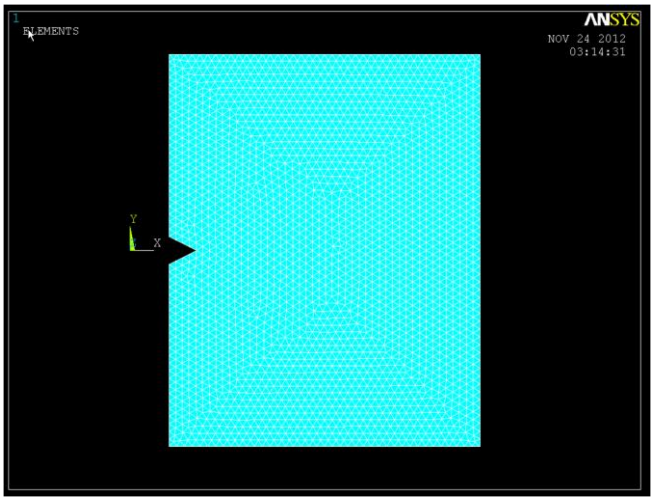

(b)

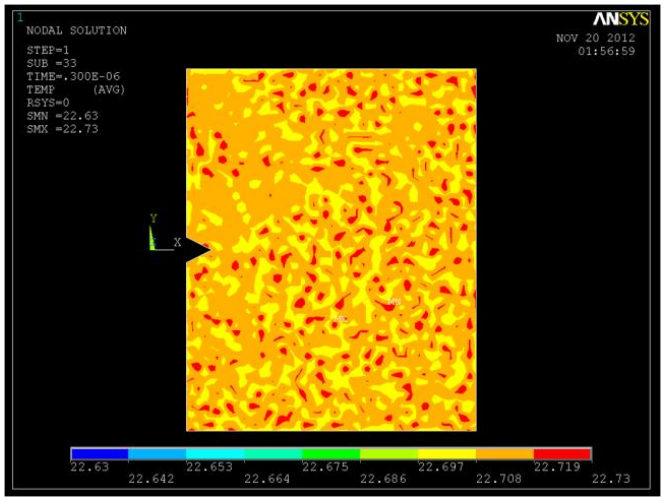

(c)

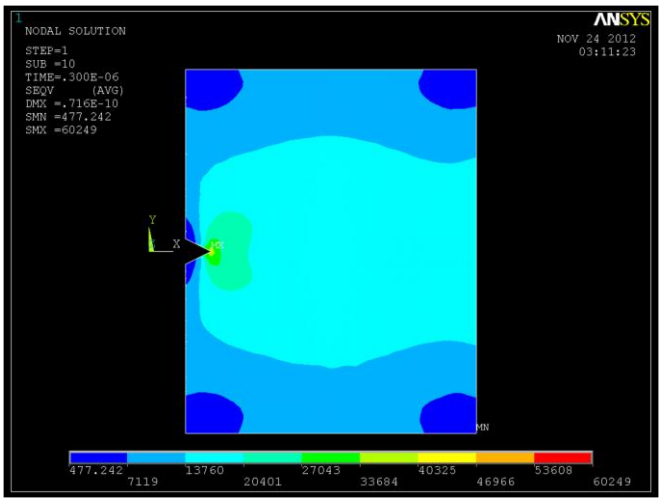

Figure 4.25 Results of surface with V-shape crack. (a) Mesh grids of component; (b) Temperature distribution; (c) Thermal stress distribution.

(a)

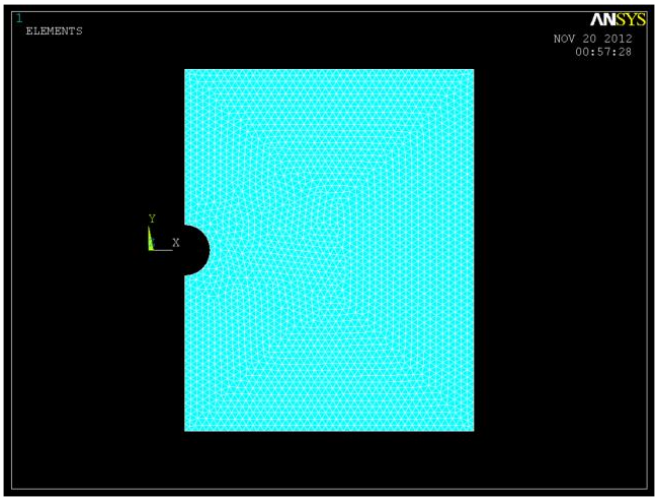

(b)

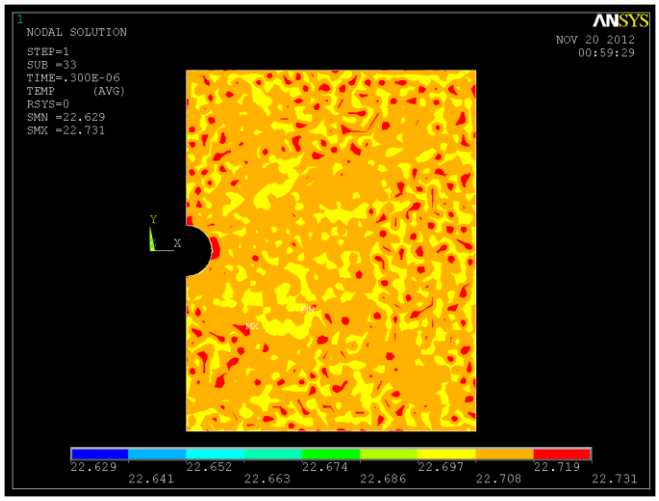

(c)

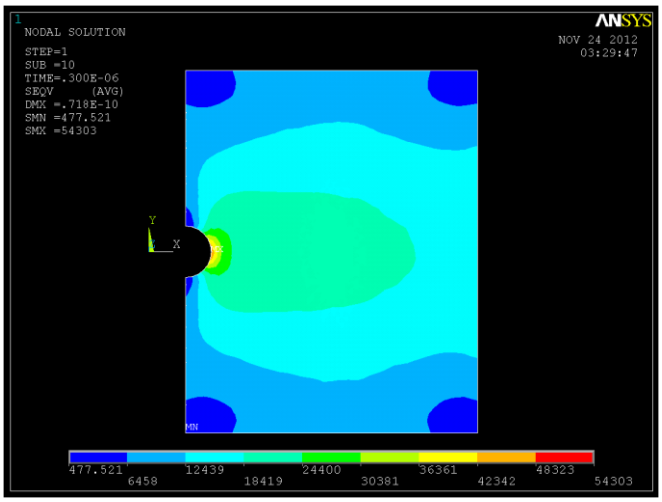

Figure 4.26 Results of surface with cylindrical groove ($r = 4\lambda$). (a) Mesh grids of component; (b) Temperature distribution; (c) Thermal stress distribution.

(a)

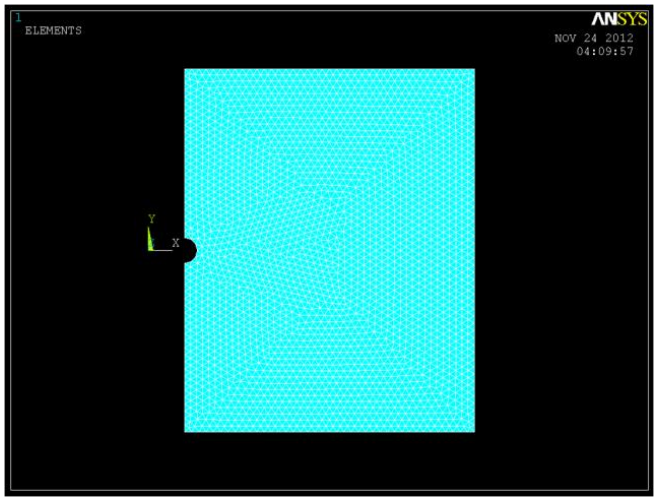

(b)

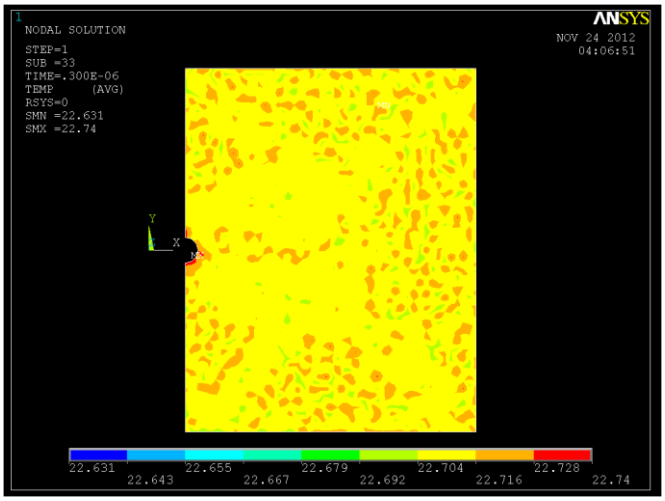

(c)

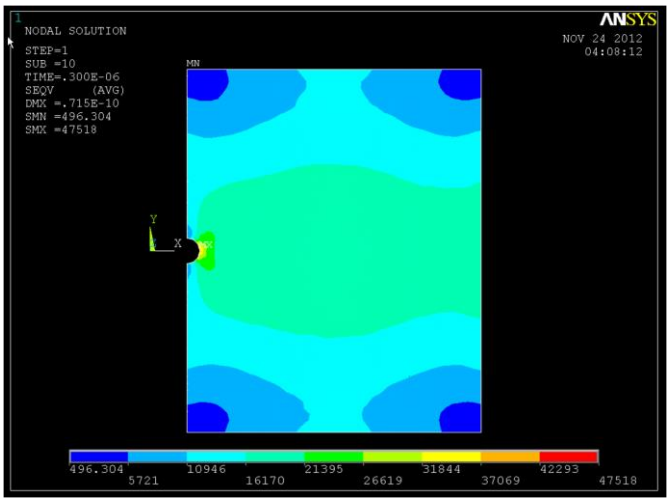

Figure 4.27 Results of surface with cylindrical groove ($r = 2\lambda$). (a) Mesh grids of component; (b) Temperature distribution; (c) Thermal stress distribution.

3. Surface with spherical pore

The condition that a spherical pore is beneath the surface is also simulated. In the simulation, the diameter of the pore is 2λ and depth from the surface is 2λ. Results, shown in Figure 4.28, indicate that still the thermal stress concentration happens at the edge of the pore defects and in the direction of the incident laser beam. The peak thermal stress is 52 KPa, which is less than V-shape crack but greater than cylindrical groove (same diameter) on the surface.

4. Impurity embedded below surface

A surface is contaminated by a metallic spherical impurity is simulated. In the simulation, diameter of pore is 2λ and depth from the surface is 2λ. Suppose the impurity has large thermal expansion coefficient (4 times of fused silica) and small heat capacity (one fourth of fused silica), then the simulated results, shown in Figure 4.29, indicate that still the thermal stress concentration happens at the impurity and the interface of the impurity and optical component. The peak thermal stress is 1.72MPa at the interface between impurity and fused silica component, which is much greater than crack on the surface. Therefore, impurity is a fatal defect for the optical surface.

4.3.3 Conclusions

The purpose of the thermal stress simulations is not for a quantitative prediction but a qualitative method to investigate the influence that surface defects applying on the LID of optical surfaces. Therefore some first conclusions are obtained that

1. Defects on the surface/sub-surface create thermal stress concentration. Therefore removing the cracks is a method to enhance the LIDT of optical surface.

2. Smoother crack generates smaller peak thermal stress. This is also verified by the light intensity enhancement simulations. Therefore to smooth the sharp crack on

(a)

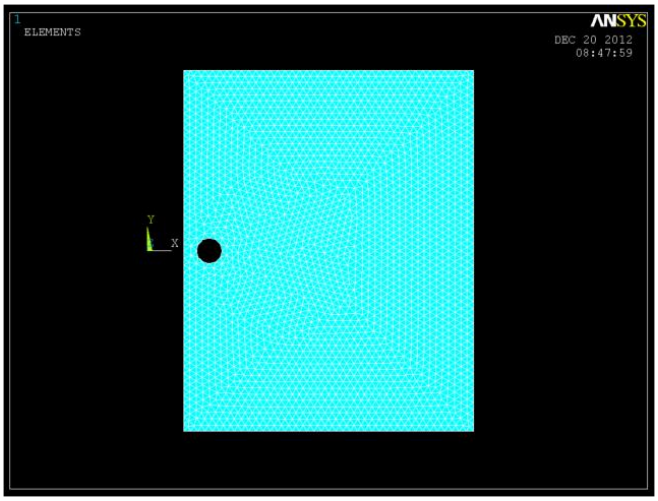

(b)

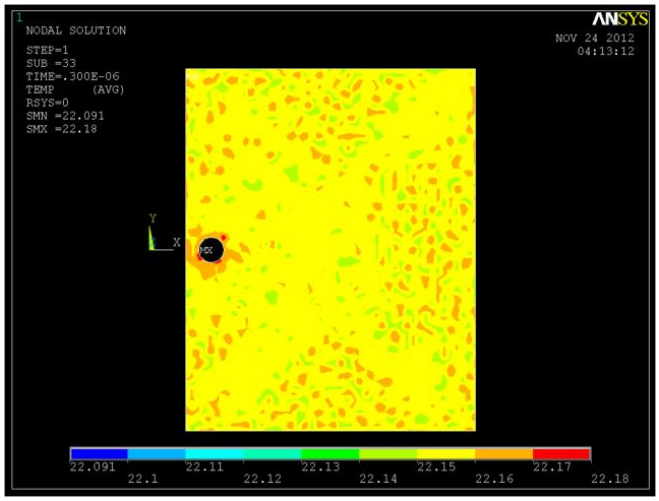

(c)

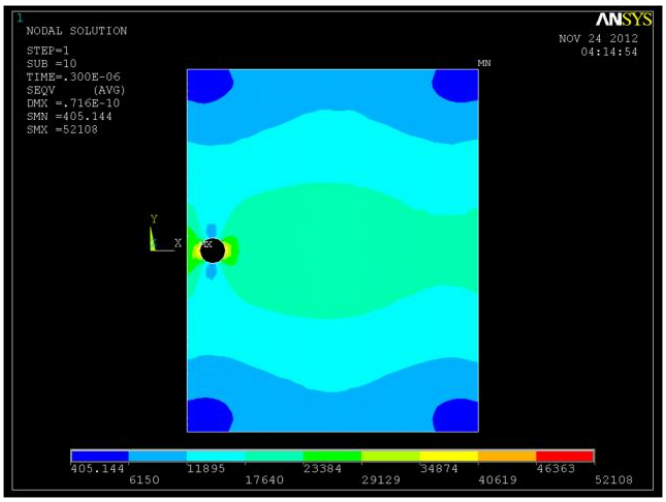

Figure 4.28 Results of surface with pore defect ($r = 2\lambda$). (a) Mesh grids of component; (b) Temperature distribution; (c) Thermal stress distribution.

(a)

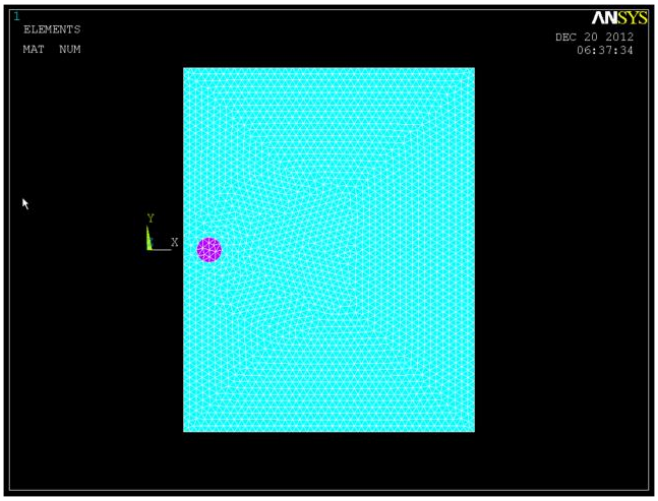

(b)

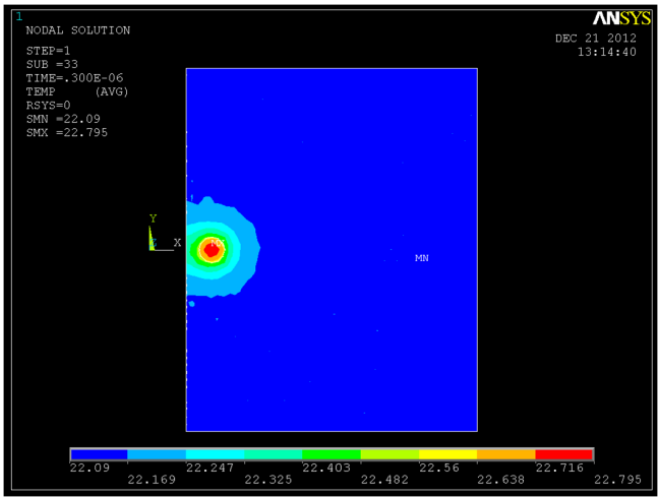

(c)

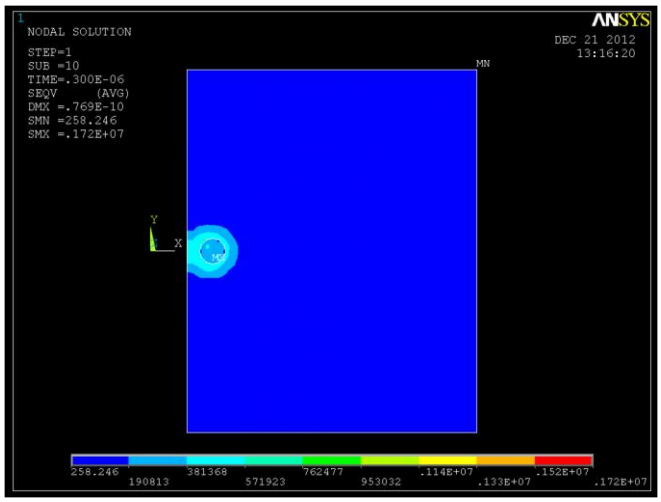

Figure 4.29 Results of surface with impurity defect. (a) Mesh grids of component; (b) Temperature distribution; (c) Thermal stress distribution.

the surface is a technique to improve the LIDT of optical surface.

3. Smaller scratches introduce weaker peak thermal stress. Therefore reducing thecrack size is a possible way to increase the LIDT of optical surface.

4. Impurities embedded in the surface are crucial. Surfaces contaminated by impurities would be subject to large thermal stress concentration. Removing the impurities is a way to improve the LIDT of optical surface.

4.3.4 Experimental results

A series of laser beam radiation experiments were conducted, in which the wavelength of incident beam was 355nm ultraviolet laser and beam frequency was 10Hz and duration was 8.2 ns. The specimens were made of Yaohua fused silica glass (China) and manufactured by CMP methods and the initial surface roughness is around Ra 1~2 nm.

Figure 4.30 and Figure 4.31 are pictures acquired by an optical microscopy of LID on fused silica surfaces. Figure 4.30 indicates the contaminants which were the impurities in the surface layer spouted out during the damaging processes and attached the surface due to the laser irradiation, and Figure 4.31 shows that LID does occur at the scratches, or at the extending line of the scratches which are probably also scratches covered by redeposition layer generated during the CMP processes, on fused silica surfaces. Therefore both figures prove that scratches and impurities on the surface/sub-surface could be the initiations of LID.

4.4 Summary

LID generally occurs at the exit surface of fused silica optics and the LIDT is usually lower than that of the bulk fused silica. In order to investigate the method to improve the LIDT of fused silica optics, the following works have been done in this chapter:

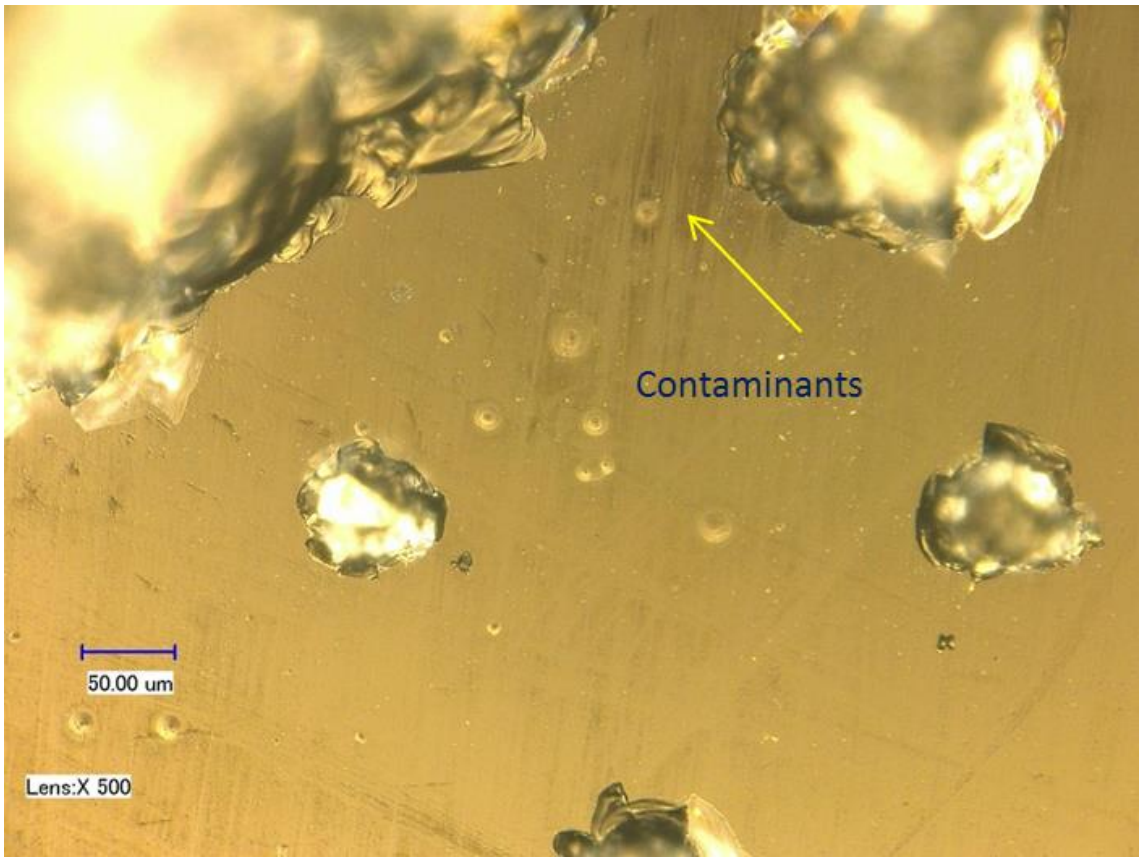

Figure 4.30 Impurities induced damage in the laser beam radiation experiments. The wavelength of incident beam was 355nm ultraviolet laser; the beam frequency was 10Hz; and duration was 8.2 ns.

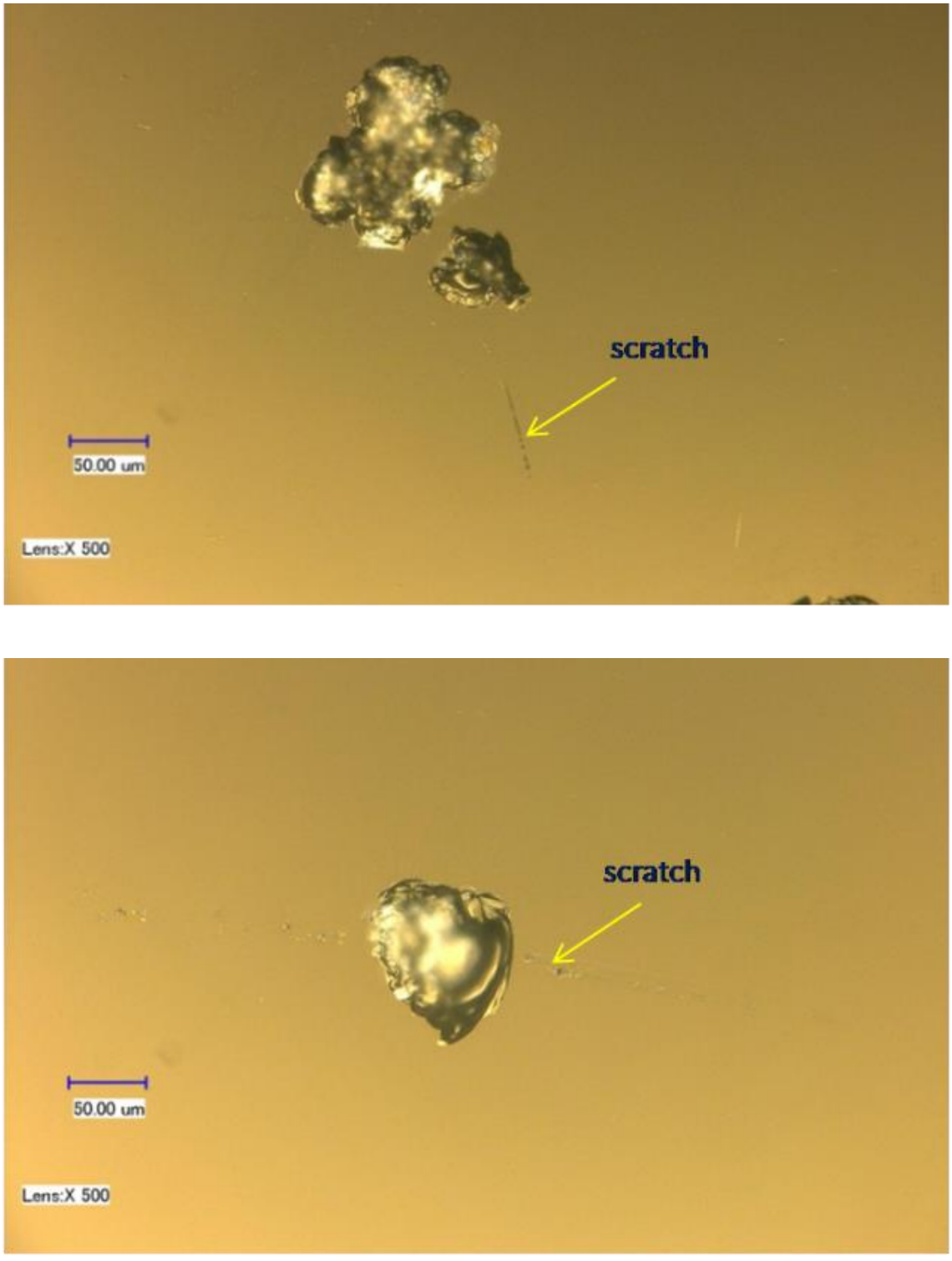

Figure 4.31 Damage is at scratch or the expanding line of scratch.

1. Analyse the defects on optical surface/sub-surface. The creation of damage on surface and sub-surface during the conventional preparation of optical surface is analysed. It is difficult to avoid the damage during polishing process due to the variation of polishing particle size. Depth of fused silica surface contaminated by impurities is measured by SIMS, which shows the result is around 100 nm.

2. Light intensity enhancement in the fused silica optical component is analysed theoretically and numerical simulations using FDTD method are conducted. Results indicate that smoother and shallower cracks introduce higher LIDT, and lower density of cracks and pores can also improve the LIDT of fused silica surface. Moreover, impurities embedded into the surface layer reduce the LIDT of fused silica obviously.

3. Thermal stress in the fused silica optical component is simulated by the means of FEA software ANSYS. Results show that smoother and smaller cracks create less thermal stress concentration and could probably enhance the LIDT, and impurities embedded into the surface layer generate much greater thermal stress concentration and could be likely to lead to LID.

4. LID experiments show that cracks and impurities on/in the surface/sub-surface could be the initiations of LID.

References

1. Bloembergen, N., "Role of cracks, pores, and absorbing inclusions on laser induced damage threshold at surfaces of transparent dielectrics". *Applied Optics*, 1973. **12**(4): pp. 661-664.

2. Wood, R.M., "Laser-Induced Damage of Optical Materials". 1 ed. Series in Optics and Optoelectronics, ed. R.G.W. Brown and E.R. Pike. 2003, Bristol: Institute of Physics Publishing.

3. Beilby, G., "Aggregation and Flow of Solids". 1921, London: Macmillan and Co.

4. Carr, J.W., E. Fearon and L.J. Summers. "Subsurface structure in polished fused silica and diamond turned single crystal silicon.". [Online]; Available from: Https://e-reports-ext.llnl.gov/pdf/236132.pdf.

5. Camp, D.W., M.R. Kozlowski and L.M. Sheehan. "Subsurface damage and polishing compound affect the 355-nm laser damage threshold of fused silica surfaces". in *Proc. SPIE*. 1998. **3244**: pp. 356-364

6. Hed, P.P., D.F. Edwards and J.B. Davis, "Edwards, and J. B. Davis. Subsurface damage in optical materials: origin, measurement and removal", Lawrence Livermore National Laboratory (LLNL) Report, 1989, pp. 1-17

7. Menapace, J. "Developing Magnetorheological Finishing (MRF) Technology for the Manufacture of Large-Aperture Optics in Megajoule Class Laser Systems". in *Proc. SPIE*. 2010. Boulder, CO, United States. pp. 1-14

8. Samuals, L.E., "Metallographic Polishing by Mechanical Methods (4th Edition)". 2003, Ohio: ASM International.

9. Lawn, B.R. and M.V. Swain, "Review Indentation Fracture: principles and

applications". *Journal of Materials Science*, 1975. **10**: pp. 1049-1081.

10. Suh, N.P., "Tribophysics". 1 ed. 1986, New Jersey: Prentice-Hall, Inc.

11. Lawn, B.R., "Fracture of brittle solids". 2 ed. Cambridge Solid State Science Series, ed. E.A. Davis and I.M. Ward FBS. 1993, Cambridge: Cambridge University Press.

12. Suratwala, T., L. Wong, P. Miller, M.D. Feit, J. Menapace, R. Steele, P. Davis and D. Walmer, "Sub-surface mechanical damage distributions during grinding of fused silica". *Non-Crystalline Solids*, 2006. **352**: pp. 5601-5617.

13. Cook, L.M., "Chemical Processes in Glass Polishing". *Journal of Non-crystalline Solids*, 1990. **120**: pp. 152-171.

14. Suratwala, T.I., R. Steele, F.M. D, L. Wong, P. Miller, J. Menapace and P. Davis, "Effect of rogue particles on the sub-surface damage of fused silica during grinding/polishing". *Journal of Non-Crystalline Solids*, 2008. **354**(2008): pp. 2023–2037.

15. Bulsara, V.H., Y. Ahn, S. Chandrasekar and T.N. Farris, "Mechanics of polishing". *Journal of Applied Mechanics-Transactions of the Asme*, 1998. **65**(2): pp. 410-416.

16. Mikosza, A.G. and B.R. Lawn, "Section-and Etch Study of Hertzian Fracture mechanics". *Journal of Applied Physics*, 1971. **42**: pp. 5540-5545.

17. Wang, Z., "Study on the Detection and Control Techniques of Subsurface Damage in Optical Fabrication" [PhD Thesis]. Changsha, China: National University of Defense Technology; 2008.

18. Yang, R. and T. Wong, "Electromagnetic field and waves". 2006, Beijing, China:

Higher Education Press.

19. Von Hipperl, A., "Dielectrics and Waves". 1995, London: Artech House Publishers.

20. Yee, K.S., "Numerical solution of initial boundary value problem involving Maxwell' s equations in isotropic media". *IEEE Trans. Antennas and Propagation*, 1966. **14**: pp. 302-307.

21. "Fused Silica, SiO_2 Glass Properties". [Online]; Available from: http://www.accuratus.com/fused.html.

CHAPTER 5

SURFACE QUALITY IMPROVEMENT BY THE MRF PROCESSES

From Chapter 4 we draw the conclusions that the damage and impurities on the surface and/or sub-surface layer are probably the initiations of LID of fused silica optics. Hence, in order to improve the LIDT of fused silica optics, it is necessary to reduce the number of potential LID initiation sites during the manufacturing processes. In this chapter, we mainly focus on removing the surface and/or sub-surface damage, which are generated by the conventional manufacturing processes of fused silica optics, by magnetorheological finishing (MRF).

5.1 Non-fracture polishing by the MRF process

5.1.1 Conditions of non-fracture polishing

A material which is ductile, when deformed in bulk, will undergo a significant amount of plastic deformation before fracture. Brittle materials, on the other hand, deform elastically and then hardly plastically before fracture by the catastrophic propagation of a crack.

Fused silica, as a kind of inorganic glass, is a brittle material because it exhibits low fracture toughness [1]. It is very likely to fracture the fused silica during grinding and conventional polishing processes. For any brittle material, however, it is believed that a critical condition does exist under which the material can be manufactured as a ductile material and no fracture is happening during the manufacturing procedure [2].

As fused silica is such a brittle material, it is however possible to be machined similar to metal-machining in some conditions. We are concerned with the criterion of ductile-brittle transition point in fused silica machining. Although there are many variants to determine the ductile-brittle transition for a brittle material, an indentation test is used generally to illustrate the criterion.

Lawn et al. [3]used a sharp point to press in to the surface of a brittle material under an increasing force and then unloaded. The indentation processes are also introduced in Chapter 3. During the static indentation process, plastic deformation, median crack, and lateral crack are produced with increasing load (though lateral crack occurs during unloading). The indentation is illustrated in Figure 5.1 [4].

From Figure 5.1, the sequence of cases, with the increasing indention load on indenter, are as follows:

1. An irreversible deformation zone is generated below the indentation and a permanent mark remains in the surface after unloading. This phenomenon illustrates that plastic deformation does occur in the indentation process (Figure 5.1a).

2. At some critical load applied on the indenter, a crack, which is commonly named median crack or radial crack, is formed below the contact zone where the indentation stress is greatest (Figure 5.1b). The direction of the median crack depends on the geometric shape of the indenter and the anisotropy of the specimen material. However it's perpendicular to the specimen surface in most conditions. The median crack does not recover after unloading. Therefore a deformed zone and several median cracks remain in the surface after unloading.

3. With increasing indentation load, the indentation mark and median cracks keep growing, until, at a critical load, cracks (called lateral cracks) are generated

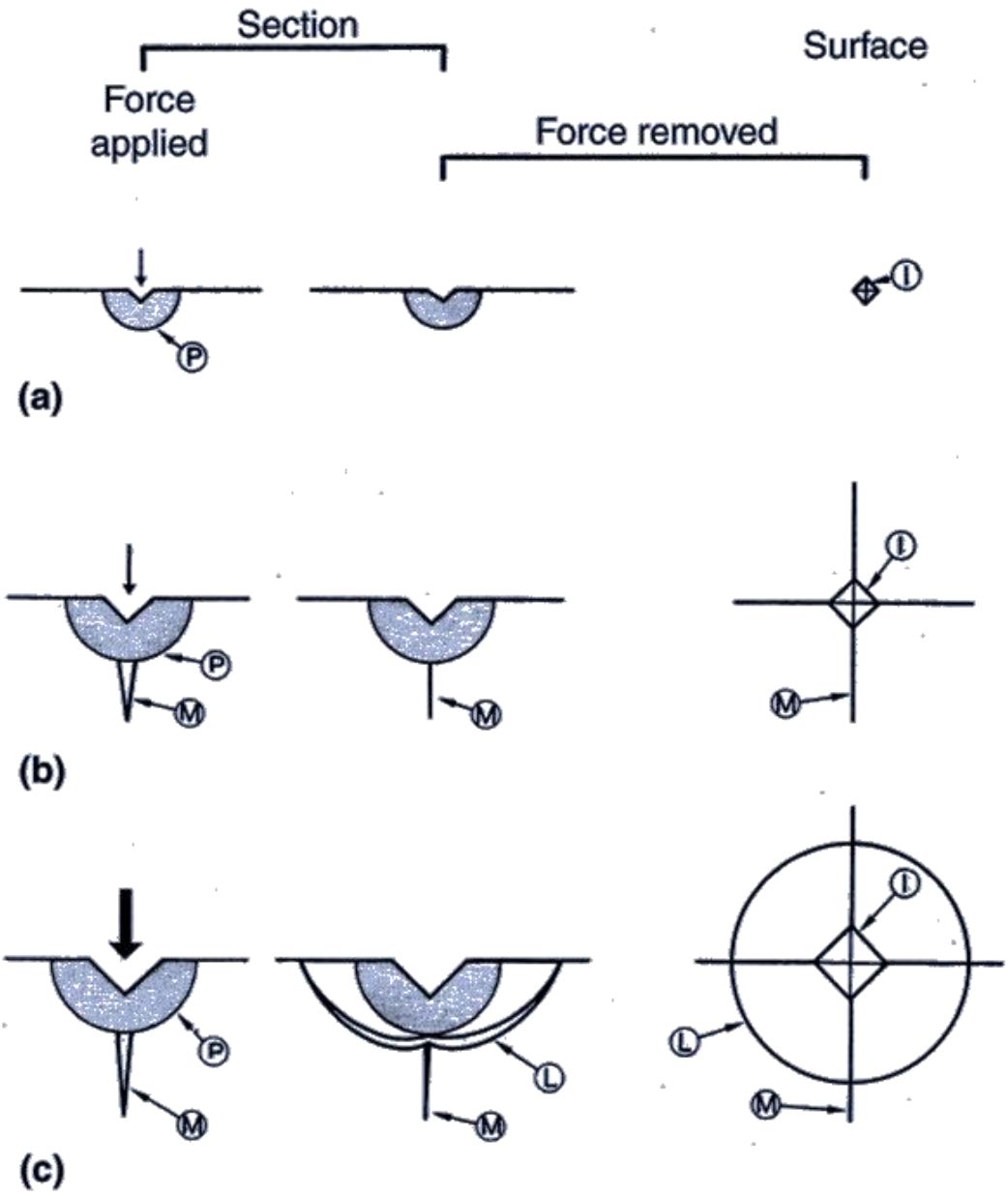

Figure 5.1 Sharp indenter impact into surface of brittle glass under increasing force (top to bottom), and the corresponding unloading events. P, plastic deformation; I, indentation mark; M, median crack; L, lateral crack [3, 4].

during unloading. The lateral cracks initially appear just before unloading of the indenter due to the residual stress on the applied stress and then extend during further unloading to free surface eventually (Figure 5.1c).

We can learn from the static indentation processes that: (a) plastic deformation does happen when the normal load acting on the indenter is small, even for a brittle material; and then (b) with increasing normal load, material fractures and cracks come out beneath and on the material surface. During this processes, the initiation load when material starts fracturing is named the critical load. In other words, this initiation load is the maximum normal load when complete plastic deformation happens during the indentation processes. The indentation depth corresponding with critical normal load is called as critical indentation depth.

Research [5] indicates that the initiation load for median crack, p_c, is given by

$$p_c = \alpha \cdot K_{IC}^4 / H_w^3 \tag{5.1}$$

where, α is a nondimensional proportionality coefficient, $\alpha = (1.0 \sim 1.6) \times 10^4$; K_{IC} is the material fracture toughness,unit $MPa \cdot m^{1/2}$; and H_w is material hardness, unit MPa.

And the initiation load for lateral crack, p_l, is given by

$$p_l = \zeta \cdot f\left(E_w / H_w\right)\left(K_{IC}^4 / H_w^3\right) \tag{5.2}$$

where, ζ is a nondimensional proportionality coefficient; E_w is the Young's modulus of material, unit MPa; and $f(E_w/H_w)$ is an attenuation coefficient of fused silica and relative to material hardness and Youngs modulus. For fused silica [5], $\zeta \cdot f(E_w/H_w)$ is around 2×10^5.

Therefore, the initiation load is relative to the material's mechanical properties, such as

hardness, Young's modulus and fracture toughness. Median cracks and lateral cracks do not happen when the load (p) acting on fused silica surface satisfies the following conditions:

$$\begin{cases} p < p_c \\ p < p_l \end{cases} \tag{5.3}$$

or

$$p < p_{\text{crit}} = \min\{p_c, p_l\} \tag{5.4}$$

In order to obtain the critical indentation depth (d_{crit}), which is the minimum indentation depth to cause brittle fracture, Moore and King [6] also drew a conclusion that it depends on the material hardness (H_w). Lawn et al. [7, 8] utilised Griffith's theory [1] and gave the equation that

$$d_{\text{crit}} \propto \left(E_w / H_w\right)\left(K_{IC} / H_w\right)^2 \tag{5.5}$$

When the ratio of fracture toughness to hardness is high or a small load is applied on each abrasive particle, the indentation depth could be smaller than the critical value. In this case, the material removal mechanism is plastic deformation rather than brittle fracture. Bifano [9, 10] gave the following quantitative equation for the critical indentation depth,

$$d_{\text{crit}} = 0.15\left(E_w / H_w\right)\left(K_{IC} / H_w\right)^2 \tag{5.6}$$

The mechanical properties of fused silica have been obtained by nanoindentation test.

1. Hardness and Young's Modulus

To get the hardness (H_w) and Young's modulus (E_w) of the fused silica substrate, nanoindentation tests were conducted on the CSM nanoindentation instrument. The

Berkovich indenter was used in these tests. The fused silica surface was polished after a CMP process and its initial roughness was around Ra 1-2 nm. The testing process and indenter are shown in Figure 5.2.

The obtained hardness and Youngs modulus are shown in Table 5.1. Notice that when to calculate the Young's modulus, the Poisson ratio is 0.17 [11]. The average hardness (H_w) and Young's modulus (E_w), which are 9.16 GPa and 69.4 GPa, respectively.

Table 5.1 Hardness and Young's modulus

#	Penetration depth (nm)	Hardness, H_w (GPa)	Young's modulus, E_w(GPa)
1	21.9	10.1	75.7
2	25.9	9.94	72.3
3	30.2	9.10	69.5
4	35.5	8.30	65.9
5	40.7	8.35	63.7
Average		9.16	69.4

2. Fracture toughness

Figure 5.3 is the photo of a Vickers indentation fracture mark obtained using the CSM indentation instrument. The properties shown in Table 5.2 were obtained by the test, so the fracture toughness for tested fused silica is 1.564 $\mathrm{MPa}\cdot\sqrt{\mathrm{m}}$.

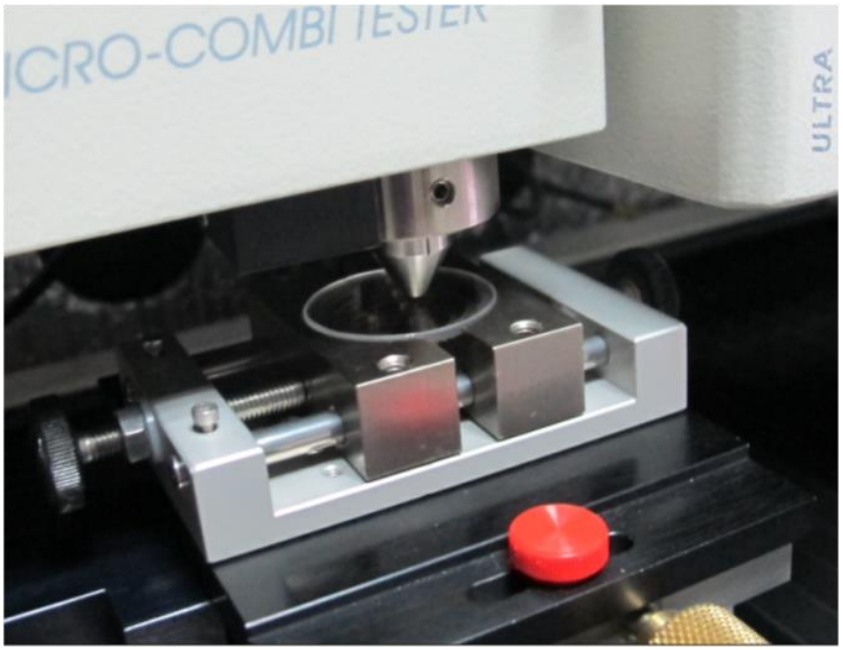

(a) Nanoindentation test

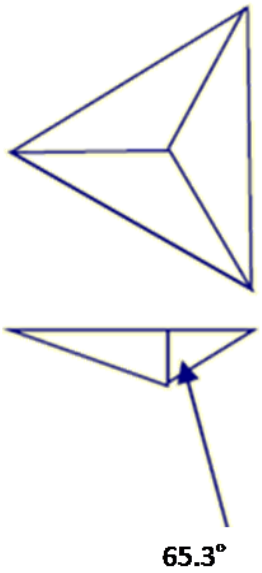

(b) Berkovich indenter

Figure 5.2 Photograph of nanoindentation test and Berkovich indenter

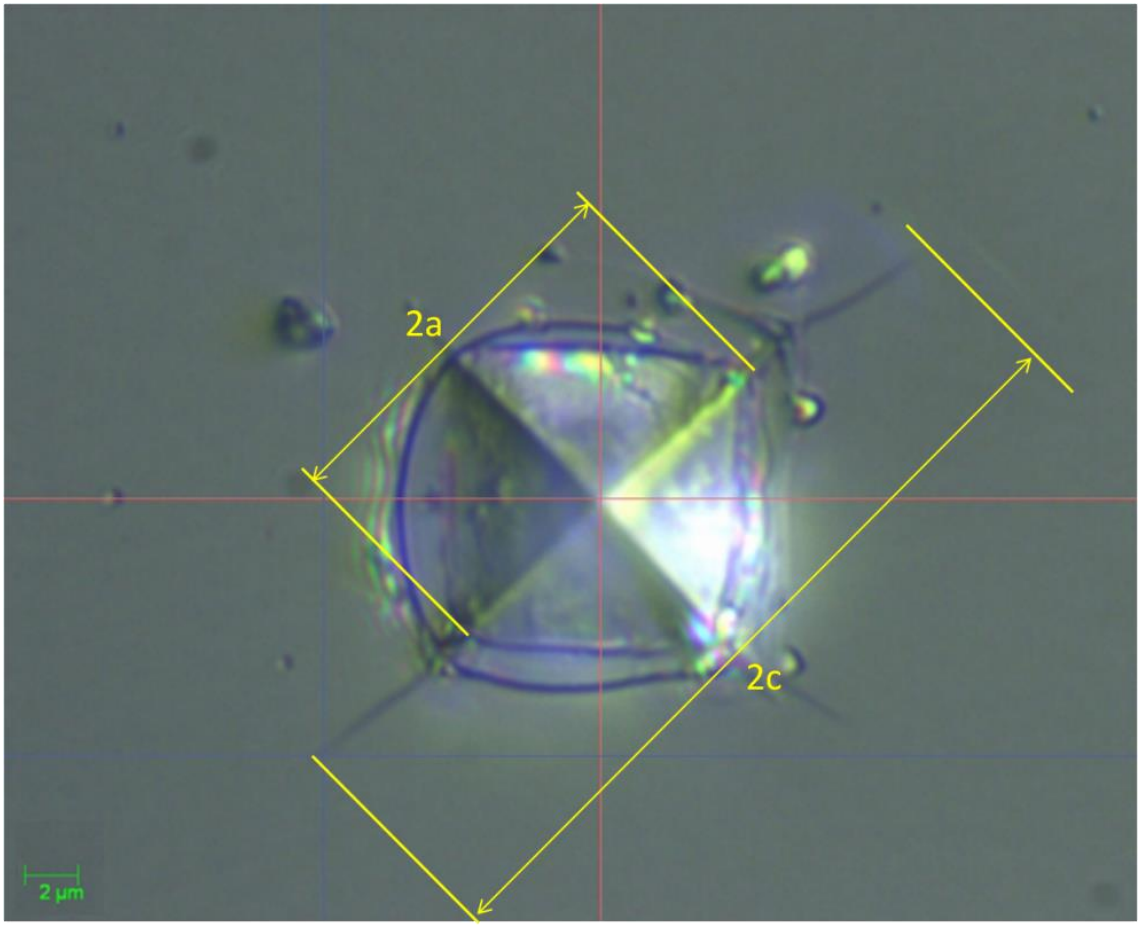

Figure 5.3 Photo of a Vickers indentation mark

Table 5.2 Properties obtained by Vickers indentation tests

#	P (N)	Hardness, H_w (GPa)	Young's modulus, E_w (GPa)	c (μm)	Fracture toughness, K_{IC} ($\mathrm{MPa}\cdot\sqrt{\mathrm{m}}$)
1	1.520	10.777	64.924	11.02	1.631
2	1.526	10.616	67.114	11.48	1.578
3	1.524	10.872	68.200	11.93	1.483
Average					1.564

Since the mechanical properties (i.e. $H_w = 9.16\mathrm{GPa}$, $E_w = 69.4\mathrm{GPa}$, and $K_{IC} = 1.564\ \mathrm{MPa}\cdot\sqrt{\mathrm{m}}$) of fused silica were obtained, we calculate p_c, p_l, p_{crit} and d_{crit} by Equations (5.4) and (5.6), and get

$$p_{\mathrm{crit}} = p_c = \alpha \cdot K_{IC}^4 / H_w^3 \approx 0.078\mathrm{N} \tag{5.7}$$

$$p_l = \zeta \cdot f\left(E_w / H_w\right)\left(K_{IC}^4 / H_w^3\right) \approx 0.156\mathrm{N} \tag{5.8}$$

$$p_{\mathrm{crit}} = \min\left\{P_c, P_l\right\} = 0.078\mathrm{N} \tag{5.9}$$

$$d_{\mathrm{crit}} = 0.15\left(E_w / H_w\right)\left(K_{IC} / H_w\right)^2 \approx 33\mathrm{nm} \tag{5.10}$$

Therefore we get the theoretical conditions that fused silica is removed by only plastic deformation. These conditions are given by

$$\begin{cases} p < p_{\mathrm{crit}} = 0.078\mathrm{N} \\ d < d_{\mathrm{crit}} \approx 33\mathrm{nm} \end{cases} \tag{5.11}$$

where d is the indentation depth by polishing particle in the MRF processes.

5.1.2 Factors influencing the MRF process

Concluding from general abrasive machining processes, Evans et al. [12] gave a basic premise that all lapping and polishing processes can be represented as a four-component system. The four-component system consists of work-piece, carrier fluid, abrasive particles, and polishing tool. Figure 5.4 illustrates the four-component system.

Evans also believed that material removal mechanisms involved in lapping and polishing can be obtained by understanding the four basic components and the interaction among them. Therefore, we suppose that the MRF processes all rely on interactions between the basic elements in the MRF contact zone, though the processes involve different and complex technologies.

The MRF process is a complex polishing method, and MR fluid, substrate materials and process parameters are factors affecting the material removal in this process [13, 14]. Figure 5.5 shows these main factors and their interactions.

1. Substrate materials

Mechanical properties (elastic Young's modulus, hardness and fracture toughness) of different substrate materials are variable due to their different compositions and crystal structure. In addition, different substrate materials differ in chemical stability and bond strength.

2. MR fluid

MR fluid is composed with magnetic carbonyl iron (CI) particles, nonmagnetic abrasive particles, base liquid and surfactants. The variable types and concentrations of components of MR fluid lead to variable viscosity, pH value, shear stress, etc. Interactions between the substrate and MR fluid could change the mechanical and

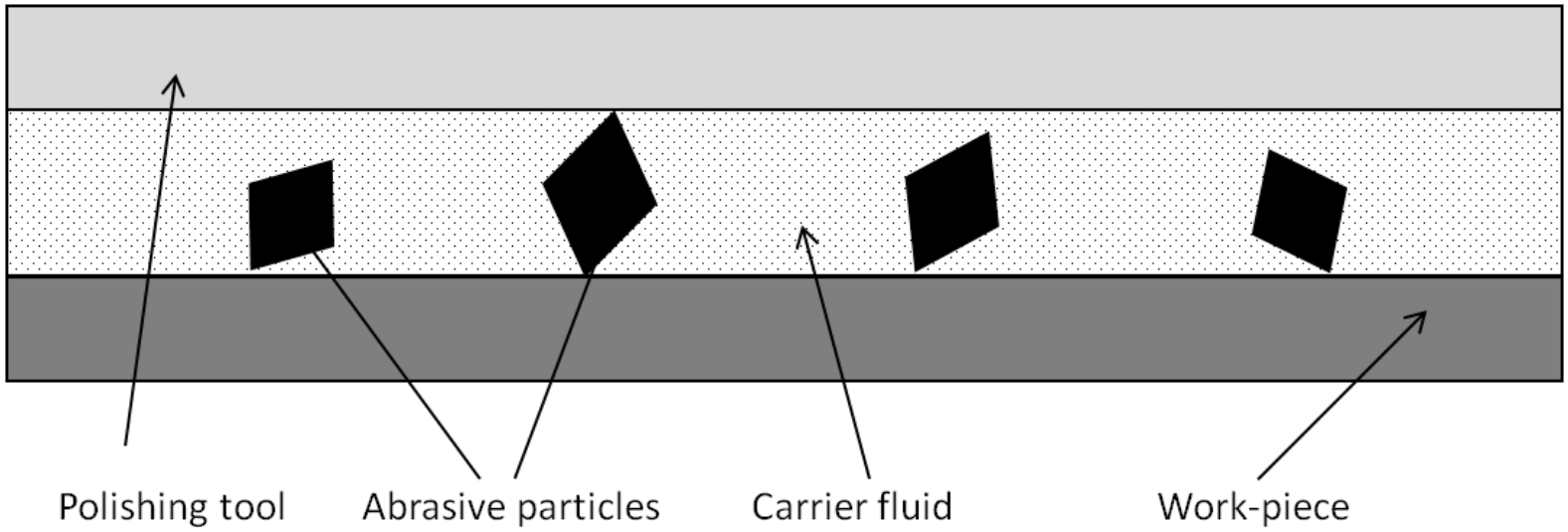

Figure 5.4 Four-component system model for lapping process

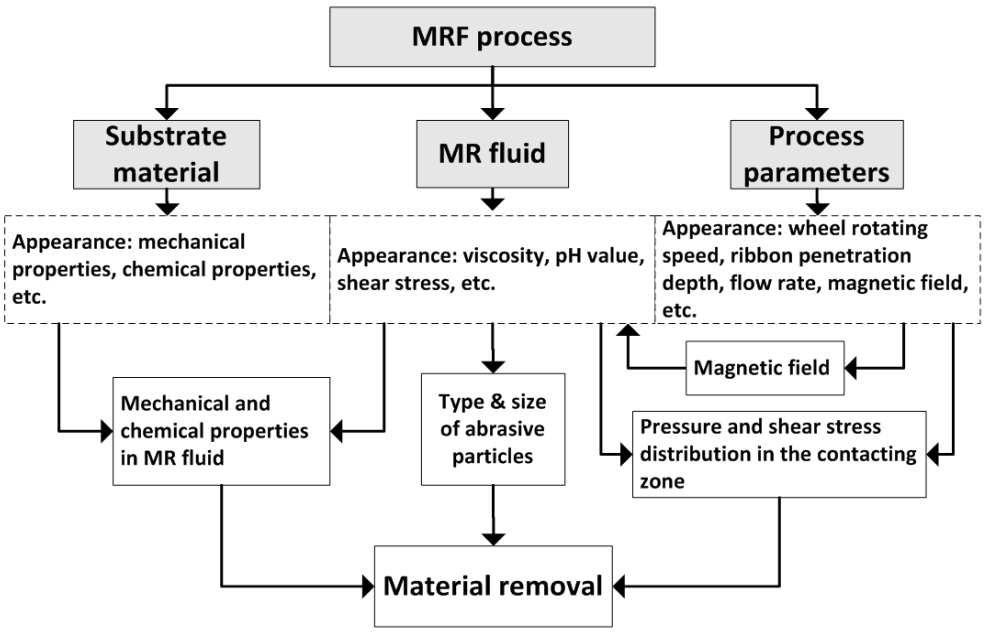

Figure 5.5 Factors affecting MRF processes

chemical properties of the substrate.

3. Process parameters

Typical process parameters in the MRF processes are wheel rotating speed, gap between wheel and work-piece surface or MR fluid ribbon penetration thickness, flow rate, and magnetic field. MR fluid behaves differently in the presence of an external magnetic field, and pressure and shear stress distributions of MR fluid in the contacting zone are also affected by process parameters.

5.1.3 Force analyses on a single abrasive particle

DeGroote et al.[15] compared the material removal with abrasive-free MR fluid and that with nanodiamond as abrasive particles, and concluded that nanodiamond MR fluid enabled an increase in the efficiency of removal significantly and achieved lower surface roughness. As the nonmagnetic abrasive particles play a significant role in the MRF processes, we consider nonmagnetic abrasive particles rather than CI particles to analyse the mechanisms of material removal in the MRF processes.

Based on the ideas from Evans and DeGroote we mentioned above, we should consider the interactions among work-piece, carrier medium of MR fluid, abrasive particles in MR fluid, and polishing wheel, to understand the mechanisms of material removal in the MRF processes.

To analyse the mechanical action, the following assumptions are adopted in this section:

1. The magnetic buoyancy force can be neglected.

The magnetic buoyancy force, applied on the nonmagnetic abrasive particles, is ignored. Saito[16] supposed that a buoyant force on the abrasive particles in presence

of magnetic field does exist. The force is proportional to the gradient in the magnetic field and is given by

$$\frac{F_z}{V} = \left(\rho_f - \rho_a\right) g - \frac{M \cdot \nabla H}{4\pi} \tag{5.12}$$

Where F_z is buoyant force, V is volume of abrasive particle, ρ_f is mass density of MR fluid, ρ_a is mass density of abrasive particle, g is acceleration due to gravity, M is ferric induction of magnetic fluid, ∇H is gradient in the magnetic field.

Peng [17] calculated the magnetic buoyancy using Equation (5.12) and result showed that it is too small (around 10^{-9} N) to affect fracturing material.

2. Centrifugal force can also be neglected.

Centrifugal force acting on a nonmagnetic abrasive particle is also negligible. In fact in the MR fluid ribbon on the fringe of a rotating wheel, abrasive particles are also affected by the centrifugal force which from the wheel to the outside of the ribbon surface. The centrifugal force is given by

$$F_{CEN} = \rho_a \frac{4\pi r_a^{\,3}}{3}\left(\frac{2\pi n_{wheel}}{60}\right)^2 R_{wheel} \tag{5.13}$$

where ρ_a and r_a are mass density and mean radius of the abrasive particle, respectively; n is wheel rotating speed (unit: r/min), R_{wheel} is the radius of polishing wheel. For a ceria (with mass density is 6.65 kg/m^3) particle of radius of 0.5 μm, given n_{wheel} is 150 r/min and R_{wheel} is 200 mm, then the centrifugal force is about 1.1X10^{-14} N, which is also too small to impose on the material removal process.

Shorey [13], DeGroote [14], and Shi [18] believed that the work-piece material is removed by the shear force rather than normal force in the MRF processes. Moreover, comparing with lapping processes, Shi provided a model for the MRF

process. The lapping model and MRF model are shown in Figure 5.6.

Unlike a lapping process, in which the pad transfers the load to abrasive particles between the pad and work-piece, a soft polishing film exists between the polishing wheel and the work-piece. Therefore, the force acting on the abrasive particle can be divided into two parts: normal force F_N, and tangential shear force F_S.

Figure 5.7 shows images of diamond and ceria particles of different diameters acquired by a scanning electron microscope (SEM, HITACHI S-4800, Japan). Figure 5.7 illustrates that abrasive particles at micron level have sharp cutting edges, which should be noted because it is close to the penetration depth which abrasive particles impress on the work-piece surface. Therefore, the two following assumptions are adopted in this section:

1. All abrasive particles are assumed to be spherical in shape with an average diameter when considering the force imposed on abrasive particles by the MR fluid ribbon.

2. When analysing the abrasive particles impressed on the work-piece surface, the cutting edge radius of the particles should be considered.

Following these two assumptions, a dual-edge radius model [18, 19] is induced in this work. The model is shown in Figure 5.8, in which x_1 is the diameter of an abrasive particle adopted for analysing the interaction between the MR fluid polishing tool and abrasive particle, while x_2 is diameter for interaction between the abrasive particle and work-piece surface; δ_p and $\delta_w$are depths for an abrasive particle penetrating into MR fluid polishing tool and work-piece, respectively; r_p and r_w are radii of indentation area on MR fluid polishing tool and work-piece, respectively.

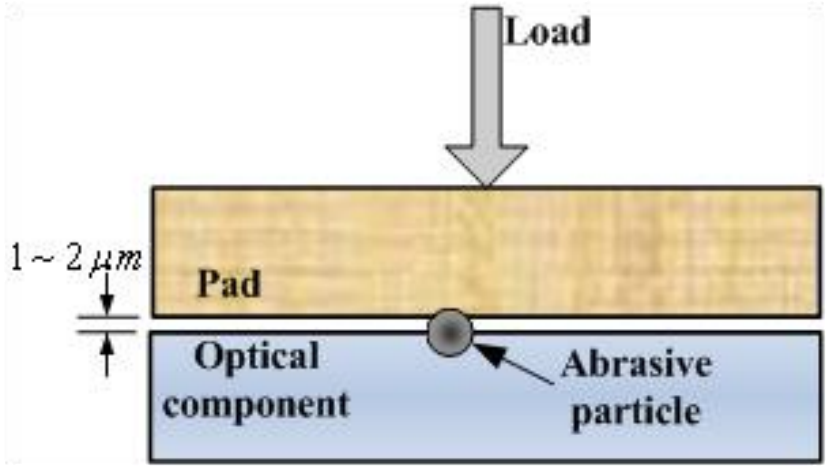

(a) Lapping process

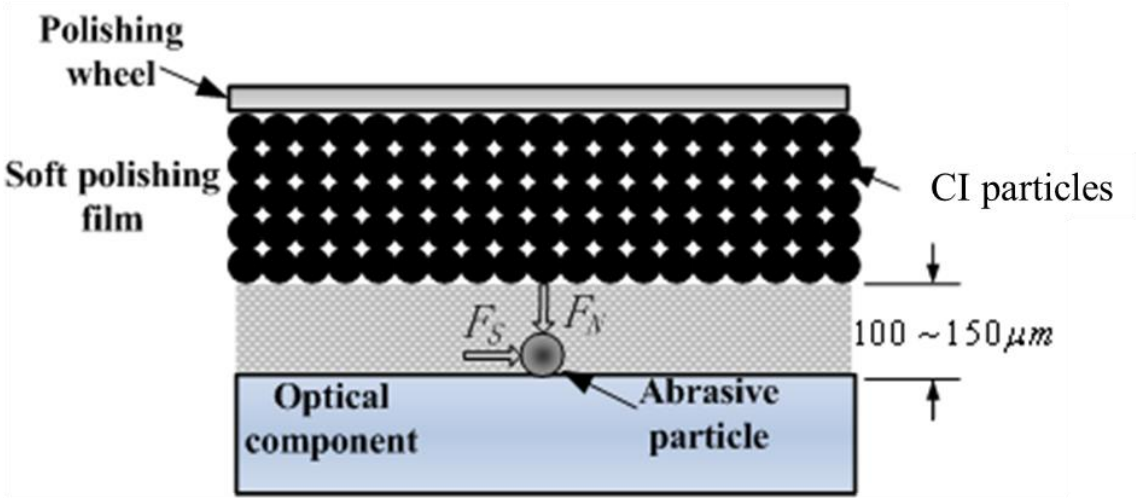

(b) MRF process

Figure 5.6 Models of lapping process and MRF process after Shi [18]

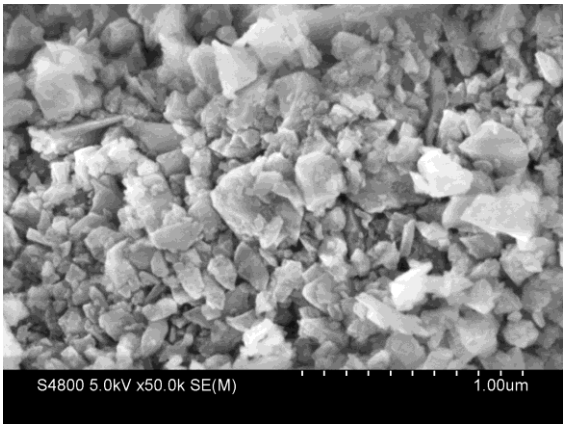

(a) Diamond particles (nominal diameter: 500 nm)

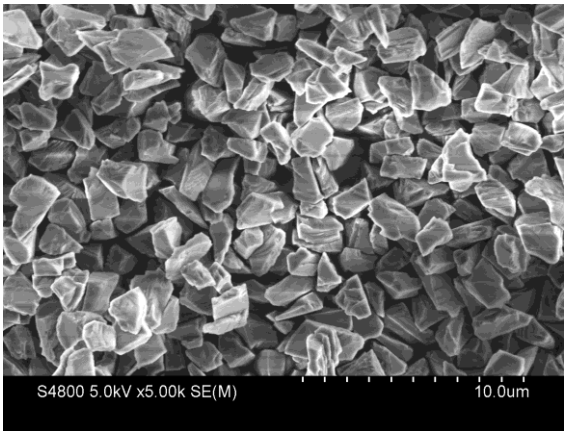

(b) Diamond particles (nominal diameter: 2.5 µm)

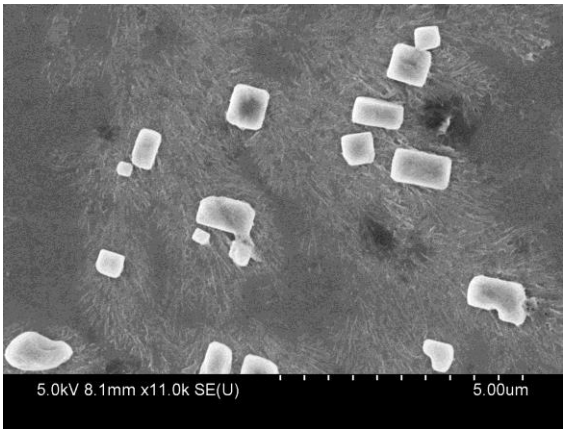

(c) Ceria particles (nominal diameter: 0.5 µm)

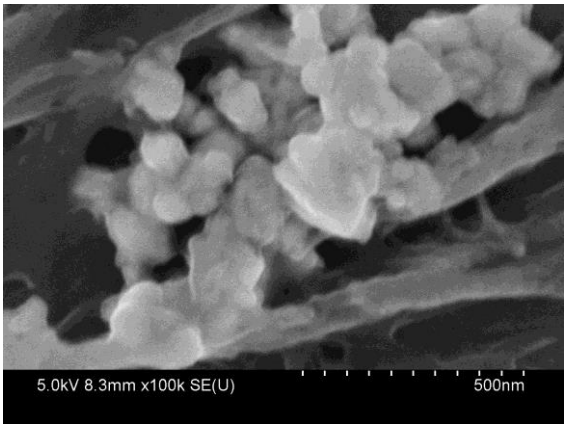

(d) Ceria particles (nominal diameter: 100 nm)

Figure 5.7 Images of different abrasive particles acquired by SEM

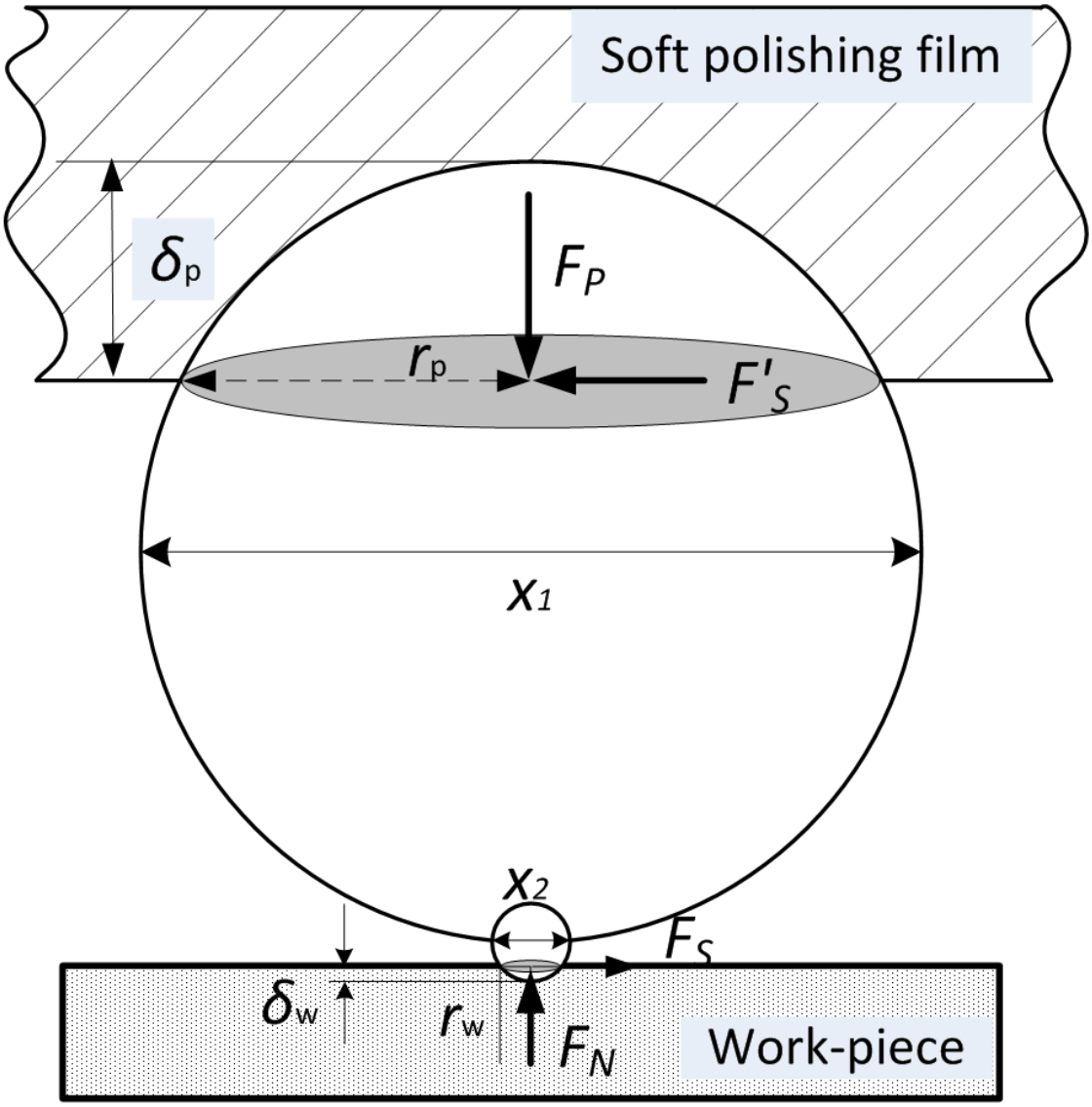

Figure 5.8 Dual-edge radius model for abrasive particle

According to Figure 5.8, it can also be obtained that

$$\begin{cases} F_p = \pi r_p^2 P \\ F_N = \pi r_w^2 H_w \end{cases} \tag{5.14}$$

and

$$F_N = F_P \tag{5.15}$$

where, F_P and F_N are the normal load on abrasive particles imposed from the soft polishing film and work-piece, respectively. P is the normal pressure from the soft polishing film.

It also can be obtained by geometry that,

$$x_2 - \sqrt{x_2^2 - r_w^2} = \delta_w \tag{5.16}$$

After transforming Equation (5.16), the following equation can be derived,

$$r_w^2 \approx 2x_2\delta_w \tag{5.17}$$

Because the MR fluid ribbon is such a soft polishing film, it is believed that [18]

$$x_1 = 2r_p \tag{5.18}$$

Therefore, Equation (5.14) can be modified to

$$\begin{cases} F_p = \dfrac{1}{4}\pi x_1^2 P \\ F_N = \dfrac{1}{2}\pi x_2 \delta_w H_w \end{cases} \tag{5.19}$$

Therefore, the indentation depth δ_w can be obtained by combining Equation (5.15) and Equation (5.19) and given by

$$\delta_w = \frac{p x_1^2}{2 H_w x_2} \tag{5.20}$$

Kang [19] supposed that the effective edge diameter for an abrasive acting on a work-piece, x_2, is given by

$$x_2 = (0.02 \sim 0.05)\, x_1 \tag{5.21}$$

And Shi [18] calculated the normal pressure distribution of the MR fluid between polishing wheel and work-piece surface and gave the maximum value as 159.8 KPa. For a fused silica work-piece, its hardness is 9.16 GPa. Hence, the maximum normal load and indentation depth can be calculated via Equation (5.19) to Equation (5.21), and given by

$$\begin{aligned} F_{N,\max} &= \frac{1}{4}\pi \times (0.5\times 10^{-6})^2 \times 159.8\times 10^3 = 3.14\times 10^{-8}\,\mathrm{N} \\ \delta_{w,\max} &= \frac{159.8\times 10^3 \times (0.5\times 10^{-6})^2}{2\times 9.16\times 10^9 \times 0.02\times 0.5\times 10^{-6}} = 0.22\mathrm{nm} \end{aligned} \tag{5.22}$$

Compared Equation (5.22) with Equation (5.11), it is obviously that the maximum normal load and indentation depth are both far less than the critical values. Therefore, it is believed the MRF process is a non-fracture polishing method.

From the aforementioned analyses, the MRF process is believed to be a non-fracture polishing method. Therefore some experiments are conducted in this section to verify the MRF process is able to remove surface structural defects and does not create new structure defects simultaneously.

5.2 Effect of rogue particles in the MRF process

As discussed in Chapter 4, in the conventional polishing process surface scratches are created by large rogue particles (such as dust or glass debris which are much bigger

than the polishing particles and involved in the polishing process due to poorly maintained polishing conditions and environment) because the loads applied on large particles are greater than the critical load which induces fracture. In this section, the effect of rogue particles in MRF process is investigated by experiments.

5.2.1 Experiment design

A fused silica (Heraeus, Germany) surface with size 45mm x 45mm was prepared by conventional CMP method. Nominal size of the polishing particles used in the CMP process is 1µm and its size distribution was measured by CILAS particle size analyser. The measured result is illustrated in Figure 5.9. Diameter distributions, at 10%, 50%, and 90%, are 0.28µm, 0.99µm, and 2.40µm, respectively.

Then the prepared surface was divided into two parts: A) it was polished by normal MRF process subsequently; and B) it was polished by the MRF process also, but some rogue large particles were added in the MR fluid. The designed surface is demonstrated in Figure 5.10.

1. MR fluid for normal MRF process

Ceria particles were used in the normal MRF process and the nominal size of the ceria particles was 0.5 µm. However, the measured size was smaller and the distributions are 0.07µm, 0.16µm, and 0.39 µm at 10%, 50%, and 90%, respectively. The result of polishing particle size is shown in Figure 5.11. In MR fluid, CI particles are the other important particles even though it is believed to be drawn to polishing wheel and not involved in the material removal process [15]. The size distribution of CI particles is indicated in Figure 5.12, and they at 10%, 50%, and 90%, are 2.51µm, 5.65µm, and 11.33µm, respectively. Figure 5.13 demonstrates the size distribution of all particles of MR fluid.

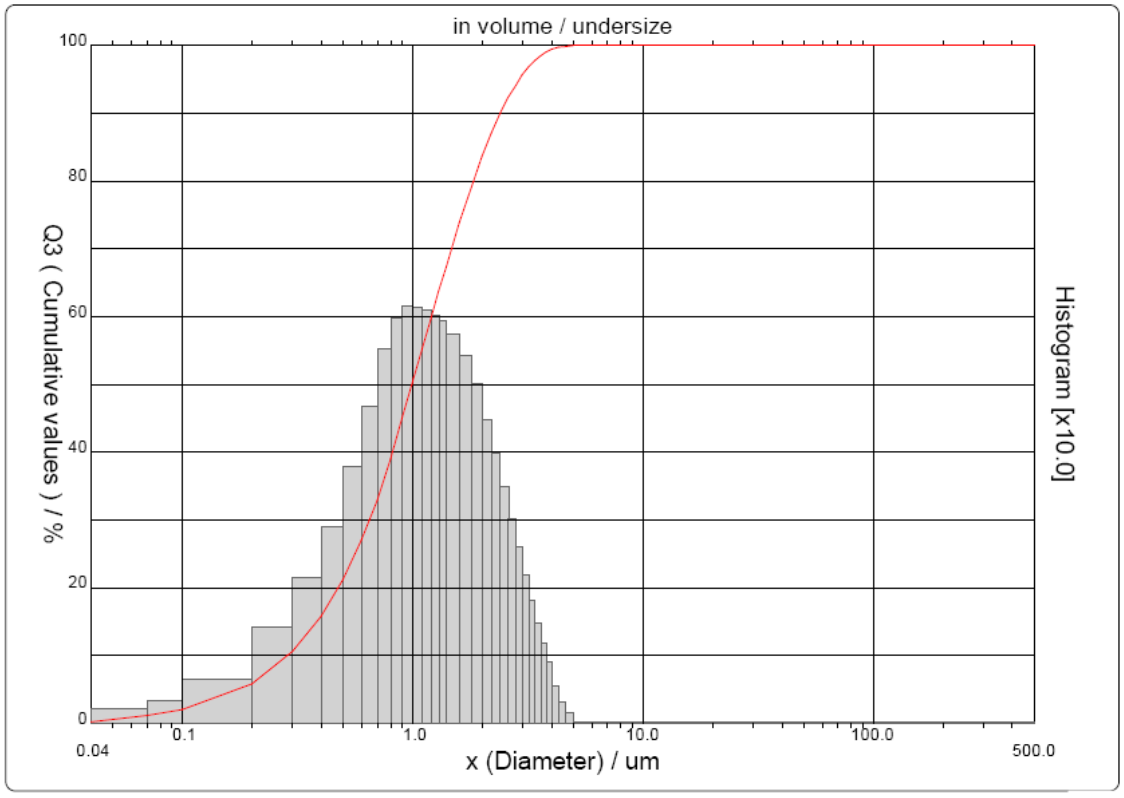

Figure 5.9 Polishing particle size used in CMP process

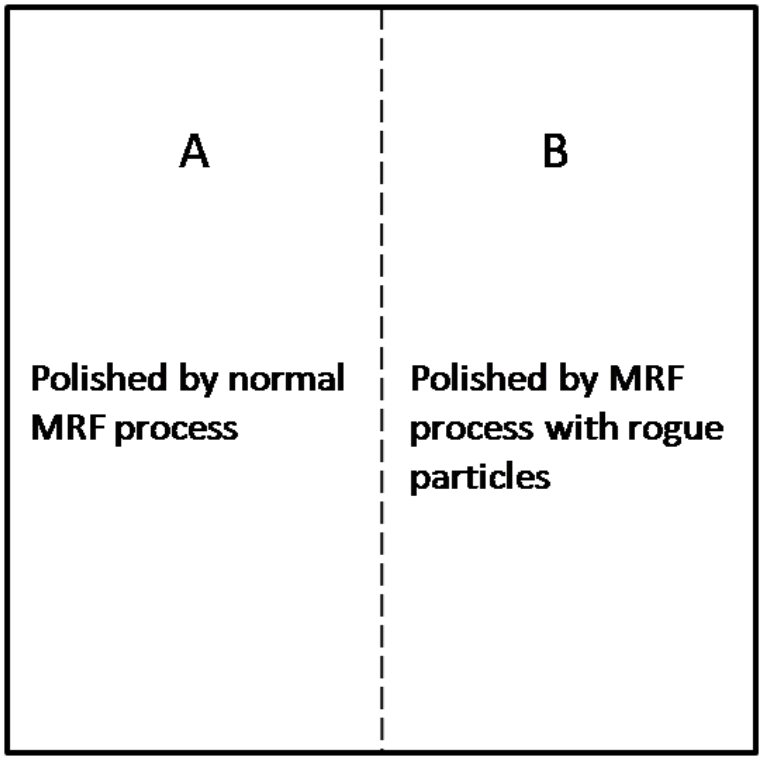

Figure 5.10 Surface designing in the experiment

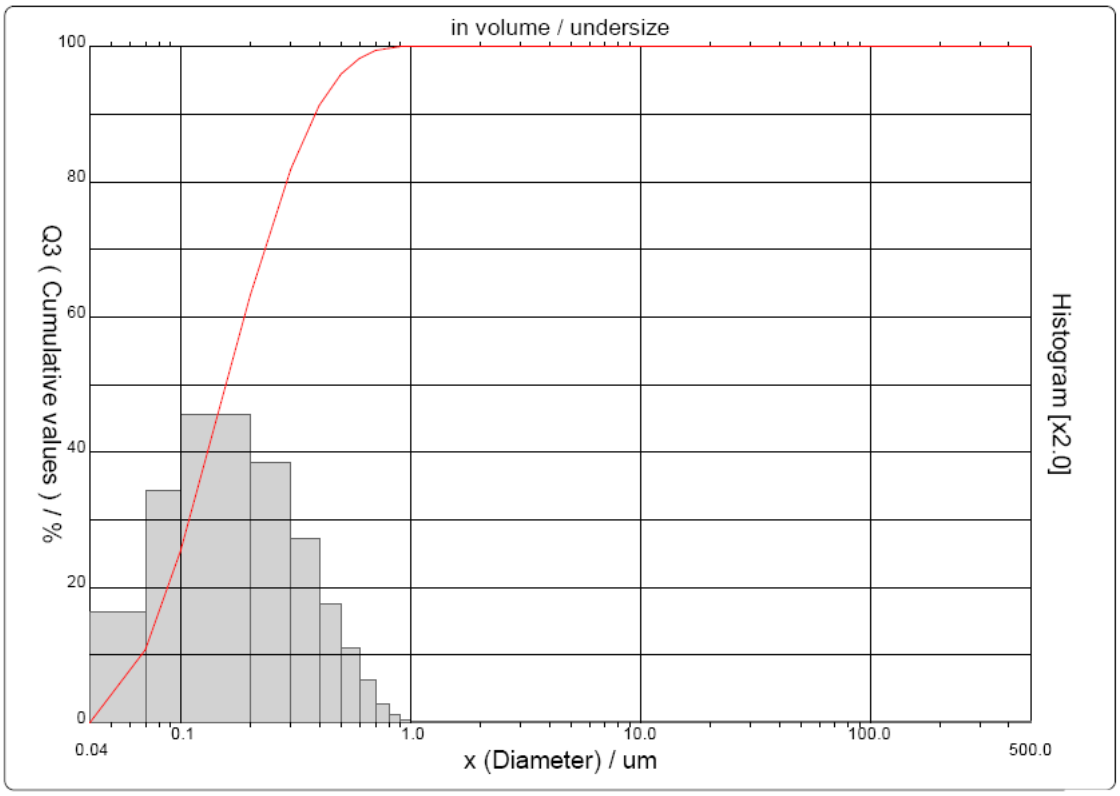

Figure 5.11 Size distribution of polishing particles used in normal MR fluid

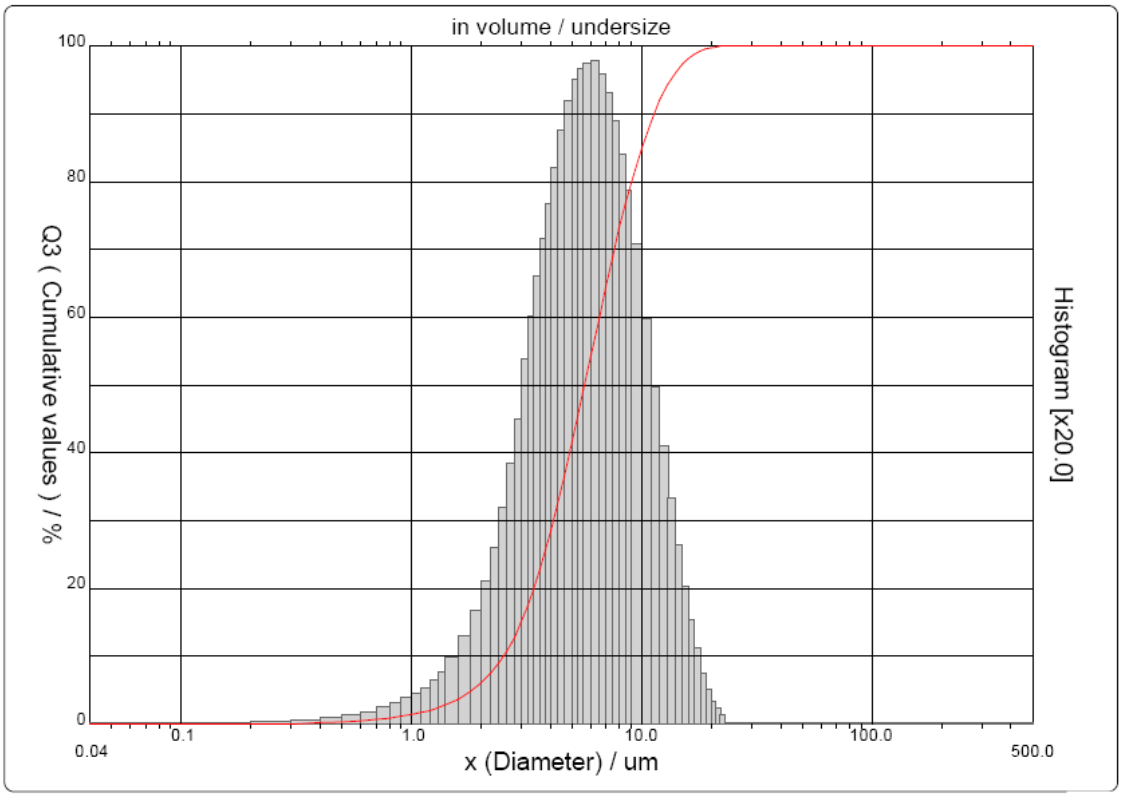

Figure 5.12 Size distribution of CI particlesused in MR fluid

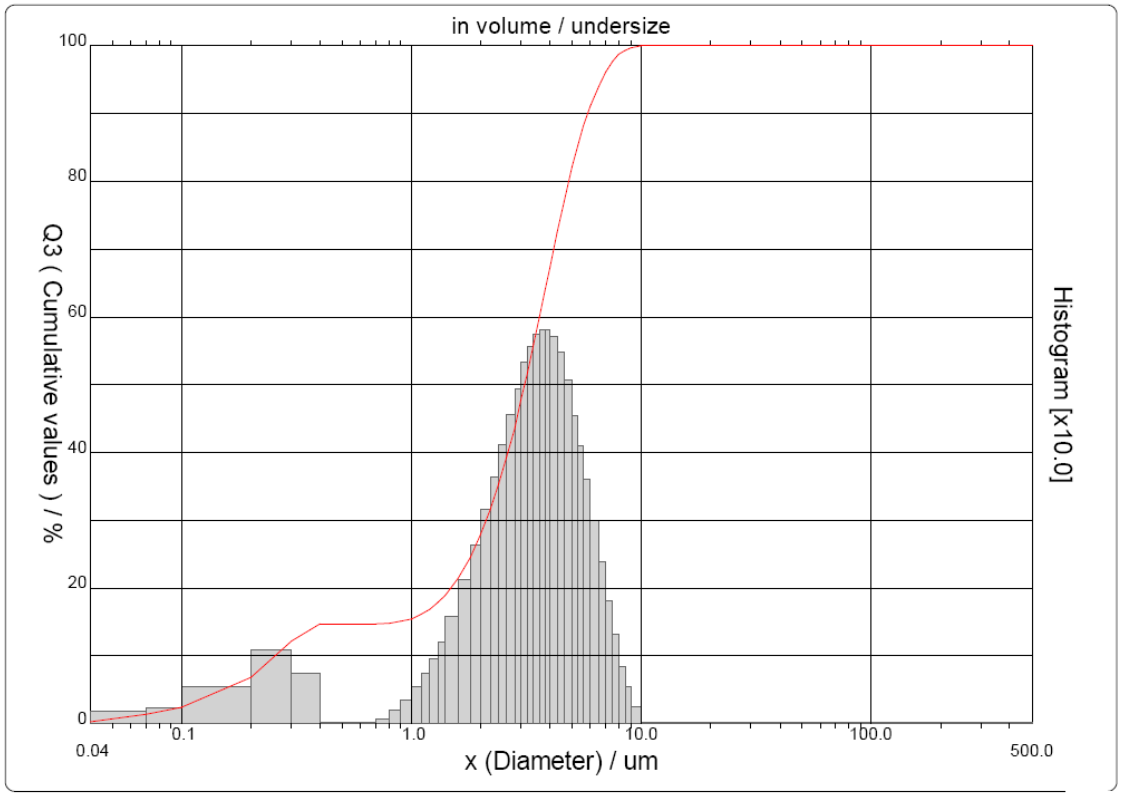

Figure 5.13 All particles size distribution of MR fluid

2. MR fluid with rogue particles

Surface section B was polished by the MRF process with rogue particles, which were SiC particles in this experiment. The nominal size of the SiC particles is 20μm, which is much larger than the ceria particles and CI particles used in the MR fluid. The measured result is shown in Figure 5.14, where the size distributions at 10%, 50% and 90% are 12.56 μm, 22.15 μm and 38.05 μm, respectively.

For confidential reason, the concentration of ceria particles and CI particles in the original MR fluid is unclear. In this experiment, 64g SiC particles (with diameter of 20 μm) were added into 600ml. MR fluid. Size distribution of the new MR fluid with rogue SiC particles was also measured, but the result (shown in Figure 5.15) did not show the rogue SiC particles because of their low concentration in the new polishing fluid.

3. Polishing parameters

The original surface was prepared by CMP under the following conditions (Table 5.3).

Table 5.3 Conditions of surface preparation

Item	**Value**
Pad material	Pitch
Polishing particles	Ceria
Particle size (μm)	1
Normal pressure (Pa)	5×10^4
Orbital speed (r/min)	55
Swing speed (cyc/min)	20
Polishing duration (min)	30

In the experiments, CMP prepared surface was cleaned by deionized water at ultrasonic frequency of 40 kHz; and then polished by two MRF processes with two different MR fluids, and the polishing parameters are shown in Table 5.4.

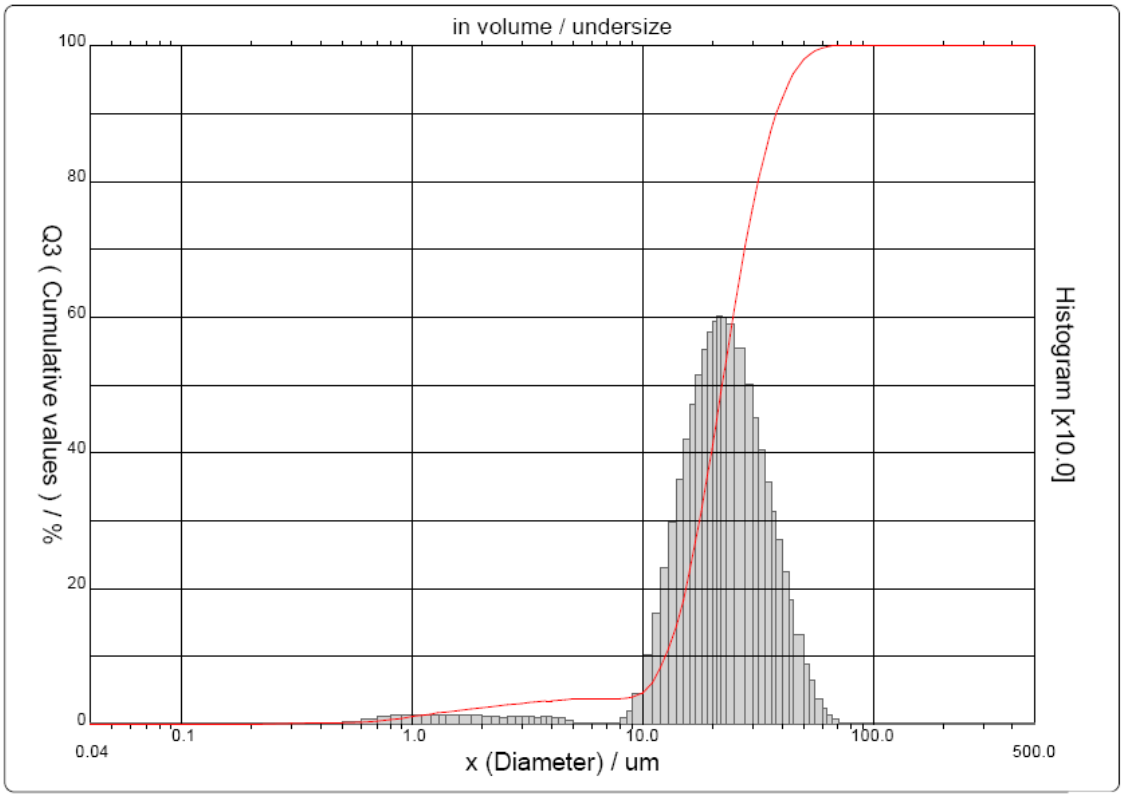

Figure 5.14 Size distribution of large particles

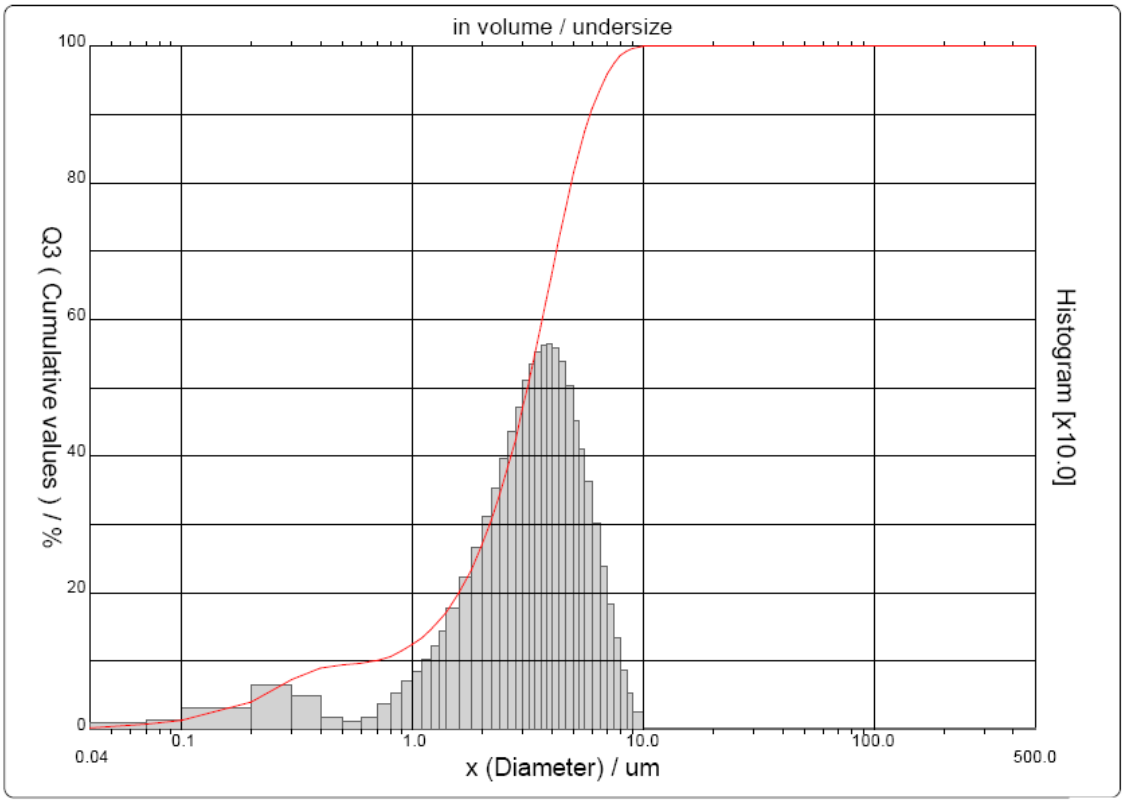

Figure 5.15 Size distribution of new MR fluid with rogue SiC particles

Table 5.4 Conditions of surface polished by MRF processes

Item	MRF process#1	MRF process#2
Rogue particles	None	SiC
Rogue particle size (μm)	N/A	≈20
Polishing particles	CeO_2	CeO_2
Polishing particle size (μm)	≈0.2	≈0.2
Nominal size of CI particles (μm)	≈5	≈5
Wheel speed ($\mathrm{r/min}$)	150	150
Ribbon penetration depth (mm)	0.20	0.20
Flow rate (L/min)	120	120
Current (A)	7.0	7.0
Polishing duration per unit area (s/mm^2)	0.36	0.36
Viscosity ($\mathrm{Pa \cdot s}$)	197	197

5.2.2 Experiment results

The original surface was prepared by conventional CMP method and its surface topography is illustrated in Figure 5.16. And the topographic pictures of surface section polished by normal MRF process and MRF with rogue SiC particles are shown in Figure 5.17 and Figure 5.18. These figures were all acquired by SWLI (Zygo NewView 700s). Roughness of original surface is Ra 0.472 nm and RMS 0.611 nm. For a normal MRF process, the roughness of polished surface section is Ra 0.505 nm and RMS 0.623 nm; and for surface section polished by MRF process with SiC particles, the roughness is Ra 0.571 nm and RMS 0.726 nm. Both surface roughness produced by the MRF processes with and without rogue particles are slightly worse than that prepared by the CMP process.

More surface features were taken by digital microscope (KEYENCE VHX-600E), and are shown in Figure 5.19.

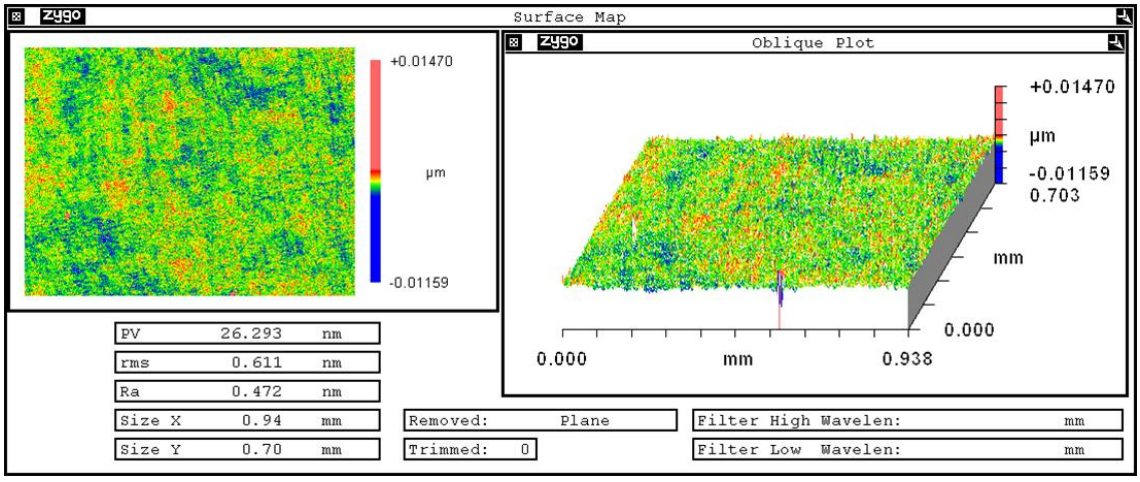

Figure 5.16 Original surface polished by conventional CMP method and measured using a SWLI (Zygo NewView 700s)

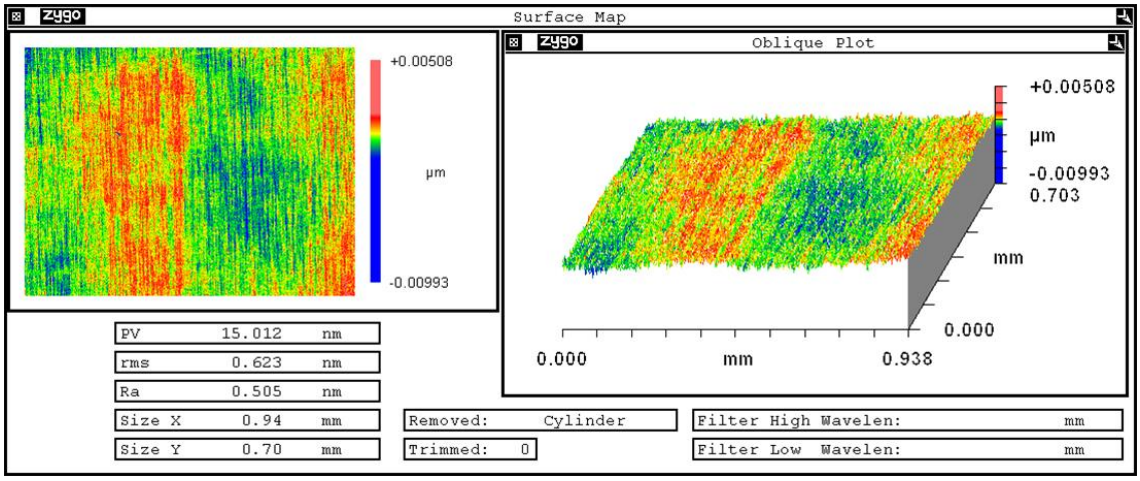

Figure 5.17 Surface polished by MRF method without rogue particles and measured using a SWLI (Zygo NewView 700s)

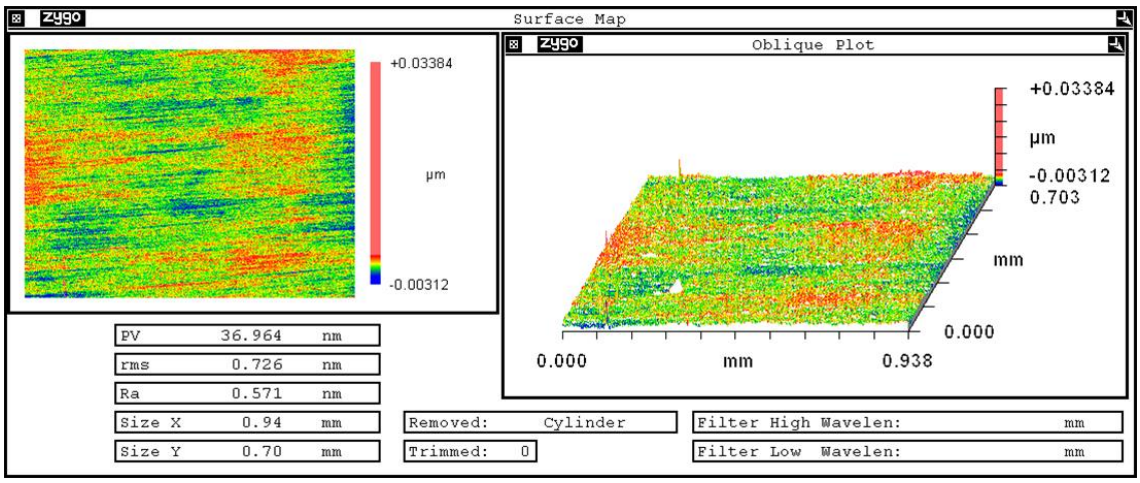

Figure 5.18 Surface polished by MRF method with rogue particles and measured using a SWLI (Zygo NewView 700s)

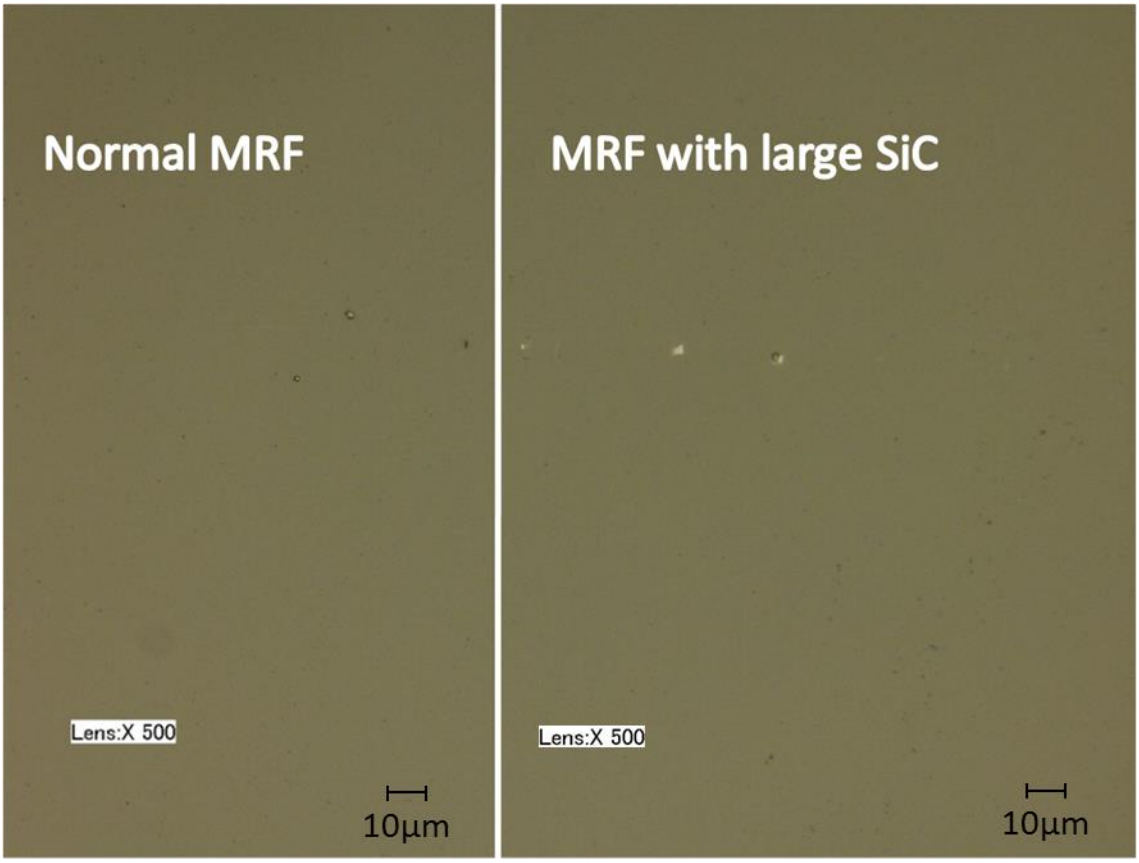

Figure 5.19 Photos of surfaces polished by two different MRF processes, acquired by digital microscope (KEYENCE VHX-600E)

5.2.3 Discussions

1. Comparing with Figure 5.17 and Figure 5.18, roughness of surface polished by MRF process with rogue SiC particles was slightly worse than that of surface polished by normal MRF. However, this little worse is light enough (surface roughness were lower than Ra 0.6 nm and RMS 0.8 nm) and is acceptable. More research on the surface roughness will be in Chapter 6.

2. From Figure 5.19 it could be seen that there was no clear difference between two surface sections and clearly no scratch was generated by MRF processes no matter which MR fluid was used.

5.3 Optical window specimen polished by MRF process

Due to the aforementioned non-fracture polishing mechanisms of the MRF processes, it is believed that no surface/sub-surface damage is created in the MRF processes. In this section, experiments were conducted to investigate the surface/sub-surface damage in the MRF processes.

5.3.1 Experiment design

Two optical window specimens, which were made of Heraeus fused silica with size of 100×100×10 mm^3 for each, were used to verify the damage-removal ability of the MRF process. Both the two specimens were prepared by same conventional polishing method.

To obtain the sub-surface damage of the specimens after the conventional polishing process, the first specimen was etched by HF (5 wt%, 40℃) for 5 minutes to remove the redeposition layer.

Then the second specimen was polished by the MRF process. The experimental

settings are shown in Table 5.5. Both front and back surfaces of this specimen were polished in a line-by-line scanning way.

Table 5.5 MRF process parameters (including the magnetic field setting)

Item	Level
Rotating Speed (r/min)	130
Flow Rate (L/min)	140
Current (A)	7.0
Penetration Depth (mm)	0.20
Viscosity of MR fluid (Pa · s)	197
Abrasive particles	CeO_2
Polishing particle size (μm)	0.2
Scanning speed (mm/min)	300
Scan-line distance (mm)	0.5

Polished after MRF process, the second specimen was also subjected to the same HF (5 wt%, 40°C) etching.

5.3.2 Result and discussions

The first specimen after HF etching is shown in Figure 5.20a, and the second specimen after HF etching process is shown in Figure 5.20b. From Figure 5.20 it can be seen that there were a lot of scratches on the first specimen surface while only few scratches were left on the second specimen surface after MRF process.

Comparing Figure 5.20b with Figure 5.20a, it can be found that surface and sub-surface damage on surfaces of fused silica specimen could be removed by the MRF process effectively. This is possibly because the MRF is a non-fracture polishing method and not sensitive to the unexpected rogue particles. Therefore, it does not create any surface/sub-surface damage during the MRF process.

(a) First fused silica specimen (without MRF process). Size: 100mm×100mm

(b) Second fused silica specimen (with MRF process). Size: 100mm×100mm

Figure 5.20 Photos of etched fused silica specimens without and with MRF process

In fact, for the rogue SiC particles in the MR fluid, according to the Equations (5.19) to Equations (5.21), the maximum normal load and indentation depth can be obtained by

$$\begin{aligned} F_{N,\max} &= \frac{1}{4}\pi \times (20\times 10^{-6})^2 \times 159.8\times 10^3 = 5.02\times 10^{-5}\,\mathrm{N} \\ \delta_{w,\max} &= \frac{159.8\times 10^3 \times (20\times 10^{-6})^2}{2\times 9.16\times 10^9 \times 0.02\times 20\times 10^{-6}} = 8.69\mathrm{nm} \end{aligned} \tag{5.23}$$

Compared Equation (5.23) with Equation (5.11), it proves that the maximum load and indentation depth for rogue SiC particles are also less than the critical values. Therefore it is really still a non-fracture polishing method for the MRF with unexpected rogue SiC particles.

5.4 Summary

MRF process was used in this chapter mainly to remove the surface and /or sub-surface damage on the fused silica surfaces. The work is listed as follows,

1. Non-fracture polishing conditions were analysed based on the static indentation process. Then the normal force imposed on a single polishing particle was calculated. The force showed that the MRF process is a polishing process without creation of fractures.

2. Experimental study was performed to investigate the effect of large rogue abrasive particles in the MRF process. The result indicated that rough particles in the MRF process did not really affect the finished surface quality.

3. Finally, two fused silica optical specimens were used to investigate the effect of the MRF process on removing the surface/sub-surface damage. The results showed that surface/subsurface damage on fused silica optical surface could be removed by the MRF process. Therefore the MRF process could be an effective method to remove the surface/subsurface damage on fused silica surface.

References

1. Suh, N.P., "Tribophysics". 1 ed. 1986, New Jersey: Prentice-Hall, Inc.

2. Wang, J.J. and Y. Liao, "Critical Depth of Cut and Specific Cutting Energy of a Microscribing Process for Hard and Brittle Materials". *Journal of Engineering Materials and Technology-Transactions of the Asme*, 2008. **130**: pp. 011002-1-011002-6.

3. Lawn, B.R. and M.V. Swain, "Review Indentation Fracture: principles and applications". *Journal of Materials Science*, 1975. **10**: pp. 1049-1081.

4. Samuals, L.E., "Metallographic Polishing by Mechanical Methods (4th Edition)". 2003, Ohio: ASM International.

5. Lee, T.C. and C.W. Chan, "Mechanism of the ultrasonic machining of ceramic composites". *Materials Process Technology*, 1997. **71**(2): pp. 195-201.

6. Moore, M.A. and F.S. King, "Abrasive wear of brittle solids". *Wear*, 1980. **60**: pp. 123-140.

7. Marshall, D.B. and B.R. Lawn, "Indentaion of Brittle Materials". *Journal of Microindentation Technology in Materials Science and Engineering*, 1986: pp. 26-46.

8. Lawn, B.R., T. Jensen and A. Arora, "Brittleness as Indentation Size Effect". *Journal of Material Science*, 1976. **11**: pp. 199-205.

9. Bifano, T.G., T.A. Dow and R.O. Scattergood, "Ductile-Regime Grinding: A New Technology for Machining Brittle Materials". *Journal of Engineering for Industry*, 1991. **113**: pp. 184-189.

10. Bifano, T.G., T.A. Dow and R.O. Scattergood. "Ductile-regime grinding of brittle materials: Experimental results and the developement of a model". in *Proceeding of SPIE*. 1988. **996**: pp. 108-115

11. "Fused Silica, SiO_2 Glass Properties". [Online]; Available from: http://www.accuratus.com/fused.html.

12. Evans, C.J., E. Paul, D. Dornfeld, D.A. Lucca, G. Byrne, M. Tricard, F. Klocke, O. Dambon and B.A. Mullany, "Material Removal Mechanisms in Lapping and Polishing". *CIRP Annals - Manufacturing Technology*, 2003. **52**(2): pp. 611-633.

13. Shorey, A.B., "Mechanisms of material removal in magnetorheological finishing (MRF) of glass" [PhD Thesis]. New York: University of Rochester; 2000.

14. DeGroote, J.E., "Surface interactions between nanodiamonds and glass in magnetorheological finishing (MRF)" [PhD Thesis]. New York: University of Rochester; 2007.

15. DeGroote, J.E., A.E. Marino, J.P. Wilson, A.L. Bishop and S.D. Jacobs. "The role of nanodiamonds in the polishing zone during magnetorheological finishing (MRF)". in *Proceeding of SPIE*. 2007. **6671**: pp. 66710Z-1 - 66710Z-15

16. Saito, Y., H. Niikura, T. Oshio and T. Hanaoka. "Floating polishing using magnetic fluid with abrasive grains". in *Proceddings of the 6th international conference on production engineering*. 1987. Osaka. pp. 335-340

17. Peng, X., "Study on the Key Techniques of Deterministic Magnetorheological Finishing" [PhD Thesis]. Changsha: National Universtiy of Defense Technology; 2004.

18. Shi, F., "Study on the Key Techniques of Magnetorheological Finishing for High-precision Optical Surfaces" [PhD Thesis]: National University of Defense

Technology; 2009.

19. Kang, N., "Study on the Material removal Mechanism and Technique in Ultra-precision Fabrication of Silicon Carbide Reflecting Mirror" [PhD Thesis]. Changsha, China: National University of Defense Technology; 2009.

CHAPTER 6

ROLE OF SURFACE ROUGHNESS ON THE LIDT

6.1 Effect of MRF machined surface roughness on LIDT

As mentioned in Chapter 2, the LIDT of optical surfaces related to the surface roughness is given by an empirical relation that[1]

$$E_{th}\sigma^{m} = \text{Constant} \tag{6.1}$$

where E_{th} is the corresponding electric field of damage threshold, the σ is the root mean square (RMS) roughness of optical surface, the exponent m and constant C are various for different surface treatments and surface materials.

Equation (6.1) provides a dependence of breakdown electric field on surface roughness for given conditions (same optical material and same finishing processes). It should be noted that the LIDT is proportional to the square of damage threshold electric field, E_{th}^{2}. Therefore Equation (6.1) can be rewrite as

$$LIDT * \sigma^{k} = \text{Constant}' \tag{6.2}$$

And the following relation can be obtained

$$k = 2m \tag{6.3}$$

The effect of the surface roughness on the LIDT for optical components finished by the same processes was investigated by the following experiments. The material of samples is fused silica (Yaohua, China), and all samples were polished by MRF process

to various tolerances with different polishing parameters and then etched in 5 % volume percent hydrofluoric acid (HF) for 10 min (at 40°C). The surface quality was good and very few visible impurities were observed under the dark-field conditions. The LIDT of these samples were tested using 355 nm wavelength laser beams. More laser details were introduced in Chapter 3 and the Appendix B. The LIDT and surface roughness are listed in Table 6.1 and plotted in Figure 6.1. Figure 6.1 plots the logarithm of RMS roughness of sample surfaces against the logarithm of LIDT. In this chapter, the roughness was measured by a scanning white light interferometer (SWLI) of Zygo NewView 700s with 10x optical lens. The sample distance is 1.46535μm, and the scanning area is 937.82×703.37 μm^2.

Table 6.1 LIDT and surface roughness for fused silica components after MRF process and HF etching

Sample #	Roughness RMS (nm)	Log(RMS)	LIDT(mJ/cm^2)	Log (LIDT)	Processes
#73	0.381±0.019	$-0.419^{+0.021}_{-0.022}$	34.40±1.56	$1.537^{+0.019}_{-0.020}$	MRF+HF
#70	0.677±0.009	$-0.170^{+0.006}_{-0.006}$	31.26±1.50	$1.495^{+0.020}_{0.021}$	MRF+HF
#37	1.736±0.308	$0.239^{+0.071}_{-0.085}$	30.28±1.52	$1.481^{0.021}_{0.022}$	MRF+HF
#35	2.247±0.210	$0.352^{+0.039}_{-0.043}$	29.99±1.40	$1.477^{0.020}_{0.021}$	MRF+HF
#23	3.732±0.452	$0.572^{+0.050}_{-0.056}$	27.66±1.46	$1.442^{0.022}_{0.024}$	MRF+HF

Table 6.2 Settings of the MRF process for each sample

Sample #	Rotating Speed (r/min)	Flow Rate (L/min)	Current (A)	PenetrationDepth (mm)	Viscosity ($\mathbf{Pa \cdot s}$)	Abrasives
#73	120	180	8.5	0.30	197	0.5μm CeO_2
#70	140	160	8.0	0.25	197	0.5μm CeO_2
#37	160	140	7.0	0.20	197	0.5μm CeO_2
#35	180	120	6.0	0.15	197	0.5μm CeO_2
#23	200	100	5.0	0.10	197	0.5μm CeO_2

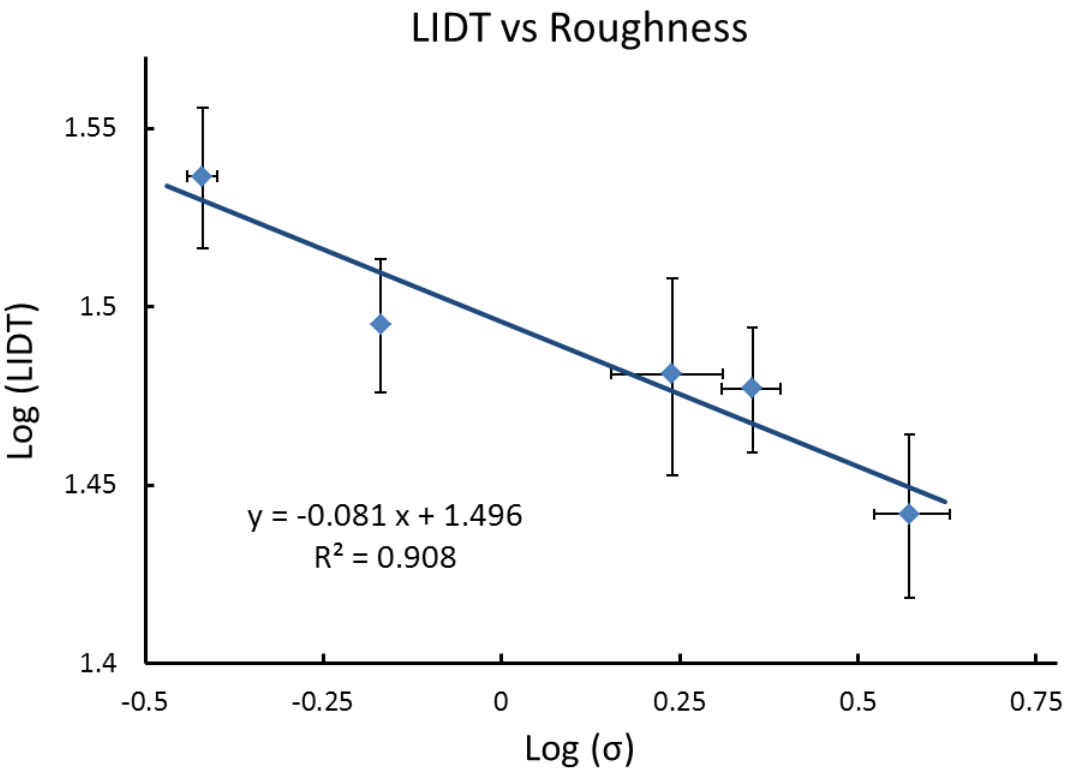

Figure 6.1 Measured LIDT versus surface roughness

In Table 6.1, the surface RMS roughness of each sample was measured at 9 different positions. The experimental settings of the MRF process used for each sample are shown in Table 6.2.

Figure 6.1 shows experimentally that for a series of optical components which are made of same material and finished by same processes, lower roughness could result in a higher LIDT. Figure 6.1 also illustrates that the data points and their regression analysis. Each data is well fitted with the straight line. The linear equation for the log-log data is given by

$$\log(LIDT) = -0.081 * \log(\sigma) + 1.496 \tag{6.4}$$

Although individual deviation for each data point does exist, the square of linear correlation coefficient ($R^2 = 0.907$) indicates that the linear regression is reliable. Laser is also electromagnetic wave, therefore Equation (6.4) can be transferred to the form of Equation (6.2) and the following equation is obtained as

$$LIDT * \sigma^{0.081} = 31.30 \tag{6.5}$$

Therefore Equation (6.5) provides experimentally the exponent $k = 0.081$ (the uncertainty is $Err\_k = 0.015$) and the constant $\text{Constant}' = 31.30$.

The exponent 0.081 is far less than House's work [4], of which the exponent is 2×0.5=1 (according to the Equation (6.3)), for lapping processed surface. This difference might be because that the surfaces in this thesis were processed by MRF and HF etching, rather than lapping in House's work.

6.2 MRF-machined surface roughness analyses

Due to the aforementioned discussion, the roughness of optical surface plays an important role in affecting the laser induced damage threshold of optics. Therefore, to

optimise the machining parameters to reduce the roughness of surface polished in the MRF processes, the Taguchi method was used in the experiment design. In addition, a set of designed experiments were performed.

6.2.1 Taguchi method used in experiment design

The Taguchi method is a statistical methods developed by Genichi Taguchi to greatly improve the quality of engineering productivity. Taguchi's Orthogonal Array design provides the method for solving parameter optimisation problem using much shorter time and expense than traditional trial-and-error techniques[2]. In this work, the Taguchi method has been used to optimise the machining parameters to minimise the roughness of surfaces machined in the MRF processes.

Generally in the MRF processes, four variable factors, i.e. polishing wheel rotating speed, MR fluid flow rate, current of electromagnet, and MR fluid ribbon penetration depth, are used to control the polishing quality. As shown in Table 6.3 and Table 6.4, the experiments were conducted using six fixed factor and four variable factors (each has three levels). The original surface texture is shown in Figure 6.2.

Table 6.3 Fixed factors and their levels in experiments

Fixed factors	**Level**
Abrasive particles	CeO_2
Diameter of abrasive particles (μm)	0.5
Viscosity of MR fluid (Pa·s)	197
Work-piece	Fused silica
Polishing time per unit area(s/mm^2)	0.36
Original RMS roughness (nm)	≈0.45±0.25 (9 positions at each sample)

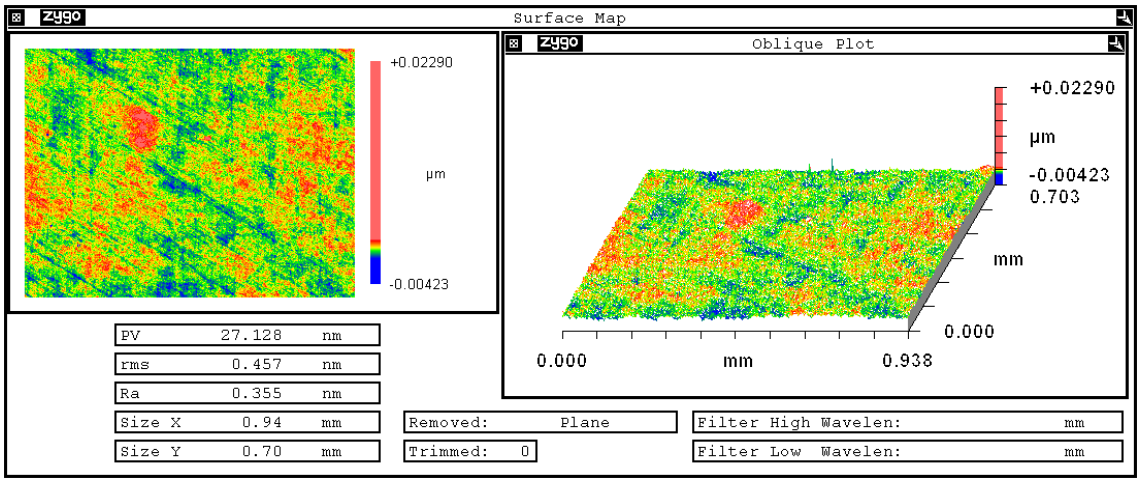

Figure 6.2 Original surface texture in the centre area

Table 6.4 Control factors and their levels in experiments

No.	Control factors	Levels		
		1	2	3
A	Rotating Speed (r/min)	125	150	175
B	Flow Rate (L/min)	120	140	160
C	Current (A)	6.0	7.0	8.0
D	Penetration Depth (mm)	0.10	0.15	0.20

Because the MRF process is a contact polishing method, the roughness results near the edge of optical surface could be worse than that of the centre area. Therefore it is necessary to optimise the surface result of the whole area of optical surface. In order to investigate the variation of surface roughness results for various positions on the surface, signal-to-noise ratio (S/N ratio) is used in the experimental design. In the Taguchi method, the term 'signal' and 'noise' represent the magnitude of the mean of a process and its variation, respectively [3].

As the lower roughness is better for LIDT, loss function (L_{LB}) for objective of the LB (lower is better) is calculated in the following equation

$$L_{LB} = \frac{1}{N}\left(\sum_{i=1}^{n} y_i^2\right) \tag{6.6}$$

where y_i represent the ith measured value in a run; and N denotes the number of measurements in a trial.

The quality characteristic, S/N ratio, of the LB is defined as follows

$$S/N_{ratio} = -10\log\left(L_{LB}\right) \tag{6.7}$$

In order to study the effect of various factors (shown in Table 6.3) and their interactions on the roughness of polished surface, an $L_{27}(3^{13})$ Taguchi orthogonal array was chosen as the experimental design. Table 6.4 indicates the factors to be investigated and the corresponding levels.

To investigate the effect of interactions between factors, the linear graph (shown in Figure 6.3) can be deduced for an $L_{27}(3^{13})$ Taguchi orthogonal array [4]. Figure 6.3 is used for assigning factors to proper columns of the orthogonal array. The first, third, fourth and fifth columns are assigned to rotating speed(factor A), flow rate (factor B), current (factor C), and penetration depth (factor D), respectively. The sixth or seventh column is assigned to the interaction between rotating speed and penetration depth ($A \times D$), the ninth or thirteenth column assigned to the interaction between flow rate and penetration depth ($B \times D$), and the tenth or twelfth column assigned to the interaction between current and penetration depth ($C \times D$).

6.2.2 Results and analyses

The experimental data for surface roughness are given in Table 6.5. The experimental data on surface roughness are measured in 18 different regions on the work-piece surface, and the S/N ratio values calculated by taking Equation (6.7). The analyses for Taguchi method were obtained using the popular statistical software known as Minitab (version 16, Minitab, Inc., USA).

1. Analysis of S/N ratio

Regardless of the type of performance characteristics of a testing process, a greater S/N ratio value is believed to correspond to a better performance. Therefore, the level of a factor with the highest S/N ratio is the optimum level for the responses measured. Figure 6.4 showed the main effects and their interaction plots for S/N ratios. Then the optimal polishing conditions of these control factors could be easily determined from

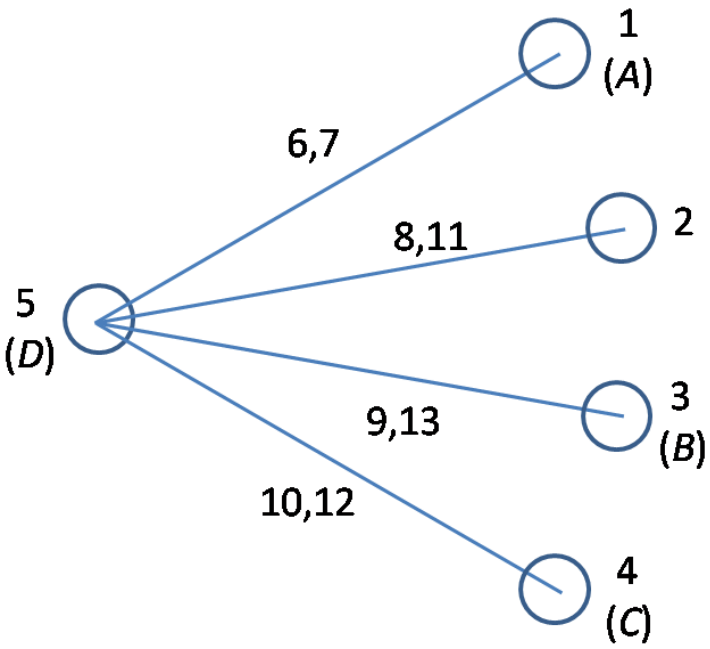

Figure 6.3 Linear graph for L_{27} orthogonal array

Table 6.5 Experimental data

Expt. No.	Factor $\boldsymbol{A}$ Rotating speed (r/min)(Column 1)	Factor $\boldsymbol{B}$ Flow rate (L/min)(Column 3)	Factor $\boldsymbol{C}$ Current (A) (Column 4)	Factor $\boldsymbol{D}$ Penetration depth (mm)(Column 5)	$\boldsymbol{A} \times \boldsymbol{D}$ (Column 6)	$\boldsymbol{B} \times \boldsymbol{D}$ (Column 9)	$\boldsymbol{C} \times \boldsymbol{D}$ (Column 10)	Average surface roughness (nm)	S/N Ratio (dB)
1	125	120	6.0	0.10	1	1	1	0.628	4.035
2	125	120	6.0	0.15	2	2	2	0.632	3.945
3	125	120	6.0	0.20	3	3	3	0.688	3.074
4	125	140	7.0	0.10	1	2	2	0.595	4.483
5	125	140	7.0	0.15	2	3	3	0.691	3.173
6	125	140	7.0	0.20	3	1	1	0.675	3.386
7	125	160	8.0	0.10	1	3	3	0.577	4.721
8	125	160	8.0	0.15	2	1	1	0.636	3.909
9	125	160	8.0	0.20	3	2	2	0.599	4.448
10	150	140	8.0	0.10	2	2	3	0.692	3.149
11	150	140	8.0	0.15	3	3	1	0.608	4.293
12	150	140	8.0	0.20	1	1	2	0.601	4.346
13	150	160	6.0	0.10	2	3	1	0.701	2.892
14	150	160	6.0	0.15	3	1	2	0.686	3.245
15	150	160	6.0	0.20	1	2	3	0.774	2.164

Expt. No.	Factor $\boldsymbol{A}$ Rotating speed (r/min)(Column 1)	Factor $\boldsymbol{B}$ Flow rate (L/min)(Column 3)	Factor $\boldsymbol{C}$ Current (A) (Column 4)	Factor $\boldsymbol{D}$ Penetration depth (mm)(Column 5)	$\boldsymbol{A} \times \boldsymbol{D}$ (Column 6)	$\boldsymbol{B} \times \boldsymbol{D}$ (Column 9)	$\boldsymbol{C} \times \boldsymbol{D}$ (Column 10)	Average surface roughness (nm)	S/N Ratio (dB)
16	150	120	7.0	0.10	2	1	2	0.926	0.645
17	150	120	7.0	0.15	3	2	3	0.823	1.558
18	150	120	7.0	0.20	1	3	1	0.609	4.293
19	175	160	7.0	0.10	3	3	2	0.681	3.279
20	175	160	7.0	0.15	1	1	3	0.677	3.334
21	175	160	7.0	0.20	2	2	1	0.660	3.548
22	175	120	8.0	0.10	3	1	3	0.623	4.060
23	175	120	8.0	0.15	1	2	1	0.780	1.904
24	175	120	8.0	0.20	2	3	2	0.990	-0.473
25	175	140	6.0	0.10	3	2	1	0.999	-0.029
26	175	140	6.0	0.15	1	3	2	0.852	1.304
27	175	140	6.0	0.20	2	1	3	0.700	3.067

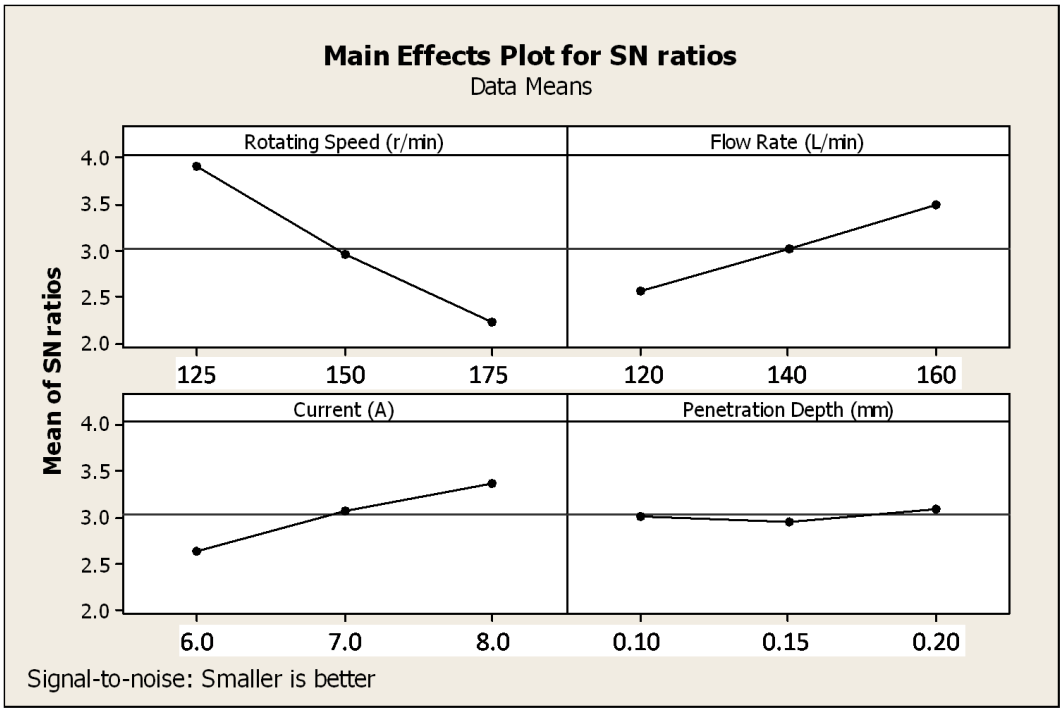

(a) Main effects plot for S/N ratios

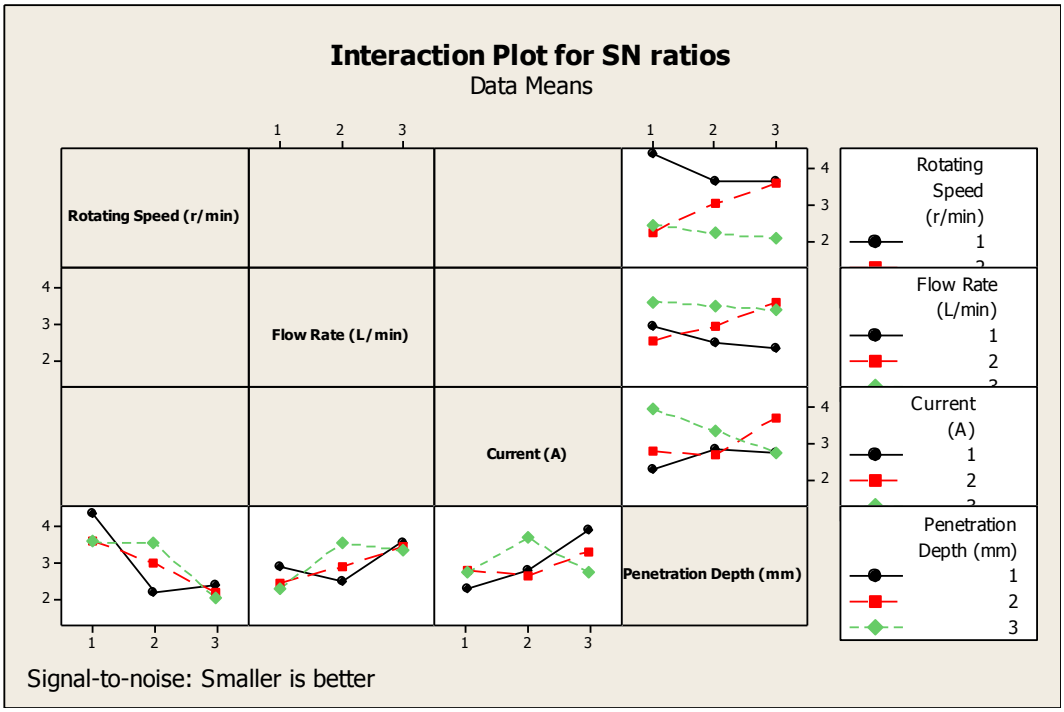

(b) Interaction effects plot for S/N ratios

Figure 6.4 Effect of various factors on roughness

these graphs.

From the S/N ratio analysis in Figure 6.4, the optimal polishing conditions for the roughness in the MRF processes were obtained at 125 r/min rotating speed (level 1), 160 L/min flow rate (level 3), 8.0 A current (level 3), and 0.20mm penetration depth (level 3), respectively. Figure 6.4 also showed that roughness decreases with a decrease in polishing wheel rotating speed, while with increasing in MR fluid flow rate and current through the electromagnet. However, it seems that penetration depth had a slight influence on roughness.

Table 6.6, the response table for S/N ratios, indicates that the factor rotating speed has the strongest influence on surface roughness, followed by flow rate, current, and penetration depth in the order of significance. Therefore an experimental conclusion could be drawn that surfaces with smaller roughness could be machined under the conditions with slower rotating speed and higher flow rate and current.

Table 6.6 Response table for S/N ratios for smaller is better

Level	**Rotating Speed(r/min)**	**Flow Rate(L/min)**	**Current(A)**	**Penetration Depth(mm)**
1	3.908	2.56	2.633	3.026
2	2.954	3.019	3.078	2.963
3	2.222	3.504	3.373	3.095
Delta	1.687	0.944	0.74	0.132
Rank	1	2	3	4

2. ANOVA analysis

ANOVA is a statistical tool for detecting any differences in the average performance of groups of items tested. In this work it was adopted to determine the significant parameters influencing the roughness in the MRF processes. The ANOVA is obtained by dividing the measured sum of the squared deviations from the total mean S/N ratio

into contributions by each of the control factors and the errors.

Table 6.7 shows the summary of ANOVA for S/N ratios. Investigation about the value of variation ratio (F), which is the variance of the factors divided by the error variance for all control factors, showed that a much higher influence of rotating speed while much less influence of penetration depth. The percentage of each factor contribution, P, on the sum of total squared deviations from the total mean S/N ratios, illustrated the degree of influence on the result. From Table 6.7, the rotating speed (51.44%) and flow rate (16.04%) have significant influence on roughness, while penetration depth (0.31%) has nearly no influence on it. The other factor, i.e. current (9.98%) and interactions$A \times D$, $B \times D$, and $C \times D$, have medium influence on roughness.

Table 6.7 Summary of ANOVA of S/N ratios

Source of variation	**DF**	**SS**	**Variance (V)**	**F-ratio (F)**	**P (%)**
A	2	12.8747	6.43734	1.92	51.44%
B	2	4.0143	2.00713	0.6	16.04%
C	2	2.4972	1.24858	0.37	9.98%
D	2	0.0782	0.03911	0.01	0.31%
$A \times D$	4	4.1584	1.0396	0.31	8.31%
$B \times D$	4	2.3609	0.59022	0.18	4.72%
$C \times D$	4	4.6073	1.15182	0.34	9.20%
Error	6	20.1266	3.35444		
Total	26	50.7175			100.00%

DF: degrees of freedom; SS: sum of squares; P: percentage of contribution

3. Confirmation experiment

To verify the optimised processing parameters, i.e. rotation speed at 125 r/min, MR

fluid flow rate at 160 L/min and current through the electromagnet of 8.0 A, a confirmation experiment was conducted on a fused silica surface. Ignoring the influence of penetration depth, 0.20 mm was used in this experiment. The initial surface roughness was 0.473 nm (shown in Figure 6.5) and the mean value after the MRF process was 0.497 nm (shown in Figure 6.6). The surface roughness did not become too much worse and are acceptable..

6.2.3 Discussions

Results show that rotation speed plays the most significant role in surface roughness. MR fluid flow rate and current of electromagnet are also important on the polished surface roughness. This could because the normal pressure and shear stress of MR fluid spot vary with various polishing parameters. Different normal stress and shear stress of MR fluid spot provide various force acted on polishing particles.

Lower rotation speed reduces the speed difference between polishing wheel and work-piece, and this could lower the hydrodynamic pressure of MR fluid.

Greater MR fluid flow rate could increase the height of MR fluid ribbon. When the penetration depth is fixed, greater ribbon height makes larger gap between polishing wheel and work-piece. This also could lower the hydrodynamic pressure of MR fluid,

Greater current of electromagnet could generate a higher magnetic field. In the presence of a higher magnetic field, the height of MR fluid ribbon could be greater. Therefore, similar with the greater MR fluid flow, lower hydrodynamic pressure will occur when the current of electromagnet is greater.

However, it is not clear that why penetration depth is not sensitive to the surface roughness. It is possibly because the variations of penetration depth in the experiments were not big enough.

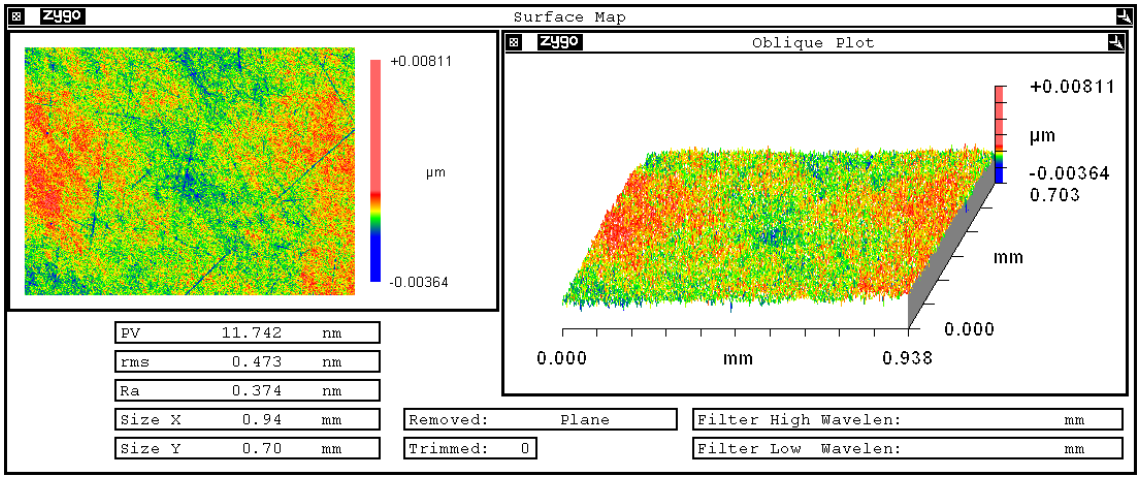

Figure 6.5 Initial surface in the confirmation experiment measured using a SWLI (Zygo NewView 700s)

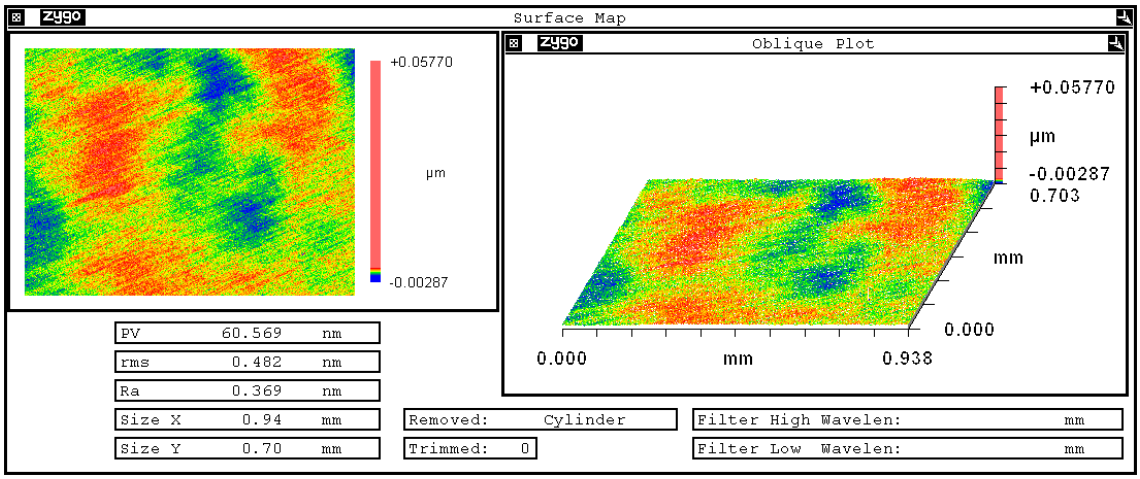

Figure 6.6 Best surface roughness in the confirmation experiment measured using a SWLI (Zygo NewView 700s)

6.2.4 Conclusions

After the experiments in which fused silica specimens were polished in different parameters of control factors (rotating speed, flow rate, current and penetration depth) by the MRF machine. The Taguchi's $L_{27}(3^{13})$ orthogonal array was adopted to determine the optimal level of control factors. From the signal-to-noise (S/N) ratio approach and analysis of variation (ANOVA) results, the following conclusions can be drawn for the MRF processes:

1. Based on the Taguchi's statistically designed experiments, S/N ratio and ANOVA results showed similar conclusions.

2. From the S/N ratio outcomes, a surface with uniformly lower roughness could be machined under the conditions with slower rotating speed and higher flow rate and current.

3. ANOVA results showed that rotating speed had a much higher influence on roughness than other factors and interactions, while penetration depth had much less influence which can be neglected.

4. Current of electromagnet and interactions $A \times D$, $B \times D$, and $C \times D$, had mediate influence on roughness.

6.3 Summary

This chapter mainly focuses on the surface roughness and its role in the laser induced damage threshold and provides the method to improve the surface roughness in the MRF processes. The work in this chapter is given as follow:

1. The effect of MRF machined surface roughness on the LIDT was investigated via experiments. An empirical relation between them was obtained. Results showed

that lower surface roughness could lead to higher LIDT value.

2. By the Taguchi design method, a set of experiments are conducted to investigate the influencing factors on polished surface roughness in the MRF processes.

3. Based on the data analyses via Taguchi S/N ratios method and ANOVA method, the experimental parameters are optimised. The outcomes show that slower rotating speed and higher flow rate and current could induce better surface roughness. The results also illustrate that rotating speed has a much higher influence on roughness than other factors and interactions while penetration depth has much less influence which can be neglected.

4. The result of a confirmation experiment shows surface roughness which is polished in the conditions of optimised parameters can reach a much better value (RMS value less than 0.5 nm) than that of other parameters.

References

1. House II, R.A., J.R. Bettis and A.H. Guenther, "Surface roughness and laser induced damage threshold". *IEEE Journal of Quantum Electronics*, 1977. **QE-13**: pp. 361-363.

2. Tsai, F.C., B.H. Yan, C.Y. Kuan and F.Y. Huang, "A Taguchi and experimental investigation into the optimal processing conditions for the abrasive jet polishing of SKD61 mold steel". *International Journal of Machine Tools & Manufacture*, 2008. **48**: pp. 932-945.

3. Kuram, E., B.T. Simsek, B. Ozcelik, E. Demirbas and S. Askin. "Optimization of the cutting fluids and parameters using Taguchi and ANOVA in milling". in *Proceedings of the World Congress on Engineering*. 2010. London, UK. **2**: pp. 1292-1296

4. Liu, W., "Design of experiments". Texts in Applied Statistics. 2005, Beijing, PR China: Tsinghua University Press.

CHAPTER 7

POST POLISHING TREATMENTS

As mentioned in Chapter 5 and Chapter 6, the fused silica surface can be polished to reduce defects and leave excellent surface finish using the MRF processes. However, it must be realised that the material could be loosened from the surface due to the MR fluid and could form a redeposition layer (Beilby layer) on the surface of the material. This layer may not itself be easily removable, but the presence of contaminants and defects may reduce the LIDT [1]. These contaminants in the Beilby layer are generally induced during the MRF processes.

As CI particles are used in the MRF process and ceria are also used as the abrasive particles, elements Fe and Ce were investigated in this this work. Figure 7.1 and Figure 7.2 show distributions of the elements Fe and Ce in the surface layer, measured by a secondary ion mass spectrometry (SIMS, Model 2100 Trift II TOF-SIMS). The fragment here is the ratio between the ion number for the specific element and total ion number, and can be given by

$$\text{Fragment} = \frac{Specific \quad ion \quad number}{Total \quad ion \quad number} \times 100\% \tag{7.1}$$

The SIMS test results show that below a depth of 14.6nm and 11.7nm, contaminants Fe and Ce are small (as small as those in bulk material) and can probably be neglected.

As Beilby layer creation is a disadvantage when MRF is used to improve the LIDT of fused silica optics, it is necessary to remove this Beilby layer on the optical surface after MRF processing. In this section, two post polishing treatments are used to

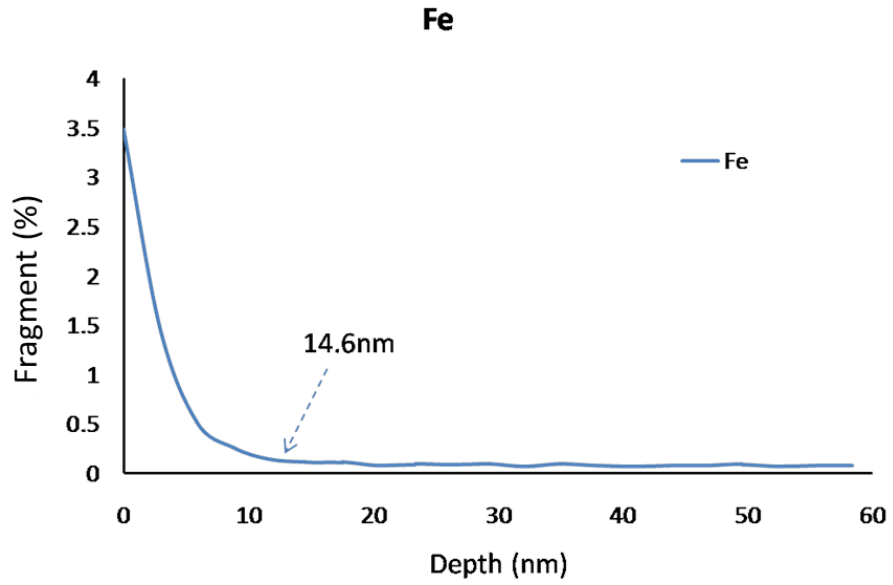

Figure 7.1 Fe distribution against depth of the surface layer after MRF measured by SIMS (Model 2100 Trift II TOF-SIMS)

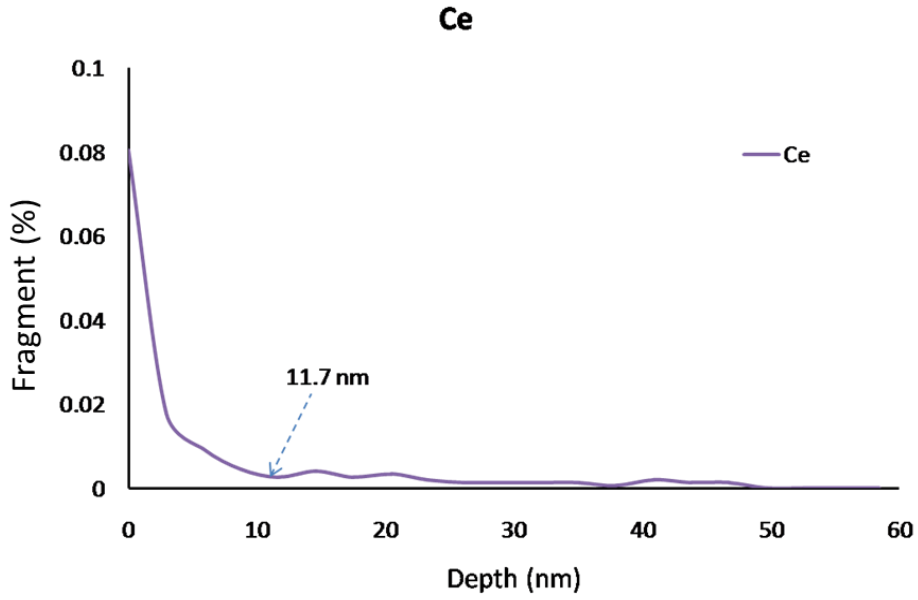

Figure 7.2 Ce distribution against depth of the surface layer after MRF measured by SIMS (Model 2100 Trift II TOF-SIMS)

remove the Beilby layer in order to clean the optical surface back to bulk material level and enhance its LIDT.

7.1 Hydrofluoric (HF)-based etching method

BOE etching treatments were conducted on MRF polished fused silica optics. In these experiments, the frequency of ultrasonic cleaning was 40kHz; the concentrations of HF and NH_4F were 5 wt% and 15 wt%, respectively.

The efficiency of the BOE etching is shown in Figure 7.3. The depth is measured by white light interferometer (Zygo NewView 700s) with 50x optical lens. The details of this measurement are as follows:

1. 10 specimens made of the same fused silica were manufactured by the same processes (CMP + MRF process).

2. An adhesive (Norland Blocking Adhesive 107) was utilised to cover half surface of the specimen. The adhesive, which is sensitive to heat and light, was used to protect the fused silica surfaces during BOE etching and the covered surfaces were used as reference layers.

3. These specimens were then etched in 1 min increments from 1 to 10 mins. The etching temperature is 40 ℃.

4. These specimens were cleaned to remove the adhesive using acetone.

5. The surface height of every specimen was measured using the white light interferometer. A typical output is shown in Figure 7.4.

Figure 7.5 and Figure 7.6 present the SIMS measured results of Fe and Ce elements on the surface layer of MRF polished fused silica optics after BOE etching treatments for 5 minutes (the depth of removed SiO_2 layer was around 100 nm) at temperature 40 ℃.

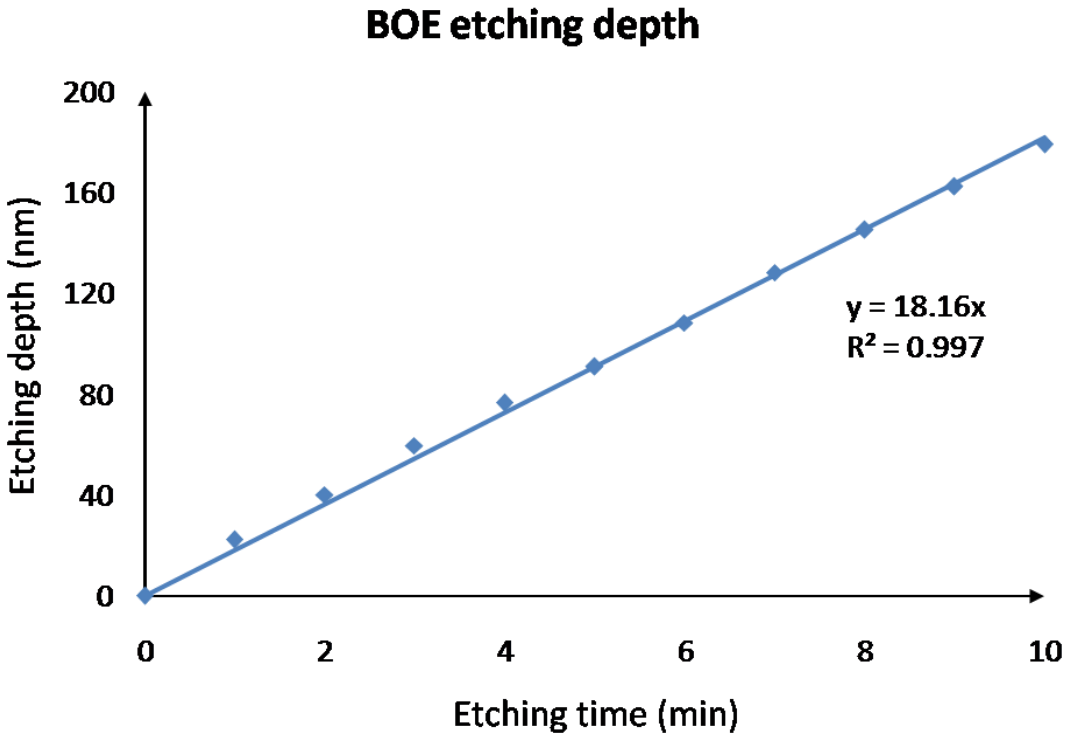

Figure 7.3 BOE etching depth as a function of etching time

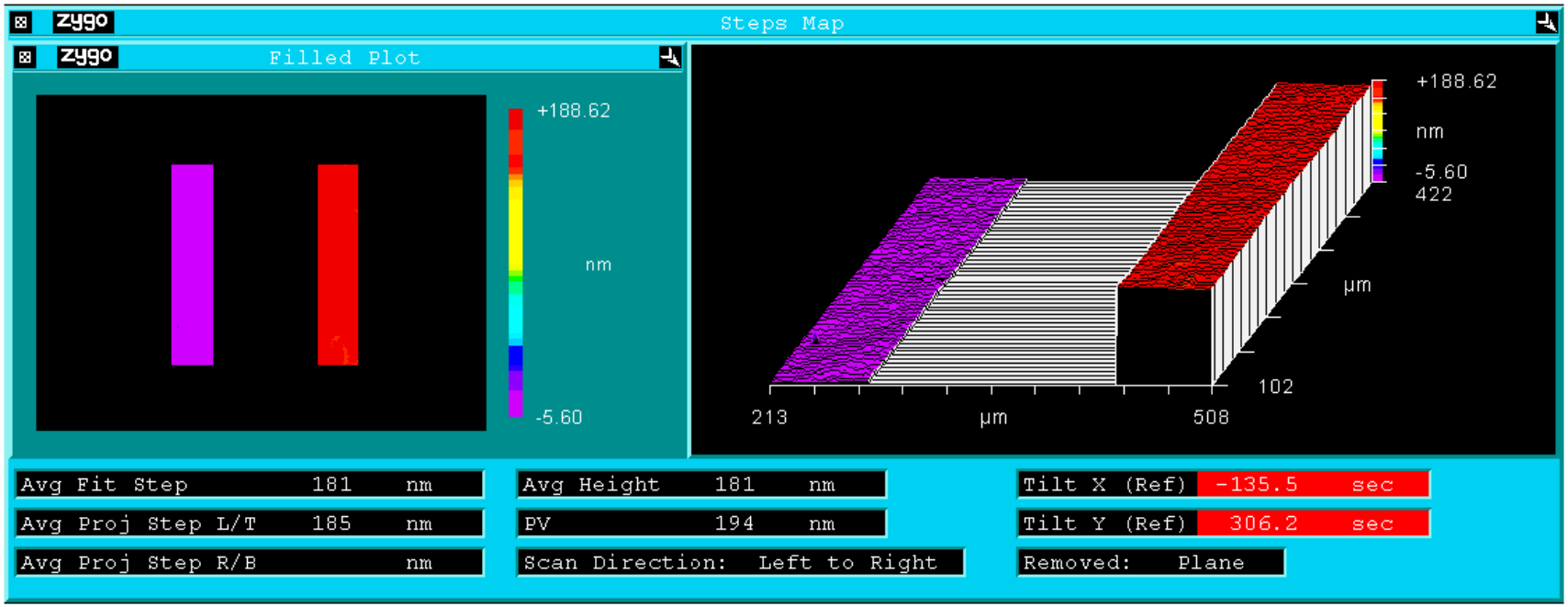

Figure 7.4 Measurement of etching depth using SWLI

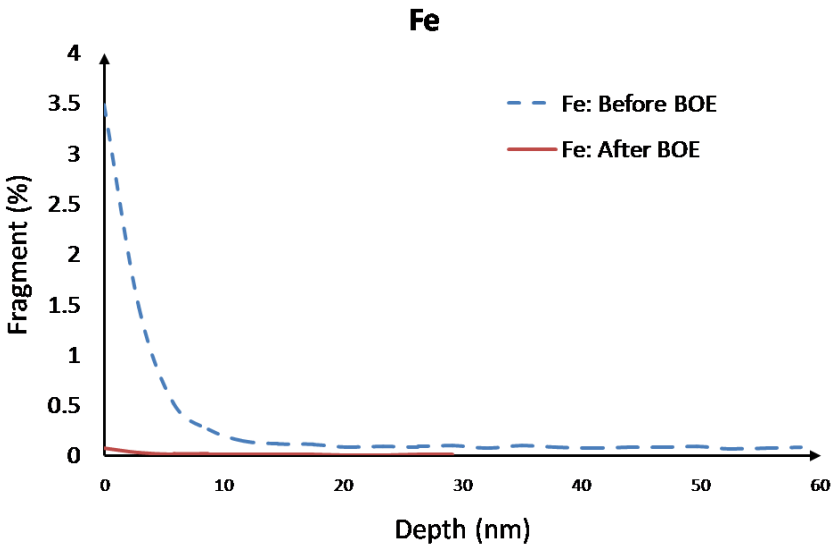

Figure 7.5 Fe distribution in depth measured by SIMS

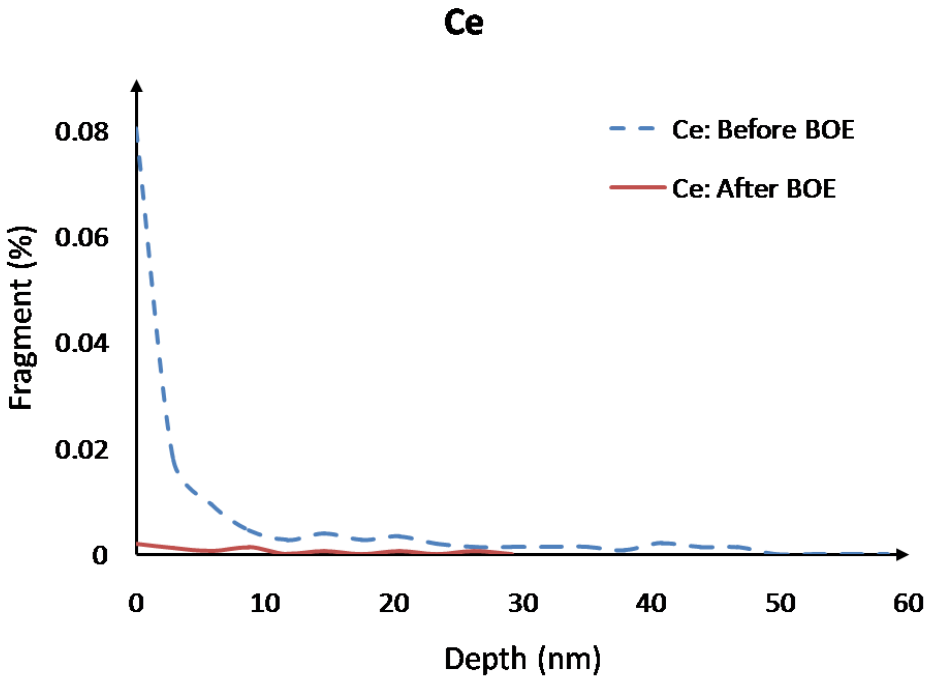

Figure 7.6 Ce distribution in depth measured by SIMS

The result shows that HF-based etching works well enough to remove the Beilby layer where the impurities are embedded and 100 nm was deep enough to remove all the Beilby layer.

Figure 7.7 shows the surface roughness before and after HF-based etching treatment. The initial surface roughness was Ra 0.449 nm, RMS 0.565 nm; and the etched surface roughness was Ra 0.565 nm and RMS 0.630 nm. The result indicates that the roughness does not change significantly after the etching processes. If we consider the surface roughness only (i.e. ignoring contaminants and defects in the blank material), the expected LIDT before and after the etching processes has the following relation in according to Equation (6.5),

$$\begin{aligned} LIDT_{after} / LIDT_{before} &= \left(\sigma_{before} / \sigma_{after}\right)^{0.081} \\ &= \left(0.565/0.630\right)^{0.081} \\ &= 0.991 \end{aligned} \tag{7.2}$$

Equation (7.2) means the surface roughness change does not affect the LIDT of fused silica optical surface significantly. However, because the HF-based etching can remove the Beilby layer, it is believed the LIDT of fused silica optics can increase.

7.2 Ion Beam Etching (IBE) method

7.2.1 Parameters optimisation of the IBE process

In order to remove the Beilby layer and maintain the surface roughness effectively and efficiently, it is necessary to improve the material removal rate of the IBE process but keep the surface roughness at same level.

In the IBE process, sputtering yield is defined by the mean number of atoms sputtered by a single incident ion. The sputtering yield Y_S describes the material removal rate

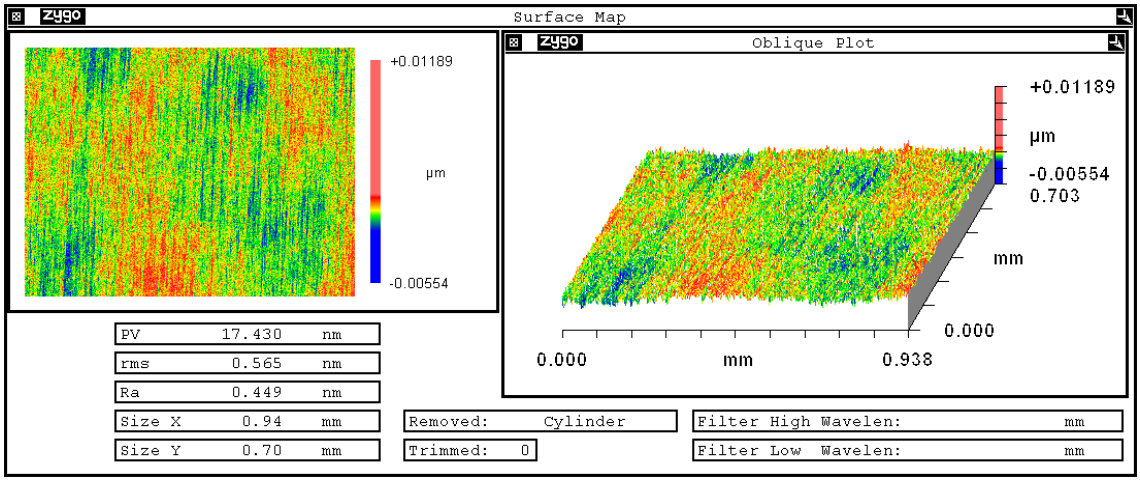

(a) Surface roughness before HF-based etching process

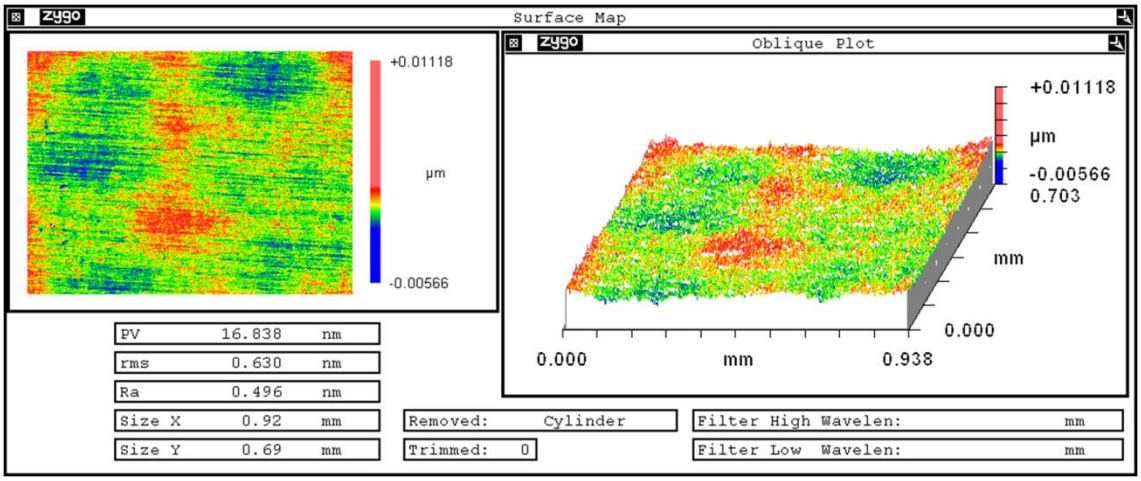

(b) Surface roughness after HF-based etching process

Figure 7.7 Roughness result after HF-based etching treatment measured by SWLI

under the effect of ion beam and is defined as[2]

$$Y_s = \frac{n_0}{n_i} \tag{7.3}$$

where n_0 is the number of atoms sputtered, and n_i is the number of incident ions.

Sigmund's theory [3] suggested the relationship between sputtering yield and the angle of incidence θ (shown in Figure 7.8) satisfies the following equation for $0 < \theta < 70°$,

$$Y_s(\theta) = Y_s(0) \bullet \cos^{-f}(\theta) \tag{7.4}$$

where $Y(0)$ is the sputtering yield at normal incidence (i.e. angle of incidence $\theta = 0°$), and f is a parameter based on atomic spatial moment and has a good approximate value of 5/3.

Jiao modified the results [2], and got the simulated results ($0 < \theta < 90°$) in Figure 7.9. Therefore it can be concluded that the largest sputtering yield is when the angle of incidence was around $70 \sim 80^{\circ}$. Ruzic [4] also got the similar conclusion at low (less than 1000 eV) ion energy.

For an ion with various energies, Jiao[2] also calculated the sputtering yield at angle of incidence $\theta = 0^{\circ}$. Jiao's result (shown in Figure 7.10) indicates that ions with greater energy can generate larger sputtering yield.

Figure 7.11 [5] illustrates the surface roughness of CaF_2 specimens as a function of angle of incidence. The result shows that for CaF_2, the best surface roughness occurs at when the angle of incidence is around 40°, where the material removal rate is lower. This leads to "better" surface roughness.

To sum up, in order to get "better" surface roughness, greater material removal rate,

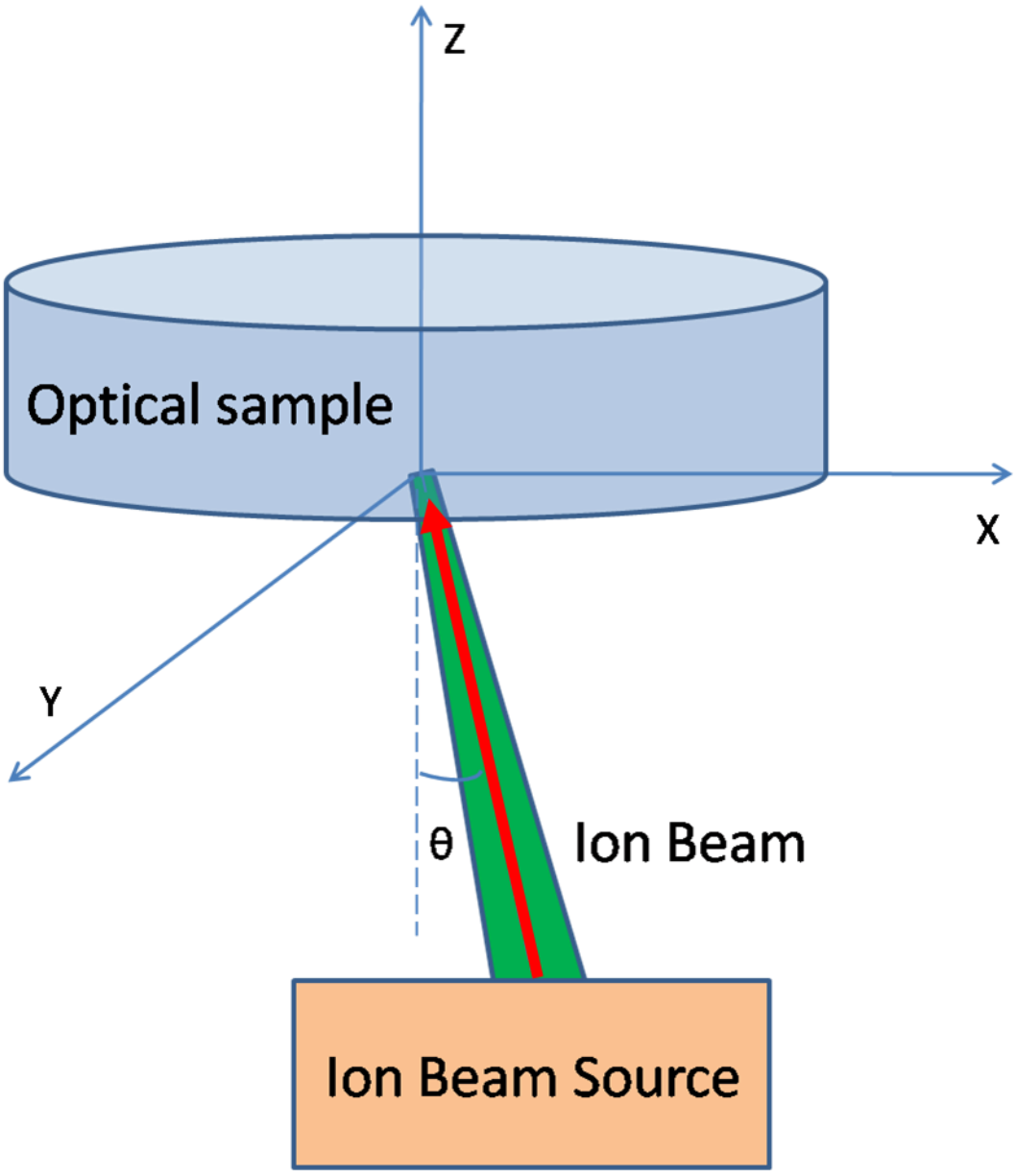

Figure 7.8 Schematic picture of IBE process

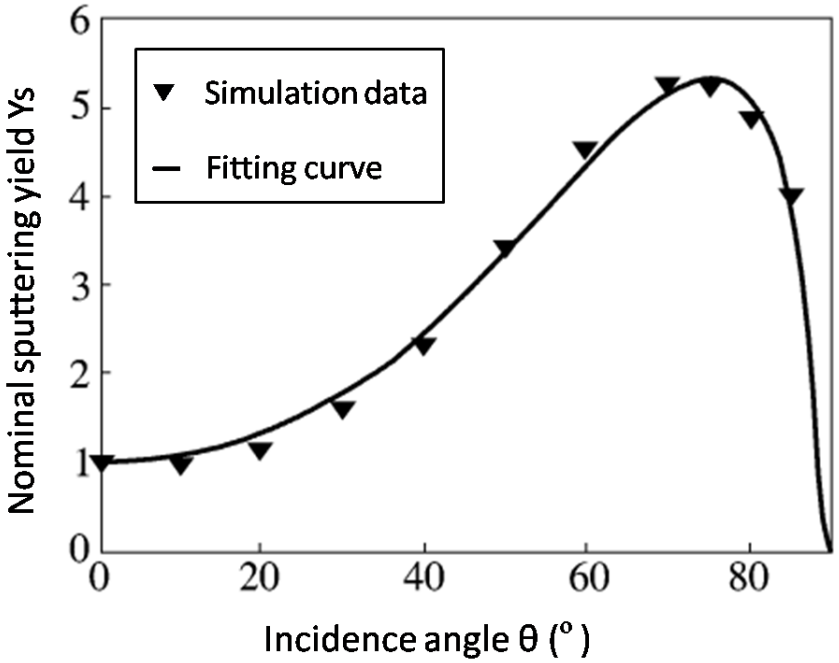

Figure 7.9 Sputtering yield versus angle of incidence for fused silica and Ar ions [2]

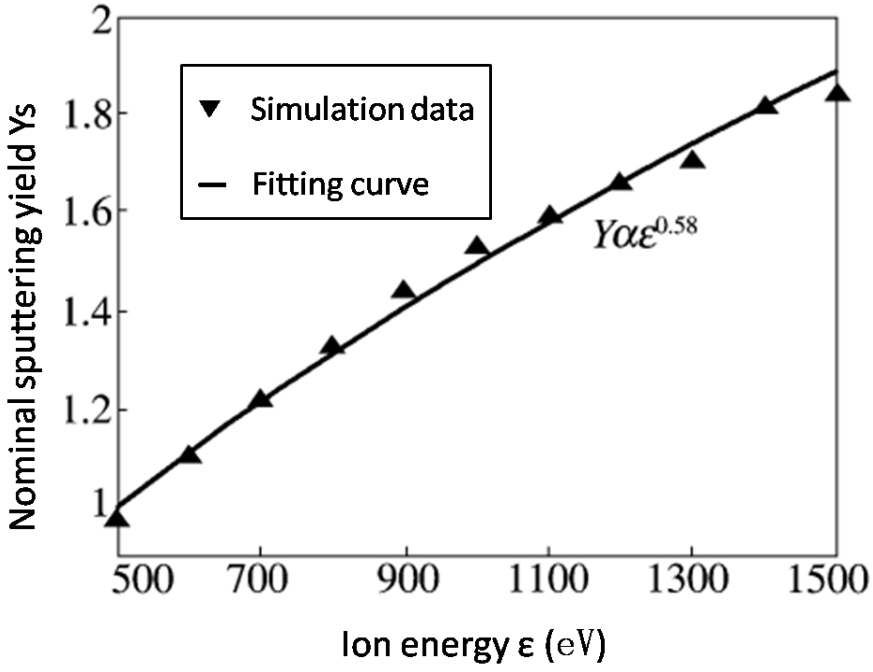

Figure 7.10 Sputtering yield versus Ar ion energy at angle of incidence $\theta = 0^{\circ}$ [2]

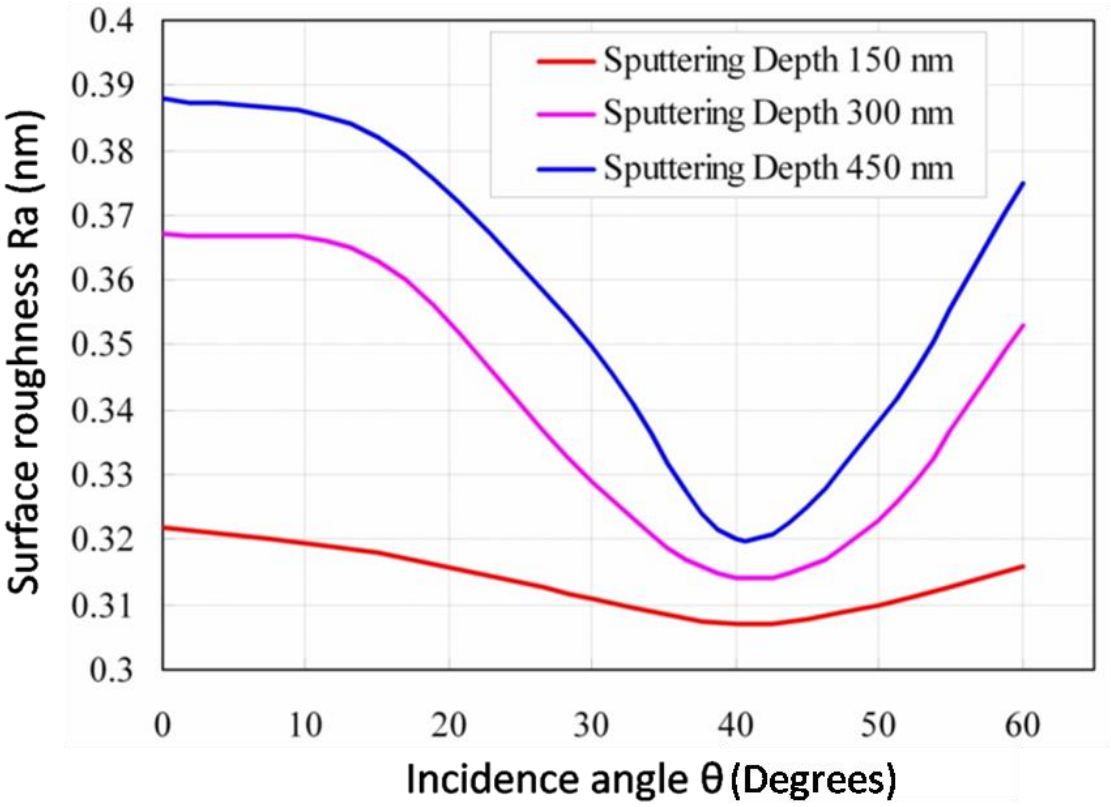

Figure 7.11 Surface roughness as a function of angle of incidence for CaF_2 and Ar ions [5]. Surface roughness for all specimens have minimum values at the angle of incidence is 40°; and surface roughness become worse with the increase of material removal depth.

and improve the LIDT of fused silica optics effectively and efficiently, the following parameter (listed in Table 7.1) were the chosen in this chapter. Figure 7.12 demonstrates the IBE process conducted in this chapter.

Table 7.1 Parameters used in the IBE processes

Parameters	**Level**
Ion energy (eV)	800
Angle of incidence (degree)	40
Etching depth (nm)	100
Processing time per unit area (sec/mm^2)	0.3
Ion type	Ar
Ion beam size on target (mm)	ϕ30

7.2.2 Results of the IBE process

After IBE process removal on a $100\text{mm} \times 100\text{mm}$ fused silica optical surface layer for 50 minutes, the removed material depth was around 100 nm. Then the impurities of Fe and Ce were measured by SIMS and the results are shown in Figure 7.13 and Figure 7.14.

The surface roughness before and after the IBE process is also illustrated in Figure 7.15. The initial surface roughness was Ra 0.444 nm, RMS 0.486 nm; and the etched surface roughness was Ra 0.558 nm and RMS 0.610 nm. The result indicates that the roughness does not change significantly after the IBE processes. If we consider the surface roughness only (i.e. ignoring contaminants and defects in the blank material), the expected LIDT before and after the etching processes has the following relation in according to Equation (6.5),

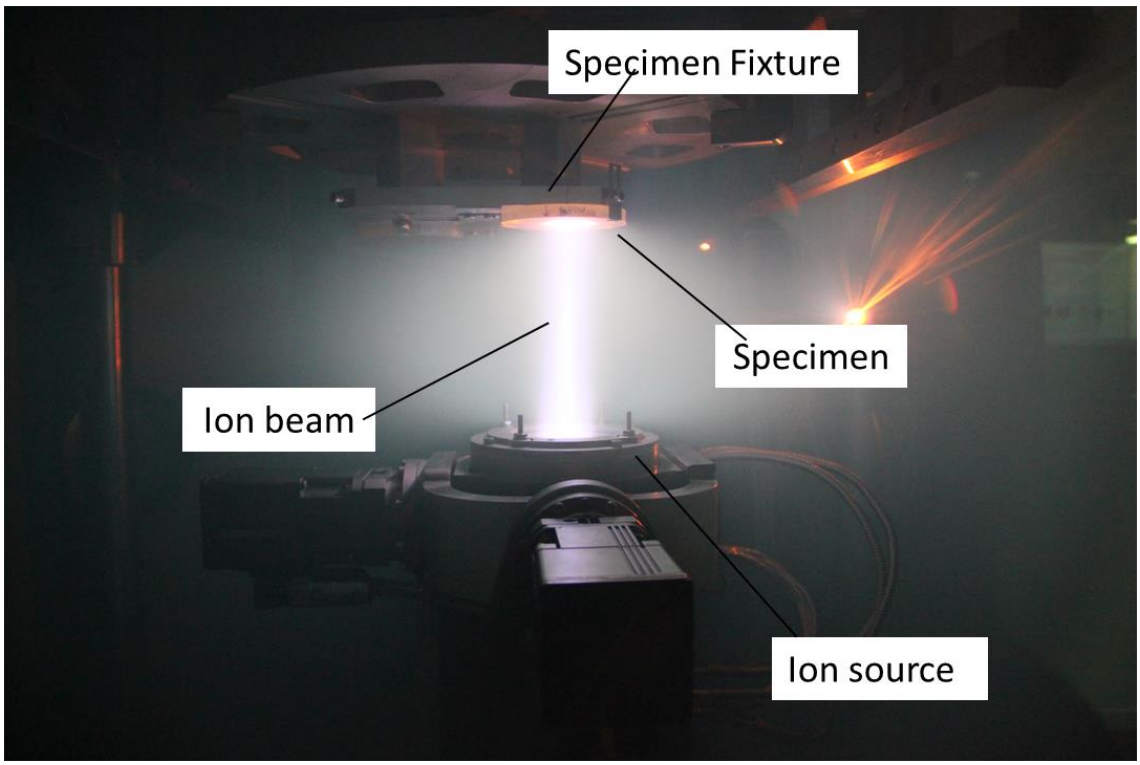

Figure 7.12 Photo of an IBE process

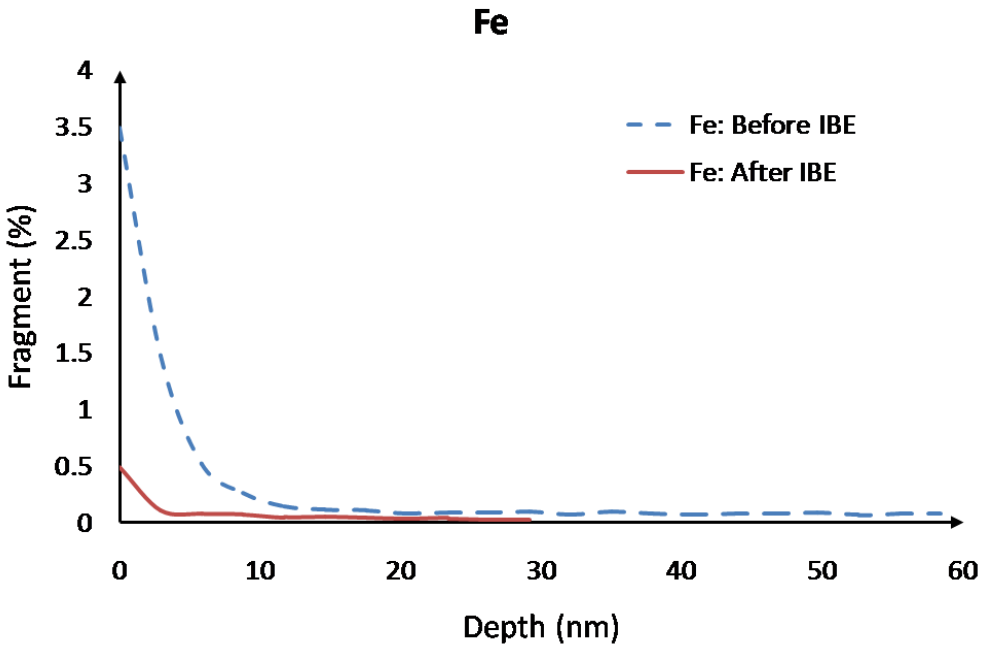

Figure 7.13 Fe distribution in depth measured by SIMS

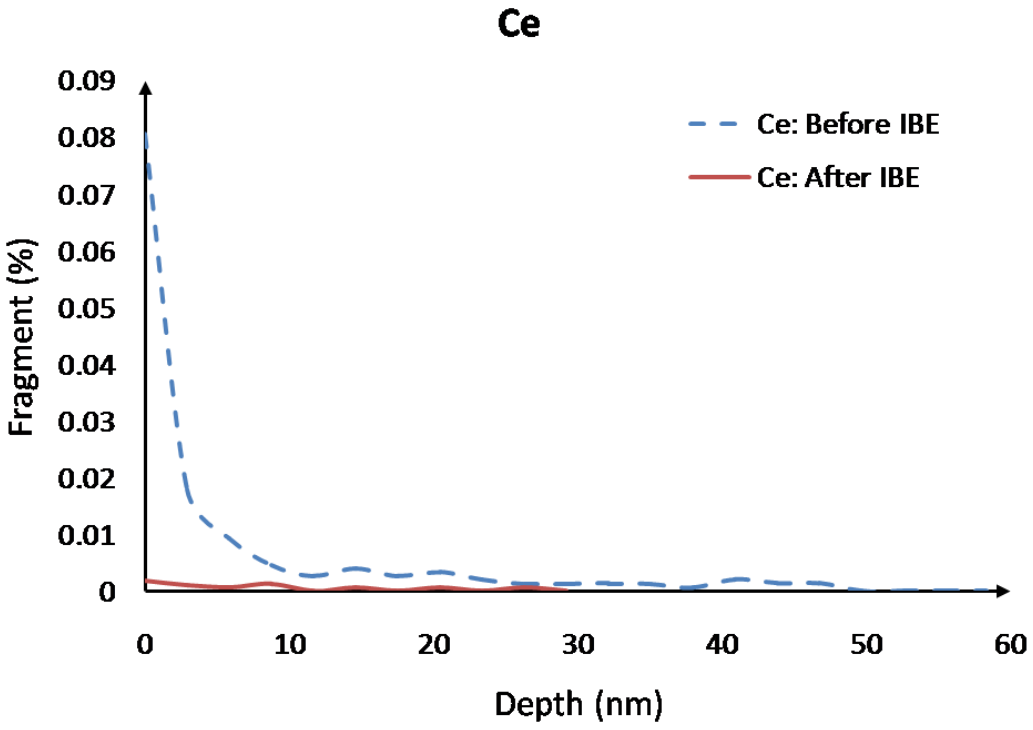

Figure 7.14 Ce distribution in depth measured by SIMS

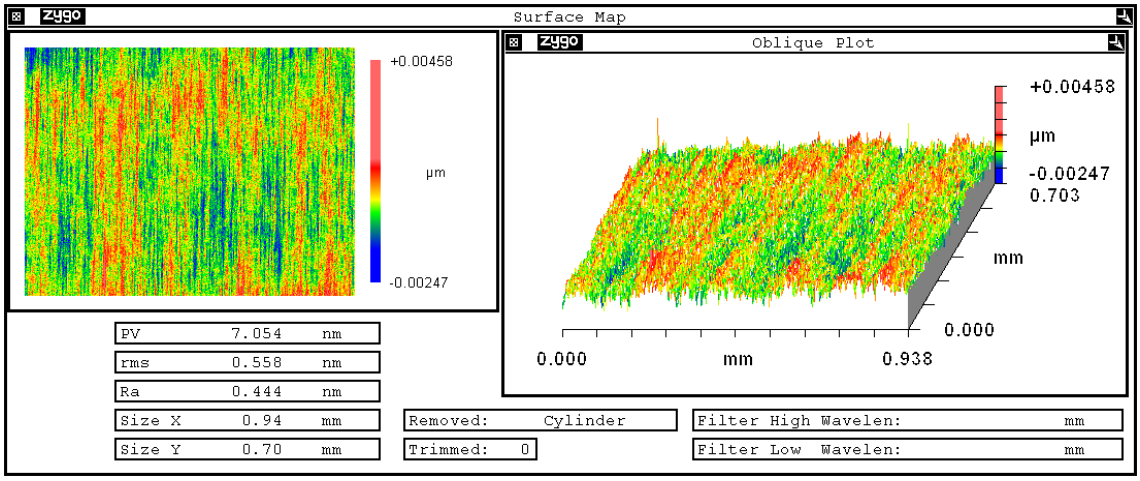

(a) Surface roughness before IBE cleaning process

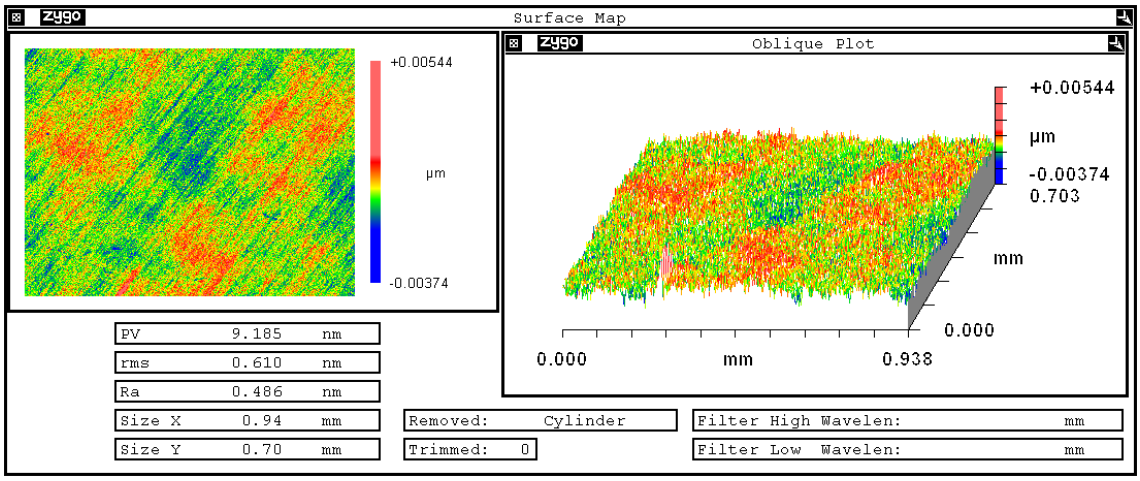

(b) Surface roughness after IBE cleaning process

Figure 7.15 Roughness result before and after IBE cleaning treatment measured by SWLI

$$LIDT_{after} / LIDT_{before} = \left(\sigma_{before} / \sigma_{after}\right)^{0.081} = \left(0.558/0.610\right)^{0.081} = 0.993 \quad (7.5)$$

Equation (7.5) means the surface roughness change does not affect the LIDT of fused silica optical surface significantly.

The above results indicate that the IBE treatment is also an effective method to remove the Beilby layer where the impurities are embedded and it also simultaneously retains the surface roughness. Therefore it is believed the LIDT of fused silica optics can increase

It should be notice that Al ions could be found by SIMS in the surface layer (shown in Figure 7.16) because the sample fixture used in the IBE machine is made by Al, this became another contaminant source for the fused silica optics. Moreover, because Ar is the noble gas in the IBE processes, it is still unclear whether (and how) Ar ions may affect the LIDT of fused silica optics. Therefore, it may be also advantages to use HF-based etching after the IBE treatment to remove contaminants (Al and Ar ions) and to reduce more impurities in the surface layer.

7.3 Summary

The MRF process can introduce redeposition layers (Beilby layers) which accompany contaminant, so post polishing treatment is necessary to remove the unexpected Beiby layer. In this chapter, the following work has been done:

1. The HF-based etching method was analysed as a post polishing treatment and some experiments were conducted on fused silica specimens polished by MRF processes. The results show that, after 5 min BOE etching (etching depth around 100 nm), impurities, such as Fe and Ce introduced by the MRF processes, have

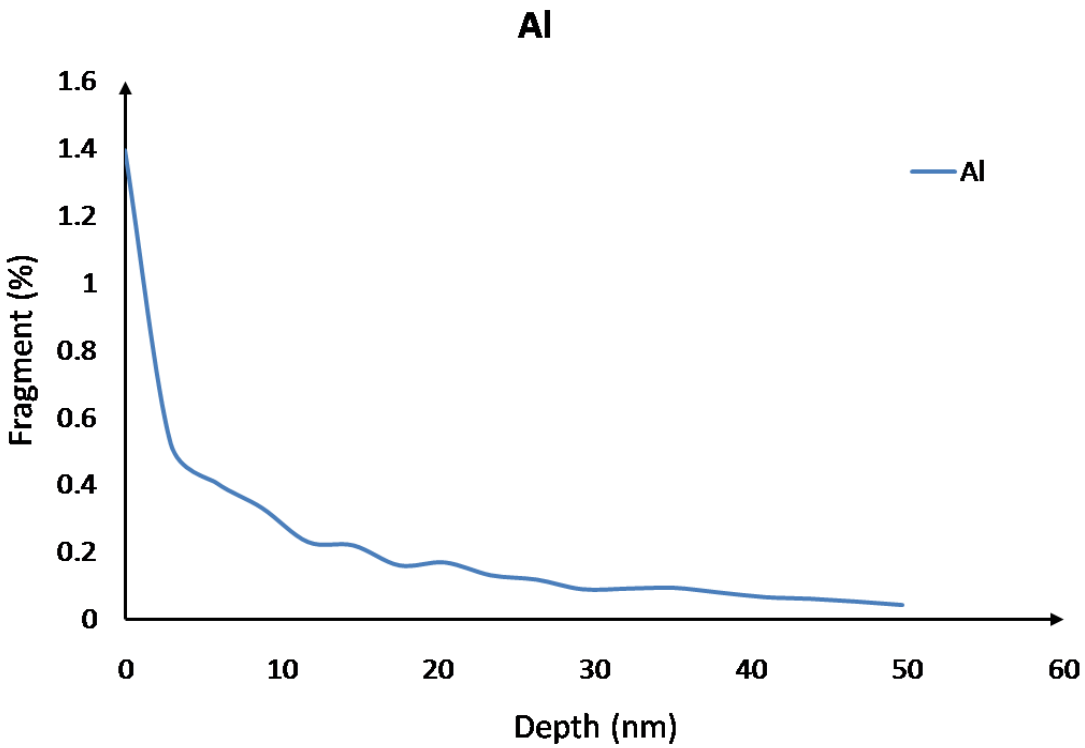

Figure 7.16 Al distribution in depth measured by SIMS

been removed and the surface roughness was simultaneously kept at the same level.

2. The IBE process was also discussed as a post polishing treatment. Experimental results illustrated that Fe and Ce could also be removed and surface roughness kept at around 100 nm in depth. However, the IBE process also introduced other contaminants such as Al which is from the specimen fixture of the IBE machine.

References

1. Suratwala, T., P. Miller, J. Bude, W. Steele and N. Shen, "HF-Based Etching Processes for Improving Laser Damage Resistance of Fused Silica Optical Surface". *Journal of American Ceramic Society*, 2011. **94**(2): pp. 416-428.

2. Jiao, C., "Study on the Material Removal Mechanisms and Fundamental Processes for Ion Beam Figuring Optical Mirrors" [PhD Thesis]. Changsha, Hunan: National University of Defense Technology; 2008.

3. Sigmund, P., "Theory of Sputtering. I. Sputtering Yield of Amorphous and Polycrystalline Targets". *Physical Review*, 1969. **184**(2): pp. 383-416.

4. Ruzic, D.N., P.C. Smith and R.B. Turkot Jr., "Measurements and modeling of the angular-resolved sputtering yield of D-soaked Be by 100, 300, 500 and 700 eV D +". *Journal of Nuclear Materials*, 1997. **241-243**: pp. 1170-1174.

5. Yuan, Z., Y. Dai, X. Xie, L. Zhou and W. Peng, "Research on ultra-precise figuring for CaF_2 single crystal". *Journal of Mechanical Engineering*, 2013. **49**: pp. 108-113.

CHAPTER 8

LASER INDUCED DAMAGE THRESHOLD TESTS

This chapter describes how LIDT tests of the specimen are used to evaluate the validity of these manufacturing and cleaning processes which were introduced in Chapter 5-7. The LIDT test work was completed in Tongji University (Shanghai, China).

8.1 LIDT test results

In order to compare the LIDT of fused silica surfaces manufactured by different processes, a series of LIDT tests was done. The manufacturing processes of these specimens are listed in Table 8.1.

Table 8.1 Specimens manufacturing processes for LIDT tests

#	CMP	MRF (5um)	IBE (100nm)	BOE (100nm)
1*	●	●	●	●
2**	●	●	●	●
3	●	●	●	
4	●	●		●
5	●	●		
6*	●		●	●
7**	●		●	●
8	●		●	
9	●			●
10	●			

*Note: * BOE process is conducted after IBE process*

*** IBE process is conducted after BOE process*

In this set of experiments the fused silica blanks are Suprasil 312 (from Heraeus,

Germany) and Yaohua (China), each specimen was polished using CMP process in advance of any further treatment. The 1-on-1 test method is used in these tests so the LIDT values in the following chapter are zero-probability damage fluence.

After the CMP process, fused silica specimens were manufactured by various processes. From Table 8.1 there are three factors (i.e. MRF, IBE, and BOE) coupled in the LIDT test, hence 10 specimens are needed to clarify the effects of various processes on LIDT of specimens. It is difficult to fabricate all the specimens simultaneously because (a) it needs 10 Heraeus blanks which cost too much (a $100 \times 100 \times 10\mathrm{mm}^3$ blank costs more than 2000 USD) and (b) the manufacturing duration is very long (quite a few days). Moreover, too many coupling factors make the issue more complex than that for single factor. Hence, in this chapter, we conduct the LIDT test by a single factor method rather than do all the tests shown in Table 8.1. Figure 8.1 is the photograph of the LIDT testing process.

In the following three experiments, processing parameters used are shown in Table 8.2 to Table 8.5.

Table 8.2 Parameters for CMP process

Item	**Value**
Pad material	Pitch
Polishing particles	Ceria
Particle size (μm)	1
Normal pressure (Pa)	5×10^4
Orbital speed (r/min)	55
Swing speed (cyc/min)	20
Polishing duration (min)	30

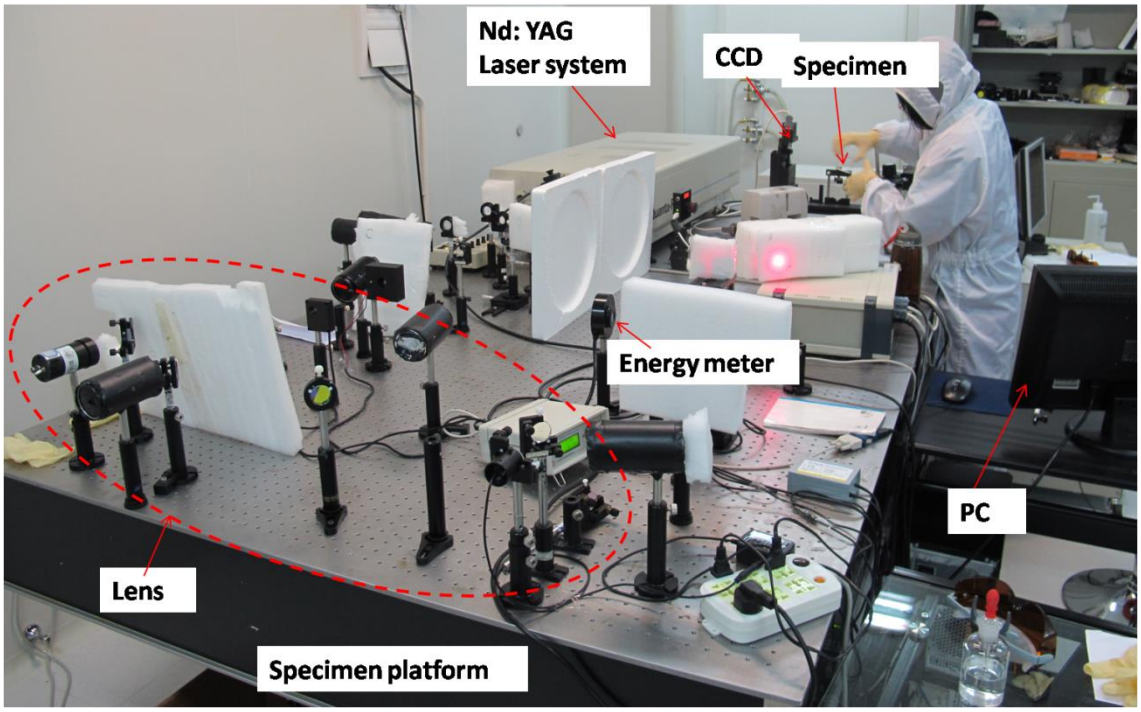

Figure 8.1 Photo of testing process in Tongji University, China

Table 8.3 Parameters of MRF processes

Item	Level
Polishing particles	CeO_2
Polishing particle size (μm)	≈0.2
Nominal size of CI particles (μm)	5
Wheel speed (r/min)	125
Ribbon penetration depth (mm)	0.20
Flow rate (L/min)	160
Current (A)	7.5
Polishing duration per unit area (s/mm^2)	0.36
Viscosity (Pa · s)	197

Table 8.4 Parameters of the BOE etching processes

Item	Level
HF concentration (wt%)	5
NH_4F concentration (wt%)	15
Etching depth (nm)	100
Cleaning ultrasonic frequency (kHz)	40

Table 8.5 Parameters of the IBE processes

Item	Level
Ion energy (eV)	800
Incidence angle (degree)	40
Etching depth (nm)	100
Processing time per unit area (sec/mm^2)	0.3
Ion type	Ar

8.1.1 Experiment 1: Factor of the MRF process

In order to clarify the role of MRF process on the LIDT of fused silica optics, two specimens (made of Heraeus fused silica) treated by various procedures were prepared.

The first specimen was manufactured by method #4 of Table 8.1, while the second was processed by method #9 of Table 8.1. It should be stated that the CMP and BOE processes used on the both specimens were same.

Figure 8.2 indicates the 1-on-1 LIDT results from these two specimens. The lines were determined by least-square fit method. From the results it can be seen that the LIDT value of the specimen with and without MRF processing (first versus second specimen) are 25.28 J/cm^2 and 33.01 J/cm^2, respectively. Hence these results indicate that with the MRF process, the specimen can get a higher LIDT value than without.

8.1.2 Experiment 2: Factor of BOE etching process

In order to find out the effect of the BOE etching treatment on the LIDT of fused silica optics, in this set of experiments three specimens (made of Heraeus fused silica) treated by various procedures were prepared. Three specimens were treated by methods #10, #5, and #4 of Table 8.1, respectively. The LIDT values of these three specimens are illustrated in Figure 8.3.

The 1-on-1 LIDT results show that the LIDT values for these specimens are 14.61 J/cm^2, 24.03 J/cm^2, and 25.19 J/cm^2, respectively. From the LIDT results it can be seen that specimen treated by only CMP has the lowest LIDT value while that processed by CMP, MRF and BOE etching gets the highest LIDT value.

8.1.3 Experiment 3: Factor of IBE process

Three specimens (made of Yaohua fused silica) were prepared, by various processes of methods #1, #2, and #4 of Table 8.1, to make clear the effect of the IBE process on the tested LIDT value for fused silica optics.

The 1-on-1 LIDT results of these specimens are illustrated in Figure 8.4. From Figure 8.4 we can see that specimen, which was manufactured by CMP, MRF, BOE etching and the

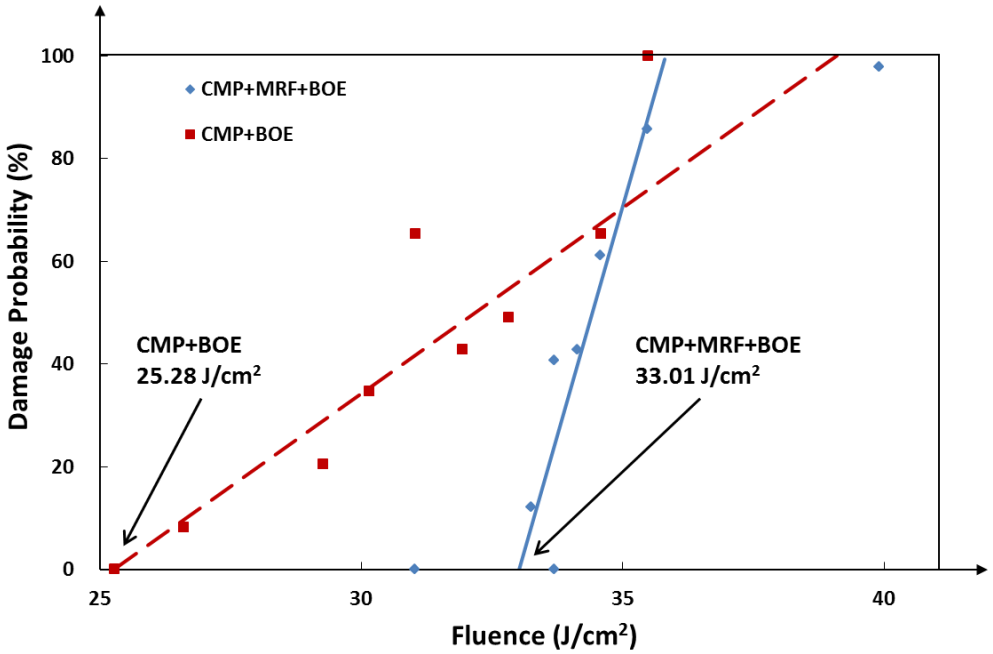

Figure 8.2 MRF process for LIDT results of Heraeus fused silica specimens

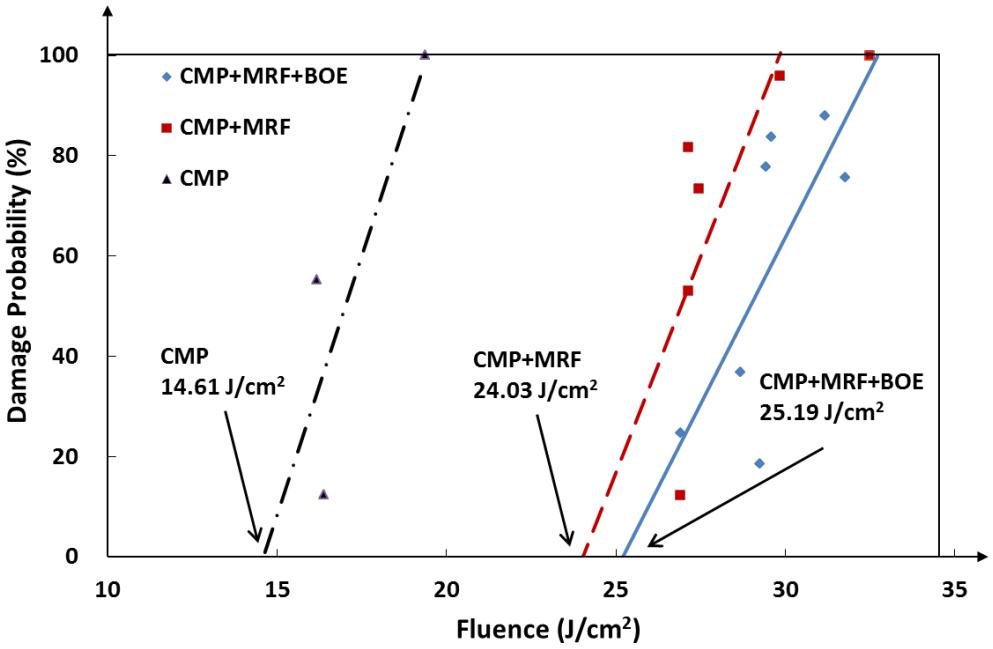

Figure 8.3 BOE and MRF processes for LIDT results of Heraeus fused silica specimens

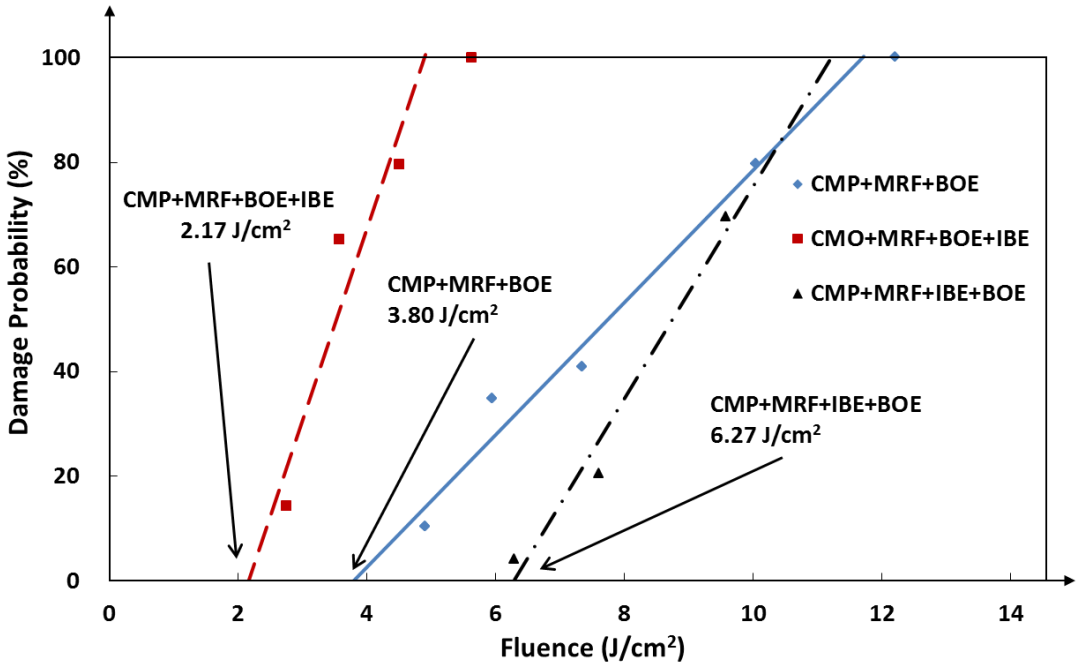

Figure 8.4 LIDT results of Yaohua fused silica specimens after various processes

IBE process in sequence, had the lowest LIDT value 2.17 J/cm^2, while the specimen processed by CMP, MRF, IBE and BOE etching in sequence had the highest LIDT value 6.27 J/cm^2. The LIDT value of the specimen machined by CMP, MRF and BOE etching is 3.80 J/cm^2.

8.2 Discussions

It can be seen that LIDT values vary obviously for all the three sets of LIDT results, especially the LIDT value of specimens treated by the same CMP, MRF and BOE processes in the each set of tests are 33.01 J/cm^2, 25.19 J/cm^{2}and 3.80 J/cm^2, respectively.

There are three ways to explain this phenomenon: (a) the tests were not conducted at the same time and parameters of the laser system were different; (b) measurement is a statistical process in nature, so for the same optical specimen it could differ when tests positions are different; and (c) different specimens, even when manufactured by same processes, could have various LIDT values due to the fact that the bulk fused silica materials which are made from different suppliers have different quality. Li [1] investigated the quality of bulk fused silica from different supplier and indicated that fused silica from Heraeus has less metallic impurities (0.01~0.05 ppm) than that from Yaohua.

However, in the aforementioned LIDT tests, the experimental conditions for each set of tests were the same, i.e. same parameters of the same laser system, same materials (guaranteed by the fused silica blanks of each set of test are from same supplier). Moreover, many positions on surface were used to get the LIDT value of a specimen.

Table 8.6 Comparisons of LIDT tests

No. of Comparison	No. of Experiment	Material supplier	Processes	LIDT value (J/cm^2)
1	1	Heraeus	CMP+BOE	25.28
			CMP+MRF+BOE	33.01
2	2	Heraeus	CMP	14.61
			CMP+MRF	24.03
3	2	Heraeus	CMP+MRF	24.03
			CMP+MRF+BOE	25.19
4	3	Yaohua	CMP+MRF+BOE+IBE	2.17
			CMP+MRF+BOE	3.80
5	3	Yaohua	CMP+MRF+BOE	3.80
			CMP+MRF+IBE+BOE	6.27
6	3	Yaohua	CMP+MRF+BOE+IBE	2.17
			CMP+MRF+IBE+BOE	6.27

If the test results are re-arranged, then the following comparisons are obtained: From Table 8.6 we can obtain that:

1. Both the first two comparisons suggest that the MRF process may improve the LIDT of a fused silica optical surface due to the mean LIDT values of specimens with MRF process and those without MRF process. This is because MRF removes the surface and/or subsurface damage.

2. The third comparison illustrates that the specimen with BOE treatment has higher LIDT value (mean value) than that without the BOE etching process. In other words, BOE etching is also a useful tool to enhance the LIDT of fused silica optics.

3. The comparisons 4-6 provide complex results. First of all, the fourth comparison

illustrates that if the specimen is treated by processes which include the IBE method it will have a lower LIDT value than those without the IBE process. However, in the fifth comparison, we get the contrary conclusion that a specimen with IBE treatment has a higher LIDT value. The last comparison points out that the LIDT values vary greatly for specimens manufactured by processes including IBE treatment. This is probably because the sequence of IBE processing is really important. If the IBE process is the last procedure in the manufacturing process, it could be disadvantage to improving the LIDT value and even lower the value because the IBE process could also induce other contaminates on the surface layer. This is proved by comparison 4 and 6. However, the last comparison illustrates that the LIDT of a fused silica specimen could be improved greatly if the IBE process is conducted before BOE process.

To sum up, the MRF process and BOE etching treatment are advantageous in enhancing the LIDT of fused silica optics. The IBE method is useful to improve the specimen's LIDT only if it is conducted before the BOE etching process. When the IBE process is the last treatment for processing the specimen, the LIDT value could be reduced. So the optimised way to improve the LIDT of fused silica optics is MRF, IBE and BOE processes in the sequence shown in Figure 8.5.

8.3 Summary

The LIDT test is a way to verify the effectiveness of the manufacturing processes for fused silica optics. In this chapter, the following work has been done:

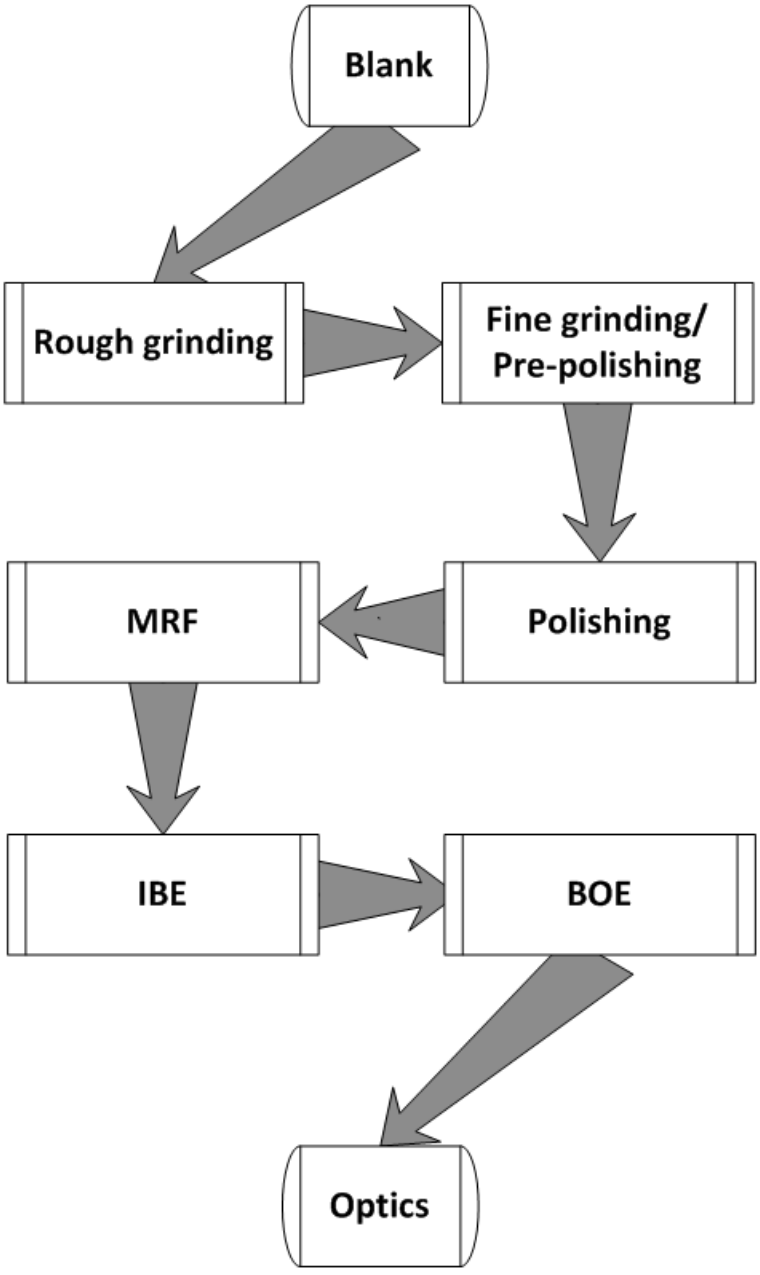

Figure 8.5 Complete processes to manufacture fused silica optics

1. Three sets of LIDT tests for fused silica surface were been conducted via a 1-on-1 method. The experimental results indicated that the MRF process and BOE etching treatment may be advantageous in enhancing the LIDT of fused silica optics. The results also showed that the IBE process can improve the LIDT of fused silica optics only if it is conducted before BOE etching process.

2. The optimised processes to manufacture fused silica optics are introduced. The processes include grinding, conventional polishing, MRF process, IBE process, and BOE etching process in a particular sequence.

References

1. Li, C.H., "Mechanism Study on High Power UV Laser-Induced Damage in Fused Silica Optics" [PhD Thesis]. Beijing, China: University of Science and Technology Beijing; 2011.

CHAPTER 9

CONCLUSIONS AND FUTURE WORK

9.1 Conclusions

This work was aimed at investigating fused silica optical surface processing techniques which are able to improve the surface quality and increase the LIDT under the irradiation of high peak power lasers. With the aim of the project (as listed on P19 Chapter 1) here, the objectives of the project were:

- To investigate the effects of surface damage and impurities on inducing the fused silica optics damage under the irradiation by high peak power lasers.
- To analyse the effect of using MRF for removing surface damage on fused silica optics.
- To optimise polishing parameters in the MRF process to improve the roughness of fused silica optical surfaces.
- To remove contaminants from fused silica surfaces after polishing processes by means of post polishing treatments.
- To conclude a set of surface processing techniques which improve LIDT of fused silica.

These objectives were met by a series of experiments and simulations as described in each chapter of the thesis.

Chapter 4 investigated the effects of surface damage and impurities on inducing the

fused silica optics damage under the irradiation by high peak power lasers. The effect of surface damage and impurities which bring light intensity enhancement and thermal stress were studied by a combination of FDTD and FEA simulation. The results of the simulations indicated that surface damage and impurities could create light intensity enhancement and thermal stress. Smoother and smaller cracks create less light intensity enhancement and less thermal stress concentration, while impurities embedded into the surface layer generate much greater thermal stress concentration and could be likely to lead to LID. Therefore, it was concluded that using a systematic approach to remove the surface damage and impurities should be an effective way to improve LIDT of fused silica optics and a number of ways to do this were investigated.

In Chapter 5, the effect of using MRF for removing surface damage on fused silica optics was analysed. Based on static indentation theory [1] and Bifano's brittle-ductile cutting theory [2], the conditions of non-fracture polishing for fused silica were analysed. Then the force imposed on a single abrasive particle in the MRF process was calculated. The result indicated that force imposed on a single abrasive particle (typically $\sim 10^{-8}$ N) and indentation depth on fused silica surface (typically ~ 0.22 nm) in the MRF process is far less than the critical force (typically $\sim 10^{-2}$ N) and critical indentation depth (typically ~ 33 nm) which would induce fracture, so it was concluded that the MRF process used in this project was a non-fracture polishing method. Experiments were also conducted and the results showed large rogue particles which may enter the MRF process or conventional polishing process do not really affect the surface quality in the MRF process. Further experiments also showed that the MRF process could remove the surface and sub-surface damage produced by conventional polishing processes. Based on these findings, it is believed that the MRF process is able to remove surface damage of fused silica optics effectively.

Chapter 6 optimised the polishing parameters in the MRF process to improve the roughness of fused silica optical surfaces. In this chapter, the relation between LIDT and

the surface roughness of fused silica optics machined by MRF process and HF etching was investigated and the results showed that lower surface roughness generally increased the LIDT of fused silica optical surfaces. Then, to get better surface roughness, the MRF process was optimised through a series of experiments which investigated surface roughness and polishing parameters via Taguchi method. Experimental data showed that the percentage contribution of each factor on surface roughness in the MRF process were 51.44 %, 16.04 %, 9.98 % and 0.31 % for rotating speed, flow rate , current and penetration depth, respectively. In other words, the results indicated that slower rotating speed, higher flow rate, and higher current could induce better surface roughness, while penetration depth may not affect surface roughness.

Chapter 7 investigated methods to remove contaminants from fused silica surfaces after polishing processes. In this chapter, two types of post polishing treatments, HF-based etching process and IBE process, were used to remove contaminants as well as the redeposition layer which is generated during polishing processes such as MRF process and CMP. The level of contaminants on fused silica surfaces after these two post polishing treatments was measured by SIMS. Measurement showed that both BOE etching and IBE process could remove impurities such as Ce and Fe which were introduced by MRF process. However, the IBE also introduced Al during the cleaning process because the specimen fixture of the IBE machine was made by Al. Changing the fixture material and optimising the IBE parameters may be ways to avoid the Al contaminant in the IBE process.

Chapter 8 concluded a set of surface processing techniques which improve LIDT of fused silica. This set of surface processing techniques includes conventional fabrications (i.e. grinding and CMP), MRF, IBE, and HF-based etching processes in sequence. The effectiveness of the MRF process and the two post polishing treatments (IBE and BOE processes) on improving the LIDT of fused silica optics were verified by sets of LIDT tests due to the values of test results(shown in Table 9.1). The LIDT test

results indicated that processes, such as MRF, IBE and HF-based etching (BOE used in this work), were all effective in improving the LIDT of fused silica optics. Results also showed that the IBE process may not be the best as the last procedure in the manufacturing process and that it would be better to be followed by a HF-based etching process.

Table 9.1 Results of LIDT tests

No. of Experiment	No. of Specimen	Fused silica supplier	Processes				LIDT value (J/cm^2)
			Step1	Step2	Step3	Step4	
1	#1	Heraeus	CMP	BOE	N/A	N/A	25.28
	#2		CMP	MRF	BOE	N/A	33.01
2	#3		CMP	N/A	N/A	N/A	14.61
	#4		CMP	MRF	N/A	N/A	24.03
	#5		CMP	MRF	BOE	N/A	25.19
3	#6	Yaohua	CMP	MRF	BOE	IBE	2.17
	#7		CMP	MRF	BOE	N/A	3.80
	#8		CMP	MRF	IBE	BOE	6.27

It is informative to compare the results in Table 9.1 with those obtained by other investigations.

After laser irradiation by raster scanning at a speed of 10 mm/s in 10^{-5} Torr vacuum, Xu [3] used focused IBE process with a beam diameter ~2 mm, and using Ar gas as the sputtering gas, to etch fused silica samples (JGS1, made in China) for 150 seconds. The etching rate was 2-3 nm/min. This treatment increased the LIDT value from 17.8 J/cm^2 to 22.8 J/cm^2 (@ 50% damage probability fluence, 1-on-1, 355nm Nd: YAG laser, 6.8 ns pulse, beam area 0.32 mm^2). The result suggested use of the IBE process was possible to improve LIDT of fused silica optics.

Before 2007 the National Ignition Facility (NIF) were focused on the surface finishing and the LIDT value obtained at 0% damage probability fluence, using a 355 nm laser beam (beam size and irradiation conditions were unclear) was around 2.6 J/cm^2 (shown in Figure 1.9), but after using AMP, also called Advance Mitigation Process, which was a method based on HF-based etching and cleaning, they increased the LIDT value to 8 J/cm^2 in 2009 [4, 5]. Their work showed the HF-based etching process could be effective in improving the LIDT of fused silica optics.

Xu's LIDT test conditions were very similar with the tests in this project and the obtained LIDT values were also closed to those in this project. However, NIF's work got lower LIDT value which could possibly be obtained under irradiation of large aperture laser beam or by different LIDT test methods such as S-on-1 and R-on-1. Another explanation is different material suppliers provided fused silica blank with different qualities. Li [6] investigated the quality of bulk fused silica from different suppliers. Fused silica materials generally include metallic impurities, such as Al^{3+}, Fe^{2+}, Na^{+}, Li^{+} ,K^{+}, Ca^{2+} ,Mg^{2+} , and hydroxyls (-OH). Li [6] also indicated that concentrations of all the metallic impurities of fused silica from Heraeus are around 0.01~0.05 ppm and that of hydroxyls is around 1000 ppm; while those from Yaohua are higher than fused silica from Heraeus. For example, the concentrations of Mg^{2+} and K^{+} for fused silica from Yaohua are 0.65 ppm and 0.34 ppm, which are much higher than those of fused silica from Heraeus (0.005 ppm for Mg^{2+} and 0.01 ppm for K^{+}). The concentration of hydroxyls of fused silica from Yaohua is around 1200~1500 ppm, which is a little higher than that of fused silica from Heraeus.

To sum up, this thesis did investigations according to the project objectives and concluded a set of fused silica optical surface processing techniques including MRF, IBE and HF-based etching in sequence, after the conventional processes such as grinding and CMP. Then surface quality measurement and LIDT tests verified the concluded processing techniques were validated to improve the surface quality and increase the

LIDT of fused silica optics.

9.2 Future work

This study was conducted to find a series of surface manufacturing processes to enhance the LIDT of fused silica optics effectively. However, there are still a significant number of issues that remain to be investigated.

1. Efficiency is a significant factor in the optics manufacturing process, especially for large laser systems. Therefore, the polishing parameters of the MRF process should be optimised by considering not only the surface roughness but also the material removal rate. The best process parameters for improving the surface roughness may not be the best ones for material removal rate. Therefore, future research should give attention to both factors.

2. This thesis considered the effects of surface roughness on LID of fused silica optics. However, waviness and form of optical surface are not addressed yet. Waviness can promote light scattering and introduce light energy loss. And surface form can affect light modulation. The mechanisms by which surface waviness and form affect LID of fused silica optics is still unclear and need to be studied.

3. Due to the limitation of the experimental apparatus used for the HF-based etching processes, only a few BOE etching experiments were conducted in this project and technique for the HF-based etching processes has not been optimised. For example, multi-frequency ultrasonics and mega-sonics could be used in future HF-based etching processes. The concentration of the etching liquid also needs to be optimised.

4. Further investigations into the IBE process should be conducted to verify its effect on improving the LIDT of fused silica optics. Because new impurities are easily

brought to the optical surface via the IBE process, parameter optimisation of IBE process is critical and needs to be investigated in the future.

5. In this work, LIDT of specimens were tested using 1-on-1 method. However, no repeatability experiments were conducted due to limitation of time and cost. More LIDT tests should be conducted to confirm the conclusion in this thesis.

6. Whether the conclusions drawn from work described in Chapter 8 still apply for S-on-1 and R-on-1 methods is not clear. Therefore, the effectiveness of LIDT test evaluation methods should be investigated. Notably LIDT tests should be conducted by laser irradiation using a large aperture because the fused silica optics in the high peak power systems are generally operating under the irradiation of a large diameter laser beam.

7. The LIDT test results (shown in Table 9.1) showed the LIDT values of Yaohua fused silica were much lower than those of Heraes materials, so more details of the blank material quality should be investigated in future.

References

1. Lawn, B.R. and M.V. Swain, "Review Indentation Fracture: principles and applications". *Journal of Materials Science*, 1975. **10**: pp. 1049-1081.

2. Bifano, T.G., T.A. Dow and R.O. Scattergood, "Ductile-Regime Grinding: A New Technology for Machining Brittle Materials". *Journal of Engineering for Industry*, 1991. **113**: pp. 184-189.

3. Xu, S., W. Zheng, X. Yuan, H. Lv and X. Zu, "Recovery of fused silica surface damage resistance by ion beam etching". *Nuclear Instruments and Methods in Physics Research B*, 2008. **266**: pp. 3370-3374.

4. Suratwala, T.I. "Optical Fabrication and Post Processing Techniques for Improving Laser Damage Resistance of Fused Silica Optics". in *International Optical Design Conference and Optical Fabrication and Testing*. 2010. Jackson Hole, Wyoming: Optical Society of America. pp. OWA1

5. Suratwala, T., P. Miller, J. Bude, W. Steele and N. Shen, "HF-Based Etching Processes for Improving Laser Damage Resistance of Fused Silica Optical Surface". *Journal of American Ceramic Society*, 2011. **94**(2): pp. 416-428.

6. Li, C.H., "Mechanism Study on High Power UV Laser-Induced Damage in Fused Silica Optics" [PhD Thesis]. Beijing, China: University of Science and Technology Beijing; 2011.

Appendix

A. 2D FDTD method for TE waves

The FDTD approach is based on a direct numerical solution of the time-dependent Maxwell's equations. For a 2D FDTD method, the wave propagation direction is along Z-direction, and the Y-direction is assumed infinite. This assumption removes all the $\partial/\partial y$ derivatives from Maxwell's equations and splits them into two (TE wave and TM wave) independent sets of equations.

The 2D computational domain is shown in Figure A.1. The space steps in the X and Z directions are Δx and Δz, respectively. Each mesh point is associated with a specific type of material and contains information about its properties such as refractive index, and dispersion parameters.

In the 2D TE case ($H_x,\ E_y,\ H_z$ - nonzero components, propagation along Z, transverse field variations along X) in lossless media, Maxwell's equations take the following form:

$$\frac{\partial E_y}{\partial t} = \frac{1}{\varepsilon}\left(\frac{\partial H_x}{\partial z} - \frac{\partial H_z}{\partial x}\right), \quad \frac{\partial H_x}{\partial t} = \frac{1}{\mu_0}\frac{\partial E_y}{\partial z}, \quad \frac{\partial H_z}{\partial t} = -\frac{1}{\mu_0}\frac{\partial E_y}{\partial x} \tag{A.1}$$

where ε is the dielectric permittivity and is $\mu_0$the magnetic permeability of the vacuum.

Each field is represented by a 2D array - $E_y(i,k)$, $H_x(i,k)$ and $H_z(i,k)$ - corresponding to the 2D mesh grid given in Figure A.1. The indices i and k account for the number of space steps in the X and Z direction, respectively. In the case of TE, the location of the fields in the mesh is shown in Figure A.2.

The TE fields stencil can be explained as follows. The E_y field locations coincide with

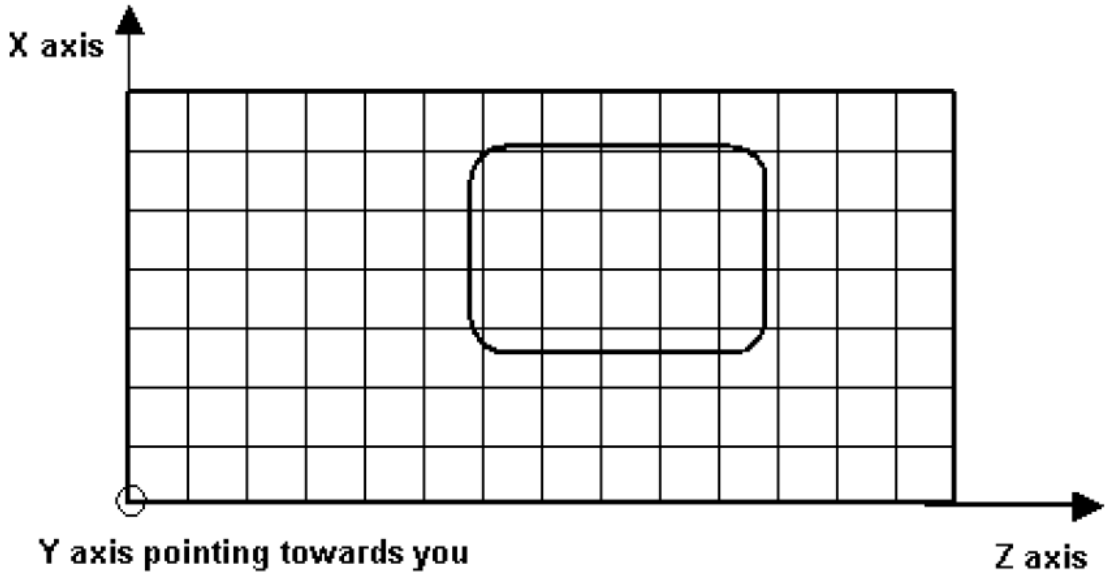

Figure A.1 Numerical representation of the 2D computational domain

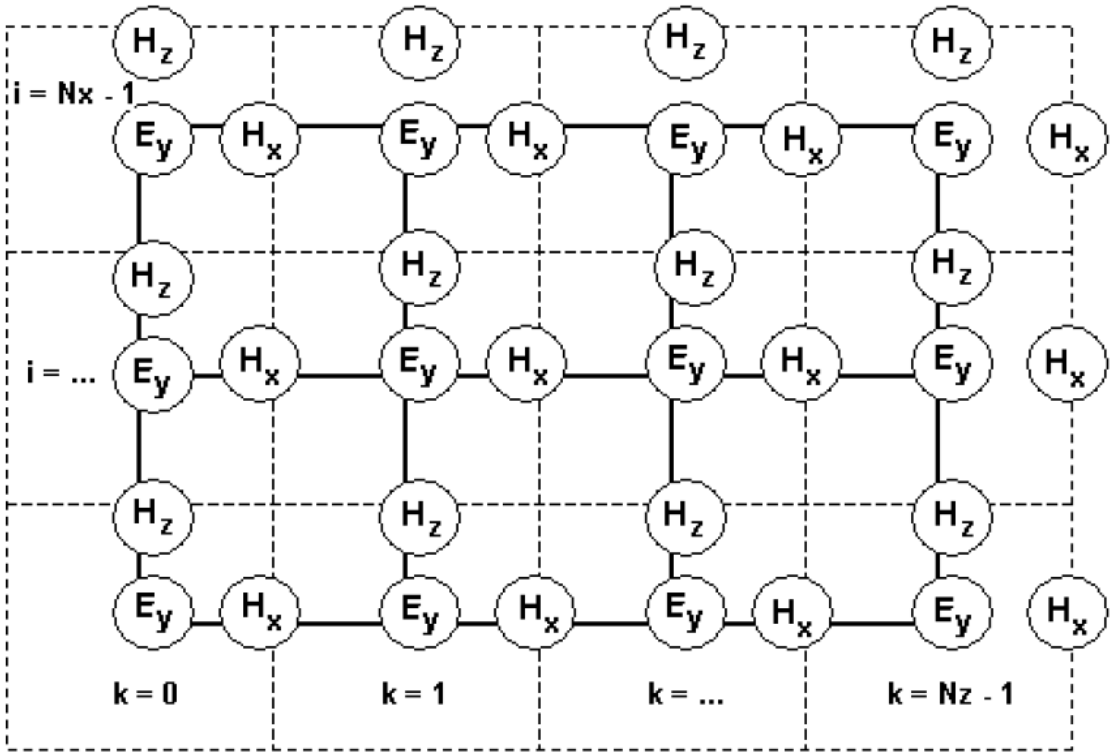

Figure A.2 Location of the TE fields in the computational domain

the mesh nodes given in Figure A.1. In Figure A.2, the solid lines represent the mesh given in Figure A.1. The E_y field is considered to be the center of the FDTD space cell. The dashed lines form the FDTD cells. The magnetic fields H_x and H_z are associated with cell edges. The locations of the electric fields are associated with integer values of the indices i and k. The H_x field is associated with integer i and $(k+0.5)$ indices. The H_z field is associated with $(i+0.5)$ and integer k indices. The numerical analog in Equation (A.1) can be derived from the following relation:

$$E_y^n(i,k) = E_y^{n-1}(i,k) + \frac{\Delta t}{\varepsilon \Delta z}[H_x^{n-1/2}(i,k+1/2) - H_x^{n-1/2}(i,k-1/2)] - \frac{\Delta t}{\varepsilon \Delta x}[H_z^{n-1/2}(i+1/2,k) - H_z^{n-1/2}(i-1/2,k)]$$

$$H_x^{n+1/2}(i,k+1/2) = H_x^{n-1/2}(i,k+1/2) + \frac{\Delta t}{\mu_0 \Delta z}[E_y^n(i,k+1) - E_y^n(i,k)] \quad \text{(A.2)}$$

$$H_z^{n+1/2}(i+1/2,k) = H_x^{n-1/2}(i+1/2,k) - \frac{\Delta t}{\mu_0 \Delta x}[E_y^n(i+1,k) - E_y^n(i,k)]$$

The superscript n labels the time steps while the indices i and k label the space steps and Δx and Δz along the x and z directions, respectively. This is the so-called Yee's numerical scheme applied to the 2D TE case. It uses central difference approximations for the numerical derivatives in space and time, both having second-order accuracy. The sampling in space is on a sub-wavelength scale. Typically, 10 to 20 steps per wavelength are needed. The sampling in time is selected to ensure numerical stability of the algorithm. The time step is determined by the Courant limit:

$$\Delta t \le 1/(c\sqrt{1/(\Delta x)^2 + 1/(\Delta z)^2}) \quad \text{(A.3)}$$

B. Nd: YAG Laser

The Nd:YAG laser used in the LIDT tests is one of Quanta-Ray series high energy laser from Spectra-Physics which is an industry-leading global supplier of advanced laser. The model of laser used is Pro-350, and its details shown in Table B.1- Table B.5.

Table B.1 Power Specifications of Pro-350

Item		**Value**
Repetition Rate (Hz)		10
Energy (mJ/p)	1064 nm	2500
	532 nm	1400
	355 nm	750
	EEO-355 nm	850
	266 nm	200

Table B.2 Performance Specifications of Pro-350

Wavelength	**Pulse Width**	**Short Term Energy Stability**	**Long Term Power Drift**
1064 nm	8-12 ns	±2 %	< 3 %
532 nm	1-2 ns < 1064 nm	±3 %	< 5 %
355 nm	2-3 ns < 1064 nm	±4 %	< 6 %
266 nm	3-4 ns < 1064 nm	±8 %	< 10 %

Table B.3 Beam Specifications - I of Pro-350

Spatial Mode Profile	**Standard Fit**	**ESM Fit**
Near field (1m)	> 70 %	Contact Spectra-Physics
Far Field (™)	> 95 %	Contact Spectra-Physics
Modulation	< 40 %	Contact Spectra-Physics

Table B.4 Beam Specifications - II of Pro-350

BeamLock Specifications	**Standard Pro Series**	**With BeamLock/D-Lok**
Beam Pointing Stability	< ±50 µrad %	< ±25 µrad
Beam Divergence	< 0.5 µrad	< 2x initial level
Lamp Lifetimes	30 million pulses	40 million pulses

Table B.5 Beam Specifications - III of Pro-350

Linewidth	**Value**
Standard	< 1.0cm^{-1}
Injection Speeded	< 0.003cm^{-1}
Timing Jitter	< 0.5ns

The dimensions of Quanta-Ray Pro-350 laser are shown in Figure A.3. In Figure A.3, the dimensions are in inches (cm).

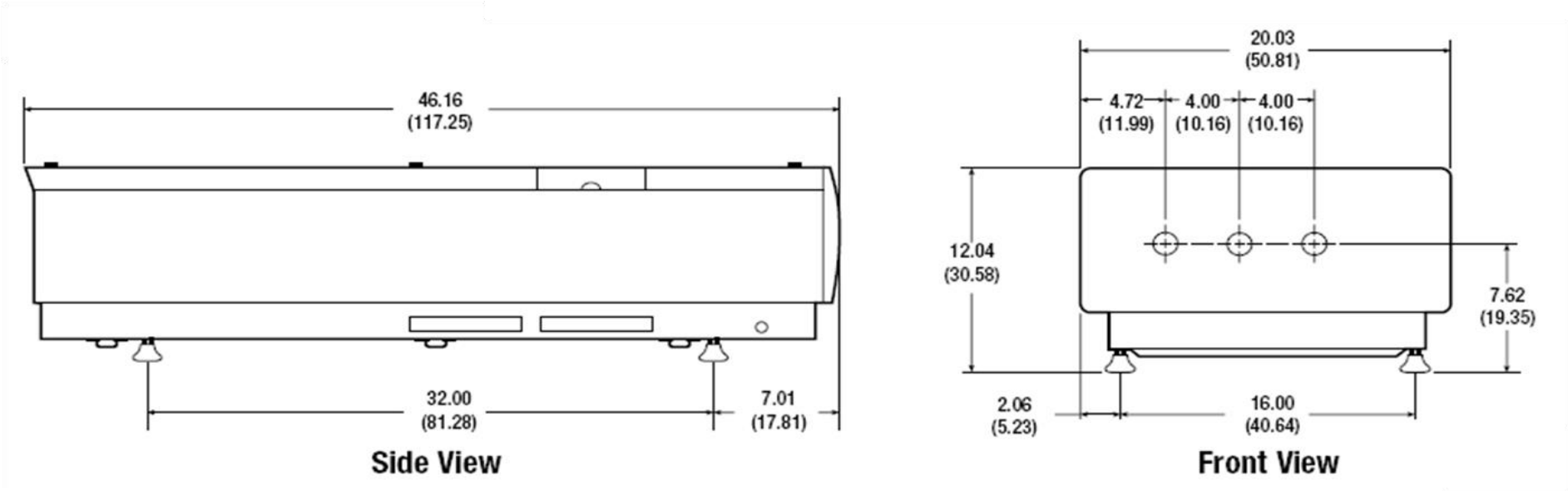

Figure A.3 Quanta-Ray Pro-350 laser dimensions

C. Experimental data for LIDT

Table C.1 LIDT data of Heraeus fused silica specimens for experiment 1

Processing method	Irradiation level (J/cm^2)	Number of test sites	Number of damage sites	Damage possibility (%)
Method #4: CMP+MEF+BOE	39.92	49	48	98
	31.05	49	0	0
	35.48	49	42	86
	34.15	49	21	43
	33.26	49	6	12
	34.59	49	30	61
	33.71	49	20	41
	33.71	49	0	0
Method #9: CMP+BOE	26.61	49	4	8
	31.05	49	32	65
	29.27	49	10	20
	30.16	49	17	35
	31.93	49	21	43
	32.82	49	24	49
	34.59	49	32	65
	35.48	49	49	100
	25.28	49	0	0

Table C.2 LIDT data of Heraeus fused silica specimens for experiment 2

Processing method	**Irradiation level (J/cm^2)**	**Number of test sites**	**Number of damage sites**	**Damage possibility (%)**
Method #10: CMP	16.38	49	6	12
	16.17	49	27	55
	19.36	49	49	100
Method #4: CMP+MRF+BOE	31.17	49	24	88
	29.57	49	21	84
	29.43	49	38	78
	31.77	49	37	76
	28.68	49	18	37
	26.91	49	12	24
	29.26	49	9	18
Method #5: CMP+MRF	26.91	49	6	12
	27.13	49	26	53
	27.45	49	36	73
	27.13	49	40	82
	29.85	49	47	96
	32.49	49	49	100

Table C.3 LIDT data of Yaohua fused silica specimens for experiment 3

Processing method	**Irradiation level (J/cm^2)**	**Number of test sites**	**Number of damage sites**	**Damage possibility (%)**
Method #4: CMP+MRF+BOE	12.19	49	49	100
	10.04	49	40	80
	7.34	49	20	41
	5.95	49	18	37
	4.90	49	5	10
Method #2: CMP+MRF+BOE+IBE	5.63	49	49	100
	4.50	49	40	80
	3.57	49	32	65
	2.75	49	8	16
Method #1: CMP+MRF+IBE+BOE	9.57	49	34	70
	7.60	49	10	20
	6.28	49	3	6

D. Published papers

Advanced Materials Research Vol. 662 (2013) pp 449-452
© (2013) Trans Tech Publications, Switzerland
doi:10.4028/www.scientific.net/AMR.662.449

Application of Taguchi methods and ANOVA in optimization of process parameters for surface roughness of fused silica in the Magnetorheological Finishing processes

Weiran Duan[1,2,a], Yifan Dai[2,b], Yong Shu[2,c], Ian Sherrington[1,d]

[1]School of Computing, Engineering, and Physical Science, University of Central Lancashire, Preston PR1 2HE, UK

[2]College of Mechatronic Engineering and Automation, National University of Defense Technology, Changsha 410073, China

[a]email: wduan@uclan.ac.uk; [b]email: dyf@nudt.edu.cn;

[c]email: shuyong_work@163.com; [d]email: isherrington@uclan.ac.uk

Keywords: Magnetorheological Finishing; Roughness; Taguchi method; ANOVA

Abstract. Surface roughness plays an important role on optical performances for optics in high-energy laser systems. In this study, optical surface of fused silica were polished by the Magnetorheological Finishing (MRF) processes. The polishing factors in term of Magnetorheological fluid (MR fluid) flow rate, polishing wheel rotational speed, electromagnet current, and polishing ribbon penetration depth, were carried out using an self-developed MRF machine to determine optimum conditions for surface roughness. The settings of the MRF processing parameters were determined by using Taguchi's experimental design method. Taguchi's $L_{27}(3^{13})$ orthogonal array, signal-to-noise (S/N) ratio and analysis of variance (ANOVA) were employed to investigate the optimal processing parameters. The experimental results indicate that surface with smaller roughness could be machined under the conditions with slower rotating speed and higher flow rate and current, and nearly independent of penetration depth.

Introduction

High quality fused silica (SiO_2) is an important material of choice for high-energy laser systems due to its excellent optical transmission performance in the ultraviolet (UV) region [1, 2]. The optical performance of such a perfect component would relate to its topographic specification. In order to obtain optical surface of high quality in terms of surface topography, choosing the best polishing method is one of the most critical cases in the optical manufacturing processes. Fused silica is such a brittle material that sub-surface damage (SSD) is easy to be generated during grinding and /or conventional polishing processes [3]. However, magnetorheological finishing (MRF) process is a well known polishing method without SSD for brittle materials such as fused silica due to its material removal mechanisms [4, 5]. Therefore MRF is commonly used in manufacturing high quality optics in high-energy laser systems [6].

In this study, the main focus was on the surface roughness. Optical surfaces of the fused silica substrate were fabricated in the MRF processes. To gain surface with fine roughness value, Taguchi's experimental design method was used to determine the setting of MRF process parameters. Taguchi's $L_{27}(3^{13})$ orthogonal array, signal-to-noise (S/N) ratio and analysis of variance (ANOVA) were employed to investigate the optimal processing parameters.

Experimental setup

Specimen preparation. Substrate material of the specimens was fused silica optical glass with dimensions of 45 mm long, 45 mm wide and 10 mm thick. There specimens were polished on both sides by conventional chemical-mechanical polishing (CMP) method in advance before MRF.

Surface roughness was measured by a white light interferometer (WLI) of Zygo New View 200 with 10x optical lens. The initial surface roughnesses of all the specimens were around RMS 0.4nm.

Advanced Materials Research Vol. 662 (2013) pp 595-598
© (2013) Trans Tech Publications, Switzerland
doi:10.4028/www.scientific.net/AMR.662.595

Compare study between planet motion and orbital motion in CCOS

YongShu[1, a], Feng Shi[1, b], Weiran Duan[1, 2, c], Shengyi Li [1, d]

[1] College of Mechanics Engineering and Automation, National University of Defense Technology, Changsha, 410073, China;

[2] School of Computing, Engineering, and Physical Science, University of Central Lancashire, Preston PR1 2HE, UK

[a]shuyong_work@163.com, [b]sf.wind@yahoo.com, [c]wduan@uclan.ac.uk, [d]syli@nudt.edu.cn

Keywords: CCOS (Computer Controlled Optical Surfacing); planet motion; orbital motion.

Abstract. In order to get a profound understanding of planet motion and orbital motion in CCOS (Computer Controlled Optical Surfacing), a compare study between them was conducted here. The material removals of two motions under the same conditions were simulated and the removal of planet motion was higher than that of orbital motion. The figuring abilities of two motions were also studied through the theory of cut-off frequency and the result showed that planet motion had a higher cut-off frequency. Then two figuring runs which employ the planet motion and the orbital motion were simulated. The convergence rates and polishing times of these two runs were compared and the result showed that planet motion had a higher figuring efficiency. As planet motion has stronger figuring ability and higher figuring efficiency, it's better to employ planet motion in CCOS to get higher convergence rate and higher accuracy when fabricating high quality mirrors.

Introduction

Computer controlled optical surfacing (CCOS) [1-2] uses a tool relatively smaller than work-piece to polish the mirror under the control of computer according to the measured surface error and control the removal at different region by varying scanning path, resident time, rotation velocity and polishing pressure of the polishing pad to fulfill the target of figuring and smoothing the surface of mirror. CCOS features in low cost, high efficiency, flexibility and plays an important role in the manufacture of mid-to-large aperture aspherical optics.

There are mainly two motions [3] which are usually employed in CCOS process: planet motion and orbital motion. The influence functions and removals of these two motions are different and play a different role in the figuring ability and figuring efficiency of a given optical surface. Full understanding of these two motions is important for the CCOS process, so a compare study was done here to analyze the properties of planet motion and orbital motion.

Removal analysis of two motions

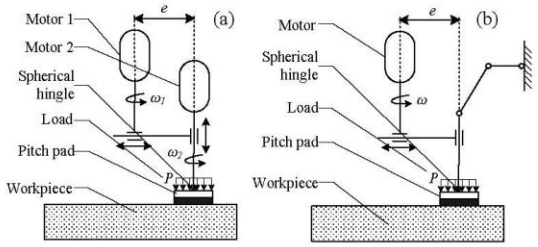

Fig.1 Schematic picture of planet motion (a) and orbital motion (b)

Fig.1 schematically shows the structure of planet motion and orbital motion. In planet motion (a), a polishing pad rotates about the tool center and orbits around the influence function center at the revolution of ω_1 and ω_2. Different from planet motion, in orbital motion (b) the polishing pad only orbits around the influence function center without rotation. From the brief introduction of these two